UNIVERSITÀ DEGLI STUDI
DELL'INSUBRIA

Department of Science and High Technology

PhD programme in **Environmental and Chemical Sciences**

Analytical investigation into the materiality and degradation of Japanese art materials

Supervisor: Prof. **Laura Rampazzi**

Candidate: **Ludovico Geminiani**

Analytical investigation into the materiality and degradation of Japanese art materials

Summary

1. Introduction

My PhD thesis reports on the research I conducted over the past three years, spanning different branches of heritage science. During this time, I worked with a range of materials, including textiles, dyes, pigments, and lacquers. I participated in several collaborative projects between Università degli Studi dell'Insubria and the Museo delle Culture in Lugano, Switzerland. Additionally, I gained valuable research experience during my internship at the Victoria and Albert Museum in London, UK. A major component of my thesis is an extensive experimental study on the degradation behaviour of silk textiles. Understanding the mechanisms of deterioration is a key objective in heritage science, as it provides a rational basis for informed conservation decisions.

The thesis is divided into two main parts.

The first focuses on the works of characterization of cultural heritage objects from diverse collections, predominantly of Japanese art. This section is designed to be cumulative, i.e. based on published manuscripts. The papers were mainly devoted to the study of textiles by means of FTIR spectroscopy and SEM-EDX, with the notable exception of the characterization works performed on some American lacquered object during the internship at the Victoria and Albert Museum.

The second part of the thesis is a monograph on my experimental study of the light-induced degradation of silk. The ageing of the fibre was obtained using a custom-made accelerated ageing protocol, and its behaviour was assessed through a specifically designed analytical method. The protocol of analyses included FTIR spectroscopy, X-ray diffraction, thermogravimetric analysis, UV-Vis spectroscopy, colourimetry, allowing to define some indicators of the extent of the degradation. The results of the work clearly indicated which combinations of dye and mordant accelerate or slow down the rate of the light-induced degradation of the fibre.

2. Characterization of Cultural Heritage Objects

2.1. From *connoisseurship* to technical art history

The most difficult thing is precisely what seems to be the simplest – that is, seeing. Not only our eye, but even more so our artistic sense, must receive thorough training, by means of much practice and prolonged reflection and engagement, before it is able, each time, to correctly see and appreciate individual forms, that is, to place them in harmonious relation to the whole.

Letter from Giovanni Morelli to Jean Paul Richter, 7 July 1878 [1]

Giovanni Morelli (Verona, 1816 – Milan, 1891) is widely recognised as one of Italy's most influential connoisseurs, particularly for his pioneering work in theorizing an experimental method of art attribution.

Connoisseurship - defined as the traditional practice of attributing artworks to specific artists or schools by comparing stylistic and formal elements - flourished from the late 19th century to the mid-20th century [2]. Although its foundations were often subjective and limited by the lack of reliable photographic reproductions, connoisseurship made vital contributions to the establishment of art history as a modern academic discipline. It developed into a practice that emphasized an expert's ability to "read" a painting, relying on deep visual knowledge and comparison with known works.

In his "Principle and Method" (Princip und Methode, 1890), Morelli delineates the craft of connoisseurship more precisely, contrasting it with the work of the coeval art historian [2]. This text is a dialogic prologue to the reissue of his earlier critical writings, where he critiques the dominant scholarly trends of his time, particularly in 19th-century Germany. Morelli's critique was directed at the rigidity of German academic traditions, which placed too much reliance on textual criticism and historical documentation rather than firsthand observation. He viewed this as a narrow and ultimately flawed approach, arguing that direct engagement with the artwork itself was indispensable for true understanding.

Morelli's primary thesis was that art could not be fully appreciated or understood by studying written texts alone. He urged his readers to go beyond the "printed page" and engage directly with the artwork: "*Art must be seen if we are to derive pleasure and true instruction from it.*" This is why he emphasized the importance of visiting museums and galleries, encouraging connoisseurs to leave libraries and archives behind in favor of in-person examination. He

believed that understanding art required a visual, experiential relationship that could only be fostered through personal observation, as he argued, "[...] the history of art must be studied solely in front of works of art. In books, man almost always loses the sense of himself.

The introduction of photography had a transformative impact on the field of art history, particularly on the practice of connoisseurship [2]. The commercial spread of photography revolutionized the ways in which artworks were studied, taught, and appreciated. Photography allowed for the reproduction of artworks, freeing them from their physical context and enabling broader access to their imagery. This shift forever altered how we perceive both the world and art itself. As a substitute for the original, photography permitted artworks to be observed outside their immediate environment, challenging traditional notions of size, scale, and authenticity. Over time, the development of colour photography and enhanced reproduction techniques further eroded the "safety distance" between the original work and its image. This gave rise to new concerns, particularly the risk of conflating the artwork with its photographic reproduction. As reproductions proliferated, there was an increasing danger that the original artwork would be reduced to its "virtual" images, with the nuances of the original lost in translation.

Nevertheless, for Morelli and others who shared his approach, artistic expertise could only be acquired through direct, firsthand experience. To separate the discipline of art history from its primary object of study - physical works of art - would be arbitrary and detrimental. Even today, with a wealth of photographs, digital databases, and high-resolution imaging techniques available, the most important tools for the connoisseur and the museum conservator remain the trained eye and cultivated intuition. Morelli's method, though lacking in scientific foundations, placed direct visual analysis at the center of art historical study.

In conservation, the first step of the methodology is the physical characterization of the object [3]. Yet, art objects possess both material and non-material qualities, creating a dual nature. Material aspects include the physical characteristics of an artwork, such as the materials it is made from, the techniques used in its creation, and the condition of its surfaces. These material features are studied through close physical examination, a skill that lies at the core of the conservator's expertise. The physical object is often thought of as the "client" in this process, with the conservator working to understand how best to care for and preserve it based on the knowledge gathered from examining its condition and construction.

In contrast, non-material aspects refer to the meanings and functions an object holds within its cultural context [3]. This includes the intended use of the artwork, the significance it held for its original audience, and the values society attaches to it today. While certain aspects, such as an object's rarity, are based on physical facts, they gain importance only through cultural judgments. For instance, rarity might influence the perceived monetary value or historical significance of an artwork, but such judgments depend on societal values rather than intrinsic physical qualities.

A complete understanding of an art object, therefore, requires a dual approach that encompasses both material and non-material aspects [3]. This broader perspective allows for a fuller appreciation of the object's significance within its cultural and historical context. Information from materials science, such as the chemical properties and physical behaviour of the materials used, enhances the physical examination by providing insights into the artwork's creation and aging process. Understanding these factors allows conservators to reconstruct the history of the object and predict how it might change over time.

In recent decades, the scientific analysis of art has transitioned from a mere auxiliary discipline into the independent field of technical art history, complete with its own institutions, conferences, and journals. The concept of technical art history emerged in the 1990s, with David Bomford coining the term to describe a field of study focused on the physical aspects of artworks, their creation, and the creative processes of the artists [4,5]. Technical art history goes beyond analyzing the physical materials and techniques used in art; it also explores the artist's intentions, the cultural context of the work, and the ways in which it was perceived by contemporary audiences. Lynn Hermens expanded on Bomford's ideas, advocating for a truly interdisciplinary approach that combines art history with scientific analysis and conservation techniques. Hermens envisioned technical art history as a field where insights from various disciplines—including chemistry, physics, and materials science—are integrated into a holistic understanding of art.

A useful analogy for understanding how technical art history gathers and analyzes information is forensic science [5]. Like forensic scientists who reconstruct a crime scene using evidence from multiple disciplines, technical art historians collect and interpret data from a wide range of sources to reconstruct the history and context of an artwork.

The technical art history research protocol begins with the artifact itself—whether a single object, a collection, or an installation—and proceeds through a series of steps, with each stage informed by the findings of the previous one. Throughout this process, evidence bases such as scientific reference data, historical documentation, and secondary literature are used to support and contextualize the results.

The collaboration between conservators, art historians, and scientists is central to technical art history. By working together, these experts can develop a more nuanced understanding of artworks, drawing on their respective areas of expertise to uncover new insights into the physical and conceptual nature of art objects. This interdisciplinary cooperation is essential for addressing complex questions about conservative issues and to develop historical arguments grounded in rigorous physical analysis of art objects.

2.1.1. The Case of Textiles

This interdisciplinary perspective is essential for gaining a holistic understanding of textiles and their significance across different fields, including conservation and restoration.

In recent years, historical textiles have increasingly been recognized as valuable cultural artifacts, reflecting the historical, social, artistic, economic, and political contexts of their production [6,7]. From ancient times, textiles have been indispensable to human life, serving a multitude of purposes - from providing comfort and protection to functioning as artistic expressions or symbols of social status and economic power. Throughout history, textiles have been highly prized by all levels of society, not only for their utility but also for the skilled craftsmanship required to produce them. The labor-intensive processes involved in acquiring raw materials and producing textiles often made them costly, further elevating their importance.

Textile production has frequently formed the economic backbone of entire communities due to its complexity and profitability. The demand for textiles peaked during the Early Modern period, when global trade routes brought a wide variety of sophisticated textile products to local markets, enriching them with goods from across the world. This period of heightened interest in textiles is mirrored today in the increasing number of exhibitions, academic studies, and publications devoted to the field [8–11].

The study of textiles often involves a multidisciplinary approach, incorporating visual, technical, and material analysis of objects alongside written and visual historical sources. This approach aims to contextualize textiles within the broader framework of their creation, usage, and cultural significance. More recently, advances in the natural sciences have emphasized the importance of material analysis to gain deeper insights into the technological processes behind textile production, as well as to develop better strategies for their long-term preservation. The integration of scientific methods, including analytical chemistry and cutting-edge technology, is becoming increasingly vital in textile research, especially when historical sources alone do not provide sufficient information [12].

2.1.2. The case of Japanese art

Japanese art and craft traditions are not confined to the rigid distinctions between applied and fine arts, as the concept of *bijutsu* (fine arts) did not emerge in Japan until the late nineteenth century[13,14]. While it is unnecessary to claim Japan's artistic tradition as uniquely exceptional, as was often done in the 1990s, it is undeniable that a broad and diffuse aesthetic permeates various Japanese arts. This aesthetic is evident in a wide range of disciplines, including painting, sculpture, ceramics, lacquerware, textiles, metalworking, architecture, gardens, calligraphy, photography, printmaking, and design. A vital aspect of this artistic heritage is represented by folk art, commonly referred to as *mingei*, which means "arts of the people." This term is associated with a philosophical movement that arose in response to the rapid industrialization of the late nineteenth century, aiming to preserve traditional folk crafts [15].

In this context, *mingei* art is not regarded as "popular" in the sense of being inferior or "poor" art, but rather as craftsmanship valued for its utility in everyday life. The meticulous dedication

and attention to detail applied to even the most humble objects is central to Japanese aesthetics and craftsmanship, reflecting an ingrained cultural ethos that prizes quality and precision in all things, even in what might seem insignificant. This approach is also a key factor in the success of modern Japanese design.

Japan is home to numerous "traditional" crafts, each with long-established, specialized practices, unique materials, and strong regional identities. These craft traditions are often viewed as *cultural property*. In the 1950s, a formal classification of these crafts as *Intangible Cultural Property* was introduced to safeguard the skills that underpin these traditions [10,11]. Two primary criteria were used to determine whether a craft was worthy of preservation: (1) its particularly high cultural value, and (2) the risk of its disappearance if not supported by government measures.

In cases where transmitted craft skills involve specialized techniques, the emphasis has been on documenting and preserving the technical processes. This system seeks to identify and protect high-value skills to ensure the continuity of these traditional practices. Individuals who embody or champion these distinct craft traditions are honored as *Holders of Intangible Cultural Property*, commonly recognized as *Living National Treasures*. To qualify for this title, the craft must hold a significant place in the history of Japanese art and exhibit unique regional characteristics. This sophisticated framework of recognizing and preserving craft skills supports a deep understanding and appreciation of handmade traditions, despite existing cultural tensions and ongoing debates.

Given this context, the technical study of Japanese art is both rewarding and challenging. On the one hand, many traditional crafts are still alive, making it relatively easy to access raw materials and gather information about past techniques. On the other hand, the scarcity of previous research on specific Japanese artistic materials presents a significant challenge to scholars and researchers in the field.

2.1.3. The case of Indigenous American art

Within decades of the Spanish conquest, Mexico became a key hub of global commerce, connecting Asia and Europe. The Manila galleons transported luxury goods like Chinese silk textiles, Japanese lacquerware, Indian ivory, and spices to Mexico, where they were sold in the bustling markets of Mexico City. These Asian goods captivated both European colonizers and indigenous populations, influencing local artistic production [16].

Asian imports, such as finely woven textiles, ceramics, lacquerware, and screens, were highly sought after in Mexico and the rest of the Americas. However, due to their high cost, fragility, and limited availability, local artisans began to replicate these items. This resulted in a blending of Asian, European, and indigenous styles. For example, Mexican craftsmen produced folding screens inspired by Japanese models, ceramics that imitated Chinese porcelain, and locally woven textiles that mirrored Asian silk and cotton fabrics. These hybrid creations were not

merely imitations but sophisticated reinterpretations, blending local materials and techniques with global artistic influences.

One of the most significant examples of this cross-cultural exchange was the development of Latin American lacquerware [17]. Indigenous artisans in Mexico, Colombia, and Ecuador adapted pre-Columbian lacquer techniques to create objects that closely resembled Asian lacquerware. Catholic missionaries likely encouraged this adaptation by providing European prints and drawings as models for decoration. By the 17th and 18th centuries, Latin American artisans had mastered Asian-inspired techniques such as inlay, carving, and the use of gold and silver flakes, producing works of exceptional complexity and beauty. These pieces became highly prized in both the Americas and Europe, rivaling imported Asian lacquerware.

The influence of Asian art on colonial Latin American production challenges traditional notions of artistic "centers" and "peripheries," which often placed Europe at the center of artistic innovation and viewed colonial regions as peripheral imitators. Instead, colonial Latin America was a dynamic artistic center in its own right, connected to global trade networks and capable of producing art that integrated diverse influences. The cosmopolitan nature of cities like Mexico City, with direct access to goods from across the world, contributed to this cultural blending. The result was a unique artistic style that reflected the fusion of indigenous, European, and Asian elements.

2.1.4. References

[1] V. Locatelli, Metamorfosi romantiche. Le teorie del primo Romanticismo tedesco nel pensiero sull'arte di Giovanni Morelli, Campanotto, Pasian di Prato, 2011.

[2] V. Locatelli, "Es sey das Sehen eine Kunst" Sull'arte della connoisseurship e i suoi strumenti, Kunstgeschichte : Open Peer Reviewed Journal (2014).

[3] Barbara. Appelbaum, Conservation Treatment Methodology, Routledge, London, 2007.

[4] S. Dupré, Materials and techniques between the humanities and science: introduction, History of Humanities 2 (2017) 173–178. https://doi.org/10.1086/690577.

[5] E. Hermens, Technical Art History: an interdisciplinary journey into the making of art, Amsterdam, 2024.

[6] A. Serrano, M.J. Ferreira, E.C. De Groot, Textile heritage and interdisciplinity, Estudos Sobre Têxteis Históricos - Studies in Historical Textiles 31 (2019).

[7] V.A., Textiles and clothing along the Silk Roads, United Nations Educational, Scientific and Cultural Organization (UNESCO) and China National Silk Museum (CNSM), Paris (France) and Hangzhou, Zhejiang (China), 2022.

[8] E. Richardson, G. Martin, P. Wyeth, X. Zhang, State of the art: Non-invasive interrogation of textiles in museum collections, Microchimica Acta 162 (2008) 303–312. https://doi.org/10.1007/s00604-007-0885-x.

[9] E.-A. Haldane, L. Hillyer, D. Kalsi, The Conservation and Display of Indian Textiles at the Victoria and Albert Museum, in: S. Jose, S. Thomas, P. Pandit, R. Pandey (Eds.), Handbook of Museum Textiles, Volume 1: Conservation and Cultural Research, John Wiley and Sons, Hoboken, New Jersey (U.S.), 2022: pp. 291–314.

[10] T. Parry-Williams, Made-by-hand: [Re]valuing traditional (Japanese) textile practices for contemporary design, Craft Research 6 (2015) 165–186. https://doi.org/10.1386/crre.6.2.165_1.

[11] M. Tada, K. Yamashiro, I. Oka, A. Goto, N. Kuwahara, Structural Analysis for Replicating Japanese Cultural Property Braids, Studies in Conservation 65 (2020) 399–410. https://doi.org/10.1080/00393630.2020.1715625.

[12] A. Timar-Balazsy, D. Eastop, Materials, in: Chemical Principles in Textile Conservation, Third Edition, Routledge, New York, NY, USA, 1998: pp. 3–66.

[13] Nobuo. Tsuji, N.Coolidge. Rousmaniere, History of art in Japan, Columbia University Press, 2019.

[14] H. Yiengpruksawan, Japanese Art History 2001: The State and Stakes of Research., Art Bulletin 83 (2001) 105–122.

[15] P.F. Campione, Japan. Arts and Life. The Montgomery Collection, Skira, Milan, 2022.

[16] D. Carr, Introduction: Asia and the New World, in: Made in the Americas: The New World Discovers Asia, Museum of Fine Arts, Boston, 2015.

[17] M. Codding, The lacquer arts of Latin America, in: Made in the Americas: The New World Discovers Asia, Museum of Fine Arts, Boston, 2015.

2.2. Unveiling the complexity of Japanese metallic threads

In the framework of an extensive survey campaign on a collection of Japanese samurai armours, metallic threads from different parts of the traditional equipment were studied by several analytical techniques. The collection of armours belongs to Museo delle Culture (Lugano, Switzerland) and it is composed of ten elements, which date back from the 15th to 20th century. Metallic threads under study come from six of ten elements of the collection and represent a complex and unique multimaterial, which shows specific characteristics in Japanese tradition (*kinran*). The multianalytical approach based on ATR-FTIR spectroscopy and SEM-EDX analysis, together with a careful observation with optical and digital microscopy, permitted to obtain a complete characterization of materials, which have shown a great variability in metal foils and in organic adhesives (urushi, animal glue, starch). Gold and silver turned out to be not so largely used as scholars thought, while aluminium showed a great diffusion. Within the collection of analysed armours, the obtained results allowed us for the first time to get a complete comprehension of materials and techniques used by Japanese craftsmen, and to observe differences in the quality of the materials and in manufacture technology over the centuries.

Available online at Unveiling the Complexity of Japanese Metallic Threads (mdpi.com)

Reproduced with permission from Heritage 2021, 4, 4017–4039

2.3. Differentiating between Natural and Modified Cellulosic Fibres using ATR-FTIR Spectroscopy

This paper presents the limitations and potential of ATR-FTIR spectroscopy applied to the study of cellulosic textile collections. The technique helps to differentiate natural fibres according to the content of lignin, pectin, hemicellulose, and wax, although some problematic issues should be considered. The spectral differences derived from the environmental humidity uptake and the plant composition are reviewed and discussed in the light of new experimental data. Diagnostic bands are proposed that can discriminate between different fibres from different plants. The contribution of ageing is also considered, demonstrating that sometimes aged fibres cannot be reliably recognised. In contrast, the potential of ATR-FTIR spectroscopy to discriminate between natural and modified fibres is discussed and proven. The best results were obtained when microinvasive ATR-FTIR spectroscopy was coupled with SEM observations. The proposed protocol was tested on microsamples of various cellulosic materials from traditional Japanese samurai armours dating from the 16th to the 20th centuries (Morigi Collection, Museo delle Culture, Lugano, Switzerland). The results facilitated a complete characterisation of the materials and demonstrated that the protocol can be used to study a wide variety of cellulosic materials, including both natural and man-modified fibres, and paper.

Available online at Differentiating between Natural and Modified Cellulosic Fibres Using ATR-FTIR Spectroscopy (mdpi.com)

Reproduced with permission from Heritage 2022, 5, 4114–4139

2.4. Historical Silk: A Novel Method to Evaluate Degumming with Non-Invasive Infrared Spectroscopy and Spectral Deconvolution

To correctly manage a collection of historical silks, it is important to detect if the yarn has been originally subjected to degumming. This process is generally applied to eliminate sericin; the obtained fibre is named soft silk, in contrast with hard silk which is unprocessed. The distinction between hard and soft silk gives both historical information and useful indications for informed conservation. With this aim, 32 samples of silk textiles from traditional Japanese samurai armours (15th–20th century) were characterized in a non-invasive way. ATR-FTIR spectroscopy has been previously used to detect hard silk, but data interpretation is challenging.

To overcome this difficulty, an innovative analytical protocol based on external reflection FTIR (ER-FTIR) spectroscopy was employed, coupled with spectral deconvolution and multivariate data analysis. The ER-FTIR technique is rapid, portable, and widely employed in the cultural heritage field, but rarely applied to the study of textiles. The ER-FTIR band assignment for silk was discussed for the first time. Then, the evaluation of the OH stretching signals allowed for a reliable distinction between hard and soft silk. Such an innovative point of view, which exploits a "weakness" of FTIR spectroscopy—the strong absorption from water molecules—to indirectly obtain the results, can have industrial applications too.

Available online at Historical Silk: A Novel Method to Evaluate Degumming with Non-Invasive Infrared Spectroscopy and Spectral Deconvolution (mdpi.com)

Reproduced with permission from Materials 2023, 16, 1819

2.5. New Evidence of Traditional Japanese Dyeing Techniques: A Spectroscopic Investigation

Japanese textile tradition is renowned for its intricate designs achieved through a variety of dyeing techniques, including *kasuri*, *shibori*, and paste-resist dyeing. These techniques are often combined within a single textile, resulting in exceptionally elaborate creations. Our paper delves into the technical aspects and complexities of these methods, highlighting the dynamic interplay between tradition and innovation in Japanese textile production. Our scientific endeavour focused on some textiles dating between the 19th and 20th centuries and belonging to the Montgomery Collection of Japanese folk art. Employing non-invasive techniques such as visible reflectance spectroscopy and ER-FTIR spectroscopy, we uncovered key insights into the materials and methods utilized in the creation of these textiles. Our analysis revealed a diverse array of pigments and dyes, including plant-derived, inorganic, and synthetic variants. These findings illuminate the cultural syncretism between traditional Japanese practices and the adoption of new materials from the West, underscoring the dynamic nature of textile production in Japan. Furthermore, ER-FTIR spectroscopy elucidated the predominant use of cotton as the primary fibre in the textiles, aligning with historical records of Japan's role as a major producer of cotton yarn. Analysis of white areas within the textiles revealed evidence of resist-paste dyeing techniques, particularly *tsutsugaki* and *katazome*, through the absence of dye penetration and the characteristic appearance of white lines. Confirmation of indigo dyeing techniques (*aizome*) was achieved through ER-FTIR spectroscopy, providing reliable identification of indigo and Prussian blue in various shades of blue present in the textiles. Additionally, the detection of Western-derived dyeing method (*utsushi-yuzen*) and free-hand painting (*kaki-e*), offers insights into the diversity of dyeing practices employed by Japanese artisans. The presence of proteinaceous materials and synthetic dyes observed in some textiles has implications for conservation practices, suggesting the need for tailored approaches to ensure the preservation of these culturally significant artifacts. Overall, these scientific results shed new light on the materials, techniques, and cultural contexts underlying Japanese textile production, advancing our understanding of this rich artistic heritage and informing future research endeavours in textile science and conservation.

Available online at New Evidence of Traditional Japanese Dyeing Techniques: A Spectroscopic Investigation (mdpi.com)

Reproduced with permission from Heritage 2024, 7, 3610–3629.

2.6. A Recently Identified Barniz Brillante Casket at Bateman's, the Home of Rudyard Kipling

A casket held at Bateman's, Rudyard and Caroline Kipling's home in Sussex—now a National Trust property—was recently recognised as a *barniz brillante* work. Objects made of *barniz brillante*, a technique featuring the Indigenous American material called *mopa mopa*, are relatively rare and have only sparingly been studied using scientific analysis techniques. A collaboration between the National Trust and the Victoria and Albert Museum has produced scientific evidence which will be invaluable in the study and the understanding of this type of object. The scientific analysis of the casket was conducted exclusively in a non-destructive and non-invasive manner, to preserve the integrity of the object which is in very good condition. The Bateman's casket is characterized by a dark underdrawing, made with a material which is transparent in the infrared region of the electromagnetic spectrum. Most of the areas decorated with silver leaf have tarnished due to the formation of what is likely to be silver chloride. This study represents a significant step towards the comparative scientific study of *barniz brillante* objects in other collections, which in turn will make it possible to suggest a timeline for their manufacture, and even identify workshops.

Available online at A Recently Identified Barniz Brillante Casket at Bateman’s, the Home of Rudyard Kipling (mdpi.com)

Reproduced with permission from Heritage 2024, 7, 1569–1588.

2.7. Mexican Lacquer at the Victoria and Albert Museum: Analysis of Three Bateas

This study investigates the materials and techniques used in three Mexican platters, or bateas, from the Victoria and Albert Museum collection. Our analytical approach included the use of non-invasive techniques, such as infrared reflectography, scanning X-ray fluorescence, and digital microscopy, which informed limited but targeted sampling. Traditional pigments were identified, including indigo, carbon black, red lead, lead white, and orpiment, and materials such as dolomite, gypsum, ochres, and clay were also found. A red organic dye was seen but could not be identified. The stratigraphy of the objects was also investigated. The condition of the objects was also evaluated, and the results will be used to inform future conservation decisions. The findings add to the published knowledge of the materials and techniques of early colonial Mexican objects and can be of use in future investigations, facilitating exchanges and collaborations focused on this type of objects, which are rare in UK collections.

Available online at Mexican Lacquer at the Victoria and Albert Museum: Analysis of Three Bateas (mdpi.com)

Reproduced with permission from Heritage 2024, 7, 4647–4665.

2.8. Non-invasive identification of historical textiles and leather by means of external reflection FTIR spectroscopy

Identifying the fibres in historical textiles presents a complex challenge due to the wide variety of plant, animal and early synthetic materials that have been used. Traditionally, this identification process involves sampling followed by either microscopic examination or ATR-FTIR spectroscopy. However, there are instances when sampling is restricted due to the good condition or significant value of the object under analysis. Additionally, the presence of leather components alongside textiles can further complicate the identification. This paper proposes a novel non-invasive method for fibre identification based on External Reflection (ER) FTIR spectroscopy, which has been rarely applied to textiles or leather. The current research demonstrates that ER-FTIR spectrum is a viable tool for fibre identification on both recent and historical textiles. The non-invasiveness of the analytical approach enables a comprehensive investigation without compromising the number or position of samples. With respect to ATR-FTIR spectra, the ER-FTIR spectra frequently exhibit an amplification of certain diagnostic bands, facilitating the identification of the various fibres examined in this study (cotton, hemp, viscose, silk, wool, leather, polyamide, acrylic, polyester). The extended spectral range (7500-375 cm-1) which is provided by ER-FTIR spectrometry also contains extra bands in the near infrared region, which can provide key information for the discrimination due to the lack of distortion phenomena. The technique was applied to the characterisation of textile materials coming from a collection of 10 traditional Japanese samurai armours spanning from the 16th to the 20th century (Museo delle Culture, Lugano, Switzerland). For the first time, the results provided a comprehensive overview of the textiles utilized in Japanese armours across various historical periods. Overall, the appearance of materials in samurai armours reflects the evolution of armour-making techniques and the influence of socio-cultural factors throughout Japanese history. Synthetic and semi-synthetic materials were easily detected, revealing the occurrence of a past conservation treatment or the early adoption of modern man-made materials in the manufacturing of traditional armours. The approach outlined in this case study can be applied to textile collections of various kinds, offering a reliable mean to discern the yarn composition and detect non-original components. The method also appears as a valuable prescreening tool for designing a less intrusive yet more informative sampling strategy, should additional details about fibre type and dyeing be necessary.

Available online at Non-invasive identification of historical textiles and leather by means of external reflection FTIR spectroscopy - ScienceDirect

2.9. Historical silks: a novel method to evaluate their condition with ATR-FTIR spectroscopy and Principal Component Analysis

Understanding the conservation condition of historical silk yarn allows to define appropriate storage, care and display of historical silk collections. This paper discusses the characterisation of silk fabrics from a collection of traditional Japanese samurai armours which date back from the 16th to the 20th century (Morigi Collection, Museo delle Culture, Lugano, Switzerland). An analytical protocol to assess silk fabrics conditions was defined, based on microinvasive ATR-FTIR spectroscopy. In particular, the amide I and II region was studied in order to extrapolate the conformational information about silk proteins. According to literature, this kind of information can be related to different degradation stages. A linear correlation was found between the amide I and the amide II shifts, allowing to assess the silk fibre condition. Along with this bivariate approach based on intensity ratios, a multivariate approach based on Principal Com- ponent Analysis was also applied to ATR-FTIR spectra. This allowed to group together silks with the same state of preservation. The findings of this research offer a valuable method to researchers and conservators to identify the most damaged textiles; the differentiation between original and restoration materials was also possible in some cases.

Available online at Historical silks: a novel method to evaluate their condition with ATR-FTIR spectroscopy and Principal Component Analysis - ScienceDirect

Reproduced with permission from Journal of Cultural Heritage 67 (2024) 9–22.

3. Experimental Study of Light-Induced Degradation of Silk

3.1 Introduction to silk degradation

3.1.1 The terminology of degradation

In 1996 the International Union of Pure and Applied Chemistry (IUPAC) prepared a list of definitions related to chemical transformation of polymers [1]. Ageing, degradation and lifetime of a polymeric material can be defined as follows:

- Ageing (or aging): Processes that occur in a polymeric material during a specified period of time, and that usually result in changes in physical and/or chemical structure and the values of the properties of the material.
- Degradation: Chemical changes in a polymeric material that result in undesirable changes in the values of in-use properties of the material
- Lifetime: the time during which a polymer keeps a fraction of its original property values to such an extent to be useful in an intended application.
- Durability: The ability of a polymeric material to retain the values of its properties under specified conditions.
- Stability: The ability of a polymer to maintain the values of its properties over a specified period of time.
- Weathering: Exposure of a polymeric material to a natural or simulated environment.

The term *ageing* of polymers is generally associated with long-term changes in polymer properties due to *weathering*, which may involve both physical processes, such as polymer recrystallization or protein denaturation, as well as chemical *degradation* processes. From a chemical point of view, the average molar mass may be reduced through macromolecular chain bond scission, or increased through cross-linking, rendering the polymer insoluble. Some degradation reactions involve changes where the average molar mass remains largely unchanged, but side groups dissociate or undergo modification. In advanced stages, polymer degradation may become visible, marked by crack formation and a significant reduction in mechanical properties. In most cases, polymer degradation is associated with a reduction in average molar mass [2].

As polymer and polymer composites are increasingly being used in a wide range of applications, there is growing demand for manufacturers to guarantee the life expectancy – *lifetime* – of their products. In the effort to estimate this crucial aspect, two aspects can be

distinguished: the first is the *stability* of a material or composite, referring to its resistance to environmental factors like oxygen, ozone, moisture, heat, and light, which primarily cause chemical changes. The second aspect is *durability*, which pertains to the material's physical resistance to changes under stress and strain during use [3].

3.1.2 Degradation Factors Affecting Polymers

The type of degradation a polymer undergoes is determined by the nature of its initiating factor. Chemical, physical and biological factors can be common causes of degradation [2,4].

Chemicals

Chemical degradation occurs when polymers react with chemicals like water, acids, or alkalis, leading to hydrolysis. This process breaks down polymer chains, reducing molecular weight, toughness, and fracture resistance. Stress can accelerate this process by increasing fluid uptake and chain scission. Environmental Stress Cracking (ESC) is a common cause of polymer failure, occurring when polymers crack under combined chemical and mechanical stress. Amorphous polymers are particularly susceptible due to their open structure, which allows easier fluid penetration. Cracking is preceded by the formation of crazes, which are small voids held together by fibrils, leading to structural failure.

Moisture, in particular, can be absorbed by polymeric materials leading to potentially harmful effects. The extent of degradation is often proportional to the amount of moisture absorbed, and this absorption can negatively impact the material in various ways. These include dimensional changes such as swelling, a reduction in the glass transition temperature (Tg), decreased mechanical and physical properties (e.g., stiffness, strength, and hardness), and surface damage like blistering. Besides that, water can influence other degradation mechanisms such as oxidation and hydrolysis.

Biological attack

While most thermoplastics resist microbial attack, natural polymers are vulnerable, especially due to pest attack.

Creep and fatigue

Creep refers to the gradual deformation of polymers under constant load over time. It occurs even at low stress levels and can lead to either ductile or brittle failure depending on the load and temperature.

Fatigue in polymers occurs when they are subjected to cyclic loads, leading to failure at stress levels lower than what they can withstand under static conditions. Fatigue failure can be sudden and occurs without much warning, making it a critical factor in polymer durability.

Heat

A critical aspect of polymer degradation is the dissociation of chemical bonds due to heat (thermolysis). For instance, carbon-carbon (C-C) bonds in a polymer dissociate into radicals at temperatures of approximately 486°C. In contrast, oxygen-oxygen (O-O) bonds dissociate at a much lower temperature of around 30°C. This significant difference in dissociation thresholds explains why hydrocarbon polymers in inert atmospheres begin to decompose into volatile compounds above 350°C. At lower temperatures, however, it is often structural defects or irregularities in the polymer chains that initiate degradation. These weak spots render the polymer susceptible to breakdown even before reaching high decomposition temperatures [2].

Prolonged or even short-term exposure to elevated temperatures can lead to irreversible chemical and physical changes in polymeric materials. These changes typically include accelerated degradation processes like oxidation, chemical attack, and mechanical creep. As temperatures rise, mechanical properties such as stiffness and strength tend to diminish. Among the various degradation mechanisms, oxidation is usually considered the most significant, as the rate of polymer degradation increases with the amount of oxygen present. In this case, the pathway of degradation is called thermo-oxidative.

The degradation process typically includes a long induction period, during which no significant deterioration is apparent. Once this period ends, the rate of degradation accelerates, leading to a sharp decline in the polymer's mechanical properties. This induction period, which is temperature-sensitive, can be considered the effective serviceable lifetime of the polymer.

Light

Exposure to solar radiation, especially UV light, causes photo-degradation in polymers. This results in the formation of free radicals that can lead to chain scission and mechanical degradation. Photooxidation is the main pathway and primarily affects the surface layers of polymers.

3.1.3 Photochemical Deterioration

Theoretical Aspects

There are a few fundamental principles in photochemistry that play crucial roles in understanding how light interacts with materials, particularly in the context of material degradation [3].

The Grotthus-Draper Law states that only the radiation absorbed by a substance can cause a chemical reaction. This principle underscores that for light to have any chemical effect on a material, it must first be absorbed by that material. However, applying this principle in practice can be complex due to phenomena like photosensitization, where the actual degradation is caused by another substance that absorbs the light and then transfers the energy to the material of interest. For example, when a coloured pigment or dye absorbs specific wavelengths of light, it may be assumed that these wavelengths are responsible for its deterioration. However, if another substance in the material absorbs the light and then transfers the energy to the pigment, causing it to degrade, the absorption spectrum of the pigment itself may not reveal the true cause of its fading. This complicates efforts to predict or prevent photodegradation in such materials.

The Stark-Einstein Law, also known as the law of photochemical equivalence, states that for every photon absorbed by a molecule, one molecule is activated. This principle implies that the energy from a photon can directly cause a chemical change, such as breaking a chemical bond (photolysis). However, the occurrence of photolysis is relatively rare, especially when involving near-ultraviolet and visible light, compared to UV-C light, which has higher energy and is more likely to cause direct bond scission. Once a molecule absorbs a photon, the energy may be dissipated in various ways, including heat, fluorescence, phosphorescence, chemical transformation, or bond breaking. It can be defined the quantum yield (Φ) for each reaction or phenomenon, that is

$$\phi = \frac{number\ of\ molecules\ reacting\ in\ a\ given\ time}{number\ of\ photons\ absorbed\ in\ the\ same\ time}$$

The photochemical efficiency of these processes, or the quantum yield, is often less than 1, meaning that not all absorbed photons result in a chemical reaction. The complexity of photochemical processes in materials like paints, varnishes, and textiles often leads to low quantum efficiencies.

Another fundamental principle states that the total amount of photochemical damage is determined by the net exposure, which is the product of irradiance intensity (or illumination, measured as luminous flux) and time, assuming other factors are negligible. Essentially, 100 lux of intensity for 1 hour is considered to cause the same amount of damage as 1 lux of the same radiation for 100 hours, as the product in both cases is 100 lux-hours. In both scenarios, the total number of photons striking the sample remains the same. This concept is known as the

principle of reciprocity. Reducing the intensity of illumination decreases the number of photons per minute but does not change their energy, as this depends on their wavelength. It is the energy of the absorbed photons that can trigger a photochemical change. Therefore, theoretically, there is no minimum intensity of light below which photochemical reactions will stop occurring.

The direct breaking of molecules (photolysis or photolytic cleavage) is rarely the primary cause of deterioration in solids and liquids exposed to visible and near-ultraviolet radiation [3]. More commonly, energy is transferred to neighboring molecules. Collisions with neighboring molecules can dissipate the excitation energy to such an extent that the quantum efficiency decreases. However, it is particularly important when energy transfer initiates a sequence of chemical events, known as secondary processes in photochemistry. These secondary reactions are sometimes referred to as post-irradiation effects and they often include oxygen and water vapor as reactants. An example of a reaction occurring in secondary processes can be seen in a simplified series of chemical steps proposed to explain the formation of hydrogen peroxide on dyed fabric.

Primary Process:

Excitation

$HD\ (dye) + h\nu\ (light) \rightarrow HD^*\ (activated\ dye)$

Transfer of excitation energy

$HD^* + O_2\ (oxygen) \rightarrow HD + O_2^*\ (activated\ oxygen)$

Secondary Processes:

Excited oxygen converts water to hydrogen peroxide summarized in the following equation:

$O_2^* + 2H_2O\ (water) \rightarrow 2H_2O_2\ (hydrogen\ peroxide)$

Ordinary chemical reactions between hydrogen peroxide and cellulose, or the dye, may then follow:

$H_2O_2 + Cellulose \rightarrow H_2O + Oxycellulose$

and/or

$H_2O_2 + HD \rightarrow H_2O + HOD\ (bleached\ dye)$

Auto-oxidation

Another reaction type of organic compounds activated by light absorption is auto-oxidation, a process where the rate of oxygen consumption increases over time until it reaches a peak, and then decreases as the more easily oxidized sites in the molecules are fully reacted.

These types of reactions typically proceed in stages, which can be understood as specific chemical process steps known as initiation, propagation, and termination reactions.

Alternatively, they can be conceptualized more broadly, as illustrated in Figure 1. Additionally, there may be specific secondary reactions involved, such as inhibition or chain transfer in free-radical processes.

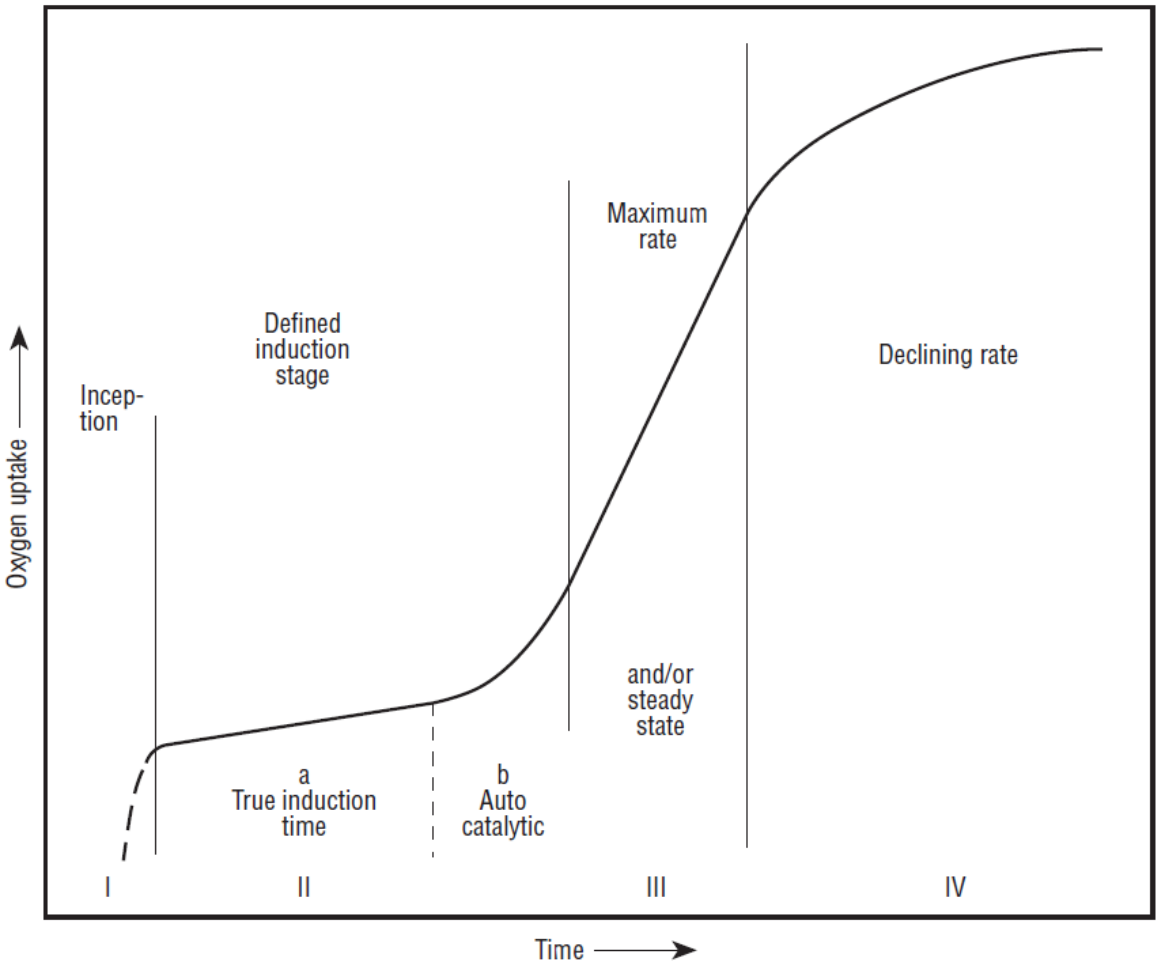

Figure 1. Possible stages of oxidative history. Reproduced after Feller [3].

The type of auto-oxidation of particular interest is one that involves the formation of organic hydroperoxides (compounds with the structure ROOH). The presence of oxygen often results in their formation through reactions with hydrocarbon free radicals, generally induced by light absorption, as shown below.

$$R\bullet + O_2 \longrightarrow ROO\bullet$$

$$ROO\bullet + RH \longrightarrow ROOH + R\bullet$$

The resulting hydroperoxides (ROOH) act either as initiators for further reactions or as intermediates in the process. The initiation step generates free radicals—either R•, RO•, or ROO•. In advanced stages of auto-oxidation, these free radicals mainly result from the decomposition of the hydroperoxides (ROOH) that form. The chain reaction propagates

through two substeps: a rapid uptake of oxygen forming a radical, ROO•, which then attacks another organic molecule in a slower second substep. The latter step, the rate of hydrogen atom abstraction from an organic molecule, is typically considered the rate-controlling substep.

Step 1: Initiation:	$2ROOH \rightarrow R\bullet + ROO\bullet + H_2O$	(k_1)
Step 2: Propagation:	$R\bullet + O_2 \rightarrow ROO\bullet$ fast	(k_2)
	$ROO\bullet + RH \rightarrow ROOH + R\bullet$	(k_3)
also,	$ROO\bullet + C{=}C \rightarrow ROOC{-}C\bullet$	(k_{3a})

Termination happens when two radicals combine or when a radical breaks down into particles that are no longer free radicals.

Step 3: Termination:	$2R\bullet \rightarrow$	(k_4)
	$ROO\bullet + R\bullet$	(k_5)
	$2ROO\bullet \rightarrow$	(k_6)

The kinetic relationship obtained from the proposed mechanism of auto-oxidation that the maximum rate is dependent primarily on the temperature because temperature influences k_3, the specific rate constant of substep 2, and k_6, a specific rate constant of termination, which are the only parameters appearing in the equations. In other words, an organic compound tends to exhibit a characteristic maximum rate of oxidation at any particular temperature, regardless of how the oxidation of an organic material may be initiated. The second conclusion is that variations in the rate of initiation do not affect the maximum rate, as k_1 need not appear in the steady state equation. This means that increasing the amount of catalyst, which influences the initiation step, shortens the time required to reach the maximum rate, but does not change the maximum rate.

A key feature of auto-oxidation is its chain-reaction nature. Through the propagation substeps 1 and 2, numerous organic molecules can be converted into ROOH from a single initiating event. This process is called a free-radical chain reaction. The average number of times the cycle of chain propagation steps repeats is referred to as the (kinetic) chain length. It is defined as the ratio of the oxidation rate to the initiation rate, where the chain carriers are formed.

The concentration of ROOH, determined by the rate of initiation, has important implications. When the maximum rate of oxidation is reached - where the initiation rate equals the oxidation rate - the chain length becomes 1. This has significant consequences when attempting to inhibit high-temperature reactions or photochemically initiated reactions. Inhibitors that target peroxide radicals to interrupt the chain will be less effective when the chain length is short.

Additionally, the chemical reaction begins slowly due to the low initial concentration of ROOH, but the reaction rate increases as more ROOH forms. The time it takes to reach the maximum rate of oxidation is known as the induction time. The induction time is related to the chain length of the propagation step. In practice, induction times can vary greatly, ranging from very long periods to almost none, depending on the materials and conditions involved.

Analyzing the kinetics of reactions provides valuable insights into how light affects auto-oxidation. Detailed studies of the chemical products from numerous oxidation reactions by various researchers have confirmed that light exposure does not change the nature of the propagation substeps. Instead, light primarily affects the initiation step. By accelerating the rate of initiation, light reduces the time needed to reach the maximum or steady-state rate of oxidation.

From hydroperoxides, even more reactive species may be formed, especially if transition metals are present in the material, at least in traces [2,3]. The reaction is named after H. J. H. Fenton, and more than a century after its discovery. A cycle - called *pseudo*-Haber-Weiss cycle of hydroperoxide decomposition – undergoes involving the transition metal, in which R can either be a hydrogen, a low molecular weight compound or a polymer.

$$\mathrm{ROOH} + \mathrm{Me}^{n+} \rightarrow\rightarrow \mathrm{RO}\cdot + \mathrm{Me}^{(n+1)+} + \mathrm{OH}^{-}$$

$$\mathrm{Me}^{(n+1)+} + \mathrm{ROOH} \rightarrow\rightarrow \mathrm{ROO}\cdot + \mathrm{Me}^{n+} + \mathrm{H}^{+}$$

In the second reaction, the transition metal can be reduced back into its catalytically active state by some other reducing compound, e.g. superoxide anion or an appropriate organic radical.

The activity of transition metals in polymeric materials depends on many parameters, including complexation with various ligands, pH and type of metal; the effects of different metals may even be synergistic [2]. In paper, for instance, iron is a commonly found in inks - iron gall inks – provoking a dramatic destruction of the cellulosic substrate. Traces of metal ions are present in virtually each polymer and may affect polymer oxidation and subsequent degradation considerably. The sequence of efficiency of metal ions crucially depends on the oxidation state and ligand type. In an aqueous reaction system at pH 7, the following order of catalytic activity was found:

Cu(II) > Cr(III) > Co(II) > Fe(III) > Mn(II) > Ni(II),

while Cd(II) and Zn(II) did not exhibit any catalytic activity. Ions of Al, Ti, Zn and V usually reduce the rate of oxidation.

Photo-oxidation VS Thermally Induced Oxidative Deterioration

Thermally induced deterioration at moderate temperatures often occurs through the formation of hydroperoxides [3]. A common subsequent reaction pathway is known as a branching or degenerate branching mechanism. This term is used because, once enough peroxides accumulate, the primary source of free radical "initiation" shifts from the original substances to the decomposition of these hydroperoxides. Two key features of thermally induced "auto-oxidation" are the initial buildup of hydroperoxide (ROOH) concentration to a peak, followed by a subsequent decline, along with a continuously increasing (autocatalytic) rate of oxygen consumption.

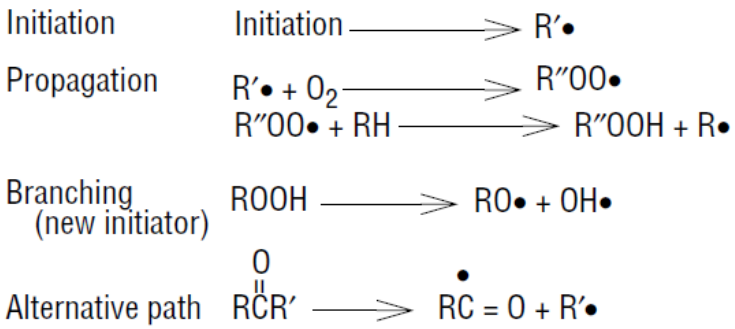

In contrast, during sensitized photo-oxidation, the rate of oxygen consumption and peroxide buildup typically proceed at a steady rate, with a maximum often not observed. This is likely because, under photochemical conditions at moderate temperatures, the accumulation of hydroperoxides can continue to rise to very high levels over a prolonged period, without reaching a peak within the study timeframe. Therefore, in normal photochemical exposures at moderate temperatures, there is usually only a progressive increase in hydroperoxide concentration, without observing a maximum. This differs from thermal deterioration studies conducted at higher temperatures, such as 100 °C or more, where a maximum in hydroperoxide concentration is almost always reached.

In weatherability studies, which make use of a light source, degradation of polymers by purely thermal energy is generally not a major concern. This is because the highest outdoor temperatures to which a polymer might be exposed (around 76 °C) do not provide enough thermal energy (70–90 kcal per mole) to break the chemical bonds in most commercial polymers. Thus, if temperature increases are limited during testing, photodegradation is a more likely pathway. Nonetheless, temperature should be monitored, as it is an important rate-controlling factor in various degradation processes, such as oxidation and hydrolysis.

Photosensitizers, UV-absorbers, antioxidants

Photochemical reactions can be categorized into two main types: direct and photosensitized reactions [5]. Direct photochemical reactions involve processes such as ionization, isomerization, aggregation, radical dissociation, and degradation. The specific reaction that occurs depends on the energy of the photons involved and the structure of the molecule being affected. Photosensitized reactions require the presence of a *photosensitizer*, an auxiliary compound that absorbs light and provides the necessary energy for the reaction. Without this photosensitizer, the reaction would not take place.

A frequent example of a photosensitized reaction is photo-oxidation, where the sensitizer absorbs light and transitions to an excited triplet state through *inter-system crossing*. In this active state, two possible pathways for oxidation arise:

- Type I Reaction: The sensitizer interacts with a substrate molecule in a radical reaction. This is followed by a reaction between the substrate and triplet oxygen, resulting in an

oxidized substrate. The rate of this reaction depends on the types and concentrations of both the sensitizer and the substrate.

- Type II Reaction: The sensitizer reacts directly with oxygen, producing singlet oxygen, which then reacts with the substrate. In this case, the reaction rate is largely determined by the concentration of oxygen.

Both types of reactions lead to the oxidation of the substrate, and they are influenced by the availability of the sensitizer, substrate, and oxygen in the environment. The distinction between the two types lies in the reaction mechanism and the specific role that oxygen plays in each.

The role of pigments and dyes as photosensitizers is well-recognized, with their ability to cause photoisomerization, photooxidation, or photoreduction reactions [6,7]. A general rule was formulated that fading usually entails oxidation of dye on non-proteins and reduction on proteins [3,8]. In polar matrices, such as textiles, photoreduction of the dye can result in sensitized oxidation of the polymer, leading to phototendering. Phototendering is a process where the fabric weakens due to the oxidative action of reactive oxygen species (ROS), which can include singlet oxygen in dry conditions and hydrogen peroxide in moist conditions [6,7].

Key points regarding phototendering mechanisms follow.

1. Most active tendering dyes are yellow and orange, though some red and blue dyes are also involved. There are also non-tendering dyes in the yellow and orange range.
2. Oxygen is essential for significant tendering to occur, as it plays a role in the oxidation processes that degrade the fabric.
3. The presence of moisture accelerates tendering, particularly in cellulosic fibers like cotton and viscose rayon, due to the formation of hydrogen peroxide.
4. The type of polymer significantly influences the degree of degradation. Cellulosic fibers (e.g., cotton, viscose rayon) and nylon are more prone to tendering, whereas wool and cellulose esters (e.g., acetate) exhibit little or no degradation.
5. The degree of aggregation (how dyes clump together in fibers) affects tendering but varies with different dyes and treatments. The overall effect is complex and depends on specific dye-fiber interactions.
6. The chemical structure of dyes is a critical factor in determining tendering activity. Certain structural features make dyes more or less prone to inducing phototendering. The mechanism of dye fading strongly influences the phototendering mechanism too.

UV-absorbers have been widely studied as additives to protect textiles and polymers from UV-induced damage [9]. By competing with photosensitizers, they can reduce the amount of harmful UV radiation absorbed. These absorbers work by converting UV radiation, typically between 290 and 400 nm, into heat. This process helps prevent the degradation of the polymer

and minimizes the fading of the dye. Organic UV absorbers, such as benzophenones and benzotriazoles, are frequently used in synthetic fibers. Their effectiveness lies in their ability to absorb UV light and dissipate the energy before it can cause damage. For natural fibers like wool and silk, specialized compounds like sulfonated benzotriazole or oxalic acid dianilide derivatives are employed. However, some natural compounds can work as UV absorbers too [10]. The UV-protective ability of natural dyes largely depends on the absorption characteristics of the functional groups present in the plants, such as tannins, flavonoids, anthraquinones, and terpenoids. Some research works showed, for example, significant UV protection due to the presence of tannins, indigo and anthraquinones [11,12].

Antioxidants are another important component in the fight against photodegradation [9]. They work by interrupting the chain reactions that cause polymers to break down when exposed to oxygen and light. Specifically, antioxidants can trap free radicals or react with peroxide radicals, thus preventing further oxidative damage. Their role is particularly crucial when used alongside UV absorbers, as the combination of the two can significantly enhance the overall stability and longevity of the material.

Finally, excited state quenchers represent a more specialized form of protection [9]. These compounds work by absorbing the excess energy from excited molecules before it can lead to harmful chemical reactions. Transition metal complexes like those of nickel, iron, or chromium are often used for this purpose. By dissipating the energy as heat, excited state quenchers prevent the polymer from undergoing photochemical reactions that would lead to degradation. This mechanism is particularly useful for polymers exposed to intense light over long periods, helping to maintain their structural integrity and prevent color fading.

Stabilizing Cultural Heritage Polymers

For museum curators and conservators, the principles of the Grotthus-Draper and Stark-Einstein laws highlight the importance of controlling light exposure to sensitive objects [3]. While reducing light intensity can slow down photochemical deterioration, it cannot entirely prevent it, as photochemical reactions will continue as long as light is absorbed by the material. Understanding these principles helps in designing better conservation strategies and selecting appropriate lighting conditions to minimize the degradation of valuable artifacts and artworks.

In conservation science, a crucial aspect to consider is the irreversible nature of photochemical damage to materials. When molecules in materials degrade, such as when oxygen breaks off pieces of these molecules and converts them into volatile gases like carbon dioxide, water, and formaldehyde, these original molecules cannot be restored to their previous state. This irreversible change is particularly significant in materials like embrittled fibres, faded dyes, or degraded linseed oil, where once the original chemical structures are altered, they cannot be reconstituted. Adhesives can consolidate the damaged fibers, but the broken molecular chains cannot be rejoined at their original sites [3].

Not all cases of oxidative deterioration in organic substances follow the hydroperoxide formation and auto-oxidation mechanism. As previously noted [3], it is essential to identify materials prone to auto-oxidation and exhibit an induction time. Additionally, it is crucial to analyze the deterioration and preservation of organic materials in museums by differentiating the aspects related to the initiation steps (such as the effects of light and catalysts) from those related to the propagation steps (including the chemical structure of compounds and oxygen concentration).

During deterioration, changes in physical properties - like increased brittleness, altered tensile strength, and discoloration - often show a period where little seems to change, followed by more pronounced changes. This period of relative stability can be considered an apparent induction time for a specific physical property or chemical reaction.

The induction time in oxidative deterioration involving the formation of organic hydroperoxides is precisely defined as the duration of exposure needed to reach the maximum rate of oxygen consumption under specific conditions. Given this definition, most conservation measures for organic materials focus on processes that occur during this induction period and aim to extend it.

3.1.4 Silk Fibre and its Degradation

Textiles durability

One of the most common ways people encounter polymers in daily life is through textiles. Textiles serve a multitude of purposes and are designed with varying levels of expected performance and lifespan, leading to a wide range of what might be considered "durable" [13]. Some textiles are disposable, while others are short-lived and utilitarian, such as T-shirts, socks, and underwear. Longer-lasting items include suits, sweaters, drapes, luggage, upholstery, and carpets. Textiles can also be ceremonial, or specialized for specific uses, such as sports uniforms, fishing nets, and hot air balloons. Critical-use items, such as firefighter gear, children's sleepwear, and parachutes, often have legal standards to meet. The intended function of a textile determines when it is deemed no longer serviceable. For example, a casual jacket, a showerproof coat for daily use, a skiing jacket, a serious mountaineer's jacket, and a coat for military or firefighter use may look similar but have vastly different performance standards and levels of acceptability. The definition and interpretation of "durable" have also evolved over time. A century ago, textiles were relatively expensive, so items were used extensively, repaired, resized, repurposed, and eventually turned into cleaning rags. Today, textiles are much cheaper, and few people find the time or need to repair them or repurpose them as rags, especially when such items can be easily purchased. As a result, the "end point" at which an item is considered no longer useful has shifted significantly.
Exploring historical textiles and their conservation requires rethinking the conventional definitions of durability and lifespan for everyday textiles. Historically, textiles were intended as "working" objects, so by the time they are included in collections, they have already undergone significant wear and tear. After their functional lives ended, these textiles might have been stored or ended up in what we now recognize as an archaeological context. Many of these items found continued use in different forms long after their original purpose was served - clothing, for instance, might be handed down, modified, or repurposed for costumes or theatrical garments, while other objects could also be recycled and reused. Given that it is rare for such items to enter collections in pristine condition, it is crucial to implement the best conservation and preservation measures to extend their lifespan [13].

To assess and control risks effectively, it is essential to have a thorough understanding of a material's condition and the factors contributing to its deterioration. Textiles are among the most sensitive items in a collection, and understanding their deterioration is fundamental to a conservator's expertise. This knowledge informs every decision made in the conservation studio [14].

Silk fibre

Silk is produced by various insect larvae and spiders, but most commercial silk comes from the domesticated silkworm, *Bombyx mori* [15,16]. Additionally, wild silk moth species, like the Chinese and Indian Tussah moths (*Antheraea pernyi* and *Antheraea mylitta*) and the African

communal caterpillar (*Anaphe moloneyi*), also produce silk that can be spun and woven. Silk threads, or bave, consist of two filaments, or brins, made from fibroin, the primary silk protein. These brins are bound together by sericin, a gum that is removed during the degumming process.

Native silk fibers typically exhibit an average diameter of 20–30 μm, but after undergoing degumming, the resulting fibroin fibers range from 10–15 μm. Each fibroin fibre is made up smaller fibrils, which reduce further to diameters of 20–100 nm. The fibroin fibers exhibit two distinct molecular weights: approximately 325–350 kDa for the heavy chains and approximately 25 kDa for the light chains. These chains are connected by a single disulfide bond.

The heavy and light chains have different amino acid sequences, which give different properties to the regions they form. The heavy chain is primarily composed of glycine, alanine and serine, specifically in the sequence (Gly-Ala-Gly-Ala-Gly-Ser) [17]. The abundance of small amino acids in fibroin enables the formation of crystalline hydrophobic regions, where water molecules are allowed. *Bombyx mori* silk has a reported crystallinity of 62–65%, while wild silks have 50–63% [16]. Larger amino acids are found mainly in the amorphous areas, and their levels decrease in deteriorated silk [16]. The full amino acid composition of *Bombyx mori* is reported by different authors [16,18]. Each silk fibroin molecule alternates between twelve crystalline and twelve amorphous regions [16,19].

In contrast, the light chains show a more undifferentiated amino acid composition, non-repetitive sequence, making them more hydrophilic properties and relatively elastic with little or no crystallinity. They contain hydrogen bonds that are easily disrupted by water. This explains why dry silk scaffolds exhibit higher tensile strength, lower strain at break, and a higher modulus compared to wet silk scaffolds.

This structural composition results in fibroin being a hydrophilic-hydrophobic-hydrophilic polymer, characterized by alternating hydrophobic crystalline regions and hydrophilic amorphous segments [15]. While the aminoacidic sequence cannot change, the fibroin folding can undergo conformational changes. Before the silk is spun by the silkworm gland, fibroin possess an amorphous form termed silk I. After the silk has been the common form is the β-sheet structure, which is hydrophobic and made up of well-organized crystalline regions, contributing significantly to the mechanical strength and durability of fibroin. Physical, chemical or mechanical treatment can induce a conformational change between the two forms. Processing techniques are considered to convert silk I to the crystalline silk II conformation, increasing the degradation time. A schematic representation of the structure of Bombyx mori silk is depicted in Figure 2.

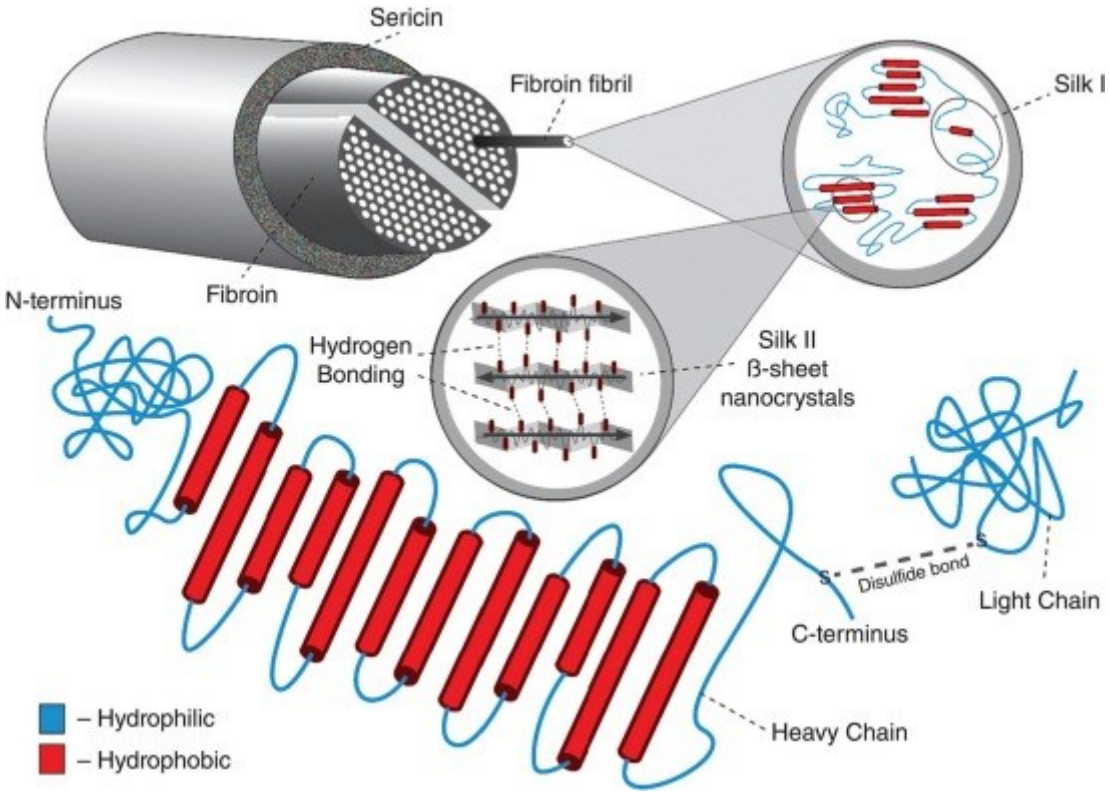

Figure 2. Structure of Bombyx mori silk. Sericin covers the fibroin protein, constructed of fibrils; a fibroin fibril consists of heavy and light chains connected by a single disulfide bond; the heavy chain is composed of 12 hydrophobic repeats connected by hydrophilic linkers; silk fibroin displays a dimorphic structure with two distinct configurations, namely disordered (silk I) and β–sheets (silk II). Reproduced with permission from [15]

Processing Treatments of Silk

Silk, often called the "queen of textiles" due to its luxurious feel, softness, sheen, and drape, requires degumming to make it comfortable, lustrous, and dyeable. Degumming removes sericin by boiling the silk in aqueous solutions, often with soap, alkali, detergents, or enzymes [20].

Other treatments have been developed to alter silk for the clothing industry. Historically, silk has been treated with inorganic salts to produce "weighted" silk, which is heavier and has better draping qualities than unweighted, degummed silk [20]. Both inorganic and organic materials, such as tannins, have been used as weighting agents and mordants during dyeing. Tannins from wood were an early weighting agent for silk, staining the fibre with a dark coloured hue. They were later decolourized since the 1890s, allowing their use on light-coloured silks [21]. Metallic weighting, which began in 1855, used various inorganic salts, with tin becoming a common weighting agent from the 1870s. The "dynamite" method patented in 1893 involved treating silk with aluminium sulphate, sodium silicate, and tin to increase its weight by up to 400% [22].

Silk Durability and Deterioration

Silk is unique among natural fibres for its strength and high breaking extension, making it more similar to synthetic fibres in its ability to absorb stress before rupture. However, silk textiles are

often reported as more vulnerable to damage, especially from light exposure, compared to other fibres [20,23]. Due to this sensitivity, museums and historic houses are advised to display silk textiles under low light levels to prevent fading and fibre embrittlement[24–26]. The durability of silk is influenced by a combination of environmental factors, processing treatments, and the inherent properties of the material itself. Understanding these factors is crucial for preserving silk textiles and maximizing their lifespan.

Silk deterioration can occur through chemical, physical, and biological processes. Silk is seen as quite resistant to biological attack, while physical deterioration strictly depends on the intended use of the textile, associated to different level of abrasion, tension and load found during use. Hydrolysis and oxidation are the most damaging chemical deterioration pathways [20].

The exact changes that occur within the internal structure of silk during degradation are still under study. Some researchers suggest that degradation begins with random scission of the polymer chains in the amorphous regions, followed by a later stage where the crystalline structures become involved [27]. Others propose a different model where there is a gradual reduction in the degree of polymerization, leading to a loss of crystal alignment with the fiber axis, but leaving the crystalline regions intact while the amorphous fibroin components break down [28]. A third theory suggests that the initial degradation affects only the amorphous regions, with the crystalline and amorphous components degrading at the same rate as the process progresses [29,30]. Despite these differing viewpoints, it is widely recognized that silk deterioration starts in the amorphous regions of silk, being more accessible to deterioration agents such as oxygen, humidity and salts [23,27,31,32]. The amorphous region is also particularly sensitive to oxidation, due to the presence of tyrosine residues [20].

Hydrolysis, particularly in the amorphous regions, breaks down the polypeptide chains in silk, reducing its molecular weight [23]. The process can be accelerated by pH changes and temperature, with silk deteriorating most quickly in highly acidic or alkaline conditions. Humidity levels also influence silk's durability, with higher RH levels leading to increased degradation [24,32]. Luxford showed through accelerated ageing experiments that displaying silk between 30% and 50% RH and at lower temperatures can significantly reduce the deterioration of silk [24,26]. Radicals will also accelerate the cleavage of neighbouring peptide bonds producing a-keto-acids and dicarboxylic amino groups that contribute to weakening of the fibres [33].

Oxidation affects amino acid side chains and peptide bonds, with tyrosine and threonine particularly vulnerable [20]. Tyrosine oxidation products, in particular, have been widely investigated. The formation of different compounds related to quinones has been proposed, including o-quinones [34,35] , 3,4-dihydroxyphenylalanine (DOPA), topaquinone (TPQ) and 2,4,5-trihydroxyphenylalanine (TOPA) [36,37]. Oxidation is exacerbated by high humidity level

[20,38], exposure to light [39] and environmental pollutants, such as ozone, which can cause yellowing and loss of tensile strength [40,41].

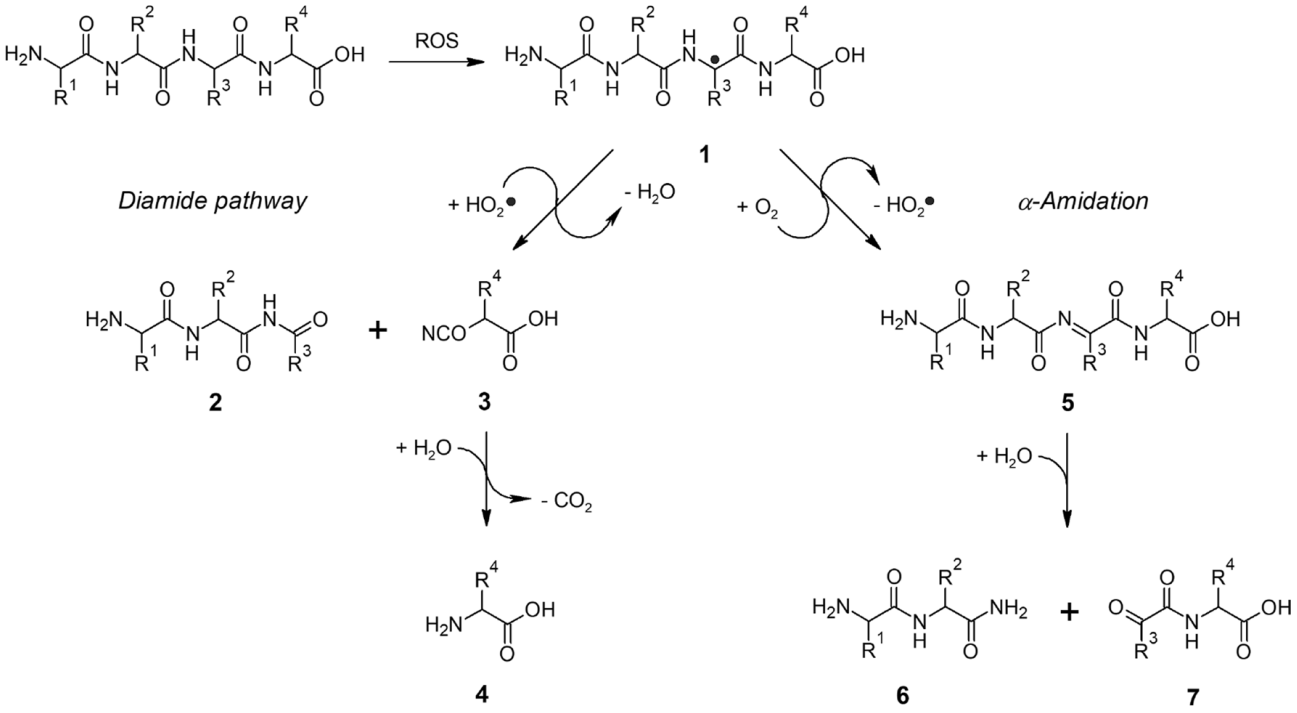

Figure 3. Mechanism of peptide backbone cleavage, initiated by attack of ROS on a peptide, abstraction of the α-C hydrogen atom, creation of a carbon-centered radical (1) and rapid decomposition via the diamide pathway or α-amidation. The former leads to the formation of an N-terminal carbonyl compound (2) and a C-terminal isocyanate (3), which can further react with water to an amino compound (4). The α-amidation leads to an unsaturated peptide species (5), further decomposing into a peptide amide (6) and an α-ketoacyl peptide (7). R_1, R_2, R_3, R_4 are amino acid side chains (reproduced with permission from [42])

The presence of oxidant species, such as oxygen and ozone, and light also creates the condition for oxidative fragmentation [33,42]. A simplified mechanism for peptide backbone cleavage is illustrated in Figure 3. The process begins with reactive oxygen species (ROS) attacking the polypeptide and abstracting an α-C hydrogen, which results in the formation of a carbon-centered peptide radical (1). This radical is stabilized by resonance with neighboring peptide groups. In the presence of oxygen, it undergoes further reactions involving highly reactive species such as peptide peroxyl and alkoxyl radicals. These radicals may decompose through two pathways: the diamide pathway or α-amidation. The diamide pathway results in the formation of an imide at the N-terminal truncated peptide (2) and an isocyanate at the C-terminal peptide (3). The isocyanate can further react with water, restoring the amino acid structure (4). On the other hand, α-amidation generates an unsaturated peptide (5), which subsequently decomposes into a peptide amide (6) and an α-ketoacyl peptide (7).

Oxidative stress is also the key to explain the well-known phenomenon of silk yellowing. The decomposition of tryptophan and tyrosine, leading to quinone products, is recognized as a key factor in the yellowing of silk upon light exposure [34–37]. However, the great abundance of glycine and alanine, which have the highest relative proportion in fibroin, determines their predominant participation in the formation of chromophores (α-keto-acids) under irradiation conditions during the photo-oxidation reaction [33].

Effects of Light on Silk

Light exposure is identified as the most detrimental factor affecting silk [20,23]. Both ultraviolet (UV) radiation and visible light induce silk degradation, with UV radiation being particularly harmful [20,34]. The rapid reduction in silk strength during UV-induced artificial aging has been well documented, especially with light sources emitting at 254 nm and 313 nm, even if the authors warn that light influence on the chemical and physical properties studied does not completely correspond to the natural degradation observed in historic samples [43–45]. The deterioration results from the breakdown of bonds between polypeptide chains, increasing the amorphous content of silk and leading to yellowing and photodegradation. Tryptophan, tyrosine, and phenylalanine amino acids in the amorphous regions absorb UV radiation, undergo photo-oxidation, and cause the material to become rigid and discoloured after prolonged exposure.

Baltova's studies [33,46] highlights the photo-oxidation behavior of silk fibroin during irradiation, focusing on changes in amino acid content and the formation of chromophoric products. Key amino acids—glycine, alanine, tyrosine, and serine—participate in this oxidative process. The photo-oxidation leads to the formation of carbonyl groups, which correlate with the yellowing of silk, introducing the concept that the build-up of α-ketoacyl groups drives this discoloration. The findings also reveal an exponential increase in carbonyl group content and the yellowness index over time, indicating that as the photo-oxidation progresses, the rate of chromophore formation slows. This deceleration is attributed not to exhaustion of the polymer but rather to a filtration effect, where the chromophores, which accumulate on the surface of the silk, absorb much of the UV radiation. This reduces the amount of radiation reaching the inner layers of the silk, thereby protecting the bulk material and prolonging its deterioration. This mechanism explains the gradual progression of yellowing and photodegradation, where the surface initially bears the brunt of UV exposure, and the resulting chromophoric compounds act as a protective barrier for the underlying silk structure.

In addition to its role in driving hydrolysis and oxidation reactions, the influence of light on the structural transformation of silk should not be underestimated. UV radiation, in particular, not only initiates chemical degradation but also promotes significant conformational changes within the fibroin structure. These structural transitions, such as the conversion from β-sheet configurations to random coil or α-helix, contribute to the gradual weakening and eventual loss of mechanical integrity in silk fibers. Numerous studies [29,32,47–50] have shown that silk degradation is accompanied by conformational changes in the secondary structure of silk before its final breakdown [30,32,51]. When silk fibroin is dissolved in water and recrystallized, it can form three distinct structural conformations—random coil, α-helix, or β-sheet—depending on concentration and casting conditions. The transition from random coil to β-sheet is influenced by various factors, such as heating [52,53], UV exposure [54,55], treatment with hydrophilic solvents like ethanol [53,56,57], and heated water [58]. During the early stages of UV-induced degradation, a slight increase in β-sheet content occurs alongside a decrease in random coil and α-helix structures, and an increase in β-turns [32,48,55]. It is widely believed that UV radiation initially impacts the amorphous phase of silk, causing it to decrease while the

crystalline regions become more prominent [28,30,51]. The crystalline regions tend to adopt an antiparallel β-sheet configuration, while the amorphous regions are less understood but likely exhibit β-turns or a disordered structure. As degradation progresses, the size of the β-sheet crystallites diminishes under continued UV exposure, eventually reverting to a random coil structure. This marks the point where the mechanical properties of silk are significantly compromised, resulting in weakened and brittle fibres [28,32,41,59].

However, light is not the sole factor influencing silk durability. Historical tapestries show that despite the lack of light exposure, samples taken from the reverse still exhibited lower molecular weight than modern materials [60]. This suggests other factors, such as heat and humidity, may contribute to silk degradation, as shown by a number of accelerated ageing tests excluding light from the experiment [27,30,31,41,44,45,61]. It is likely that real-world aging involves synergistic interactions among environmental factors, as shown by some studies about synergetic action of UV light and heat [62,63].

Effects of Processing Methods on Silk

Dyeing, bleaching, and mordanting processes can also affect silk's long-term durability, highlighting the impact of manufacturing techniques on silk's longevity.

The practice of metallic "weighting" of silk, common in historical textiles, is widely believed to increase their susceptibility to degradation [20,64]. More recently, some research works [37,65] showed that tin-weighting could restrict the flexibility of polymer chains, impacting the physical properties and potentially the degradation behaviour of silk textiles. Despite this, there is no standardized conservation treatment for textiles that have absorbed excess metal ions. The primary recommendation remains to store these textiles in the dark, with low relative humidity and temperature, while avoiding both wet and dry cleaning. The impact of metal ion absorption on the tensile properties of silk and wool, as well as their influence on ageing, remains a subject of ongoing debate [21].

Metal ions can bind to carboxylate, amino, thiol, and sulphonate groups, potentially either strengthening fibres through cross-linking of peptide chains or weakening them by disrupting their molecular structure [20]. Tensile strength and degradation have been widely studied, though findings vary. For example, Appel and Jessup [66] found that the decrease in tensile strength in weighted silk cannot be directly correlated to the amount of metal ions absorbed, while Needles et al. [67] found that silk mordanted with metals such as alum, chromium, copper, and tin often experienced a decrease in tensile strength. Copper ions, however, appeared to stabilize silk against photo-degradation, while metals like zinc, iron, and chromium accelerated it. Indictor and Ballard [22] stated that iron mordants seem particularly corrosive to fibres. Smith et al. [68,69] found that artificially light aged iron and copper mordanted and dyed wool showed decreased tensile strength and strain, but that alum mordanted wool showed inversed features.

The varying effects of metal ions on silk and wool depend on factors such as oxidation state, pH, and application methods, as well as interactions with dyes. These metal-protein complexes can significantly alter the fibers' properties during thermolysis (heat degradation) and photolysis (light-induced degradation). The presence of metal ions can stabilize the fibers by forming strong metal-protein bonds that increase thermal stability, thus slowing down the rate of thermal degradation. However, the same metal ions can also destabilize the fibers through acid hydrolysis, where the presence of acids weakens the bonds between protein chains, or through oxidative degradation, where the metal ions catalyze oxidation reactions, accelerating fiber degradation. Smith [68,69] found that aluminum ions could increase the tensile strength of wool through cross-linking, while in silk, alum mordanting did not significantly alter tensile properties. This may be attributed to the lower temperature used in alum mordanting silk compared to wool. Additionally, the presence of iron or copper in dyes, especially in combination with oak gall, seemed to reduce the rate of tensile loss in silk and wool following artificial aging.

Hacke [60] conducted wide research about the interaction between mordants, dyes, and fibres. Tensile strength tests revealed that various mordanting and dyeing procedures significantly influenced the initial tensile properties of wool, but they had a lesser impact on the extent of degradation after accelerated ageing. The effects of metal ion complexation, particularly with aluminium, iron, and copper ions, were also examined in relation to the tensile properties of wool and silk. Alum mordanting was found to have a strengthening effect on wool fibres, while dyeing procedures using weld, dyer's greenweed, oak gall mordanting, and black dyeing significantly weakened the fibres. However, silk fibers showed a different response, as their tensile properties were generally unaffected by dyeing and mordanting processes. Despite this, silk exhibited greater variability in tensile strength after accelerated ageing. Interestingly, the black dyeing process using ferrous sulphate with an oak gall mordant initially weakened the fibres but offered a photo-protective effect, reducing the rate of degradation during accelerated aging for both wool and silk. This suggests that certain mordanting and dyeing techniques can offer long-term protective benefits, despite their initial weakening of the fibers.

In sum, a number of authors suggested that the shattering of silk may not be due to weighting but a result of other factors such as previous treatment, processing and finishing. Metal ion absorption can either strengthen or weaken silk and wool depending on the treatment conditions, and the resulting changes in tensile properties and photo-stability depend on complex interactions between the fibre, metal ions, and any accompanying dyes.

As for dyes, their role as photosensitizer is commonly recognized. This means that they can sensitises or accelerates the breakdown in molecular structure of a textile (phototendering). While studies have focused on the environmental effects on dye fading [39,70,71], there is limited research on the long-term effects on textile substrates [60,68,69,72–75].

Flavonoids are well-known antioxidants [76], so dyestuffs containing flavonoid chromophores, such as weld, dyer's greenweed, and young fustic, may provide some protection against oxidative photodegradation of fibers, as suggested by some authors [68,77]. On the other hand, anthraquinones, which are oxidizing agents, may contribute to increased photodegradation [6,39]. This assumption applies to dyestuffs like madder and cochineal, which contain anthraquinone chromophores.

Indigo demonstrates excellent lightfastness when used as a dye on protein fibres [70], and also offers strong UV-protective properties [11,12]. It is therefore expected to contribute to the protection of fibres from photodegradation. However, the exact mechanism by which the support material influences lightfastness remains unclear, and no specific explanation has yet been provided to account for this interaction between the dye and the substrate.

Preserving historic silk items

Deteriorated textiles are particularly susceptible to mechanical or physical damage and may no longer be strong enough for their original use. While small damaged areas can be supported with patches, extensive damage might require a full support, where new material is added to stabilize the entire object. Careful consideration should be given to mounting, assessing whether a proposed display method is appropriate or poses a risk to the textile's stability. If necessary, treatments or alternative display methods should be explored to mitigate these risks [14]. Although chemical treatments like consolidation have been explored for preserving historic textiles [77–79], no aesthetically suitable methods have been developed. As a result, conservation efforts focus on using environmental control to maintain the condition of silk.

Proper storage and display conditions are crucial to preventing further deterioration. Controlling light exposure and maintaining a stable environment are essential, with standardized guidelines for light levels, temperature, and relative humidity serving as valuable benchmarks. Maintaining a stable environment without dramatic fluctuations is widely recognized as key. However, achieving these conditions can be challenging, costly, and raises sustainability concerns [14]. Storage and exhibition conditions must balance several competing factors. Different materials often require distinct environments, which may not always be compatible. Additionally, limitations in resources, budget, equipment, and technology, as well as the needs of staff working near the artifacts, must be considered. Generally, temperatures around 20°C and humidity levels between 45–60% RH offer a reasonable compromise between ideal and practical conditions. Light levels should be adjusted based on the sensitivity of the objects and visitor needs, but for non-display storage, keeping objects in dark conditions is generally recommended [13].

Luxford's study [24] is a milestone in re-evaluating environmental factors affecting the deterioration of silk in historic textile collections, with a focus on accelerated ageing experiments under varying humidity (RH), temperature, and light conditions. The results revealed that UV radiation increases silk degradation, while light exposure alone has a relatively

smaller impact compared to thermal ageing. The most significant factor in silk degradation was humidity, with increasing RH levels leading to a rapid loss of tensile strength. This highlights the importance of RH control in preventive conservation strategies, as thermal ageing at high humidity had a greater effect on silk than light exposure, even under low light levels. While low light levels are traditionally maintained in historic houses to prevent textile fading, the study suggests that increased light exposure, up to 200 lux, may not significantly accelerate deterioration compared to 50 lux. The study also shows that UV radiation intensifies degradation, which supports the use of UV filters in display environments. Moreover, despite concerns about embrittlement at low RH levels, the research found no signs of brittleness in tensile strength tests. The study concluded that maintaining lower RH and temperature levels is crucial for the long-term preservation of historic silk, and it called for a re-examination of current conservation practices, especially regarding the prioritization of light control over humidity management. Additionally, the research underscores the need for further studies on already faded textiles, as further fading from increased light exposure might be negligible in such cases.

3.1.5. Review of Analytical Methods for testing silk properties

As silk ages, its performance declines due to the deterioration of internal components. Silk colour, morphology, strength, composition, molecular weight, crystallinity and conformation undergo changes which can be monitored using a variety of analytical methods.

Table 1 reports on the analytical techniques which have been used in the main silk degradation studies.

Ageing Type	Analytical techniques	Reference
Light-aged silk		
	Mechanical test	Appel 1935 **[66]**
	Colorimetry, UV-Vis absorbance	Zhang 2008 [80] **(wool)**
	Colorimetry, mechanical test	Korenberg 2007 [81]
	SEM, FTIR, mechanical test	Liu 2019 [32]
	UV-Vis absorbance, fluorescence, FTIR, SDS-PAGE chromatography	Sionkowska 2011 **[43]**
	FTIR, FT-Raman	Shao 2005 [82]
	SEM, AA analysis, FTIR, XRD, DSC	Li 2013 [29]
	FTIR	Luo 2012 [55]
	TGA, FTIR, DMTA	Wang 2018 [83]
	FTIR, SEM, TGA-DSC, PIXE	Kavkler 2018 [84]
	HP-SEC, SDS-PAGE chromatography, electrophoresis	Tse 2000 [85]
	Colorimetry, SEM, AA analysis, solubility test, gel-permeation chromatography	Becker 1993 **[23]**
	SEM, colorimetry, FTIR, ^{13}C CPMAS NMR	Gong 2024 [86]
	Colorimetry, mechanical test, AA analysis	Solazzo 2011 [37]
	Mechanical test, FTIR	Garside 2005 [87]

	SR-FTIR	Zhu 2017 [88]
	Mechanical test, pH measure	Kim 2008 [89]
	Mechanical test, pH measure	Garside 2010 [64]
	ATR-FTIR, SEC, mechanical test	Nilsson 2013 [44]
	pH, UV-Vis reflectance, FTIR, AA analysis, SEC, mechanical tests	Vilaplana 2015 [45]
	Colorimetry, mechanical tests	Korenberg 2007 [81]
	Mechanical test	Luxford 2009 **[61]**
	FTIR, TGA-DSC, SEM, OM	Badillo sanchez 2019 [90]
	Mechanical test, AA analysis	Zhang 2011 **[91]**
	Colorimetry, UV–Vis Absorbance and Fluorescence, FTIR, SDS-PAGE	Lee 2021 [92]
	Colorimetry, FTIR, UV-Vis absorbance	Dang 2024 [34]
	colorimetry	Dang 2020 [93]
Thermal-aged silk		
	Mechanical test, AA analysis	Zhang 2011 **[91]**
	pH, UV-Vis reflectance, FTIR, AA analysis, SEC, Mechanical tests	Vilaplana 2015 [45]
	FTIR, FT-Raman, XRD, UV-Vis reflectance, SEC	Koperska 2014 [94]
	Colorimetry, viscosity, pH, mass loss, mechanical test	Koperska 2015 [95]
	SEM, AA analysis, FTIR, XRD, DSC	Li 2013 [29]
	SEC	Pawcenis 2016 [41]
	Mechanical test, FTIR	Garside 2005 [87]
	FTIR, WAXD, TGA	Zhang 2019 [31]
	SEM, mechanical test, FTIR, XRD, SDS-PAGE, AA analysis	Zhou 2023 [27]
	SR-FTIR	Zhu 2017 [88]
	TGA, FTIR, DMTA	Wang 2018 [83]
	Mechanical test, pH measure	Kim 2008 [89]
	Mechanical test, pH measure	Garside 2010 [64]
	Mechanical test	Luxford 2009 [26]
Hydrolytically aged sillk	AA analysis, SDS-PAGE	Chen 2020 [30]
	SEM, AA analysis, FTIR, XRD, DSC	Li 2013 [29]
	SR-FTIR	Zhu 2017 [88]
	mass loss, OM, TGA, FTIR, SDS-PAGE	Carissimi 2019 [96]
Historical silk		
	SEM, WAXD, XPS, EPR, ^{13}C CPMAS NMR	Gong 2022 [50]
	pH, UV-Vis reflectance, FTIR, AA analysis, SEC, Mechanical tests	Vilaplana 2015 [45]
	FTIR, Raman, SERS, SEM-EDX	Aguayo 2014 [97]
	FTIR, TGA-DSC, SEM, OM	Badillo sanchez 2019 [90]
	AA analysis, SDS-PAGE	Chen 2020 [30]
	SEM, AA analysis, FTIR, XRD, DSC	Li 2013 [29]
	FTIR, FORS	Badillo 2019 [90]
	AA analysis, mechanical test	Becker 1997 [98]
	ATR-FTIR	Koperska 2015 [38]
	ATR-FTIR	Akyuz 2019 [99]
	SR-XRD, XRD, TGA, SEM, OM	Gong 2019 [31]
	FTIR, WAXD, TGA	Zhang 2019 [31]

	SR-FTIR	Zhu 2017 [88]
	SR-XRD	Hermes 2005 [100]
	ATR-FTIR, SEM	Geminiani 2024 [101]

Table 1. Review of the analytical methods used for assessing silk degradation

Colour, morphology and strength

According to ISO 105-B02, the term "change in colour" encompasses alterations in hue, chroma, and lightness. To measure this, textiles are subjected to artificial light in conjunction with blue wool references, numbered from 1 to 8, which represent increasing levels of color fastness. Each higher number corresponds to approximately double the light resistance of the previous reference. Throughout the test, the textile and the blue wool references are continuously evaluated. The exposure continues until the color difference between the exposed and unexposed parts of the sample reaches Grey Scale Grade 3. The result is then compared to the blue wool reference that exhibits a similar color change, determining the textile's color fastness.

Colorimetry is an effective indicator in quantitatively assessing photodegradation. Either the yellowing index [37,46] or the color difference (ΔE) [80,81,86,92,95] can be calculated from the colorimetric measurements. The spectral reflectance curve can be evaluated as well [23].

UV/Vis spectra can inform about the oxidation of fibroin [43,92,94].

Scanning Electron Microscopy (SEM) is used to examine the surface morphology of a fabric, informing about fabric roughness and fibre surface changes after exposure. This information can be related to its damage status [23,27,29,32,49,50,84,86,100].

Different mechanical tests are used to assess the residual tensile strength of the fabric, such as partial strength loss, strain at break, as well as the Young's modulus [32,64,81,89,91]. For instance, dynamic mechanical thermal analysis (DMTA) being a hybrid technique combining thermal analysis and dynamic mechanical analysis, can detect the associated mechanical property changes caused during the structural transition [83].

Composition

The physical modifications are generally related to changes in the amino acid composition and to the formation of new degradation products.

Amino acid analysis provides direct evidence for silk composition [23,29,37,73,91]. Amino acid compositions and ammonia content of previously hydrolysated silk samples are determined by ion-exchange chromatography [23,29]. An HPLC system coupled with a fluorescence detector can also be used [73,91]. LC–MS⁄MS can be performed after chymotryptic digestion of the silk [37] providing information about the photodegradation products of silk. Unlimited degradation mass spectrometry (ULiD-MS) is useful to assess changes in protein and peptide components coming from the degradation processes [27]. Immunoblotting, based on an

antigen–antibody binding reaction, is an alternative approach to characterize target proteins, evaluating the protein expression, modification, and degradation [30].

Carbonyl group content can be determined by colorimetric analysis after partial acid hydrolysis of the silk [46]. UV/Vis spectra can inform about the oxidation of fibroin as well [94]. FTIR signals can inform about the amount of specific amino acids, such as tyrosine [29], and oxidation products [83,86]. Fluorescence spectra can be used to monitor the formation of di-tyrosine bonds [43,92].

Acidity measurement (pH) also gives an indication about the degradative status of the fibre [28,64,89,95]. The acidic groups of the backbone are normally involved in secondary bonding, supporting the secondary structure of the polymer, but when the fibres deteriorate, the became accessible to water, thus increasing the measured pH value.

Thermogravimetric analysis (TGA) is used to qualitatively investigate the degradation status of historic silk [29,31,49,84,102]. The decomposition temperature seems to be dependent on crystallinity and molecular orientation [103,104].

Molecular weight

The reduction in strength correlates with the shortening of fibroin polymers and the disorientation of fibroin crystallites. These changes can be evaluated using methods that analyze molecular weight distribution and crystallite orientation.

SDS–PAGE chromatography revealed the lengths of the peptides [27,43,85,92,96] present in the sample. Peptide length can also be related to the measured value of viscosity [95].

Solubility tests can be used to evaluate the mass loss after rinsing the sample with a solution of urea. The same solution can be analyzed by gel permeation chromatography to determine molecular weight range [23].

Size-exclusion chromatography (SEC) is used to study molecular weights distribution of silk after dissolution with LiBr [28,41,45,85,94]. This kind of data can be used to measure the degree of polymerization (DP) pf the polymer.

Cristallinity and conformation

Different characterization methods are employed to distinguish between the two primary structures of silk fibroin—silk I and silk II, as well as the random-coil structure of fibroin [105].

X-ray Diffraction (XRD) offers a direct and accurate method to quantitatively study the crystallinity of silk [50,102]. The degree of crystallinity is generally evaluated by calculating the ratio between the sum of the integrated intensity of the Bragg peaks (200 and 210) and the integrated intensity of the amorphous halo [27,31,50]. Some works have also given tentative conformational percentages based on XRD data [94,106]. XRD can effectively differentiate

between silk I (the amorphous form) and silk II (the more stable, crystalline β-sheet structure), as well as random-coil fibroin [106].

Wide angle X-ray scattering (WAXS) is also used to determine the size of the b-sheet crystalline regions in silk fibers using the Scherrer equation [31,107].

Synchrotron radiation (SR) microdiffraction is introduced as a novel method for characterizing the state of a silk fabric [100]. The beam size used (about 1 μm) is well below the average size of a single *B. mori* fiber (<10 μm) and is therefore sensitive to single fibers, whose orientation distribution can be measured. This parameter was found to be sensitive to the overall state of decay of the fabric.

Nuclear Magnetic Resonance (NMR) is particularly useful for identifying the crystalline forms of fibroin [50,108,109]. In particular, ^{13}C CPMAS NMR works well for estimating the content of amino acid [86] and further revealing the intensity ratio of β-sheet and random-coil peaks of silk.

Photoelectron spectroscopy (XPS) investigates the elemental composition of silk surface along with the chemical state, indicating the deterioration of silk [50].

Electron paramagnetic resonance spectroscopy (EPR) is applied in determining the free radicals which are believed to take part in the degradation process of ancient silk fabrics [50].

Fourier-Transform Infrared (FTIR) and Raman spectroscopy are commonly used to observe the absorbance peaks related to the amide functional groups of silk fibroin and their changes [29,43,55,82,83,102]. For FTIR, key amide peaks are Amide I peaks (related to C=O stretching) appearing in the 1700–1600 cm^{-1} range, Amide II peaks (related to N-H bending and C-N stretching) occurring in the 1600–1500 cm^{-1} range and Amide III peak at around 1300-1200 cm^{-1}. The conformational differences give rise to peak modifications, which attest the prevalence for β-sheet structure, α-helix structure or random-coil structure. Differences are visually evaluated or through methods which are used to evaluate conformation percentages. In this case, intensity values are evaluated, or peak fitting procedures are implemented to calculate areas. Then, the average percentages of the α-helix and β-sheet structures are calculated [32,49,83]. Common evaluators are the crystallinity index [27,84,94], oxidation index [94] and hydrolysis estimator [94].

Furthermore, ATR-FTIR combined with polarizer, so called Pol-ATR FTIR was employed to investigate the orientation of fibres [28,87]. Polarization artefacts can appear in ATR-FTIR spectra of anisotropic materials, such as collagen fibres [110,111]. The reason is due to intrinsic limitations of the spectrophotometer - it can exhibit a degree of polarization [110] – or to orientation effects phenomena [111,112]. Imaging 2D FTIR techniques have also been tested [49,88].

3.1.6 References

[1] K. Hatada, R.B. Fox, J. Kahovec, DEFINITIONS OF TERMS RELATING TO DEGRADATION, AGING, AND RELATED CHEMICAL TRANSFORMATIONS OF POLYMERS, Pure and Applied Chemistry 68 (1996) 2313–2323.

[2] M. Strlic, J. Kolar, Ageing and Stabilization of Paper, National and University Library, Ljubljana, Slovenia, 2005.

[3] R.L. Feller, Accelerated ageing - Photochemical and Thermal Aspects, The Getty Conservation Institute, Ann Arbor, Michigan (USA), 1994.

[4] A.S. Maxwell, W.R. Broughton, G. Dean, G.D. Sims, Review of accelerated ageing methods and lifetime prediction techniques for polymeric materials, Teddington, UK, 2005.

[5] M.S. Baptista, J. Cadet, P. Di Mascio, A.A. Ghogare, A. Greer, M.R. Hamblin, C. Lorente, S.C. Nunez, M.S. Ribeiro, A.H. Thomas, M. Vignoni, T.M. Yoshimura, Type I and Type II Photosensitized Oxidation Reactions: Guidelines and Mechanistic Pathways, Photochem Photobiol 93 (2017) 912–919. https://doi.org/10.1111/php.12716.

[6] N.S. Allen, Photofading and light stability of dyed and pigmented polymers, Polym Degrad Stab 44 (1994) 357–374.

[7] N.S. Allen, Photofading mechanisms of dyes in solution and polymer media, Rev. Prog. Coloration 17 (1987) 61–71.

[8] C.H. Giles, C.D. Shah, W.E. Watts, R.S. Sinclair, Oxidation and Reduction in light fading of dyes, Journal of the Society of Dyers and Colourists 88 (1972) 433–435.

[9] V. Rubeziene, Effects of light exposure on textile durability, in: A.P. Annis (Ed.), Understanding and Improving the Durability of Textiles, Woodhead Publishing Limited, Cambridge, 2012.

[10] A. Sankaran, A. Kamboj, L. Samant, S. Jose, Synthetic and Natural UV Protective Agents for Textile Finishing, in: Luqman Jameel Rather, Aminoddin Haji and Mohd ShTechnologies for Textile Dyeing and Finishing, Scrivener Publishing, 2021: pp. 301–324.

[11] L. Zhou, J. Shao, L. Chai, Study on the UV-protective performance of cotton fabrics dyed with natural dyes, in: Adv Mat Res, 2011: pp. 1408–1413. https://doi.org/10.4028/www.scientific.net/AMR.332-334.1408.

[12] A.K. Sarkar, An evaluation of UV protection imparted by cotton fabrics dyed with natural colorants, BMC Dermatol 4 (2004). https://doi.org/10.1186/1471-5945-4-15.

[13] P. Garside, Durability of historic textiles, in: A.P. Annis (Ed.), Understanding and Improving the Durability of Textiles, Woodhead Publishing Limited, Cambridge, 2012.

[14] E.-A. Haldane, L. Hillyer, D. Kalsi, The Conservation and Display of Indian Textiles at the Victoria and Albert Museum, in: S. Jose, S. Thomas, P. Pandit, R. Pandey (Eds.), Handbook of Museum Textiles, Volume 1: Conservation and Cultural Research, John Wiley and Sons, Hoboken, New Jersey (U.S.), 2022: pp. 291–314.

[15] F.V. dos Santos, R.L. Siqueira, L. de Morais Ramos, S.A. Yoshioka, M.C. Branciforti, D.S. Correa, Silk fibroin-derived electrospun materials for biomedical applications: A review, Int J Biol Macromol 254 (2024). https://doi.org/10.1016/j.ijbiomac.2023.127641.

[16] E.S. Sashina, A.M. Bochek, N.P. Novoselov, D.A. Kirichenko, Structure and solubility of natural silk fibroin, Russian Journal of Applied Chemistry 79 (2006) 869–876. https://doi.org/10.1134/S1070427206060012.

[17] P. Taddei, P. Monti, Vibrational infrared conformational studies of model peptides representing the semicrystalline domains of Bombyx mori silk fibroin, Biopolymers 78 (2005) 249–258. https://doi.org/10.1002/bip.20275.

[18] K. Sen, M. Babu K, Studies on Indian Silk. I. Macrocharacterization and Analysis of Amino Acid Composition, J Appl Polym Sci 92 (2004) 1080–1097. https://doi.org/10.1002/app.13609.

[19] F. Lucas, S.G. Smith, 43—The moisture sorption of the silk of bombyx mori in relation to the proportion and chemical composition of the crystalline and amorphous phases, Journal of the Textile Institute Transactions 50 (1959) T695–T700. https://doi.org/10.1080/19447025908659947.

[20] A. Timar-Balazsy, D. Eastop, Materials, in: Chemical Principles in Textile Conservation, Third Edition, Routledge, New York, NY, USA, 1998: pp. 3–66.

[21] M. Hacke, Weighted silk: history, analysis and conservation, Studies in Conservation 53 (2008) 3–15. https://doi.org/10.1179/sic.2008.53.supplement-2.3.

[22] N. Indictor, M. Ballard, The effects of aging on textiles that contain metal: implications for analyses, in: International Restorer Seminar, 1989: pp. 67–75.

[23] M.A. Becker, N. Tuross, Initial Degradative Changes Found in Bombyx mori Silk Fibroin , (1993) 252–269. https://doi.org/10.1021/bk-1994-0544.ch022.

[24] N. Luxford, Reducing the Risk of Open Display: Optimising the Preventive Conservation of Historic Silks, University of Southampton, UK, 2009.

[25] N. Luxford, D. Thickett, P. Wyeth, Applying Preventive Conservation Recommendations for Silk in Historic Houses, in: Multidisciplinary Conservation : A Holistic View for Historic Interiors. Joint Interim Meeting of Five ICOM-CC Working Groups, ICOM-CC, Rome, 2010.

[26] N. Luxford, D. Thickett, P. Wyeth, Preserving silk: Reassessing deterioration factors for historic silk artefacts, in: Natural Fibres in Australasia: Proceedings of the Combined (NZ and AUS) Conference of The Textile Institute, Textile Institute (NZ), 2009: pp. 151–156.

[27] J. Zhou, X. Zhou, L. Pan, Y. Deng, H. Zheng, Z. Peng, J. Wan, Y. Zhou, B. Wang, Molecular Evidence of Structural Changes in Silk Using Unlimited Degradation Mass Spectrometry, ACS Omega 8 (2023) 34410–34419. https://doi.org/10.1021/acsomega.3c02254.

[28] P. Garside, P. Wyeth, Crystallinity and degradation of silk: Correlations between analytical signatures and physical condition on ageing, Appl Phys A Mater Sci Process 89 (2007) 871–876. https://doi.org/10.1007/s00339-007-4218-z.

[29] M.Y. Li, Y. Zhao, T. Tong, X.H. Hou, B.S. Fang, S.Q. Wu, X.Y. Shen, H. Tong, Study of the degradation mechanism of Chinese historic silk (Bombyx mori) for the purpose of conservation, Polym Degrad Stab 98 (2013) 727–735. https://doi.org/10.1016/j.polymdegradstab.2012.12.021.

[30] R. Chen, M. Hu, H. Zheng, H. Yang, L. Zhou, Y. Zhou, Z. Peng, Z. Hu, B. Wang, Proteomics and immunology provide insight into the degradation mechanism of historic and artificially aged silk, Anal Chem 92 (2020) 2435–2442. https://doi.org/10.1021/acs.analchem.9b03616.

[31] X. Zhang, D. Gong, Y. Gong, Insight into the orientation behavior of thermal-aged and historic silk fabrics by polarized FTIR microspectroscopy, J Cult Herit 38 (2019) 53–63. https://doi.org/10.1016/j.culher.2019.02.007.

[32] H. Liu, S. Zhao, Q. Zhang, T. Yeerken, W. Yu, Secondary structure transformation and mechanical properties of silk fibers by ultraviolet irradiation and water, Textile Research Journal 89 (2019) 2802–2812. https://doi.org/10.1177/0040517518803788.

[33] S. Baltova, V. Vassileva, Photochemical behaviour of natural silk-II. Mechanism of fibroin photodestruction, 1998.

[34] R. Dang, Y. Kang, H. Tan, Y. Yang, Color Damage of Visible Light on Plain-Woven Silk in Different Conservation States of Paintings and Calligraphy in Collections, Fibers and Polymers 25 (2024) 235–242. https://doi.org/10.1007/s12221-023-00414-2.

[35] G.D. Kang, K.H. Lee, Crosslinking reaction of Phenolic Side Chains in silk fibroin by Tyrosinase, Fibers and Polymers 5 (2004) 234–238.

[36] A.J. Grosvenor, J.D. Morton, J.M. Dyer, Profiling of residue-level photo-oxidative damage in peptides, Amino Acids 39 (2010) 285–296. https://doi.org/10.1007/s00726-009-0440-7.

[37] C. Solazzo, J.M. Dyer, S. Deb-Choudhury, S. Clerens, P. Wyeth, Proteomic profiling of the photo-oxidation of silk fibroin: Implications for historic tin-weighted silk, Photochem Photobiol 88 (2012) 1217–1226. https://doi.org/10.1111/j.1751-1097.2012.01167.x.

[38] M.A. Koperska, T. Łojewski, J. Łojewska, Evaluating degradation of silk's fibroin by attenuated total reflectance infrared spectroscopy: Case study of ancient banners from Polish collections, Spectrochim Acta A Mol Biomol Spectrosc 135 (2015) 576–582. https://doi.org/10.1016/j.saa.2014.05.030.

[39] G.S. Egerton, The Mechanism of the Photochemical Degradation of Textile Materials, Journal of the Society of Dyers and Colourists (1949).

[40] D. Sargunamani, N. Selvakumar, A study on the effects of ozone treatment on the properties of raw and degummed mulberry silk fabrics, Polym Degrad Stab 91 (2006) 2644–2653. https://doi.org/10.1016/j.polymdegradstab.2006.05.001.

[41] D. Pawcenis, M. Smoleń, M.A. Aksamit-Koperska, T. Łojewski, J. Łojewska, Evaluating the impact of different exogenous factors on silk textiles deterioration with use of size exclusion chromatography, Appl Phys A Mater Sci Process 122 (2016). https://doi.org/10.1007/s00339-016-0052-5.

[42] J. Sajapin, M. Hellwig, Studies on the synthesis and stability of α-ketoacyl peptides, Amino Acids 52 (2020) 1425–1438. https://doi.org/10.1007/s00726-020-02902-8.

[43] A. Sionkowska, A. Planecka, The influence of UV radiation on silk fibroin, Polym Degrad Stab 96 (2011) 523–528. https://doi.org/10.1016/j.polymdegradstab.2011.01.001.

[44] J. Nilsson, F. Vilaplana, S. Karlsson, J. Bjurman, T. Iversen, The validation of artificial ageing methods for silk textiles using markers for chemical and physical properties of seventeenth-century silk, Studies in Conservation 55 (2010) 55–65. https://doi.org/10.1179/sic.2010.55.1.55.

[45] F. Vilaplana, J. Nilsson, D.V.P. Sommer, S. Karlsson, Analytical markers for silk degradation: comparing historic silk and silk artificially aged in different environments, Anal Bioanal Chem 407 (2015) 1433–1449. https://doi.org/10.1007/s00216-014-8361-z.

[46] S. Baltova, V. Vassileva, E. Valtcheva, Photochemical behaviour of natural silk-I. Kinetic investigation of photoyellowing, 1998.

[47] X. Hu, D. Kaplan, P. Cebe, Determining beta-sheet crystallinity in fibrous proteins by thermal analysis and infrared spectroscopy, Macromolecules 39 (2006) 6161–6170. https://doi.org/10.1021/ma0610109.

[48] X. Chen, D.P. Knight, Z. Shao, β-turn formation during the conformation transition in silk fibroin, Soft Matter 5 (2009) 2777–2781. https://doi.org/10.1039/b900908f.

[49] D. Badillo-Sanchez, D. Chelazzi, R. Giorgi, A. Cincinelli, P. Baglioni, Characterization of the secondary structure of degummed Bombyx mori silk in modern and historical samples, Polym Degrad Stab 157 (2018) 53–62. https://doi.org/10.1016/j.polymdegradstab.2018.09.022.

[50] Y. Gong, Z. Li, J. Hu, G. Zhou, G. Xu, W. Yang, J. Zhang, Insight into the measurements for determining the ageing degree of ancient silk, Polym Degrad Stab 196 (2022). https://doi.org/10.1016/j.polymdegradstab.2022.109833.

[51] Purnomo, P.H. Setyarini, D. Sulistyaningsih, Degradation behavior of silk fibroin biomaterials - a review, Journal of Engineering Science and Technology Review 12 (2019) 67–74. https://doi.org/10.25103/jestr.125.08.

[52] L. Jeong, K.Y. Lee, J.W. Liu, W.H. Park, Time-resolved structural investigation of regenerated silk fibroin nanofibers treated with solvent vapor, Int J Biol Macromol 38 (2006) 140–144. https://doi.org/10.1016/j.ijbiomac.2006.02.009.

[53] J. Magoshi, Y. Magoshi, S. Nakamura, N. Kasai, M. Kakudo, Physical Properties and Structure of Silk. Thermal Behavior of Silk Fibroin in the Random-Coil Conformation., J Polym Sci Polym Phys Ed 15 (1977) 1675–1683. https://doi.org/10.1002/pol.1977.180150915.

[54] N. V Bhat, S.M. Ahirrao, Investigation of the Structure of Silk Film Regenerated with Lithium Thiocyanate Solution, n.d.

[55] X. Luo, J. Wu, A. Intisar, J. Geng, L. Wu, K. Zheng, Y. Du, Study on Light Aging of Silk Fabric by Fourier Transform Infrared Spectroscopy and Principal Component Analysis, Anal Lett 45 (2012) 1286–1296. https://doi.org/10.1080/00032719.2012.673098.

[56] X. Chen, Z. Shao, N.S. Marinkovic, L.M. Miller, P. Zhou, M.R. Chance, Conformation transition kinetics of regenerated Bombyx mori silk fibroin membrane monitored by time-resolved FTIR spectroscopy, Biophys Chem 89 (2001) 25–34. https://doi.org/10.1016/S0301-4622(00)00213-1.

[57] M. Tsukada, G. Freddi, P. Monti, A. Bertoluzza, N. Kasai, Structure and Molecular Conformation of Tussah Silk Fibroin Films: Effect of Methanol, Journal of Polymer Science 33 (1995) 1995–2001.

[58] J. Magoshi, M. Mizuide, Y. Magoshi, Physical Properties and Structure of Silk. VI. Conformational Changes in Silk Fibroin Induced by Immersion in Water at 2 to 130°C, Journal of Polymer Science 17 (1979) 515–520.

[59] W. Lamoolphak, W. De-Eknamkul, A. Shotipruk, Hydrothermal production and characterization of protein and amino acids from silk waste, Bioresour Technol 99 (2008) 7678–7685. https://doi.org/10.1016/j.biortech.2008.01.072.

[60] M. Hacke, Investigation into the Nature and Ageing of Tapestry Materials, University Of Manchester, 2006. https://doi.org/10.13140/RG.2.2.32890.08646.

[61] N. Luxford, D. Thickett, Designing accelerated ageing experiments to study silk deterioration in historic houses, in: Journal of the Institute of Conservation, Routledge, 2011: pp. 115–127. https://doi.org/10.1080/19455224.2011.581118.

[62] N. Vagkidis, L. Li, J.M. Marsh, V. Chechik, Synergy of UV light and heat in peptide degradation, J Photochem Photobiol A Chem 439 (2023). https://doi.org/10.1016/j.jphotochem.2023.114627.

[63] P. Ruzza, C. Honisch, R. Hussain, G. Siligardi, Free radicals and ROS induce protein denaturation by UV photostability assay, Int J Mol Sci 22 (2021). https://doi.org/10.3390/ijms22126512.

[64] P. Garside, P. Wyeth, X. Zhang, The Inherent Acidic Characteristics of Silk, Part II – Weighted Silks, E-PRESERVATION Science 7 (2010) 126–131. https://www.researchgate.net/publication/49587328.

[65] I. Elrefaey, H. Mahgoub, C. Vettorazzo, M. Marinšek, A. Meden, A. Jamnik, M. Tomšič, M. Strlič, Investigation of the Structural Changes in Silk Due to Tin Weighting, Polymers (Basel) 16 (2024). https://doi.org/10.3390/polym16172481.

[66] W.D. Appel, D.A. Jessup, ACCELERATED AGING TEST FOR WEIGHTED SILK, Part of Journal of Research of the National Bureau of Standards 15 (1935).

[67] H.L. Needles, V. Cassman, M.J. Collins, Mordanted, Natural-Dyed Wool and Silk Fabrics, in: Historic Textile and Paper Materials, American Chemical Society, Washington DC, 1986: pp. 199–210. https://doi.org/10.1021/ba-1986-0212.ch011.

[68] I.J. Miller, G.J. Smith, Protection against phototendering of wool by metal salts and mordanted dyes, Journal of the Society of Dyers and Colourists 111 (1995) 103–106.

[69] G.J. Smith, I.J. Miller, V. Daniels, Phototendering of wool sensitized by naturally occurring polyphenolic dyes, J Photochem Photobiol A Chem 169 (2005) 147–152. https://doi.org/10.1016/j.jphotochem.2004.06.014.

[70] T. Padfield, S. Landi, The Light-Fastness of the Natural Dyes, Studies in Conservation 11 (1966) 181–196.

[71] P.M. Whitmore, G. Cass, The ozone fading of Traditional Japanese Colorants, Studies in Conservation 33 (1988) 29–40.

[72] M. Yatagai, Y. Magoshi, M.A. Becker, C. Sano, H. Ikuno, N. Kohara, M. Saito, Degradation and color fading of silk fabrics dyed with natural dyes and mordants, ACS Symposium Series 779 (2001) 86–97. https://doi.org/10.1021/bk-2001-0779.ch007.

[73] I. Vanden Berghe, Towards an early warning system for oxidative degradation of protein fibres in historical tapestries by means of calibrated amino acid analysis, J Archaeol Sci 39 (2012) 1349–1359. https://doi.org/10.1016/j.jas.2011.12.033.

[74] A. Manhita, V. Ferreira, H. Vargas, I. Ribeiro, A. Candeias, D. Teixeira, T. Ferreira, C.B. Dias, Enlightening the influence of mordant, dyeing technique and photodegradation on the colour hue of textiles dyed with madder - A chromatographic and spectrometric approach, Microchemical Journal 98 (2011) 82–90. https://doi.org/10.1016/j.microc.2010.12.002.

[75] H.E. Ahmed, S.S. Darwish, Effect of Museum Conditions on Historical Dyed Silk Fabric with Madder Dye, J Polym Environ 20 (2012) 596–606. https://doi.org/10.1007/s10924-012-0421-x.

[76] P.G. Pietta, Flavonoids as antioxidants, J Nat Prod 63 (2000) 1035–1042. https://doi.org/10.1021/np9904509.

[77] Y. Zhou, J. Zhang, R.C. Tang, J. Zhang, Simultaneous dyeing and functionalization of silk with three natural yellow dyes, Ind Crops Prod 64 (2015) 224–232. https://doi.org/10.1016/j.indcrop.2014.09.041.

[78] J.J. Lee, H.H. Lee, S.I. Eom, J.P. Kim, UV absorber aftertreatment to improve lightfastness of natural dyes on protein fibres, Coloration Technology 117 (2001) 134–138. https://doi.org/10.1111/j.1478-4408.2001.tb00051.x.

[79] H. Cai, L. Gao, L. Chen, X. Chen, Z. Liu, Z. Li, F. Dai, An effective, low-cost and eco-friendly method for preparing UV resistant silk fabric, Journal of Natural Fibers 19 (2022) 5173–5185. https://doi.org/10.1080/15440478.2021.1875362.

[80] H. Zhang, P. Cookson, X. Wang, A Comparative Study on Accelerated Weathering Tests of Wool Fabrics, Textile Research Journal 78 (2008) 1004–1010. https://doi.org/10.1177/0040517507087857.

[81] C. Korenberg, The Effect of Ultraviolet-filtered Light on the Mechanical Strength of Fabrics, The British Museum Technical Research Bulletin (2007). https://www.researchgate.net/publication/312952564.

[82] J. Shao, J. Zheng, J. Liu, C.M. Carr, Fourier transform Raman and Fourier transform infrared spectroscopy studies of silk fibroin, J Appl Polym Sci 96 (2005) 1999–2004. https://doi.org/10.1002/app.21346.

[83] J. Wang, J. Guan, N. Hawkins, F. Vollrath, Analysing the structure and glass transition behaviour of silks for archaeology and conservation, J R Soc Interface 15 (2018). https://doi.org/10.1098/rsif.2017.0883.

[84] K. Kavkler, I. Pucić, P. Zalar, A. Demšar, B. Mihaljević, Is it safe to irradiate historic silk textile against fungi?, Radiation Physics and Chemistry 150 (2018) 101–110. https://doi.org/10.1016/j.radphyschem.2018.04.030.

[85] S. Tse, A.L. Dupont, Measuring silk deterioration by high-performance size-exclusion chromatography, viscometry, and electrophoresis, ACS Symposium Series 779 (2001) 98–114. https://doi.org/10.1021/bk-2001-0779.ch008.

[86] Y. Gong, G. Zhou, C. Qiao, Y. Pan, Study on the photodegradation behaviors of thermal-aged silk, Herit Sci 12 (2024). https://doi.org/10.1186/s40494-024-01270-w.

[87] P. Garside, S. Lahlil, P. Wyeth, Characterization of Historic Silk by Polarized Attenuated Total Reflectance Fourier Transform Infrared Spectroscopy for Informed Conservation, Appl Spectrosc 59 (2005).

[88] Z. Zhu, N. Tse, P. Nel, M. Tobin, Degradation profiles of silk textiles in diverse environments: Synchrotron based infrared micro-spectroscopy analysis, in: MRS Adv, Materials Research Society, 2017: pp. 3939–3949. https://doi.org/10.1557/adv.2017.596.

[89] J. Kim, X. Zhang, P. Wyeth, THE INHERENT ACIDIC CHARACTERISTICS OF AGED SILK, E-PRESERVATION Science 5 (2008) 41–46. www.e-PRESERVATIONScience.org.

[90] D. Badillo-Sanchez, D. Chelazzi, R. Giorgi, A. Cincinelli, P. Baglioni, Understanding the structural degradation of South American historical silk: A Focal Plane Array (FPA) FTIR and multivariate analysis, Sci Rep 9 (2019). https://doi.org/10.1038/s41598-019-53763-5.

[91] X. Zhang, P. Wyeth, Performance measurement of sericin-coated silks during aging, Sci China Chem 54 (2011) 1011–1016. https://doi.org/10.1007/s11426-011-4270-6.

[92] S. Lee, S.H. Kim, Y.Y. Jo, W.T. Ju, H.B. Kim, H. Kweon, Effects of ultraviolet light irradiation on silk fibroin films prepared under different conditions, Biomolecules 11 (2021) 1–11. https://doi.org/10.3390/biom11010070.

[93] R. Dang, F. Zhang, D. Yang, W. Guo, G. Liu, Spectral damage model for lighting paper and silk in museum, J Cult Herit 45 (2020) 249–253. https://doi.org/10.1016/j.culher.2020.03.001.

[94] M.A. Koperska, D. Pawcenis, J. Bagniuk, M.M. Zaitz, M. Missori, T. Łojewski, J. Łojewska, Degradation markers of fibroin in silk through infrared spectroscopy, Polym Degrad Stab 105 (2014) 185–196. https://doi.org/10.1016/j.polymdegradstab.2014.04.008.

[95] M.A. Koperska, D. Pawcenis, J.M. Milczarek, A. Blachecki, T. Łojewski, J. Łojewska, Fibroin degradation - Critical evaluation of conventional analytical methods, Polym Degrad Stab 120 (2015) 357–367. https://doi.org/10.1016/j.polymdegradstab.2015.07.006.

[96] G. Carissimi, A.A. Lozano-Pérez, M.G. Montalbán, S.D. Aznar-Cervantes, J.L. Cenis, G. Víllora, Revealing the influence of the degumming process in the properties of silk fibroin nanoparticles, Polymers (Basel) 11 (2019). https://doi.org/10.3390/polym11122045.

[97] T. Aguayo, M. Carolina Araya, T. Mónica Icaza, M. Campos-Vallette, A vibrational approach for the study of historical weighted and dyed silks, J Mol Struct 1075 (2014) 471–478. https://doi.org/10.1016/j.molstruc.2014.07.016.

[98] M.A. Becker, Y. Magoshi, T. Sakai, N.C. Tuross, Chemical and Physical Properties of Old Silk Fabrics, Studies in Conservation 42 (1997) 27–37.

[99] S. Akyuz, Investigation of the degradation stages of archaeological and historical silk textiles: An ATR-FTIR spectroscopic study, Archaeology & Anthropology: Open Access 3 (2019) 447–451. https://doi.org/10.31031/AAOA.2019.03.000573.

[100] A.C. Hermes, R.J. Davies, S. Greiff, H. Kutzke, S. Lahlil, P. Wyeth, C. Riekel, Characterizing the decay of ancient Chinese silk fabrics by microbeam synchrotron radiation diffraction, Biomacromolecules 7 (2006) 777–783. https://doi.org/10.1021/bm0508313.

[101] L. Geminiani, F.P. Campione, C. Corti, B. Giussani, G. Gorla, M. Luraschi, S. Recchia, L. Rampazzi, Historical silks: a novel method to evaluate their condition with ATR-FTIR spectroscopy and Principal Component Analysis, J Cult Herit 67 (2024) 9–22. https://doi.org/10.1016/j.culher.2024.01.015.

[102] G. Freddi, P. Monti, M. Nagura, Y. Gotoh, M. Tsukada, Structure and molecular conformation of Tussah silk fibroin films: Effect of heat treatment, J Polym Sci B Polym Phys 35 (1997) 841–847. https://doi.org/10.1002/(SICI)1099-0488(19970415)35:5<841::AID-POLB13>3.0.CO;2-A.

[103] M. Tsukada, M. Obo, H. Kato, G. Freddi, Fab. Zanettv, Structure and Dyeability of Bombyx mori Silk Fibers with Different Filament Sizes, J Appl Polym Sci 60 (1996). https://doi.org/10.1002/(SICI)1097-4628(19960606)60:10<1619::AID-APP14>3.0.CO;2.

[104] J. Magoshi, Y. Magoshi, S. Nakamura, Physical properties and structure of silk. III. The glass transition and conformational changes of tussah silk fibroin, J Appl Polym Sci 25 (1980) 1813–1813. https://doi.org/10.1002/app.1980.070250830.

[105] M. McGill, G.P. Holland, D.L. Kaplan, Experimental Methods for Characterizing the Secondary Structure and Thermal Properties of Silk Proteins, Macromol Rapid Commun 40 (2019). https://doi.org/10.1002/marc.201800390.

[106] L.F. Drummy, D.M. Phillips, M.O. Stone, B.L. Farmer, R.J. Naik, Thermally induced α-helix to β-sheet transition in renegated silk fibers and films, Biomacromolecules 6 (2005) 3328–3333. https://doi.org/10.1021/bm0503524.

[107] L.F. Drummy, B.L. Farmer, R.R. Naik, Correlation of the β-sheet crystal size in silk fibers with the protein amino acid sequence, Soft Matter 3 (2007) 877–882. https://doi.org/10.1039/b701220a.

[108] T. Asakura, J. Yao, 13 C CP/MAS NMR study on structural heterogeneity in Bombyx mori silk fiber and their generation by stretching , Protein Science 11 (2002) 2706–2713. https://doi.org/10.1110/ps.0221702.

[109] T. Asakura, M.P. Williamson, A review on the structure of Bombyx mori silk fibroin fiber studied using solid-state NMR: An antipolar lamella with an 8-residue repeat, Int J Biol Macromol 245 (2023). https://doi.org/10.1016/j.ijbiomac.2023.125537.

[110] A.M. Coats, D.W.L. Hukins, C.T. Imrie, R.M. Aspden, Polarization artefacts of an FTIR microscope and the consequences for intensity measurements on anisotropic materials, J Microsc 211 (2003) 63–66. https://doi.org/10.1046/j.1365-2818.2003.01198.x.

[111] D.J. Walls, Application of ATR-IR to the Analysis of Surface Structure and Orientation in Uniaxially Drawn Poly(ethyleneterephthalate), Appl Spectrosc 45 (1991) 1193–198.

[112] PerkinElmer, Inc, Orientation effects in ATR spectra, 2012. www.perkinelmer.com.

3.2 Accelerated Ageing

3.2.1 Aims of Accelerated Ageing

Accelerated aging tests serve three primary purposes [1]. First, they quickly establish the relative ranking of materials or their combinations based on chemical stability or physical durability. Second, they predict the long-term behaviour of material systems under expected usage conditions. Third, they accelerate deterioration processes in the lab to understand the chemical reactions (degradation mechanisms) and their physical consequences.

Three main factors - light, heat, and moisture - primarily cause weather-related degradation. These factors broadly define exposure conditions. In any weathering test, at least one of these elements influences material degradation, with secondary factors, like local climate or specific material stresses, also playing a role.

Depending on the test's purpose, conditions may vary. For ranking materials, harsher conditions might be used, while long-term predictions require careful consideration of all degradation factors and their interactions. For mechanism studies, using a single aging agent or a simplified system can clarify the impact of each factor.

Photochemical and thermal ageing aspects, as well as the effects of other environmental factors such as humidity or outdoor and indoor generated air pollutants, are often studied on museum and archival materials. In the field of art conservation, accelerated ageing tests are conducted for various purposes [2].

Comparative studies are often employed to assess the sensitivity of various materials to light, which can guide decisions on suitable display conditions for artifacts [2]. These tests help compare materials to determine which are most light-sensitive, such as classifying the fugitive nature of dyestuffs or lake pigments, or evaluating the suitability of conservation materials [2–4]. Additionally, comparing the effects of different light sources and filters on the same material can help establish safer display conditions at specific illumination levels. A second area of study focuses on understanding how light has affected the current appearance of objects. For instance, paintings that now appear blue or whitish may have originally featured green or yellow hues due to the presence of organic yellow pigments that have since faded [2]. A third purpose of light-ageing experiments is to create materials that are sufficiently degraded from their original state to serve as models for the chemical or mechanical behaviour of naturally aged materials [5].

Kinetics of ageing

When laboratory-ageing tests are aimed at predicting the condition of a material at a future time, understanding the aging mechanism—whether it is linear, slows down, or accelerates over time - is crucial. Addressing the problem of changes in properties with time involves studying the kinetics of change, which includes how reaction rates vary with conditions like temperature, humidity, and reactant concentration [1].

If a single chemical reaction drives the observed changes, chemical kinetics can offer a clear interpretation. However, multiple reactions often occur simultaneously, leading to complex degradation data. For example, in paper exposed to light, lignin may darken under UV radiation, while cellulose remnants bleach, with temperature and humidity adding further complexity. This interplay means that the net discolouration depends on which process dominates under specific conditions. In cases where multiple processes contribute to changes in properties like yellowness or fading, it is unlikely that temperature, humidity, or UV radiation will uniformly accelerate each underlying chemical step.

Most degradation processes in heritage materials do not follow zero-order kinetics (where changes are linear over time). Situations frequently occur in which a process appears linear but if the very first moments of change are observed, an initial change may be noted that is particularly rapid. Hence the importance to collect a reasonable amount of data throughout the whole experiment. One can be alerted to this possibility if, when extrapolated to zero time, the apparently linear set of data points does not intercept at the initial concentration (or physical property) at time zero. In some other cases, an induction time can occur, that is an initial period when only slight change is observed. If the reaction is not carried out far enough, the fact that there were actually two stages can easily be overlooked. In both cases, unnoticing these processes can alter significantly the overall description of the whole degradation mechanism and rate.

When a single well-defined chemical substance or process is studied, its degradation can usually be described by established kinetic equations. The fading of dyes in solution, for example, often follows first-order kinetics, showing a consistent behaviour over time. However, complex mixtures like textiles, paints, varnishes, and adhesives deteriorate in non-constant or non-monotonic ways, typically in stages that involve specific chemical steps like initiation, propagation, and termination, with possible subsidiary reactions like inhibition or chain transfer in free-radical processes. Given the non-linear nature of material degradation, it is essential to determine the overall pattern of changes in physical properties or specific chemical substances up to the point of failure when designing and conducting accelerated aging tests.

3.2.2 Artificial Vs. Natural Ageing

The efforts of the material scientists since the 1950s have provided us with a number of protocols which have been developed to test the life expectancy of a variety of materials. In

applications where inspection is difficult or failure could be catastrophic, such as gas pipelines, chemical storage tanks, underground cabling, aerospace components, personnel safety equipment, and medical implants, a deep understanding of failure mechanisms is essential for predicting product lifespan. Consumers are increasingly demanding stringent product guarantees, especially for engineering components in cars and domestic appliances, where extended warranties are seen as indicators of quality. While the life expectancy of products in less demanding applications has traditionally been based on past experience, critical or long-term uses of plastics require more precise lifetime predictions [6]. In many cases, materials are tested for durability and behaviour by exposing them to natural aging conditions, either outdoors or indoors, within the environments they are expected to encounter during their lifetime. Laboratory aging tests are conducted under more controlled conditions than natural exposure and are designed to study the impact of individual weathering factors while accelerating material degradation and potential product failure.

Relating the results from accelerated weathering tests to actual-use conditions is challenging due to the variability between natural and artificial ageing conditions and the reduction of the causes of environmental stresses [7]. No single laboratory test can fully simulate natural exposures, which vary widely due to differences in solar radiation, moisture, temperature, pollutants, and other factors. For instance, frequent temperature cycling and unrealistic moisture levels in accelerated tests can produce effects that do not accurately reflect natural exposure, potentially leading to different mechanisms of change. Besides, ageing protocols generally reproduce simplified systems with few variables to reduce the complexity of the interactions of all degradation factors.

Therefore, while accelerated weathering tests are useful for comparing the relative durability of materials in a specific location and understanding weathering mechanisms, they cannot reliably predict the long-term durability and aging behaviour of materials in their intended exposure conditions [1].

A critical issue is the calculation of the acceleration factor. Numerous mathematical models have been developed to assess how well accelerated aging tests reflect the behaviour of materials during outdoor aging, even if demonstrating a satisfactory correlation between accelerated and natural aging conditions is not straightforward. Acceleration factors determined for a specific material formulation are valid only if they are based on a sufficient number of separate outdoor, indoor, and accelerated weathering tests, allowing for statistical analysis of the results. As a general rule, it is invalid to apply a "general acceleration factor" that equates a specific number of hours of radiant exposure in a laboratory device to months or years of natural exposure for all materials. Brown [8] noted that the degree of correlation between natural and artificial aging tends to be inversely related to the acceleration factor. This implies that as the acceleration factor increases, the comparability between the results from artificial aging and natural aging decreases. Hence, it is suggested that an acceleration factor of between five to ten times is generally acceptable [9]. Keeping in mind that the acceleration

factor is not solely dependent on the intensity of irradiance but is significantly influenced by other environmental parameters such as temperature and humidity, the evaluation of the radiant exposure may be helpful in making rough estimates of potential speed-up factors.

Another critical concern in these tests is selecting which properties to monitor as indicators of aging [1]. Relying on a single chemical property can lead to incorrect conclusions, as opposing reactions, like cross-linking versus chain breaking or yellowing versus bleaching, can occur simultaneously. Thus, choosing the right property to measure is essential. Depending on the objectives, it could be more valuable to measure a property showing early changes, dramatic shifts near failure, or predictable behaviour throughout the entire useful life span of the material being tested.

3.2.3 Variables Controlling Artificial Ageing

Light, heat, and humidity are the primary factors influencing material aging, so they are the most frequently controlled in accelerated aging devices. Sunlight, particularly the ultraviolet (UV) portion of the solar spectrum, often initiates weathering degradation. The shorter wavelengths of light, which have higher photon energies, are more strongly absorbed by most organic materials and have a greater potential to break chemical bonds. In some instances, materials may not directly absorb short-wavelength light, but impurities and additives within the material can facilitate absorption. Accelerated aging tests often involve shifting the radiation spectrum toward shorter wavelengths to reduce test time. However, this approach can initiate degradation processes that would not occur under natural sunlight exposure, as these short-wave UV wavelengths are typically absent in solar radiation reaching the Earth's surface [10]. Conversely, if a test light source lacks certain wavelengths found in sunlight, similar deviations in degradation may occur. Another issue is the choice of exposing samples to continuous lamp emissions for accelerated-aging tests, while natural conditions involve alternating periods of daylight and darkness. Continuous exposure can produce different results than those observed under alternating conditions [1,9,10]. For instance, continuous illumination can increase sample temperature, reducing moisture content. This is significant because fading or other photochemical damage often depends on moisture content.

Heat is another critical factor in acceleration [9]. Comparable conditions of heat are often measured using the 'Black Panel Temperature,' which theoretically represents the maximum surface temperature during exposure. The black panel sensor, typically a black-coated steel panel with a thermocouple attached, is commonly used to control and replicate actual exposure conditions in a weathering device. The closer the temperature used in accelerated aging tests is to ambient temperature, the more realistic the aging conditions are. An approximate rule drawn from reaction kinetics states that a temperature increase of 10 °C will approximately double the reaction rate. The assumption that elevated aging temperatures simply accelerate natural aging reactions without significantly altering their nature has been largely abandoned.

Water presence is necessary for certain degradation reactions, depending on the material [9]. Water can be delivered to a specimen's surface in various forms, such as humidity, rain, dew, or condensation. In accelerated weathering tests, water is applied similarly, with relative humidity controlled and spray cycles used to simulate rainfall. Water can cause damage both physically and chemically, such as through absorption leading to volume expansion and subsequent stress within the material. Cycling between wet and dry periods can cause further stress, leading to fatigue and setting the stage for additional chemical and mechanical degradation. In metals, water promotes corrosion reactions.

Beyond light, heat, and water, gaseous and saline pollutants, as well as particulate matter, play fundamental roles in degradation [9]. Gaseous pollutants like SO_2, NO_X, HCl, HF, O_3, and acids like H_2SO_4 and HNO_3 are particularly significant. Pollutants can be deposited on surfaces through dry deposition (direct accumulation) or wet deposition (incorporation into precipitation). Factors like gas concentration, wind velocity, and wetness time affect the interaction between pollutants and exposed surfaces. In the presence of multiple pollutants, synergistic interactions can occur.

3.2.4 Practical Aspects of Photochemical Deterioration

To accurately simulate a specific environment, understanding the distribution and intensity of wavelengths is crucial [9]. Sunlight's intensity and spectral energy distribution vary with factors like season, location, and atmospheric conditions such as aerosols or pollutants. Therefore, accelerated test conditions must align closely with real exposure conditions for the results to be applicable in developing and applying predictive models. Two key factors are critical when selecting a light source for accelerated testing. First, the spectrum should ideally have a cutoff at a wavelength similar to that of the actual exposure environment, as the presence of short wavelengths in an artificial source can induce unnatural chemical degradation, leading to inaccurate test results. Second, the intensity of the irradiance level should be carefully controlled and maintained at the desired level.

Spectral Distribution and Photochemical Degradation

Approximately 42% of solar radiation falls in the infrared range ($\lambda > 800$ nm), which significantly contributes to the heating of irradiated objects [9]. This portion of radiation, however, does not initiate photochemical reactions that cause polymer degradation. In contrast, visible radiation (400-800 nm) makes up about 52% of total solar radiation. While it also contributes to heating, it is capable of initiating photochemical processes, such as those affecting dyes or sensitized plastics. The remaining 6% of solar radiation lies in the ultraviolet (UV) range ($\lambda < 400$ nm), which, despite its minimal contribution to heating, plays a crucial role in the photochemical degradation of polymers due to its higher quantum energy. The Earth's ozone layer absorbs most of the UV radiation from the sun, especially the more harmful short-wave UV rays.

Depending on the conditions which the test aims to recreate, choosing the correct cutoff wavelength is crucial. For testing organic materials, especially polymers, the UV content (300-400 nm) of the radiation is particularly decisive. Therefore, measurements within this UV range provide more valuable data for understanding photochemical degradation than total irradiance measurements. Narrow-band measurements within the UV spectrum, such as at 340 nm, can offer even more detailed insights into the degradation processes, helping to improve material protection strategies. If the aim is recreating outdoor exposure, the light source should supply sufficient radiant energy in the UV region 280 to 315 nm, deprived of the short-wave UV wavelengths using filters or specific sources. In the case of indoor conditions, such as those occurring under ordinary museum circumstances, it is recommended that such wavelengths be avoided in most accelerated photochemical testing that is related to conservation problems, as such interval is not significantly transmitted by ordinary window glass. The irradiance between 315 and 340 nm should be reduced consequently as well [1].

Choosing the appropriate cutoff wavelength is crucial depending on the conditions the test aims to replicate. For testing organic materials, particularly polymers, the UV content (300-400 nm) of the radiation plays a decisive role in degradation [9]. Therefore, measurements within this UV range are more informative for understanding photochemical degradation than total irradiance measurements. Narrow-band measurements, such as at 340 nm, can provide even more detailed insights into degradation processes, aiding in the development of better material protection strategies.

For tests that aim to recreate outdoor exposure, the light source should supply sufficient radiant energy in the UV range from 280 to 315 nm, while avoiding short-wave UV wavelengths by using filters or specific sources. In the context of indoor conditions, such as typical museum environments, it is advisable to avoid including these wavelengths in accelerated photochemical testing related to conservation, as they are not significantly transmitted through ordinary window glass. Consequently, irradiance between 315 and 340 nm should also be reduced according to the shape of the absorbing curve [1] (Figure 4).

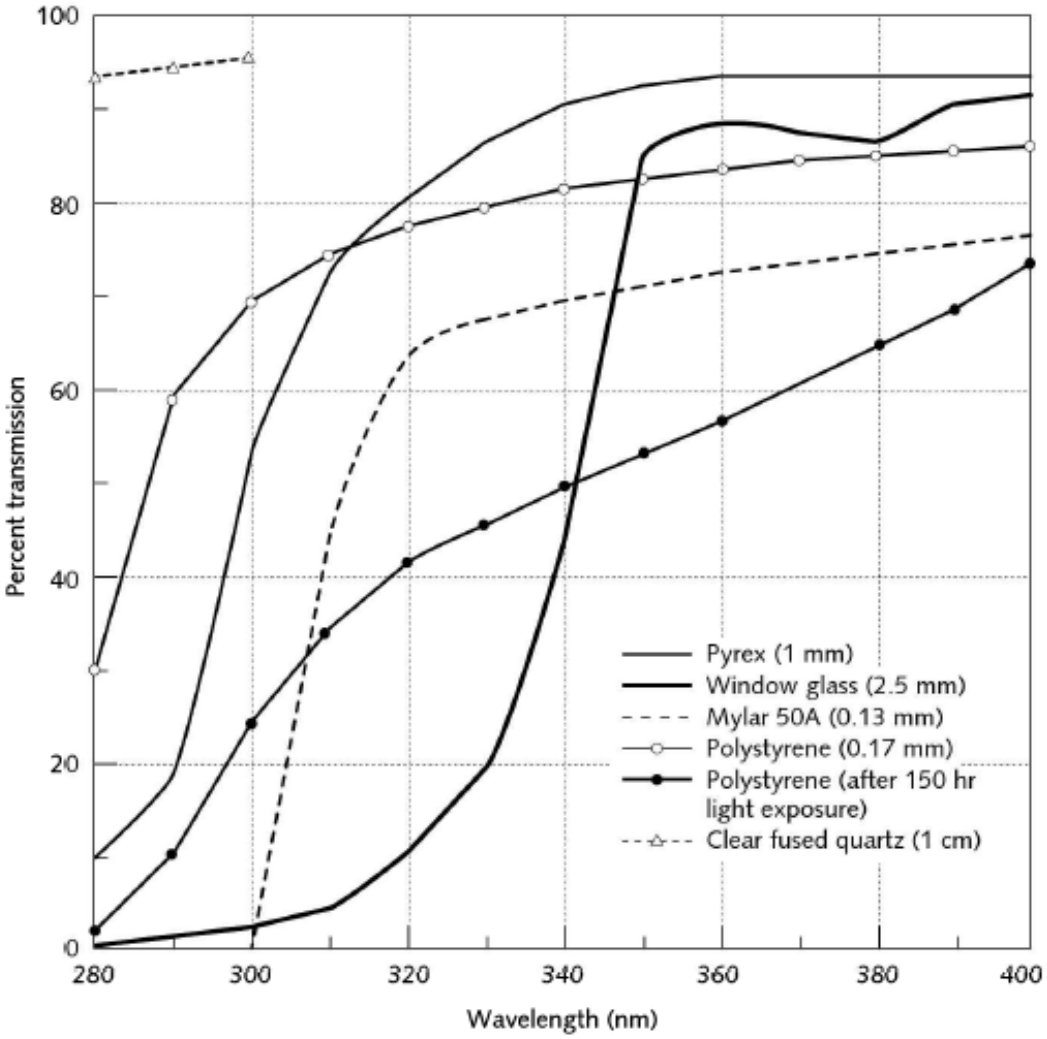

Figure 4. Transmission spectra in the UVA-UVB regions of various materials used as light filters [11].

Sources of light

Commercially available light sources for accelerated aging tests include carbon arc, xenon arc, and fluorescent lamps [1]. The carbon arc has been employed as a solar simulator in accelerated weathering and lightfastness tests since 1918, and many ASTM and Federal Test Methods still specify its use. However, when comparing the light output of the carbon arc to natural sunlight, certain deficiencies become apparent. Notably, the carbon arc emits a significant amount of energy in the UV-C portion of the spectrum, which falls below the typical solar cutoff point of 295 nm. As a result, these short wavelengths can lead to unrealistic degradation when compared to natural exposure.

Xenon arc lamps, when modified with specific filters, can closely simulate sunlight, providing a good approximation for most applications. The xenon arc was adapted for accelerated weathering tests in Germany in 1954. Operating xenon arc systems involves addressing certain specific issues. Firstly, the inevitable light output decay due to lamp aging requires that a light monitoring system to compensate for it. Secondly, Xenon arc lamps require a combination of

filters to minimize unwanted radiation. Automotive test methods that use xenon arc exposure often specify the use of quartz inner and borosilicate outer filters, which allow severe and unrealistic short-wavelength UV radiation down to 270 nm. The most common filter combination, however, is borosilicate for both inner and outer filters. This combination provides a better simulation of sunlight UV, as it has a cutoff wavelength of around 280 nm, which is closer to the natural sunlight cutoff of 295 nm.

Other commonly used lamps are fluorescent UV ones. The emission spectra of the main fluorescent UV lamp are reported in Figure 5. They have gained widespread use for accelerated weathering tests. These testers employ various types of fluorescent lamps, each with distinct spectral outputs tailored for specific exposure applications. For example, UVA 340 lamps emit peak wavelengths at 343 nm, which closely replicate the short and middle UV regions of daylight, while UVA 351 lamps are peaked at 351 nm, simulating UV wavelengths filtered through window glass. Unlike arc testers that aim to replicate the full spectrum of sunlight, fluorescent UV testers focus on reproducing the damaging effects of sunlight, primarily the short-wavelength UV radiation that causes most of the degradation in durable outdoor materials. As a result, these testers primarily emit radiation within the UV portion of the spectrum.

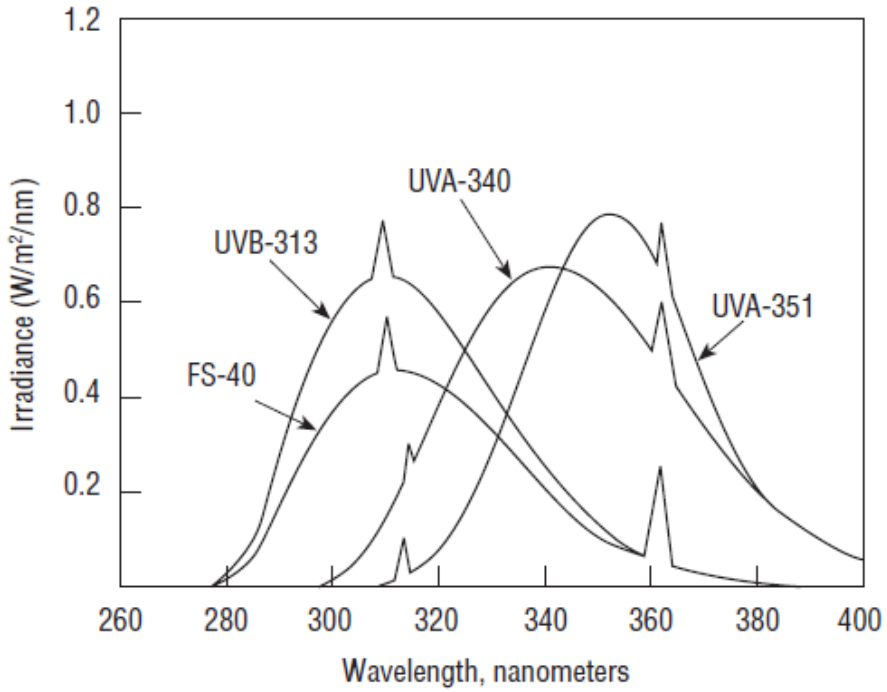

Figure 5. Spectral distribution of irradiance from various fluorescent lamps emitting mainly in in the UVA-UVB regions [1].

Introduced in the early 1970s, the FS-40 was the first fluorescent UV lamp to gain widespread use, particularly in some automotive specifications for coatings. This lamp emits mostly in the UV-B portion of the spectrum, with some UV-A output, and has shown good correlation with outdoor exposures for gloss retention in coatings and the integrity of plastics. However, its

short-wavelength output below the solar cut-off can sometimes produce inconsistent results, especially in terms of colour retention for plastics and textiles.

Introduced in 1984 as a second-generation FS-40, the UVB-313 lamp shares the same spectral power distribution (SPD) as the FS-40 but offers higher and more stable output. The UVB-313 is now the most widely used light source for ASTM G-53 devices, except in the automotive industry.

Introduced in 1987 to improve correlation with outdoor exposures, the UVA-340 lamp primarily emits in the UV-A region, with a minor output in UV-B. It has been tested on both plastics and coatings and greatly enhances the correlation with outdoor exposures.

The UVA-351 lamp provides an excellent simulation of sunlight filtered through ordinary window glass, making it highly suitable for testing interior applications. Its spectral output closely matches that of sunlight as it passes through window glass, effectively filtering out the shorter UV wavelengths, thus offering a realistic assessment of photochemical effects under indoor conditions.

These fluorescent UV lamps and testers provide valuable insights into the durability and degradation of materials by simulating the key damaging aspects of sunlight, particularly in specific testing scenarios for both indoor and outdoor environments [12].

Measuring light irradiance

The measurement of irradiance (the power of radiation per unit area, [W/m^2]) is crucial for understanding the impact of radiation on materials [1,9,10]. The CIE recommends an irradiance of 1000 W/m^2 within the 300-3000 nm wavelength range for testing purposes, simulating conditions at the equator under a clear sky at noon during the equinox. A commonly used reference is the 'average optimum daylight' for Miami, which has been measured with a spectroradiometer, with average data taken throughout the day during the spring equinox. Using the Miami average as a baseline, a setting of 0.35 $W/m^2/nm$ can simulate sunlight intensity. The spectral range of 300-800 nm, which is of particular interest for photochemical processes, accounts for 580 W/m^2 of this irradiance.

Radiant exposure, defined as the total radiant energy received by a surface, can be calculated by multiplying irradiance by time, and is expressed in joules per square meter (J/m^2). This measure is crucial in understanding the photochemical effects of radiation on materials, particularly in the context of natural vs. accelerated aging tests. For instance, in Miami, the annual radiant exposure in the spectral range of 300-800 nm has been measured at 3480 MJ/m^2. When conducting accelerated aging tests, achieving an intensity comparable to that of sunlight can lead to an acceleration factor relative to natural weathering conditions. According to Kockott [9], a typical accelerated aging test simulating sunlight radiant energy can produce an acceleration factor of five times compared to exposure in Miami. This means that conditions

in the test could simulate approximately five years of natural aging in Miami in just one year of testing.

Irradiance meters, or radiometers, are used to measure irradiance but are often expensive and have limitations when measuring low irradiance levels. Alternatively, light meters, which are more affordable and sensitive in low-light conditions, measure light perceived by the human eye, are calibrated to follow the CIE (International Commission on Illumination) photopic luminosity curve, which represents the sensitivity of human vision to different wavelengths of light [13]. The unit of illuminance, lux (lx), represents lumens per square meter, or luminous flux per unit area. The luminous flux is expressed in lumen and it is a derived unit that combines Candela (cd), the SI base unit for luminous intensity, with Steradian (sr), a unit of solid angle. One Candela is defined as the luminous intensity of monochromatic radiation at a frequency of 540×10^{12} Hz, corresponding to a wavelength of about 555 nm. This wavelength, close to the peak sensitivity of human vision, represents where humans see light most effectively. One Candela projected over a full sphere (4π steradians) produces approximately 12.57 lumens. When spread over an area of one square meter, this results in an illuminance of about 12.57 lux, which is a measure of the amount of visible light perceived by the human eye.

While it would be beneficial to have a direct conversion factor between irradiance (W/m^2) and illuminance (lx) for using light meters in photovoltaic applications under low solar irradiance conditions, there is no universal or straightforward conversion standard. This is largely because irradiance measures the total energy across the electromagnetic spectrum, while illuminance only pertains to visible light, which represents a small portion of the solar spectrum. As a result, the relationship between W/m^2 and lx depends on several factors, including the spectral distribution of light and the sensitivity of the meter to different wavelengths. Michael [13] reviewed the main literature on the subject and established a theoretical and laboratory measurement guide for the conversion between solar irradiance and illuminance.

Activation Spectra and Material Degradation

To better understand the impact of different wavelengths on material degradation, the concept of "activation spectra" has been introduced. Developed from the work of Searle [14], this technique helps identify which spectral ranges contribute most significantly to the degradation of a polymer. The activation spectrum shows how a material's properties change as a function of wavelength when irradiated by a given light source, whether solar or artificial.

By using a series of cut-off filters that block specific UV wavelengths, researchers can isolate and measure the effects of different spectral ranges on the material. This allows for the identification of the most detrimental wavelengths, which are critical for improving the material's stability. For example, in studies using xenon radiation filtered to simulate open-air solar radiation, the most harmful wavelengths for polycarbonate yellowing were found to be between 300 and 320 nm (**Figure 6**).

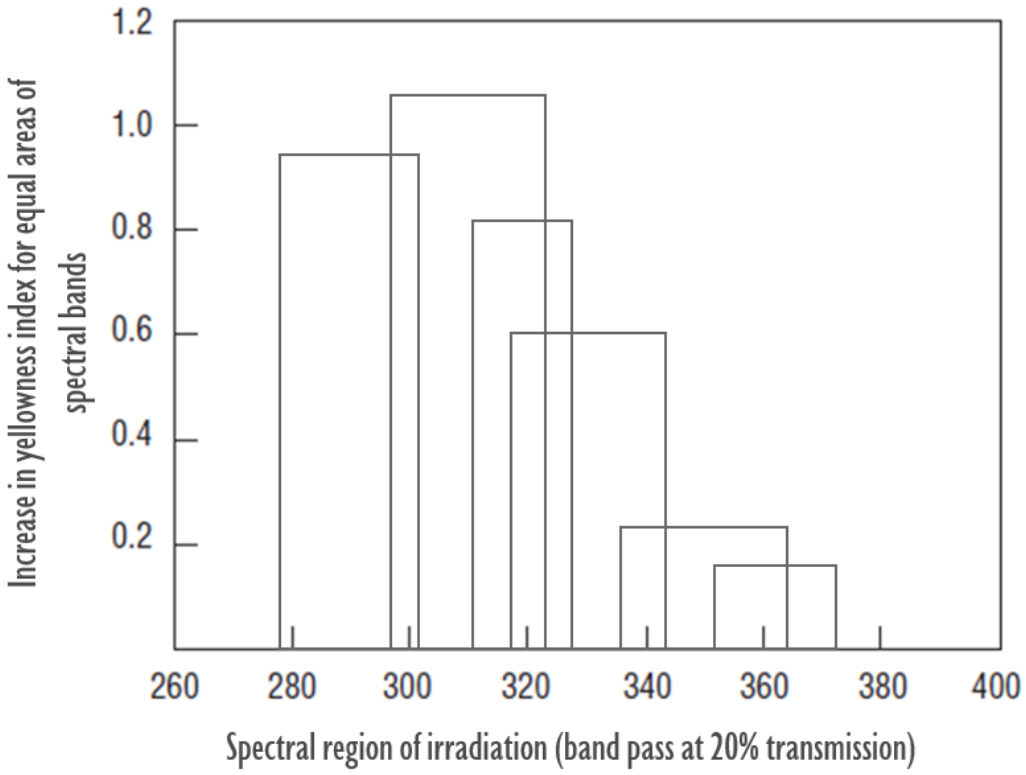

Figure 6. Activation spectrum for yellowing of a polycarbonate film, Adapted from [14]

Depth of Photochemical Penetration

The depth of photochemical degradation within a material is influenced by the wavelengths of light use [1]. Shorter wavelengths tend to be absorbed more readily, leading to degradation primarily on the surface of the material. This surface-level action was recognized early on by textile scientists, who observed that finer fibres deteriorate more rapidly than coarser ones. For instance, the surface-to-volume ratio of fibres is therefore an important consideration when comparing the photochemical stability of different textile materials.

3.2.5 Artificial ageing procedures for textiles

In order to set properly the artificial ageing experiment of the material under analysis, the main standards for textiles are reviewed in the following. Despite these rules have been set for industrial checks and comparison of the performance of different in-service materials, they can provide useful recommendations on the setting of an accelerated ageing experiment aimed at pretending the actual ageing of heritage materials in their regular display conditions.

Colour fastness is one of the most extensively studied properties in textiles, as changes in colour due to exposure to light, washing, or other environmental factors can significantly affect both the appearance and performance of fabrics [15]. When textiles undergo testing for light fastness, it generally refers to indoor applications, where fabrics such as apparel, carpets, and upholstery are exposed primarily to solar radiation through window glass or artificial lighting. To simulate these conditions, xenon-arc instruments with optical window glass filters are used to mimic the light exposure in indoor environments. Weather fastness, however, pertains to outdoor applications, where materials are exposed to natural solar radiation, rain, and dew. In these cases, the testing includes optical daylight filters and periodic water spray to replicate outdoor conditions more accurately.

After exposure, the extent of colour change is assessed either visually or through a colourimeter, and results are compared to blue wool reference materials to determine the degree of lightfastness. For applications where the colour's integrity is less significant, such as in geotextiles, ropes, and seat belts, the focus shifts toward evaluating the mechanical properties of the textile, such as tensile strength. In these cases, ensuring the textile's durability and resistance to environmental factors takes precedence over the preservation of colour.

It is noteworthy that colour changes often occur more quickly than any degradation in the mechanical strength of the textile. This is why the industry tends to prioritize colour quality assurance over mechanical evaluations, except in technical applications where the functional strength of the material is more crucial than its appearance. In this case, there are certified methods to test strength and abrasion resistance [16]. Strength tests are designed to ensure that textiles reaching the market are durable and not prone to failure under stress. While most fabrics rarely fail such tests, they serve to identify any weaknesses in materials, such as the tendering of cotton caused by sulfur dyes during storage. Among them, there are the grab test (ASTM D5034, ISO 9073), the strip test (ASTM D5035), the ball burst test (ASTM D3787, ISO 9073-5) and the hydraulic burst test (ASTM D3786, ISO 139382), and some others. Abrasion resistance tests aim to simulate the gradual wear that textiles experience. A variety of testing instruments, such as the Universal Wear Tester (Stoll), Martindale (ASTM D4966, ISO 12947-1), and Wyzenbeek (ASTM D4157) is used to evaluate textiles performances.

While certified methods for evaluating the photodegradation of natural textiles are not apparently available, there are different methods for the photoageing of geotextiles [17].

Alternatively, also different protocols give indications for the accelerated ageing testing of plastics (ISO 4892) [12] or coatings and paints (ISO 16474) [7].

In conservation science, the interest in accelerated ageing testing is mostly aimed at reproducing accurately the features of naturally aged objects of art in order to understand the factors affecting their degradation/ageing, to test new analytical techniques for their investigation and to develop new restoration/preservation strategies. Few scientific papers in the conservation science field deal with accelerated ageing of textiles, as the majority of them deals with light fastness of the dyes.

Standard Methods to Evaluate Colour Fastness

For most textile applications, including apparel, sportswear, and garments, colour fastness is a crucial material characteristic. Since the 1960s, xenon-arc technology has been predominantly used in the textile industry to assess the colour fastness of textiles to light. Numerous test methods and standards outline how to expose textile samples to xenon-arc radiation, all aiming to evaluate colour fastness to light. However, subtle yet significant differences among these methods can make it challenging for users to select the appropriate test conditions.

Colour fastness standards have been established by various national organizations, such as the Society of Dyers and Colourists (SDC), the American Association of Textile Chemists and Colourists (AATCC), and the Japanese Industrial Standards (JIS). Notably, the International Organization for Standardization (ISO) developed the ISO 105 series, which is widely recognized globally. These ISO colour fastness standards have been adopted without technical changes by the European Standard (EN) of the European Committee for Standardization (CEN) and are mandatory for all member countries.

As a general guideline for colour fastness testing against light, there is the international standard ISO 105-B02 Textiles - Tests for colour fastness - Part B02: Colour fastness to artificial light: Xenon arc fading lamp test. ISO 105-B02 uses window glass filtered Xenon-arc radiation (ISO WG). This standard was originally developed in 1988 and revised several times [18].

Exposure duration for most light fastness test methods is typically based on the fading behaviour of the Blue Wool scale or the equivalent value of delta E, even if there are testing philosophies avoiding the use of Blue Wool for test duration and simply base it on a defined test time or radiant exposure.

ISO 105-B02 describes:

- ISO Blue Wool reference materials (#1 to 8)
- Xenon-arc apparatus requirements, control, and calibration
- Spectral irradiance
- Preparation of the test specimens
- Cycles A1 (normal), A2 (extreme low RH), A3 (extreme high RH), B (American conditions)
- Procedure

- Exposure Methods 1-5
- Evaluation (Assessment of colour fastness)
- Irradiance uniformity requirements in the test area
- Test report

The methods for the assessment of the colour fastness are visual observation and colorimetric measurements. Both rely on the comparison on the original sample with the Grey Scale for colour change or with test specimens which are part of the Blue Scale [15].

The Grey Scale has nine levels, each existing of pairs of grey fields with a contrast according to grades 5 (no contrast), 4, 3, 2 to 1 (strong contrast) with intermediate ratings (1/2, 2/3, 3/4 and 4/5). The Grey Scale of a textile corresponds to the grade which is closest to the contrast between the original unfaded and the faded part of the sample.

An alternative method to measure the amount of light or energy received by exposed samples was developed to facilitate reproducibility in the same location and enable comparisons between different exposure sites. To address this challenge, the Blue Wool Scale Standard was introduced, which is based on the visual scales of coloured wool textile substrates. The European ISO Blue Scale was developed in Germany by the German Colour Fastness Committee (DEK) in 1913. It consists of eight wool fabrics dyed with specific colourants, each possessing increasing levels of light fastness. The goal of the scale is to create a geometric progression, where each standard takes approximately twice as long to fade as the previous one.

The ISO specify different values of irradiance, temperature and relative humidity which should be followed to reproduce specific conditions [18]. For example, under normal conditions, the irradiance is set to 42 W/m^2 within the broad band 300-400 nm, the chamber air temperature is set to 32 °C and the relative humidity (RH) to 40%, but different conditions can be chosen, with the temperature varying between 32 °C and 43 °C and the RH% varying between 15 and 85.

Standard Methods to Evaluate the Photo-Degradation of Textiles

As stated before, there is no certified method for assessing the photo-degradation of natural fibres, as the primary concern with these materials lies in certifying their colourfastness rather than their mechanical properties. However, there are currently three primary methods for assessing the photo-degradation of geosynthetics, which are textiles intended for specific uses [17]. ASTM D5970 evaluates geotextiles using natural outdoor sunlight exposure, simulating real-world conditions. ASTM D4355, on the other hand, employs a Xenon-Arc weatherometer, an artificial light source, to expose geotextiles to accelerated weathering. Geomembranes are tested using GRI-GM11, which utilizes a UV-fluorescent weatherometer to simulate UV exposure. Additionally, ASTM G90 is an outdoor accelerated weathering method, but its use is restricted to specific climatic zones within the United States. These methods are essential for

understanding the long-term durability of geosynthetic materials under UV and weather exposure.

In the case the xenon-arc lamp is used, the exposure consists of 120 min cycles: 90 minutes of light only, followed by 30 minutes of water spray and light. During the 90 minutes light only fraction of the cycle, the black panel temperature is set at 65±5 C and relative humidity of 30±5%. In addition, the light spectrum is controlled by setting the irradiance to 0.35 W/m^2 x nm^{-1} at 340 nm.

In the case of UV lamps, which are UVA-340, the exposure consists of 24 h cycles as follows: 20 hours of light only at 75 °C, followed by 4 hours of condensation (light off) at 60 °C. In addition, the light spectrum is controlled by setting the irradiance to 0.70 W/m^2 x nm^{-1} at 340 nm.

As a general guideline for plastic photodegradation, there is the international standard ISO 4892, which takes into consideration the use of xenon-arc lamps, fluorescent UV-lamps, and carbon-arc lamps [12]. The ISO specify for each lamp type different exposure period and values of irradiance and temperature which should be followed to reproduce specific conditions. For example, UVA-351 lamps are used for a test time of 24 h, with an irradiance value of 0.76 W/m^2 x nm^{-1} at 340 nm, while the black panel temperature is set to 50±3 °C and the RH value is 0%. For UVA-340 and UVB-313 some cycles with water moisture are allowed too.

Methods Used in Museums and Cultural Heritage Studies

Various photoageing devices have been employed by museums and institutions involved in cultural heritage studies to simulate the effects of light on materials [2]. Still nowadays, the choice of light source depends on the material being tested and the objective of the study and it is not rare to come across custom-made ageing chamber within literature [19–24]. Although it is possible to tailor experiments using different light sources and conditions to suit specific research objectives, the lack of a standardized method can sometimes make it difficult to compare the results of experiments even when working with the same materials. The absence of a uniform standard across studies has contributed to inconsistencies in findings and methodologies. Furthermore, it is noteworthy that reliable standards for accelerated aging tests have only been established recently. In the past, many aging apparatuses, even those used by prominent museums, lacked proper control mechanisms and appropriate light sources, leading to less accurate or inconsistent results in preserving and studying material degradation [2,25]. For example, the use of lux meters instead of irradiance meters poses difficulties in comparing their results [13].

In the most recent literature, authors generally refer to standardized methods and use commercial testing chambers or set properly the conditions of their custom-made set-up. For instance, for testing the behaviour of protective coatings under outdoor conditions, xenon arc lamps or UVA-340 lamps are commonly used [26,27]. When the goal is to recreate naturally aged mock-ups or to understand how light has contributed to the current appearance of

objects, xenon arc lamps or UVA-351 lamps are preferred [19,28,29]. Sometimes, also different types of lamps are tested and compared [20,23,30]. Attention should be paid because it is not sufficient to use a commercial set up to perform a realistic accelerated ageing test: the choice of the light source and conditions is still fundamental, as shown by quite recent papers ignoring the recommendations to avoid UVA-313 and UVB light [25,31].

A particular field of developing accelerated ageing tests is for studying material degradation under typical museum conditions. In this case, as only minimal UV radiation is allowed [32], filtered xenon arc, UVA-351 fluorescent, or LED lamps are utilized [23]. Interestingly, narrow-band LEDs have enabled specific aging tests to identify the most harmful regions within the visible spectrum [33,34]. This targeted approach helps to better understand and mitigate the impact of light on cultural heritage materials.

Review of silk ageing apparatus

As previously mentioned, standardized methods for the degradation assessment of natural fibres are not available. Previous authors have chosen a wide range of solutions for conducting accelerated ageing tests on silk. Table 2 reports the conditions of the light-based experimental set-ups which are available in literature.

Lamp Type	Model	Spectral region	Lighting details	Temperature – RH%	Reference and year
Hg arc lamp	Glass-enclosed carbon-arc lamp	>315		55 - 67 °C 30 – 75%	Appel 1935 [35]
	Philips 500 W MBTF (W-Hg)	360, vis		20 ± 2 °C 65 ± 2%	Zhang 2008 [21] (wool)
	Philips 500 W MBTF (W-Hg)		24000 lux (600 µW/lumen in the UV)	35 ± 3 °C 26 ± 6%	Korenberg 2007 [20]
	250W UV	365			Liu 2019 [36]
	Philips TUV-30	254	25.7 W/m^2		Sionkowska 2011 [31]
	42-220 laboratory UV/ozone instrument	184-254			Shao 2005 [37]
		254		50 ± 10 °C 55 ± 5%	Li 2013 [38]
		254	800 µW /cm^2		Luo 2012 [39]
	TLC plate reading UV lamp (120 W)	254			Wang 2018 [40]
	Metal-halide lamp		100Wm^{-2}	40 °C	Kavkler 2018 [41]
Xe arc lamp	Atlas Q-65 Weather-ometer		0.76 W/m^2 (at 420 nm) 0.40 W/m^2 (at 340 nm)	21 °C 55-63 %	Becker 1993 [42]
	SN-500F ageing test chamber	Vis*	100,000 lx	20 ℃ 50% RH	Gong 2024 [29]
	Q-Sun Xe1 Test Chamber	Vis	0.4 W/m^2 (at 340 nm)	28 ℃ 50% RH	Solazzo 2011 [43]
	Xenotest 'Weatherometer"	Vis		25 ℃ 60% RH	Garside 2005 [44]
	QUV Accelerated Weathering Tester (Q-Lab Corporation)		1.2 W/m^2		Zhu 2017 [45]
	Q-Sun Xe1 Test Chamber		0.4 W/m^2 (at 340 nm)	40 °C	Kim 2008 [46]
	Q-Sun Xe1 Test Chamber		0.4 W/m^2 (at 340 nm)	28 °C	Garside 2010 [47]
Fluorescent lamp	QUV weather chamber (Q-Lab Corporation)	313 nm	0.5 W/m^2	50 ± 2 ºC 95% RH	Nilsson 2013 [25]
	QUV weather chamber (Q-Lab Corporation)	313	0.5 W/m^2	50±2 °C	Vilaplana 2015 [48]
	8 x Philips 18W/930 TL-D 90	Vis*	15000 lux (2 µW/lumen in the UV)	22 ± 2 °C 28 ± 5%	Korenberg 2007 [20]
	12 x F20W/AD	Vis*	7000 lux (2 µW/lumen in the UV)	22 ± 2 °C 30-50-70%	Luxford 2009 [49]

	Neon Light Colour 765 Basic daylight Beghelli	Vis	160 mW/lm 11000 Lux	36 °C 40%	Badillo sanchez 2019 [50]
		365	20W/m^2/nm	38 °C 10±5%	Zhang 2011 [51]
	LF215LM, UVITEC	365	2.37-2.12 mW/cm^2		Lee 2021 [52]
LED	4000 K LED	Vis	20 ± 1.07 W/m^2		Dang 2024 [53]
	Narrow-band source	Vis	23 ± 0.5 °C 50%		Dang 2020 [33]
Gamma radiation	^{60}Co gamma-source		4-120 kGy		Kavkler 2018 [41]

Table 2. Review of the experimental parameters used in the light-ageing tests on silk available in literature. Some authors use a polycarbonate filter to filter UV light (*)

3.2.6 References

[1] R.L. Feller, Accelerated ageing - Photochemical and Thermal Aspects, The Getty Conservation Institute, Ann Arbor, Michigan (USA), 1994.

[2] D. Saunders, J. Kirby, A COMPARISON OF LIGHT-ACCELERATED AGEING REGIMES IN SOME GALLERIES AND MUSEUMS, The Conservator 25 (2001) 95–104.

[3] T. Padfield, S. Landi, The Light-Fastness of the Natural Dyes, Studies in Conservation 11 (1966) 181–196.

[4] P.M. Whitmore, G. Cass, The ozone fading of Traditional Japanese Colourants, Studies in Conservation 33 (1988) 29–40.

[5] N. Khandekar, Preparation of cross-sections from easel paintings, Studies in Conservation 48 (2003) 52–64. https://doi.org/10.1179/sic.2003.48.supplement-1.52.

[6] A.S. Maxwell, W.R. Broughton, G. Dean, G.D. Sims, Review of accelerated ageing methods and lifetime prediction techniques for polymeric materials, Teddington, UK, 2005.

[7] Various, BSI Standards Publication Paints and varnishes-Methods of exposure to laboratory light sources, BS EN ISO 16474-1:2013, 2014.

[8] R.P. Brown, Survey of Status of Test Methods for Accelerated Durability Testing, 1991.

[9] D. Kockott, Natural and artificial weathering of polymers, Polym Degrad Stab 25 (1989) 181–208. https://doi.org/10.1016/S0141-3910(89)81007-9.

[10] L.F.E. Jacques, Accelerated and outdoor/natural exposure testing of coatings, Prog Polym Sci 25 (2000).

[11] T. Schaeffer, Effects of Light on Materials in Collections, Getty Conservation Institute, Los Angeles,USA, 2001.

[12] Various, Plastic - Methods of exposure to laboratory light sources - Part 3: Fluorescent UV lamps, ISO 4892-3:2016(E), 2016.

[13] P.R. Michael, D.E. Johnston, W. Moreno, A conversion guide: Solar irradiance and lux illuminance, Journal of Measurements in Engineering 8 (2020) 153–166. https://doi.org/10.21595/jme.2020.21667.

[14] A.L. Andrady, Wavelength Sensitivity in Polymer Photodegradation, in: Advances in Polymer Science, Springer, Berlin, Germany, 1997.

[15] J. VALLDEPERAS-MORELL, Colour fastness, in: A.P. Annis (Ed.), Understanding and Improving the Durability of Textiles, Woodhead Publishing Limited, Cambridge, 2012.

[16] M. Bide, Testing textile durability, in: V.P. Annis (Ed.), Understanding and Improving the Durability of Textiles, Woodhead Publishing Limited, Cambridge, 2012.

[17] L.D. Suits, Y.G. Hsuan, Assessing the photo-degradation of geosynthetics by outdoor exposure and laboratory weatherometer, Geotextiles and Geomembranes 21 (2003) 111–122. https://doi.org/10.1016/S0266-1144(02)00068-7.

[18] Various, Textiles - Xenon-Arc Weathering and Colour Fastness to Light Summary of Testing Standards, 2023. www.atlas-mts.com.

[19] K. Vizárová, M. Reháková, S. Kirschnerová, A. Peller, P. Šimon, R. Mikulášik, Stability studies of materials applied in the restoration of a baroque oil painting, J Cult Herit 12 (2011) 190–195. https://doi.org/10.1016/j.culher.2011.01.001.

[20] C. Korenberg, The Effect of Ultraviolet-filtered Light on the Mechanical Strength of Fabrics, The British Museum Technical Research Bulletin (2007). https://www.researchgate.net/publication/312952564.

[21] H. Zhang, P. Cookson, X. Wang, A Comparative Study on Accelerated Weathering Tests of Wool Fabrics, Textile Research Journal 78 (2008) 1004–1010. https://doi.org/10.1177/0040517507087857.

[22] N. Luxford, Reducing the Risk of Open Display: Optimising the Preventive Conservation of Historic Silks, University of Southampton, UK, 2009.

[23] M. Farke, M. Binetti, O. Hahn, Light damage to selected organic materials in display cases: A study of different light sources, Studies in Conservation 61 (2016) 83–93. https://doi.org/10.1179/2047058414Y.0000000148.

[24] R. Dang, B. Wang, X. Song, F. Zhang, G. Liu, The mathematical expression of damage law of museum lighting on dyed artworks, Sci Rep 11 (2021). https://doi.org/10.1038/s41598-021-90520-z.

[25] J. Nilsson, F. Vilaplana, S. Karlsson, J. Bjurman, T. Iversen, The validation of artificial ageing methods for silk textiles using markers for chemical and physical properties of seventeenth-century silk, Studies in Conservation 55 (2010) 55–65. https://doi.org/10.1179/sic.2010.55.1.55.

[26] G. Pellis, B. Giussani, P. Letardi, T. Poli, P. Rizzi, B. Salvadori, A. Sansonetti, D. Scalarone, Improvement in the sustainability and stability of acrylic protective coatings for outdoor bronze artworks, Polym Degrad Stab 218 (2023). https://doi.org/10.1016/j.polymdegradstab.2023.110575.

[27] M.T. Molina, E. Cano, B. Ramírez-Barat, Testing protective coatings for metal conservation: the influence of the application method, Herit Sci 11 (2023). https://doi.org/10.1186/s40494-023-00937-0.

[28] M.T. Doménech-Carbó, M.F. Silva, E. Aura-Castro, L. Fuster-López, S. Kröner, M.L. Martínez-Bazán, X. Más-Barberá, M.F. Mecklenburg, L. Osete-Cortina, A. Doménech, J.V. Gimeno-Adelantado, D.J. Yusá-Marco, Study of behaviour on simulated daylight ageing of artists' acrylic and poly(vinyl acetate) paint films, in: Anal Bioanal Chem, 2011: pp. 2921–2937. https://doi.org/10.1007/s00216-010-4294-3.

[29] Y. Gong, G. Zhou, C. Qiao, Y. Pan, Study on the photodegradation behaviours of thermal-aged silk, Herit Sci 12 (2024). https://doi.org/10.1186/s40494-024-01270-w.

[30] A. Spencer, S. Patel, A. Burnstock, J. Lee, The Impact of Accelerated Light Ageing on MS3 for Use as a Picture Varnish, Studies in Conservation (2024). https://doi.org/10.1080/00393630.2024.2360828.

[31] A. Sionkowska, A. Planecka, The influence of UV radiation on silk fibroin, Polym Degrad Stab 96 (2011) 523–528. https://doi.org/10.1016/j.polymdegradstab.2011.01.001.

[32] H. Tan, R. Dang, Review of lighting deterioration, lighting quality, and lighting energy saving for paintings in museums, Build Environ 208 (2022). https://doi.org/10.1016/j.buildenv.2021.108608.

[33] R. Dang, F. Zhang, D. Yang, W. Guo, G. Liu, Spectral damage model for lighting paper and silk in museum, J Cult Herit 45 (2020) 249–253. https://doi.org/10.1016/j.culher.2020.03.001.

[34] B. Villmann, C. Weickhardt, Wavelength Dependence of Light Induced Changes in Reflectance Spectra of Selected Dyes and Pigments, Studies in Conservation 63 (2018) 104–112. https://doi.org/10.1080/00393630.2017.1345088.

[35] W.D. Appel, D.A. Jessup, ACCELERATED AGING TEST FOR WEIGHTED SILK, Part of Journal of Research of the National Bureau of Standards 15 (1935).

[36] H. Liu, S. Zhao, Q. Zhang, T. Yeerken, W. Yu, Secondary structure transformation and mechanical properties of silk fibers by ultraviolet irradiation and water, Textile Research Journal 89 (2019) 2802–2812. https://doi.org/10.1177/0040517518803788.

[37] J. Shao, J. Zheng, J. Liu, C.M. Carr, Fourier transform Raman and Fourier transform infrared spectroscopy studies of silk fibroin, J Appl Polym Sci 96 (2005) 1999–2004. https://doi.org/10.1002/app.21346.

[38] M.Y. Li, Y. Zhao, T. Tong, X.H. Hou, B.S. Fang, S.Q. Wu, X.Y. Shen, H. Tong, Study of the degradation mechanism of Chinese historic silk (Bombyx mori) for the purpose of conservation, Polym Degrad Stab 98 (2013) 727–735. https://doi.org/10.1016/j.polymdegradstab.2012.12.021.

[39] X. Luo, J. Wu, A. Intisar, J. Geng, L. Wu, K. Zheng, Y. Du, Study on Light Aging of Silk Fabric by Fourier Transform Infrared Spectroscopy and Principal Component Analysis, Anal Lett 45 (2012) 1286–1296. https://doi.org/10.1080/00032719.2012.673098.

[40] J. Wang, J. Guan, N. Hawkins, F. Vollrath, Analysing the structure and glass transition behaviour of silks for archaeology and conservation, J R Soc Interface 15 (2018). https://doi.org/10.1098/rsif.2017.0883.

[41] K. Kavkler, I. Pucić, P. Zalar, A. Demšar, B. Mihaljević, Is it safe to irradiate historic silk textile against fungi?, Radiation Physics and Chemistry 150 (2018) 101–110. https://doi.org/10.1016/j.radphyschem.2018.04.030.

[42] M.A. Becker, N. Tuross, Initial Degradative Changes Found in Bombyx mori Silk Fibroin , (1993) 252–269. https://doi.org/10.1021/bk-1994-0544.ch022.

[43] C. Solazzo, J.M. Dyer, S. Deb-Choudhury, S. Clerens, P. Wyeth, Proteomic profiling of the photo-oxidation of silk fibroin: Implications for historic tin-weighted silk, Photochem Photobiol 88 (2012) 1217–1226. https://doi.org/10.1111/j.1751-1097.2012.01167.x.

[44] P. Garside, S. Lahlil, P. Wyeth, Characterization of Historic Silk by Polarized Attenuated Total Reflectance Fourier Transform Infrared Spectroscopy for Informed Conservation, Appl Spectrosc 59 (2005).

[45] Z. Zhu, N. Tse, P. Nel, M. Tobin, Degradation profiles of silk textiles in diverse environments: Synchrotron based infrared micro-spectroscopy analysis, in: MRS Adv, Materials Research Society, 2017: pp. 3939–3949. https://doi.org/10.1557/adv.2017.596.

[46] J. Kim, X. Zhang, P. Wyeth, THE INHERENT ACIDIC CHARACTERISTICS OF AGED SILK, E-PRESERVATION Science 5 (2008) 41–46. www.e-PRESERVATIONScience.org.

[47] P. Garside, P. Wyeth, X. Zhang, The Inherent Acidic Characteristics of Silk, Part II – Weighted Silks, E-PRESERVATION Science 7 (2010) 126–131. https://www.researchgate.net/publication/49587328.

[48] F. Vilaplana, J. Nilsson, D.V.P. Sommer, S. Karlsson, Analytical markers for silk degradation: comparing historic silk and silk artificially aged in different environments, Anal Bioanal Chem 407 (2015) 1433–1449. https://doi.org/10.1007/s00216-014-8361-z.

[49] N. Luxford, D. Thickett, Designing accelerated ageing experiments to study silk deterioration in historic houses, in: Journal of the Institute of Conservation, Routledge, 2011: pp. 115–127. https://doi.org/10.1080/19455224.2011.581118.

[50] D. Badillo-Sanchez, D. Chelazzi, R. Giorgi, A. Cincinelli, P. Baglioni, Understanding the structural degradation of South American historical silk: A Focal Plane Array (FPA) FTIR and multivariate analysis, Sci Rep 9 (2019). https://doi.org/10.1038/s41598-019-53763-5.

[51] X. Zhang, P. Wyeth, Performance measurement of sericin-coated silks during aging, Sci China Chem 54 (2011) 1011–1016. https://doi.org/10.1007/s11426-011-4270-6.

[52] S. Lee, S.H. Kim, Y.Y. Jo, W.T. Ju, H.B. Kim, H. Kweon, Effects of ultraviolet light irradiation on silk fibroin films prepared under different conditions, Biomolecules 11 (2021) 1–11. https://doi.org/10.3390/biom11010070.

[53] R. Dang, Y. Kang, H. Tan, Y. Yang, Colour Damage of Visible Light on Plain-Woven Silk in Different Conservation States of Paintings and Calligraphy in Collections, Fibers and Polymers 25 (2024) 235–242. https://doi.org/10.1007/s12221-023-00414-2.

3.3 Rationale and aim of the work

This research originates from observations made by various authors studying samurai armours. Both conservators [1,2] and art historians [3] have noted that certain textiles used in armours seem more prone to degradation, especially when dyed with specific hues. Dark, saturated colours are reported to be the most susceptible to degradation, but even more expensive dyes, such as the flame red from *Carthamus tinctorius* and purple from *Lithospermum erythrorhizon*, appear to have had short lifespans despite their high cost. In contrast, indigo derived from *Persicaria tinctoria* is considered remarkably stable. In fact, a prominent 1800 Tokyo text on armor manufacturing recommends indigo as the best choice for dying armor textiles [4].

Indigo, or *kon*, has often been described as one of the most popular colours used to lace armor. Its dark hue was practical for concealing dirt and stains, and it was cheaper than other dyes. However, some experts [3] believe the widespread appearance of indigo-dyed lacing on surviving armors may reflect its superior resistance to light damage rather than its historical popularity. Contemporary illustrations, indeed, indicate that many warriors favoured armour with bold colours, such as red (*aka*). In this view, the scarcity of surviving armour originally laced with bold colours, as opposed to those with blue lacing, can be attributed to the superior resistance of indigo-dyed lacing to light damage. Therefore, indigo-dyed *odoshi* might not have been the most popular lacing colour historically, but rather the one that has best endured over time. Brightly coloured lacing, such as red, was often relaced every few years [2,5], possibly explaining why less armor with vibrant lacing remains intact today.

This issue of textile degradation in samurai armors highlights the broader phenomenon of "phototendering," where certain dyes accelerate fiber degradation when exposed to light. Conversely, some dyes act as UV-absorbers, protecting the fiber from light damage. While Allen [6,7] discussed this issue extensively, only a few natural dyes were included in his analysis. Most research on textile degradation has focused on the fading of dyes [6,8,9], as it is a visible sign of deterioration that impacts the aesthetic value of artifacts. However, understanding the early stages of fiber degradation, particularly in textiles that must bear weight (e.g., garments and tapestries), is crucial for effective preventive conservation. Knowing whether a dye can accelerate fibre degradation is essential in assessing the risk posed by certain textiles during display and ensuring their longevity.

Despite the importance of textile degradation, there is limited research on the influence of dyes and mordants on this process. Some studies examine the UV-protective properties of dyes from a technological perspective, without considering historical materials or recipes [10–15]. Conservation scientists have conducted a few studies on the degradation behaviour of wool and silk in relation to dyes and mordants, but the findings are often inconsistent and fragmented [16–22].

In recent years, research on silk degradation has been promoted. The EU-funded project MODHT (2002–2005) evaluated methods to monitor historic tapestries' damage, including studies on dyed silk [17,23]. Further work by Luxford (2009) [24] and Koperska (2015) [25] contributed to understanding silk degradation processes and their interaction with environmental factors. More recently, the EU-funded project SAFESILK aims to investigate metal salt-induced silk degradation and develop effective treatments for damaged silk artifacts [26].

Given that silk is highly sensitive to UV radiation, this research focuses on evaluating how different dye/mordant combinations influence the degradation rate of silk textiles, as suggested by experimental evidence [27,28]. Silk was chosen for its historical importance and sensitivity to light-induced damage. The dyes used in this study are traditional Asian plant-based dyes, and various mordants (alum, potassium tartrate, iron sulfate, tannic acid) were employed to explore their impact on silk degradation. The dyed silk samples underwent accelerated aging under both UVA and visible light to compare the effects of different light sources.

By examining the degradation mechanisms in dyed silk using UV-Vis reflectance spectroscopy, ATR-FTIR, X-ray diffraction, and thermal gravimetric analysis, this study aims to identify specific dye/mordant combinations that pose a significant risk to the conservation of silk textiles. The findings will provide valuable insights for evaluating the risks associated with displaying such artifacts and help in planning effective preventive conservation strategies.

In detail, the workflow is planned as follows:

- In the first part, undyed silk is considered. As literature review highlighted a wide variety of methods used for silk ageing and testing, a proper protocol of accelerated ageing and analysis is set up. Three different lamps emitting in the UVA region are considered to evaluate differences in the accelerated ageing behaviour of silk. A set of in-house analytical techniques are applied every 2 or 4 days to record the change of the chemical properties of silk throughout the ageing. Ageing indicators are obtained and elaborated to get the ageing trends which are compared with data from previous literature. The most efficient lamp and analytical protocol are finally chosen.
- In the second part, mordanted and dyed silk is considered. The mock-ups of silk are produced with a standardized method and aged under the chosen UVA lamp and a visible light lamp. The differences in ageing behaviour are evaluated to detect if particular combinations of dyes and mordants can induce an increase or a decrease of the ageing indicators.

The choice of conditions and methods is justified in section 3.4.

3.4 Experimental

3.4.1 Materials

Silk yarn

The silk textile was kindly donated by Ongetta S.r.l (Ponte di Piave (TV) Italy). It is a plain weave textile.

As far the degumming process, Marseille soap was purchased from Nesti Dante S.r.l. (San Donnino, Florence, Italy), while sodium bicarbonate was supplied by Carlo Erba Reagenti SpA (Rodano, Milan, Italy).

Mordants

Mordants such as potassium alum (K64170), potassium bitartrate (K64170), and tannic acid (K94500) were supplied by Kremer Pigmente Gmbh (Aichstetten, Germany), and iron sulfate ($FeSO_4$) by Sigma-Aldrich (St. Louis, Missouri, USA).

Dyes

The choice of dyes was made following a study of the literature to better understand which dyes were primarily used in the past, especially in Japan. Table 3 reports a comprehensive list of dyes used in the Asiatic area. The total number of identifications in previous works has been reported to evaluate the most representative dyes. The bibliographical references are presented in other works [29,30].
From the multitude of available dyes, a selection of nine dyes was made for this project. At least one dye from each chemical family was chosen. The chosen dyes are: *Ai, Shikon, Beni, Ukon, Kihada, Suo, Enju, Yamahaji, Akane*.

Dye class	Japanese name/Common name	Dyeing molecules	Hue and class	Natural source	Total number of references
Indigoid	Ai/ Indigo	Indigotine Indirubine	Blue, vat	Indigofera tinctoria L., Polygonum tinct.	81
Alcaloid	Kihada / Amur cork tree	Berberine	Yellow, mordant	Bark of *Phellodendron amurense*	21
	Woren/goldthread	Coptisin	Yellow, mordant	Roots of *Coptis Japonica*	3
Anthraquinone	Akane/Madder	Alizarine Purpurine	Red, mordant	Roots of *Rubia tinctororum* (Western) *l./Rubia Akane Nakai* (Japanese)	37
	Beni/Safflower	Carthamin	Red, vat	Petals of *Carthamus tinctorius*	30
	Shikon-murasaki/Purple gromwell	Shikonin	Purple, mordant	Roots of *Lithospermum erythrorhizon*	20
	Shiko/lac dye	Laccaic acid	Red, mordant	*Coccus lacca Kerr. Kerria lacca* (powdered insect)	12
	our lady's bedstraw	Alizarine Purpurine Xantopurpurine Pseudopurpurine	Red, mordant	Roots of *Galium verum L.*	3
	Enji/Cochineal – Kermes	Carminic acid	Red, mordant	*Dactylopius coccus cacti* (powdered insect)	3
Flavonoid (condensed tannins)	Suo/Sappanwood – brazilwood	Brasilin Brasilein Ematossilin	Red, purple, mordant	Wood of *Caesalpinia Sappan/ Brasiliensis*	20
	Enju/ Pagoda tree	Rutin	Yellow, mordant	Fruits of *Sophora Japonica* L.	19
	Buckthorn	Chrysophanic acid Emodine Franguline A,B Ramnetine	Yellow, mordant	Fruits and bark of *Rhamnus frangula* L.	14
	Venice Sumac/ Young Fustic	Fisetine Sulfuretine Gallic acid Ellagic acid	Yellow, mordant	Leaves, roots, wood of *Cotinus coggyria* S.	7

	Kariyasu/ Silver grass	Artraxine	Yellow, mordant	Miscantus tinctorius, M. sinensis	7
	Sandalwood	Xantalin A Xantalin B	Red, mordant	Wood of *Pterocarpus santalinus* L.	4
	Dragon's blood	Dracorodine Dracorubine	Red, mordant/vat	*Daemonoropos Draco*	4
	Yenji /Four o'clock flower	Betalaine	Red, mordant	Petals of *Mirabilis jalapa L.*	3
	Aigami/Dayflower	Commelinin	Blue, unstable	Petals of *Commelina communis* L.	1
Carotenoid	Kuchinashi /Gardenia	Crocine	Yellow, mordant	Fruits of *Gardenia Jasminoides*	16
	Ukon/Indian saffron, Turmeric	Curcumin	Yellow, vat (cotton), mordant (silk)	Roots of *Curcuma longa* L., *Curcuma aromatica*	14
	Saffron	Crocetin Crocin	Yellow, mordant	Flowers of *Crocus sativus L.*	6
Tannin (hydrolysable)	Shio/Gamboge	Gambogic acid	Yellow, mordant	Resin of *Garcinia Morella*	14
	Megi/ Japanese Barberry		Yellow	*Berberis thungbergii*	5
	Yamahaji/ Japanese Sumac	Fustin Ellagic acid Gallic acid	Yellow, mordant	Wood of *Toxicodendron vernicifluum, Rhus cotinus*	4
	Walnut	Juglone	Brown	Fruit of *Junglas regia* L.	5
	Oak	Gallic acid	Brown	Wood of *Quercus acutissima* C.	4
	Rhubarb		Red	Leaves of *Rheum officinale*	6
	Yamamomo/ Chinese Bayberry	Miricitrin	Yellow	Fruits of *Myrica rubra*	3

Table 3. Natural dyes commonly used in the Asiatic area

Most of the dyes were purchased as dried raw materials from Pigment Tokyo (Tokyo, Japan):

- Roots of *Lithospermum Erythrorhizon*;
- Bark of *Phellodendron Amurense*;
- Dried wood of *Caesalpinia Sappan*;

- Dried flowers of *Sophora Japonica*;
- Dried wood of *Toxicodendron Vernicifluum*;
- Dried roots of *Rubia Akane*.

The powdered root of *Curcuma Longa* (K37220) was purchased from Kremer Pigmente Gmbh (Aichstetten, Germany). Dried flowers of *Chartamus Tinctorius* were supplied by Laboratorio d'erbe Sauro (Bosco Chiesanuova, Verona, Italy).

The dye molecule indigotine was synthesized in the lab by reacting 1 g of 2-nitrobenzaldehyde in 15 mL of acetone with 30 mL of H2O. A 5 mL aqueous solution of sodium hydroxide (2 M) was slowly added. After maintaining the solution at 50°C for 30 minutes, it was filtered and washed with 10 mL of H2O and 10 mL of EtOH, and finally dried under vacuum for 30 minutes. All reagents were purchased from Sigma-Aldrich (St. Louis, Missouri, USA) except for EtOH, which was purchased from Merck KGaA (Darmstadt, Germany).

Potassium hydroxide was obtained from Carlo Erba Reagenti SpA (Rodano, Milan, Italy). Acetic acid (6%) was purchased from Acetum S.p.A. (Cavezzo, Modena, Italy). Citric acid and sodium dithionite were purchased from Sigma-Aldrich (St. Louis, Missouri, USA).

Lamps

To carry out the accelerated aging process, several lamps with specific characteristics were used. Their emission spectra are shown in Figure 7. Below are the specifications and manufacturers for each lamp:

- UVA @380 nm: TL15W – MOEL (Montecchio Emilia (RE), Italy), providing light > 350 nm;
- UVA @355 nm: G5 15W CLEO COMPACT - JW Sales GmbH - Brand Division iSOLde (Stuttgart, Germany), simulating indoor exposure;
- UVA @335 nm: UVB T8 10% Desert – 15W – Arcadia Reptile (London, United Kingdom), simulating outdoor exposure;
- Visible Light: L18W/840 Luminux cool light – OSRAM (Augsburg, Germany), shielded with a polycarbonate UV-filter, providing light > 400 nm.

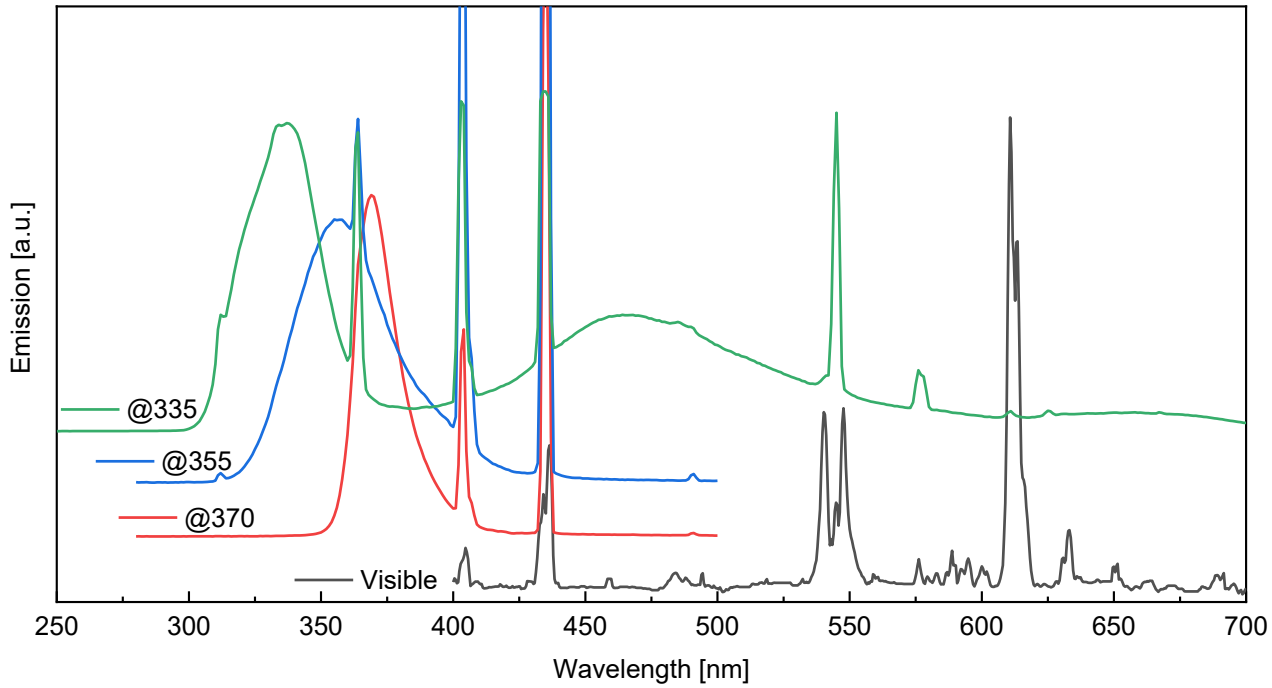

Figure 7. Emission spectra of the selected lamps. Visible (L18W/840 - OSRAM); @370 (TL15W - MOEL); @355 (G5 15W CLEO COMPACT); @335 (UVB T8 10% Arcadia Desert - 15W).

The preliminary investigation about the best lamp for silk ageing is related to the idea of activation spectrum proposed by Andrady and Searle [31]. The hypothesis is that silk is more responsive to degradation when a specific wavelengths interval is used as source of excitation. The activation spectrum for silk is not available in literature, so three lamps close in wavelengths and showing similar irradiance values were tested to assess whether a significant variation is present. The test was designed to select a proper light source, characterized by efficiency and consistency with realistic ageing conditions. As shown by the extensive literature search about ageing protocols for silk, the choice of the lamp is crucial to conduct efficient, reproducible and realistic accelerated ageing, although such principles were not always taken into account in previous research.

In the present work, three different UVA light sources were considered, together with a source of visible light. While 335nm light is generally used to simulate outdoor ageing, 355nm light source is considered as the best for reproducing indoor ageing conditions [32]. Lower wavelengths were not taken into account due to the very harsh conditions, which are not possible during the lifetime of silk objects. Conversely, 370nm light source, which is not generally used for accelerated ageing, was also considered to assess whether the wavelength interval delivered by this lamp could be harmful for the silk, known as a particularly fragile material [31,33]. Visible light is not able to damage silk fibre, but it was tested too to verify whether any change takes place and if some dangerous interactions with silk are made possible by the presence of dyes or mordants.

3.4.2 Experimental design

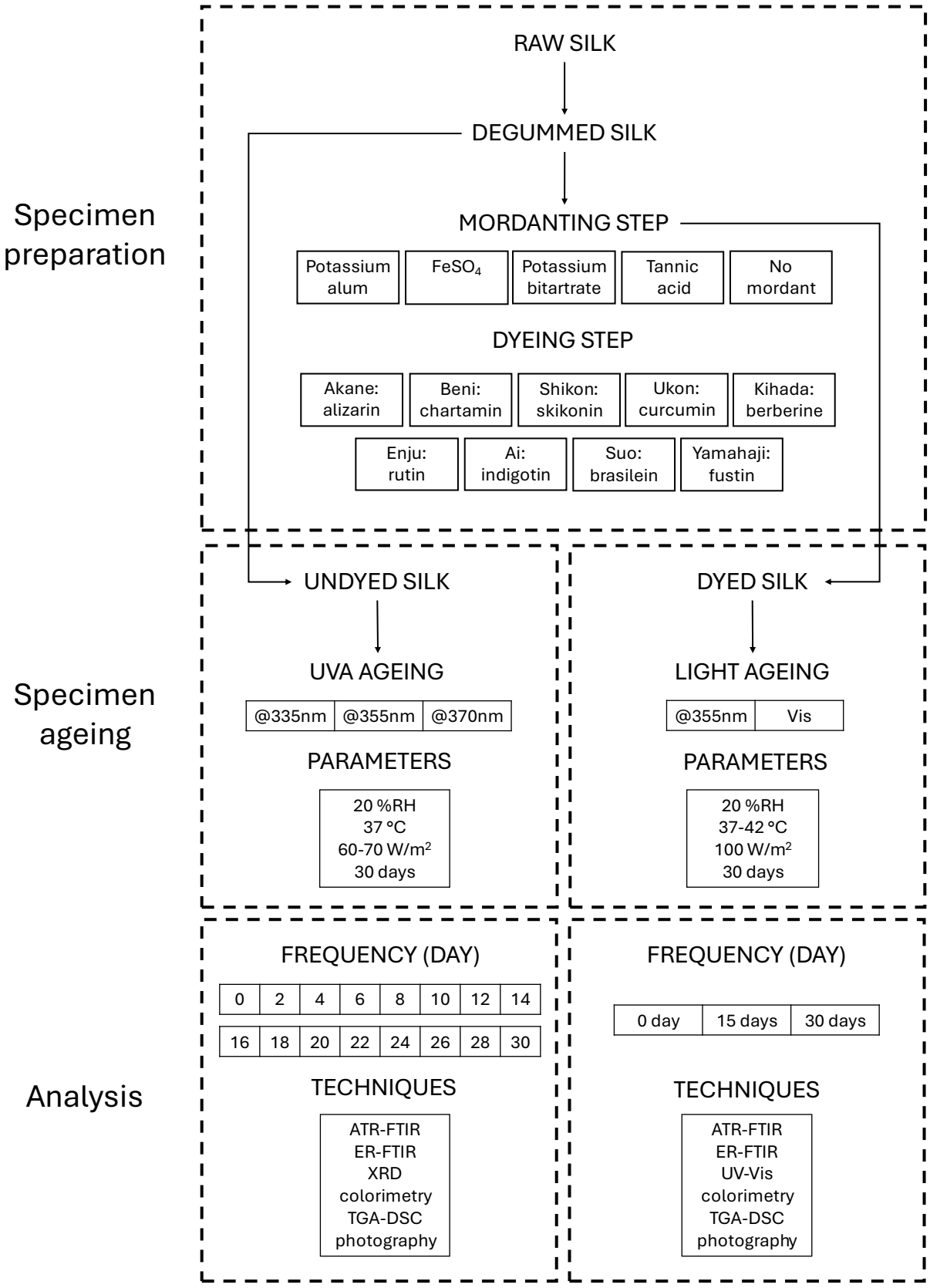

Figure 8. Experimental design flow chart.

Figure 8 graphically summarizes the experimental design of the research work.

The first step was the preparation of samples. All the samples were degummed, while only a part of the silk underwent the mordanting and dyeing steps.

The second step was the accelerated ageing of specimens. Different conditions were chosen according to each part of the work. The first part was aimed at identifying the most efficient ageing conditions and set of analytical methods. As a consequence, three UVA lamps emitting within different wavelengths intervals were tested. The number of days of ageing was established based on the visual decay of samples. The second part involved the mordanted and dyed samples, aiming at assessing whether the presence of dyes and mordants slowed down or accelerated the ageing. The most efficient lamp chosen from the previous experiment was used to perform the ageing, as well as a UV-free visible light was used too as a reference. Visible light causes lightfastness of dyes, whose extent can be compared with the damage caused by UVA light.

The third step involved analyzing the aged samples. The selection of analytical techniques was guided by an extensive literature review and the principles of novelty, micro-invasiveness, and in-house availability. A multi-analytical approach was adopted to monitor a broad range of parameters, as relying on a single chemical property could lead to misleading conclusions due to the simultaneous occurrence of opposing reactions [32]. ATR-FTIR spectroscopy was chosen as the primary technique due to its proven viability, speed, and minimal invasiveness for textile analysis. In particular, the indicators proposed in a previous study showed a promising correlation with the state of preservation of historical silk [28]. Colorimetry and UV-Vis spectroscopy were employed to document color variations, a parameter frequently considered in heritage science studies. X-ray diffraction (XRD) was used to assess silk crystallinity, a common metric in similar research. Additionally, thermal analysis was explored as a novel technique for silk degradation studies, as preliminary findings suggested a correlation between experimental data and silk ageing, warranting further investigation. In the first part of the study, a broader range of analytical techniques was applied to monitor the aging behavior of silk. ATR-FTIR spectroscopy, XRD, colorimetry, and TGA-DSC were conducted at regular intervals to establish degradation trends over time. For the second part, focusing on mordanted and dyed samples, analyses were performed at 0, 15, and 30 days. UV-Vis spectroscopy was also conducted to assess changes in the light absorption properties of the samples. Aging indicators obtained from dyed and mordanted silk were compared with those of undyed and unmordanted samples to identify differences in their degradation behavior.

3.4.3 Preparation of Samples

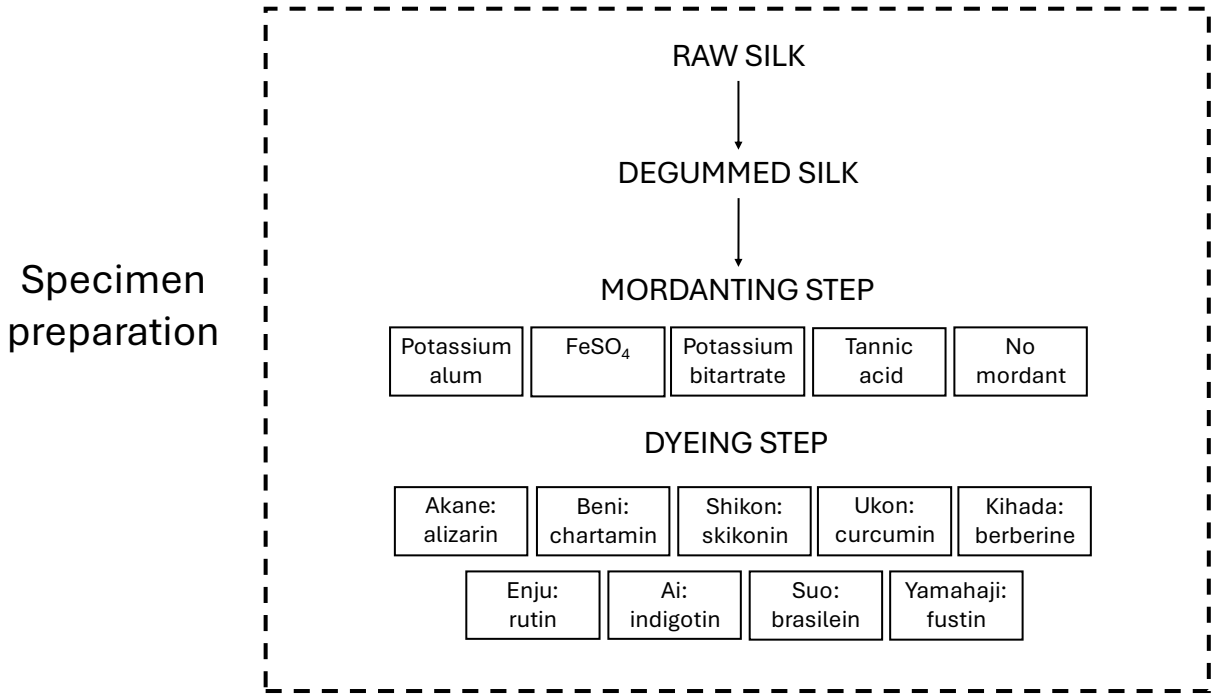

Degumming Process

The degumming process is fundamental for silk, as it removes sericin, the gum that coats the silk thread, making the silk smooth and shiny. After this process, the silk is referred to as degummed silk.

Traditional degumming methods involve a thermochemical treatment of silk with hot water and alkaline salts or soap, or both [34,35]. In the present work, it was decided to follow traditional recipes as closely as possible to replicate ancient procedures. Among the various recipes found in the literature, some use sodium bicarbonate, while others propose sodium carbonate. However, there is consensus on the use of Marseille soap. The experimental parameters of each work are reviewed in Table 4.

Reactants	Experimental parameters	Liquor Ratio	References
5g/L Marseille soap 5g/L sodium bicarbonate 5g/L Irgasol Na	95 °C 30-60 min pH 8-9	1:30	[36]
4g/L soap 1 g/L sodium carbonate	85-100 °C 1-2 h pH 8.5-10	1:30	[37]
12g/L Marseille soap	85-90°C 45 min pH 10-11	1:60	[38]
10 g/L Marseille soap 1 g/L sodium carbonate	98°C 1 h	1:200	[39]
1g/L sodium carbonate	90°C 30-60 min	1:40	[40]

0.5g/L sodium carbonate	95 °C 30 min	1:100	[41]
15% Marseille soap 1.5% sodium carbonate 0.05% non-ionic surfactant Noigen HC	98°C 30 min	1:30	[42]

Table 4. Review of the procedures for silk degumming. Liquor ratio is defined as the ratio between the mass of silk and the volume of dyebath

In the present work, the degumming process was carried out using Marseille soap and sodium bicarbonate ($NaHCO_3$), both at 5g/L with a liquor ratio (ratio between the mass (kg) of silk used and the volume (L) of aqueous solution) of 1:30. After combining water, soap, bicarbonate, and silk in a beaker, the mixture was placed on a heating plate and brought to 95°C for 55 minutes. The silk was then rinsed thoroughly with distilled water and placed in an oven at 30°C overnight. For convenience, the silk was cut into 10x10 cm pieces.
To verify the efficiency of the process, i.e., the loss of sericin after degumming, the weight loss of the degummed silk was calculated using the following formula:

$$\Delta m\% = \frac{w_b - w_a}{w_b} \times 100$$

where w_b is the weight of the undegummed silk and w_a is the weight of the degummed silk [40] [42]. The result was a 24.6% weight loss, which is consistent with literature data. Figure 9 shows raw silk and silk obtained after the degumming process.

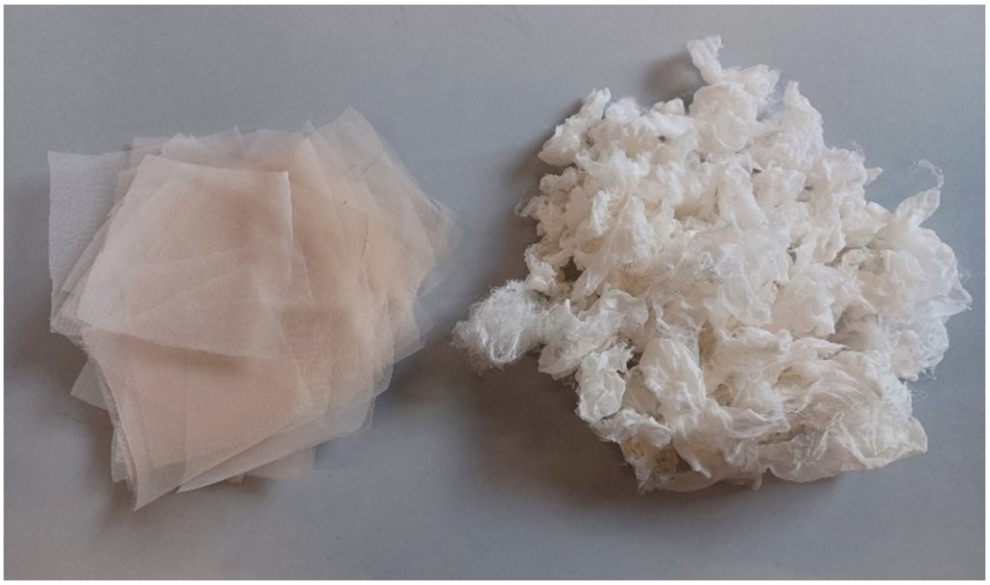

Figure 9. Undegummed (left) and degummed silk (right) used in the experiment

Mordanting Process

Mordants are substances that bond with textile fibers and dyes, where there would otherwise be little affinity between them [34].
The mordants most commonly used in the West include potassium alum, chromium-based

compounds, tin-based compounds, copper sulfate, iron sulfate, tartaric acid, and tannic acid [34]. In the Asiatic area, potassium alum, tannic acid, and green vitriol, i.e. iron sulfate ($FeSO_4$), have been predominantly used [8,43–45].

Therefore, the silk was mordanted using four of the most commonly cited and least toxic mordants: potassium alum, $FeSO_4$, potassium tartrate, and tannic acid. Mordants concentration and mordanting recipes were selected in accordance to specific literature [46] [47].
The selected concentrations were the following: 20% w/w for potassium alum, 20% w/w for tannic acid, 1% w/w for iron sulfate, and 5% w/w for potassium tartrate The mordanting recipe was the same for all four mordants: after weighing the appropriate amount of mordant, it was dissolved in distilled water, and then silk was added with a liquor ratio of 1:30. All solutions were brought to 85/90°C for about 55 minutes using a heating plate. The final concentration of salt adhering to the fibre - the mordant load - was not directly measured but was assumed to be constant, given the strict replication of the recipe.

Dyeing Process

It was necessary to extract the dye from the raw materials, and the procedures are reported in Table 5.

After the extractions, the silk dyeing was carried out. Each combination of dye and mordant was tested. For indigo and safflower, being direct dyes, the silk was dyed with and without mordants.
Three replicates were dyed for each dye/mordant combination. The dyeing procedures used are reported in Table 6.

Dye	Extraction Procedure	References
Shikon	Place 2 g of root fragments in a solution of 1.5% acetic acid and 50% ethanol. Place the solution in an ultrasonic bath for 1 hour at 25-30°C. Repeat the procedure 3-4 times until color extraction is observed. Mix the different extractions in a flask.	[48]; [49]; [50]; [51]
Beni	Weigh 2 g of petals and prepare 24 ml of aqueous solution. Leave the petals in the solution for 1 day to remove all the yellow color. Then, treat the remaining petals with 0.11 g of KOH and let it act for 1 hour. Adjust the pH to 6 with a citric acid solution (1 g/10 ml). Finally, filter the liquid, discarding the petals.	[52]; [46]; [53]
Ukon	Prepare a solution of 100 ml distilled water with 8 g of powdered root and place it in an ultrasonic bath for 1 hour at 80-90°C.	[52]; [48]; [46]; [54]
Kihada	Weigh 2 g of bark and extract it in 50 ml of distilled water for 15-30 minutes at 80°C. Repeat the procedure at least 3-4 times and combine the extractions.	[51]; [52]; [55]; [49]

Dye	Extraction Procedure	References
Suo	Place 2 g of wood in 50 ml of distilled water and heat it in an ultrasonic bath at 80°C for 30-60 minutes. Repeat the procedure at least 3-4 times and combine the extractions.	[52]; [48]
Enju	Prepare a solution with 2 g of flowers, 50 ml of distilled water, and 50 ml of ethanol. Place the mixture in an ultrasonic bath at 70°C for 30 minutes. Repeat the extraction at least 3-4 times and combine the extractions.	[56]
Yamahaji	Weigh 2 g of bark and place it in 100 ml of distilled water. Place the solution in an ultrasonic bath at 70°C for 30 minutes. Repeat the extraction at least 3-4 times and combine the extractions.	[46]
Akane	Weigh 2 g of roots in 100 ml of distilled water and place it in an ultrasonic bath at 70-80°C for 30 minutes. Repeat the extraction at least 3-4 times and combine the extractions.	[51]; [52]; [46]; [57]; [58]; [59]

Table 5. Extraction methods of the selected dyes for dyeing tests.

Dye	Dyeing Procedure	Mordants Used	Reference
Ai	Place 40 ml of distilled water in a beaker and dissolve a tablet (~0.11 g) of NaOH. Add 0.1 g of indigo powder and 0.5 g of sodium dithionite. Heat the solution to 55-60°C. Turn off the heating plate and immerse the silk for 15-20 minutes. Rinse the silk.	None, potassium alum, FeSO4, potassium bitartrate, tannic acid	[51]; [52]; [57]
Shikon	Immerse the silk in the dye bath for 30 minutes at 60°C.	Potassium alum, FeSO4, potassium bitartrate, tannic acid	[51]; [48]; [50]
Beni	Immerse the silk in the dye bath for 30 minutes at 40-50°C.	None, potassium alum, FeSO4, potassium bitartrate, tannic acid	[52]; [53]; [50]
Ukon	Immerse the silk in the dye bath for 60 minutes at 40°C.	Potassium alum, FeSO4, potassium bitartrate, tannic acid	[52]; [48]
Kihada	Immerse the silk in the dye bath for 15-20 minutes at 80°C.	Potassium alum, FeSO4, potassium bitartrate, tannic acid	[51]
Suo	Immerse the silk in the dye bath for 30 minutes at 40°C.	Potassium alum, FeSO4, potassium bitartrate, tannic acid	[52]; [48]
Enju	Immerse the silk in the dye bath for 15-20 minutes at 60-70°C.	Potassium alum, FeSO4, potassium bitartrate, tannic acid	[50]
Yamahaji	Immerse the silk in the dye bath for 30 minutes at 80°C.	Potassium alum, FeSO4, potassium bitartrate, tannic acid	[46]
Akane	Immerse the silk in the dye bath for 30 minutes at 80°C.	Potassium alum, FeSO4, potassium bitartrate, tannic acid	[58]; [51]; [52]; [59]

Table 6. Dyeing procedures for the selected dyes.

3.4.4 Accelerated Ageing Set-Up and Testing

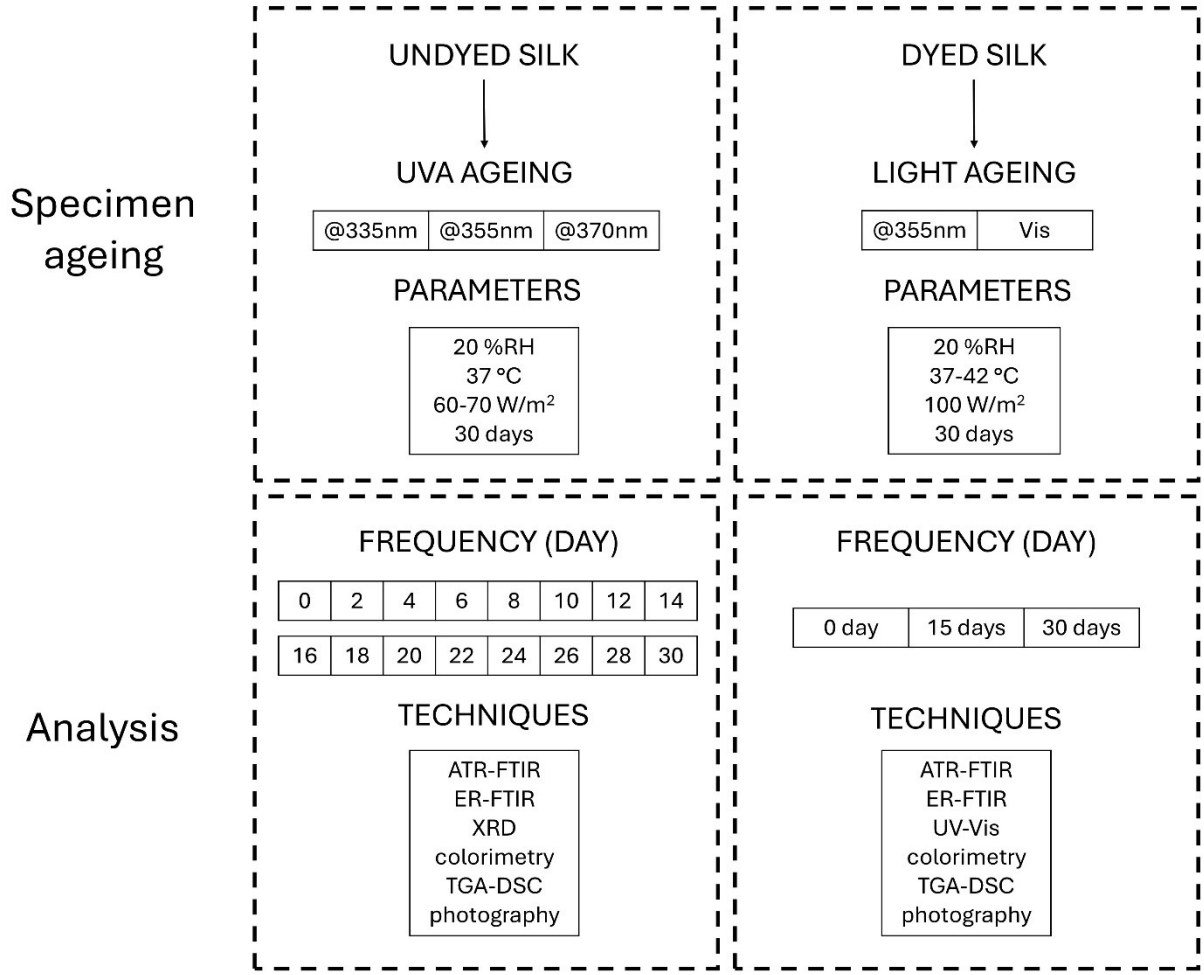

Experimental set-up for Undyed silk samples (SET A and SET B)

The ageing protocol was carried out using three UVA lamps with maximum emission peaks at different wavelengths (Figure 7):

- 1 x UVA @370 nm (TL15W - MOEL)
- 1 x UVA @355 nm (G5 15W CLEO COMPACT)
- 1 x UVA @335 nm (UVB T8 10% Arcadia Desert - 15W)

The lamps were placed in a dark chamber custom-built to prevent any interference from natural light. An air recirculation system was not implemented because the heat produced by the lamps was modest (37-38 °C). The use of a closed system allowed for constant temperature and humidity values by inserting a container of saturated aqueous NaCl solution (20% RH) inside the chamber. A thermocouple was used to monitor the surface temperature of the samples throughout the aging process, recording a constant value of 37-38 °C. The samples were aged for 30 days. The experimental conditions are summarized in Table 7.

	UVA @370nm	UVA @355nm	UVA @335nm
Temperature (°C)	37-38	37-38	37-38
Humidity (% RH)	20	20	20
Irradiance (W/m^2)	60-70	60-70	60-70

Table 7. Experimental conditions for aging undyed silk.

Before proceeding with the accelerated aging protocol, preliminary studies were conducted to assess the irradiance uniformity across sample surface. Irradiance values for each lamp were measured in different positions by means of a thermal sensor (OptoSigma®). A schematic representation of the collected values is depicted in **Figure 10**.

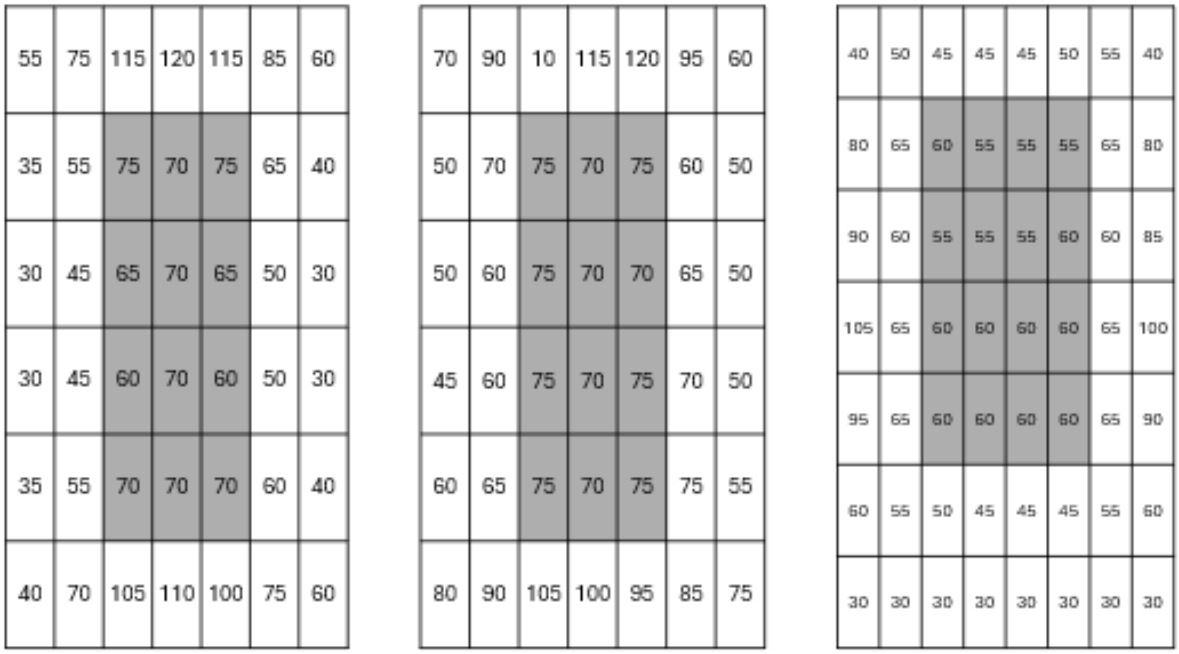

Figure 10. Measured irradiance values of the UVA lamps. From left to right: @370 nm (TL15W - MOEL); @355 nm (G5 15W CLEO COMPACT); @335 nm (UVB T8 10% Arcadia Desert - 15W).

The silk samples were positioned in the central area of the three lamps (highlighted in Figure 10) where the measured irradiance values were approximately constant. The distance of each sample from the lamp was adjusted to obtain an irradiance value between 60 and 75 W/m^2.

The samples for accelerated aging required a support to ensure the complete extension of the fabric during irradiation. The silk samples were therefore secured with metal pins to a previously prepared support, which consisted of a layer of drawing cardboard and a layer of aluminum foil to avoid any influence during aging and analysis from the paper support. The samples were prepared with both a single layer of silk and by overlapping two layers, as the weave of the fabric chosen for the experiment was very thin, and it was necessary to test whether this would pose a problem for reflectance measurements.

Four samples were aged under each lamp (SET A): two with a single layer of silk and two with a double layer. The dimensions of the samples were 2x8 cm. Identifying codes were used based on the ageing conditions. C, R or M are the first letter, identifying the lamp (@355nm, @335nm, @370nm respectively). 1 or 2 stands for the layers of silk fabric. A or B are the two replicates of each sample. The final number, preceded by *d*, indicates the number of days of ageing. For instance, C1A_d2 stands for the replicate A composed of 1 layer of silk aged for 2 days under UVA@355nm.
The samples were analysed every 2 or 4 days depending on the invasiveness of the technique. FTIR spectroscopy, XRD and colorimetry allowed to perform non-invasive analyses every 2 days, while every 4 days the specimens were sampled to perform TGA-DSC.

In order to obtain more precise data, the experiment was replicated using three more samples of silk (SET B). Each sample was aged under a different lamp for 15 and 30 days. The dimensions of the samples were 6x6 cm, as shown in Figure 11. Identifying codes were used as follows: C, R or M are the first letter, identifying the lamp (@355nm, @335nm, @370nm respectively). A couple of letters identify the sampling position (AA, AB, AC, …). The final number, preceded by *d*, indicates the number of days of ageing. For instance, C_AA_d2 stands for the sampling point AA aged for 2 days under UVA@355nm.
The samples were analysed by FTIR spectroscopy.

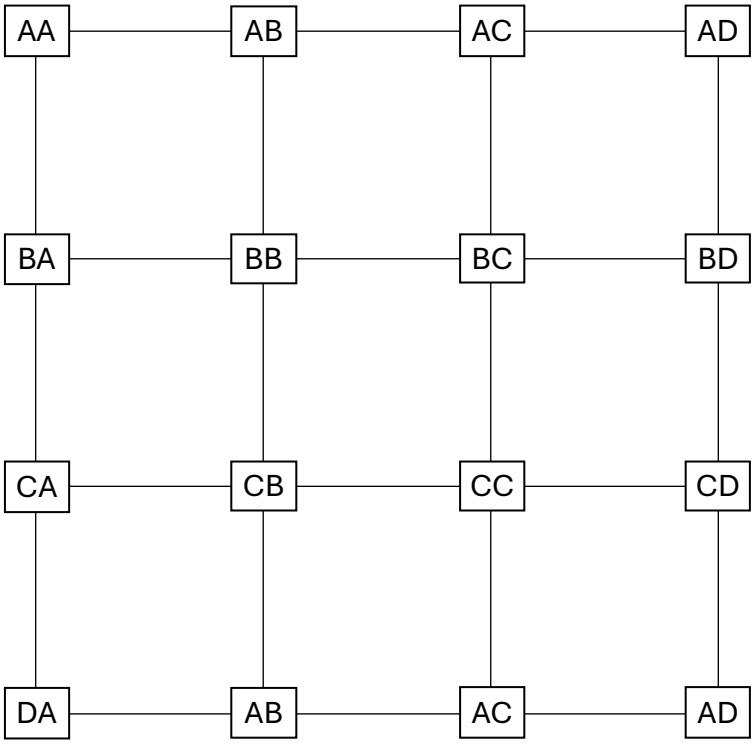

Figure 11. Model of undyed sample C_XX aged under UVA@355nm

Experimental set-up for Dyed silk samples (SET C and SET D)

The aging protocol was carried out using two sets of lamps, whose emission spectra are shown in Figure 7:

- 6 x VIS (OSRAM 18 W)
- 6 x UVA@355 nm (CLEO 20 W)

The lamps were placed in a chamber custom-built to avoid any interference from natural light. An air recirculation system was not implemented because the heat produced by the lamps was modest (37-42 °C). The use of a closed system allowed for constant temperature and humidity values by inserting a container of saturated aqueous NaCl solution (20% RH) inside the chamber. The irradiance value was measured within the irradiated area to confirm its uniformity by means of a thermal sensor (OptoSigma®). The samples were aged for 30 days. The experimental conditions are summarised in Table 8.

	VIS	UVA@355nm
Temperature (°C)	37-38	40-42
Humidity (% RH)	20	20
Irradiance (W/m^2)	100	100

Table 8. Experimental conditions for ageing dyed silk.

The samples were prepared according to the previously described method and secured with metal pins to a cardboard-aluminum foil support. The dimensions of the samples at the beginning of ageing were 5 cm x 10 cm. At the halfway point of ageing (15 days), the samples were cut in half, allowing only half of the sample (5 cm x 5 cm) to continue ageing (Figure 12). In this case, only two layers of silk were used. One sample for each mordant-dye combination were aged under each lamp (SET C). Due to the limited dimensions of the ageing chamber, the samples were divided into two groups. Reference samples of undyed and only mordanted silk were added to each group of samples during the ageing.
Identifying codes were used based on the dyeing features. The first two letters identify the dye. The third letter identify the mordant (A=alum, T=tannic acid, C=potassium tartrate, F=$FeSO_4$). This is followed by the number of the dyebath. The lower number (1 or 4) was aged by UVA@355nm. The higher number (3 or 5) was aged by visible light. The final number, preceded by *d*, indicates the number of days of ageing. For instance, AKA1_d2 stands for alum-mordanted akane-dyed sample aged for 2 days under UVA@355nm.

The samples were analysed at time zero and after 15 and 30 days of ageing. FTIR spectroscopy, UV-Vis spectroscopy and colorimetry allowed to perform non-invasive analyses, while the specimens were sampled to perform TGA-DSC. Figure 12 depicts a model of the samples AKA1 and AKA3, aged respectively under UVA@355nm and visible light. The numbers represent the sampling points for FTIR analysis, while the circle represents the area of the sample where UV-Vis analysis was performed.

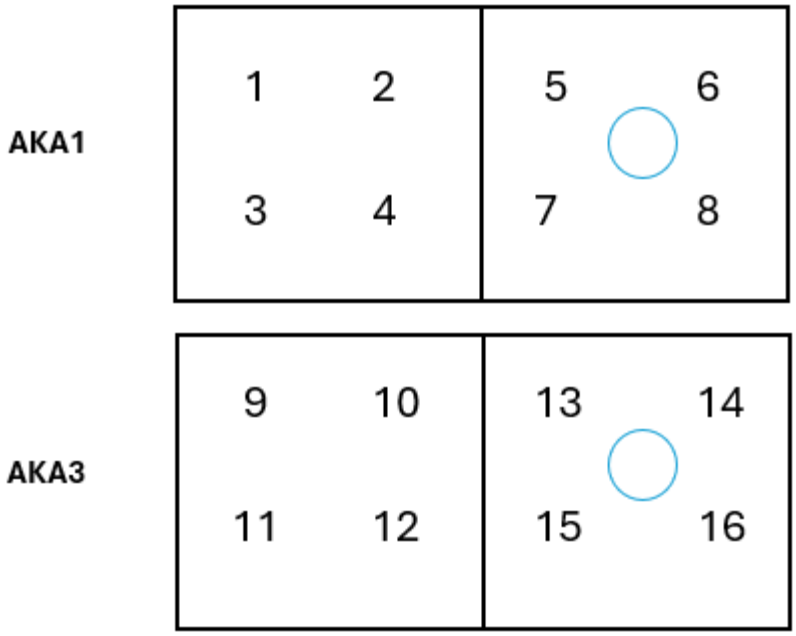

Figure 12. Model of dyed silk samples. The half with the hole (for UV-vis analysis) is the one that underwent ageing for up to 30 days.

In order to obtain more accurate results, the experiment was partially replicated using undyed and only mordanted samples of silk (SET D). Each sample was aged under 6xUVA@355nm lamp. Undyed silk samples were sampled every 4 days for 36 days, while mordanted silk was analysed after 15 and 30 days. The dimensions of the samples were 3x3 cm. Identifying codes were used as follows: SS are the first letters, identifying the undyed silk. The final number, preceded by *d*, indicates the number of days of ageing. For instance, SS_d4 stands for undyed silk aged for 4 days under 6xUVA@355nm. For the mordanted silk, the first letter and number identify the mordant and the relative concentration (A=alum, T=tannic acid, C=potassium tartrate, F=$FeSO_4$). The final number, preceded by *d*, indicates the number of days of ageing. For instance, F1_d4 stands for silk mordanted with 1% $FeSO_4$ and aged for 4 days under 6xUVA@355nm.
The samples were analysed by TGA-DSC.

3.4.5 Experimental Parameters

Visible Photography

Photographs of the dyed samples were taken with an Olympus E-PL10 camera with a M.ZUIKO DIGITAL 14-42 mm 1:3.5-5.6 II R lens, and with the help of an iFergo lightbox to eliminate the effects of reflected light and shadows. Images were white-balanced using the software GIMP (v. 2.10.38).

Colorimetry

Colorimetric measurements were performed using a Lovibond® SP60 portable spectrophotometer equipped with an integrating sphere. The illuminator used simulates daylight (D65), using a standard CIE 1964 10° observer. The instrument calibration was performed using a white reference (white ceramic disk) and a black reference (trap). The CIE L*a*b* colour coordinates of the undyed and dyed silk samples were measured before and during aging, and the colour differences during accelerated aging were calculated using the following formula (CIE76) [60]:

$$\Delta E = \sqrt{(\Delta L^*)^2 + (\Delta a^*)^2 + (\Delta b^*)^2} = \sqrt{(L^* - L^*_0)^2 + (a^* - a^*_0)^2 + (b^* - b^*_0)^2}$$

Alternatively, only the yellowing index was calculated as:

$$\Delta b = \sqrt{(\Delta b^*)^2} = \sqrt{(b^* - b^*_0)^2}$$

Data processing was performed using Microsoft Excel.

The formula used in this study is not the most recent, as it was revised to account for the non-uniformity of the color space and was subsequently replaced by the CIEDE2000 formula [61]. However, the updated standard was not applied due to the limitations of the instrumentation, which does not support a viable implementation of the revised formula. While the obtained data are subject to systematic error, this error remains minimal when neutral colors are considered [61]. Moreover, this study does not rely on colorimetric results as a primary focus; rather, they serve as complementary qualitative information. It is also worth noting that many recent publications continue to use the CIE76 formula due to its ease of application and, more importantly, its compatibility with historical datasets [62,63].

Fourier Transform Infrared Spectroscopy (FTIR)

The silk samples were analyzed as-is using the ATR-FTIR technique with a Thermo Scientific Nicolet iS10 instrument, and data were acquired with Omnic Spectra Software (Thermo Scientific) in the range of 4000-600 cm^{-1}, with a resolution of 4 cm^{-1} and 32 scans. A periodic background analysis was performed to automatically correct the spectra. To visualize and

modify the spectra and extract intensity values, the software Spectragryph for optical spectroscopy, version 1.2.16.1, was used. Data processing was performed using Microsoft Excel.

Intensity ratios were calculated for each spectrum from raw data, transformed into a data matrix. Three different ratios were considered:

- $I_{1625\ cm^{-1}}/I_{1617\ cm^{-1}}$ is defined as shift ratio [28]
- $I_{1503\ cm^{-1}}/I_{1515\ cm^{-1}}$ is defined as conversion ratio [28]
- $I_{1725\ cm^{-1}}/I_{1900\ cm^{-1}}$ is defined as oxidation ratio [64]

For the undyed silk samples (SET A), two spectra were recorded for each specimen at each analysis time. Considering the 4 samples aged under the same ageing conditions 4 replicates of each analysis time, cumulative variance was calculated with following formula:

$$S^2 = \frac{(n_1 - 1)s_1^2 + \cdots + (n_4 - 1)s_4^2}{n_1 + \cdots + n_4 - 4}$$

Intensity ratios for each set of 8 spectra were averaged, while the standard error was calculated with the following formula:

$$se\ (95\%) = 3.74\sqrt{\frac{S^2}{n_1} + \cdots + \frac{S^2}{n_4}}$$

For the undyed silk samples (SET B), 32 spectra were recorded for each specimen at each analysis time. This allowed to use the standard deviation formula and the standard error equal to $2\sigma/\sqrt{N}$.

For spectra visualization, only the spectral range of 1400-1800 cm^{-1} was considered, and peak normalization was performed to highlight the shift of Amide I during aging.

Polarization artifacts were taken into account due to the anisotropic nature of silk textiles [65,66]. These artifacts appeared randomly in the spectra, manifesting as variations in the relative intensities of the amide absorption bands. However, they were not considered significant, as the calculated ratios depended solely on the intensity values of a single amide band.

Ultraviolet-Visible Spectroscopy (UV-Vis)

The silk samples were analyzed as-is using UV-Vis spectroscopy with a Shimadzu UV-2600 (IVDD) instrument. The spectra were recorded in the 250-900 nm range in transmission, using the external detector (2Detector) at medium scan speed, and the background was periodically measured. The spectra were acquired using the UVProbe 2.70 software. The samples were analyzed as-is. Data processing was performed using Spectragryph for optical spectroscopy, version 1.2.16.1. The spectral range of 250-800 nm was considered, and intensity values were

normalized, setting absorbance to 0.3 at the value corresponding to 800 nm. Smoothing was applied using the Savitzky-Golay filter, with a range of 10 and polynomial order of 3. The analysis was conducted only on the dyed silk samples, and one spectrum was recorded for each sample at all analysis times.

Thermal Analysis

Thermal analysis (TGA/DSC) was performed using a NETZSCH STA 409 PC instrument. Between 5 and 8 mg of silk were weighed for each sample analyzed, reduced to fragments of about 1 mm^2, and placed in a Al_2O_3 crucible. The temperature program ranged from room temperature to 500°C, with a heating rate of 10°C/min in a pure nitrogen atmosphere. The raw TGA-DSC data were corrected to eliminate the buoyancy effect. The corrected data were exported in the range of 120°C - 499°C at 0.25°C intervals. Data between room temperature and 120°C were not considered because they were influenced by moisture evaporation in random percentages within the sample. Data processing was performed using Microsoft Excel and Spectragryph, version 1.2.16.1.

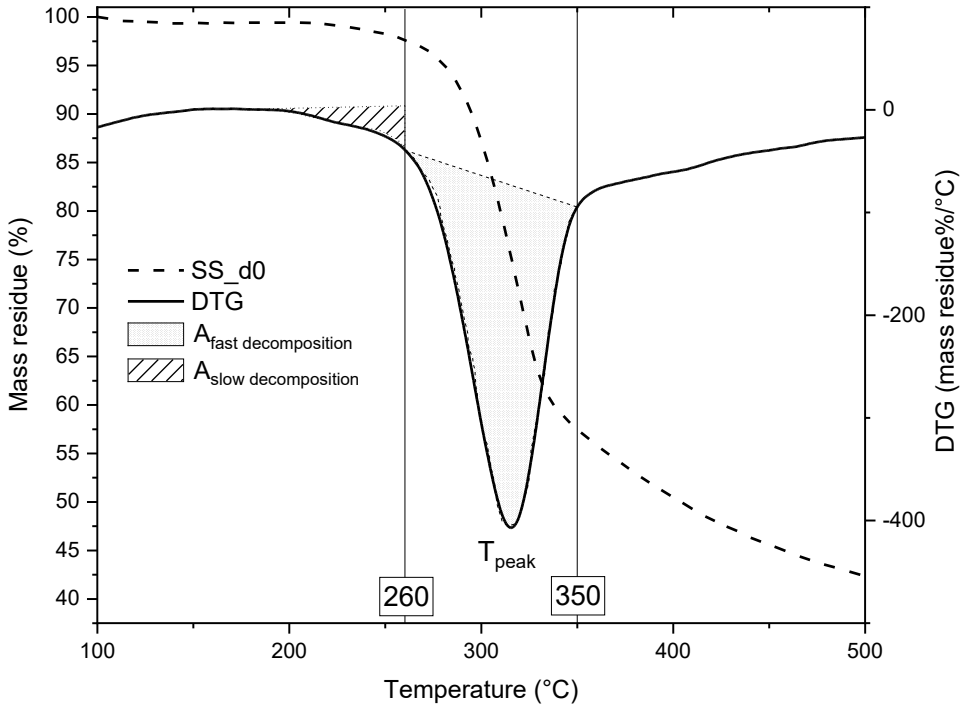

Figure 13. TGA plot and DTG plot of sample SS_d0. The integrated areas defined as "slow decomposition" and "fast decomposition" are highlighted.

The temperature values 260°C and 350°C appear as the lower and upper limits of the main decomposition event, as highlighted by the first derivative plot (DTG). Thus, a fast decomposition region between the two values can be identified. Its area, calculated applying an individual baseline integral, represents the mass lost during the decomposition event. For the 120-260°C range, defined as slow decomposition, the area value was obtained using the zero baseline (Figure 13).

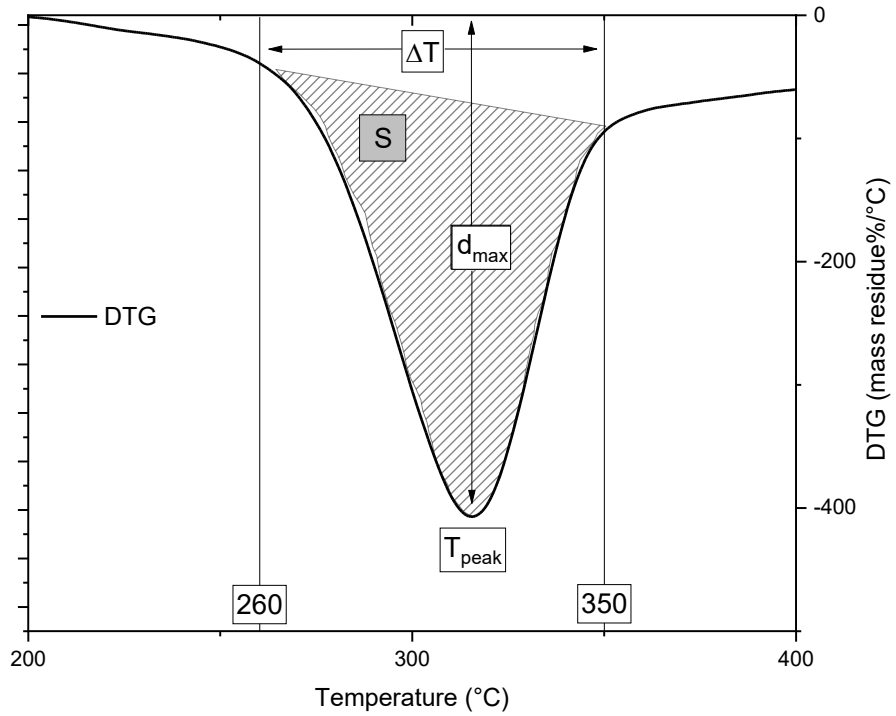

Figure 14. Representation of the integration area of a DTG curve. The features characterizing the DTG curve, that is the maximum decomposition temperature of the peak (T_{max}), peak depth (d_{max}) integral area (S), and the temperature difference between the beginning and end of the derivative curve (ΔT) are highlighted.

The level of silk degradation during ageing was calculated according to a method adapted from a paper evaluating the fire-retardant properties of different additives [67]. The features characterizing the DTG curve, that is the maximum decomposition temperature of the peak (T_{max}), peak depth (d_{max}) integral area (S), and the temperature difference between the beginning and end of the derivative curve (ΔT), are shown in Figure 14 and can be summarized by the A factor, calculated using the following formula:

$$A = \frac{1}{d_{max}} \times \frac{1}{S} \times \frac{\Delta T}{T_{max}}$$

Finally, the aging factor E, which quantifies the efficiency of the aging process (the higher its value, the greater the degradation), was calculated using the following formula:

$$E\% = {A_{aged} - A_0}\Big/{A_0} \times 100$$

where A_{aged} corresponds to the A factor calculated for each sample at different aging times, while A_0 is the reference factor for unaged silk or undyed aged silk.

X-ray Diffraction Analysis

X-ray diffraction analysis was conducted using a Bruker AXS D8 ADVANCE diffractometer at 40 V, 40 mA, with Cu-Kα radiation (λ = 1.5418 Å). The scans were collected on as-is undyed silk samples in the 5–35° 2θ range, with step scans Δ2θ = 0.02° and a counting time t = 1s. For peak deconvolution, Origin Pro 2018 software was used, following the most common method

found in the literature [65,69,70]. Peak fitting was performed using Gaussian peak shape and the peak centers listed in Table 9 [71].

Index	2θ/°	*d*/nm	attribution
(110)	15.8	0.56	α-helix
(200)	18.93	0.47	α-helix
amorphous	19.87	0.45	random coil
(210)	20.89	0.43	β-sheet
(211)	24.57	0.37	β-sheet
(002)	25.78	0.35	β-sheet

Table 9. Parameters of silk II lattice (drummy 2005)

The diffractograms were processed with Spectragryph software, version 1.2.16.1. They were truncated at 2θ value of 14 and normalized by area. This analysis was only applied to undyed silk samples. An example of the peak fitting analysis is shown in Figure 15.

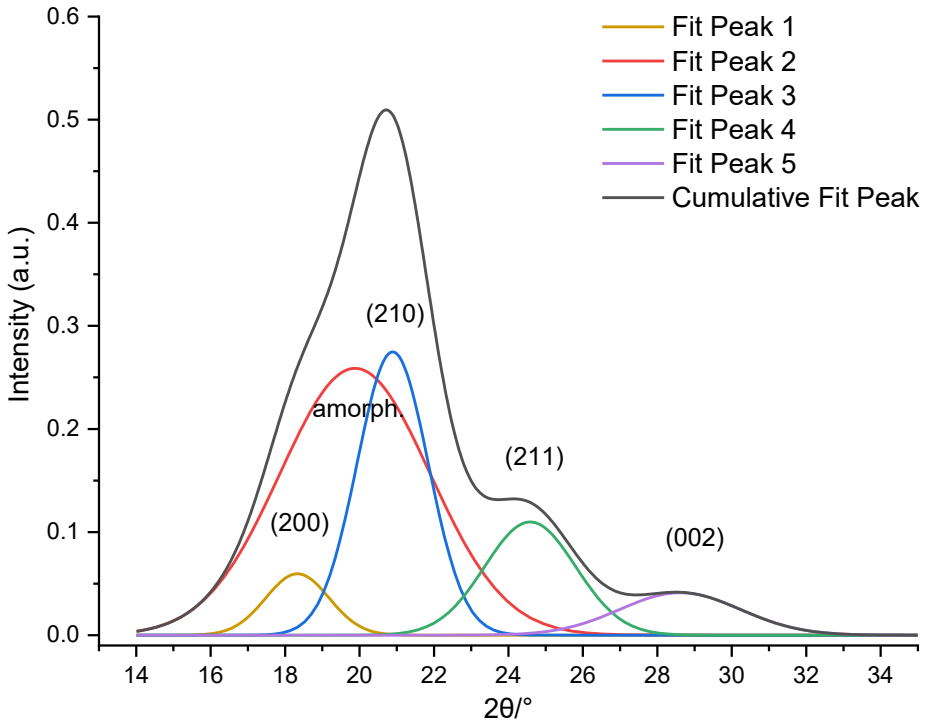

Figure 15. Peak fitting for sample SS_d0

Two different approaches were chosen for data evaluation:

- A crystallinity index was calculated, according to the following formula:

$$\chi_c = \frac{I_c}{I_c + I_a} \times 100$$

  I_c is the sum of the integrated intensity of the (200) and (210) Bragg peaks, I_a is the integrated intensity of the amorphous halo [65,69,70];

- The percentages of different conformations (α-helix, β-sheet, random coil) were calculated, using the following formula [72]:

$$\%_{\alpha-helix} = \frac{A_{\alpha-helix}}{A_{\alpha-helix} + A_{\beta-sheet} + A_{random\ coil}} \times 100$$

Principal Component Analysis

The spectroscopic data collected from the various analyses described above were exported into Excel matrices, where each row represents a sample, and the columns contain the variables of interest. While the traditional PCA is applied to two-dimensional matrix, data collected from a batch process, as a temporal evolution, exhibit a three-dimensional structure. To apply PCA-based modeling methods of batch process, data were unfolded into a two-dimensional structure [73], as schematized in Figure 16.

The software used was MATLAB (version r2012b – Mathworks, Natick, Massachusetts, USA) with the additional software PLS-Toolbox (Eigenvector Research, Inc. Manson, WA, USA). Before performing PCA, the data were truncated to the range 1800-1400 cm^{-1}. Different preprocessing methods were tested, including standard normal variate (SNV), multiplicative signal correction (MSC), normalization by area. Then, data were centered.

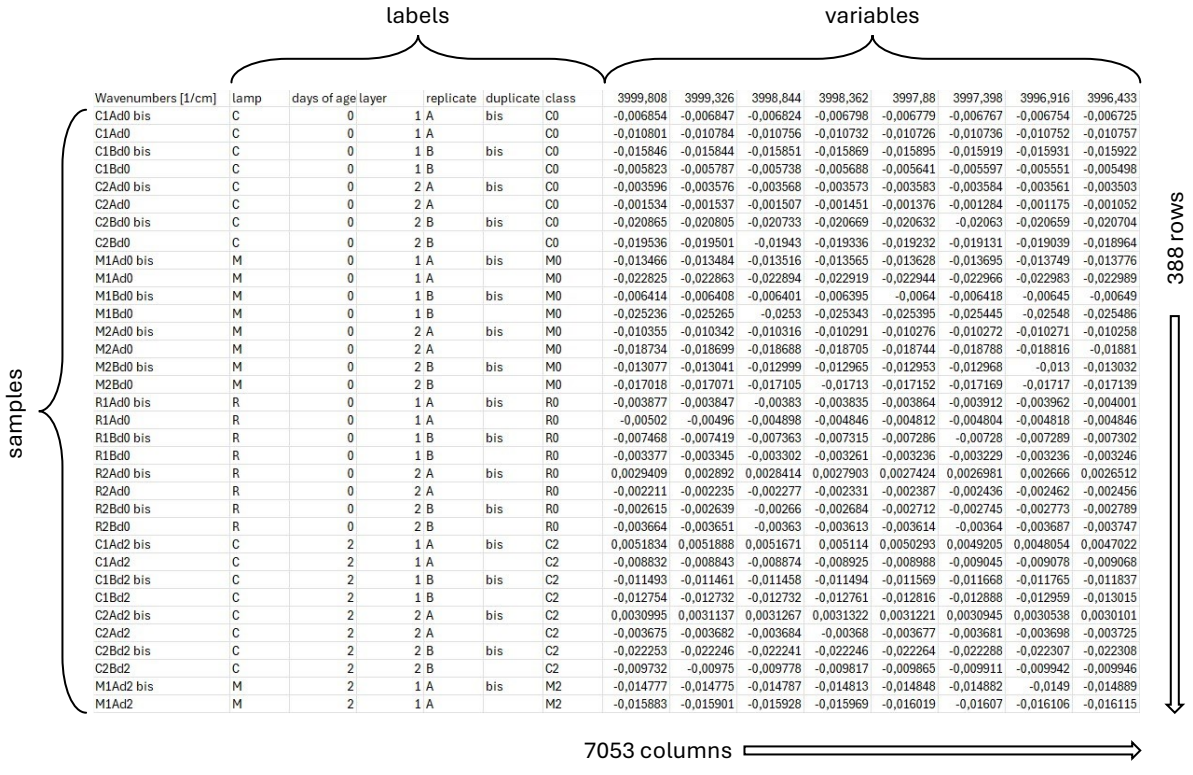

Wavenumbers [1/cm]	lamp	days of age	layer	replicate	duplicate	class	3999,808	3999,326	3998,844	3998,362	3997,88	3997,398	3996,916	3996,433
C1Ad0 bis	C	0	1	A	bis	C0	-0,006854	-0,006847	-0,006824	-0,006798	-0,006779	-0,006767	-0,006754	-0,006725
C1Ad0	C	0	1	A		C0	-0,010801	-0,010784	-0,010756	-0,010732	-0,010726	-0,010736	-0,010752	-0,010757
C1Bd0 bis	C	0	1	B	bis	C0	-0,015846	-0,015844	-0,015851	-0,015869	-0,015895	-0,015919	-0,015931	-0,015922
C1Bd0	C	0	1	B		C0	-0,005823	-0,005787	-0,005738	-0,005688	-0,005641	-0,005597	-0,005551	-0,005498
C2Ad0 bis	C	0	2	A	bis	C0	-0,003596	-0,003576	-0,003568	-0,003573	-0,003583	-0,003584	-0,003561	-0,003503
C2Ad0	C	0	2	A		C0	-0,001534	-0,001537	-0,001507	-0,001451	-0,001376	-0,001284	-0,001175	-0,001052
C2Bd0 bis	C	0	2	B	bis	C0	-0,020865	-0,020805	-0,020733	-0,020669	-0,020632	-0,02063	-0,020659	-0,020704
C2Bd0	C	0	2	B		C0	-0,019536	-0,019501	-0,01943	-0,019336	-0,019232	-0,019131	-0,019039	-0,018964
M1Ad0 bis	M	0	1	A	bis	M0	-0,013466	-0,013484	-0,013516	-0,013565	-0,013628	-0,013695	-0,013749	-0,013776
M1Ad0	M	0	1	A		M0	-0,022825	-0,022863	-0,022894	-0,022919	-0,022944	-0,022966	-0,022983	-0,022989
M1Bd0 bis	M	0	1	B	bis	M0	-0,006414	-0,006408	-0,006401	-0,006395	-0,0064	-0,006418	-0,00645	-0,00649
M1Bd0	M	0	1	B		M0	-0,025236	-0,025265	-0,0253	-0,025343	-0,025395	-0,025445	-0,02548	-0,025486
M2Ad0 bis	M	0	2	A	bis	M0	-0,010355	-0,010342	-0,010316	-0,010291	-0,010276	-0,010272	-0,010271	-0,010258
M2Ad0	M	0	2	A		M0	-0,018734	-0,018699	-0,018688	-0,018705	-0,018744	-0,018788	-0,018816	-0,01881
M2Bd0 bis	M	0	2	B	bis	M0	-0,013077	-0,013041	-0,012999	-0,012965	-0,012953	-0,012968	-0,013	-0,013032
M2Bd0	M	0	2	B		M0	-0,017018	-0,017071	-0,017105	-0,01713	-0,017152	-0,017169	-0,01717	-0,017139
R1Ad0 bis	R	0	1	A	bis	R0	-0,003877	-0,003847	-0,00383	-0,003835	-0,003864	-0,003912	-0,003962	-0,004001
R1Ad0	R	0	1	A		R0	-0,00502	-0,00496	-0,004898	-0,004846	-0,004812	-0,004804	-0,004818	-0,004846
R1Bd0 bis	R	0	1	B	bis	R0	-0,007468	-0,007419	-0,007363	-0,007315	-0,007286	-0,00728	-0,007289	-0,007302
R1Bd0	R	0	1	B		R0	-0,003377	-0,003345	-0,003302	-0,003261	-0,003236	-0,003229	-0,003236	-0,003246
R2Ad0 bis	R	0	2	A	bis	R0	0,0029409	0,002892	0,0028414	0,0027903	0,0027424	0,0026981	0,002666	0,0026512
R2Ad0	R	0	2	A		R0	-0,002211	-0,002235	-0,002277	-0,002331	-0,002387	-0,002436	-0,002462	-0,002456
R2Bd0 bis	R	0	2	B	bis	R0	-0,002615	-0,002639	-0,00266	-0,002684	-0,002712	-0,002745	-0,002773	-0,002789
R2Bd0	R	0	2	B		R0	-0,003664	-0,003651	-0,00363	-0,003613	-0,003614	-0,00364	-0,003687	-0,003747
C1Ad2 bis	C	2	1	A	bis	C2	0,0051834	0,0051888	0,0051671	0,005114	0,0050293	0,0049205	0,0048054	0,0047022
C1Ad2	C	2	1	A		C2	-0,008832	-0,008843	-0,008874	-0,008925	-0,008988	-0,009045	-0,009078	-0,009068
C1Bd2 bis	C	2	1	B	bis	C2	-0,011493	-0,011461	-0,011458	-0,011494	-0,011569	-0,011668	-0,011765	-0,011837
C1Bd2	C	2	1	B		C2	-0,012754	-0,012732	-0,012732	-0,012761	-0,012816	-0,012888	-0,012959	-0,013015
C2Ad2 bis	C	2	2	A	bis	C2	0,0030995	0,0031137	0,0031267	0,0031322	0,0031221	0,0030945	0,0030538	0,0030101
C2Ad2	C	2	2	A		C2	-0,003675	-0,003682	-0,003684	-0,00368	-0,003677	-0,003681	-0,003698	-0,003725
C2Bd2 bis	C	2	2	B	bis	C2	-0,022253	-0,022246	-0,022241	-0,022246	-0,022264	-0,022288	-0,022307	-0,022308
C2Bd2	C	2	2	B		C2	-0,009732	-0,00975	-0,009778	-0,009817	-0,009865	-0,009911	-0,009942	-0,009946
M1Ad2 bis	M	2	1	A	bis	M2	-0,014777	-0,014775	-0,014787	-0,014813	-0,014848	-0,014882	-0,0149	-0,014889
M1Ad2	M	2	1	A		M2	-0,015883	-0,015901	-0,015928	-0,015969	-0,016019	-0,01607	-0,016106	-0,016115

Figure 16. Unfolded data matrix for undyed silk samples (SET A)

3.4.6 References

[1] C.M. Breeze, Preventative Conservation of Samurai Armor, Andover, Massachusetts, 2008.

[2] S. Dalewicz-Kitto, F. McLaughlan, E. Schmuecker, J. Hood, Japanese armour and the conservation of a Sakakibara family armour at the Royal Armouries, Journal of the Institute of Conservation 36 (2013) 35–52. https://doi.org/10.1080/19455224.2013.774250.

[3] T. Absolon, Armour lacing methods and materials, in: Samurai Armour - The Japanese Cuirass, Osprey publishing, Oxford, UK, 2017.

[4] Sakakibara Kozan, The Manufacture of Armour and Helmets in Sixteenth Century Japan (Cho-kokatchu- Seisakuben), Charles E. Tuttle Company Inc., Rutland (Vermont), Tokio (Japan), 1964.

[5] M. Tada, K. Yamashiro, I. Oka, A. Goto, N. Kuwahara, Structural Analysis for Replicating Japanese Cultural Property Braids, Studies in Conservation 65 (2020) 399–410. https://doi.org/10.1080/00393630.2020.1715625.

[6] N.S. Allen, Photofading and light stability of dyed and pigmented polymers, Polym Degrad Stab 44 (1994) 357–374.

[7] N.S. Allen, Photofading mechanisms of dyes in solution and polymer media, Rev. Prog. Coloration 17 (1987) 61–71.

[8] P.M. Whitmore, G. Cass, The ozone fading of Traditional Japanese Colorants, Studies in Conservation 33 (1988) 29–40.

[9] T. Padfield, S. Landi, The Light-Fastness of the Natural Dyes, Studies in Conservation 11 (1966) 181–196.

[10] L. Zhou, J. Shao, L. Chai, Study on the UV-protective performance of cotton fabrics dyed with natural dyes, in: Adv Mat Res, 2011: pp. 1408–1413. https://doi.org/10.4028/www.scientific.net/AMR.332-334.1408.

[11] J.J. Lee, H.H. Lee, S.I. Eom, J.P. Kim, UV absorder aftertreatment to improve lightfastness of natural dyes on protein fibres, Coloration Technology 117 (2001) 134–138. https://doi.org/10.1111/j.1478-4408.2001.tb00051.x.

[12] R. Mongkholrattanasit, DYEING CHARACTERISTICS AND UV PROTECTION PROPERTIES OF SILK FABRIC DYED WITH NATURAL DYE FROM MANGROVE BARK (RHIZOPHORA APICULATA BLUME) EXTRACT, in: J. Fu (Ed.), Dyeing: Processes, Techniques and Applications, Nova Science Publishers, 2013: p. 271.

[13] Z. Motaghi, An Economical Dyeing Process for Cotton and Wool Fabrics and Improvement their Antibacterial Properties and UV protection, Journal of Natural Fibers 15 (2018) 777–788. https://doi.org/10.1080/15440478.2017.1364204.

[14] A.K. Sarkar, An evaluation of UV protection imparted by cotton fabrics dyed with natural colorants, BMC Dermatol 4 (2004). https://doi.org/10.1186/1471-5945-4-15.

[15] Y. Zhou, J. Zhang, R.C. Tang, J. Zhang, Simultaneous dyeing and functionalization of silk with three natural yellow dyes, Ind Crops Prod 64 (2015) 224–232. https://doi.org/10.1016/j.indcrop.2014.09.041.

[16] I.J. Miller, G.J. Smith, Protection against phototendering of wool by metal salts and mordanted dyes, Journal of the Society of Dyers and Colourists 111 (1995) 103–106.

[17] M. Hacke, Investigation into the Nature and Ageing of Tapestry Materials, University Of Manchester, 2006. https://doi.org/10.13140/RG.2.2.32890.08646.

[18] G.J. Smith, I.J. Miller, V. Daniels, Phototendering of wool sensitized by naturally occurring polyphenolic dyes, J Photochem Photobiol A Chem 169 (2005) 147–152. https://doi.org/10.1016/j.jphotochem.2004.06.014.

[19] M. Yatagai, Y. Magoshi, M.A. Becker, C. Sano, H. Ikuno, N. Kohara, M. Saito, Degradation and color fading of silk fabrics dyed with natural dyes and mordants, ACS Symposium Series 779 (2001) 86–97. https://doi.org/10.1021/bk-2001-0779.ch007.

[20] I. Vanden Berghe, Towards an early warning system for oxidative degradation of protein fibres in historical tapestries by means of calibrated amino acid analysis, J Archaeol Sci 39 (2012) 1349–1359. https://doi.org/10.1016/j.jas.2011.12.033.

[21] A. Manhita, V. Ferreira, H. Vargas, I. Ribeiro, A. Candeias, D. Teixeira, T. Ferreira, C.B. Dias, Enlightening the influence of mordant, dyeing technique and photodegradation on the colour hue of textiles dyed with madder - A chromatographic and spectrometric approach, Microchemical Journal 98 (2011) 82–90. https://doi.org/10.1016/j.microc.2010.12.002.

[22] H.E. Ahmed, S.S. Darwish, Effect of Museum Conditions on Historical Dyed Silk Fabric with Madder Dye, J Polym Environ 20 (2012) 596–606. https://doi.org/10.1007/s10924-012-0421-x.

[23] Various, Monitoring of damage in historic tapestries, (n.d.). https://cordis.europa.eu/project/id/EVK4-CT-2001-00048/results (accessed October 15, 2024).

[24] N. Luxford, Reducing the Risk of Open Display: Optimising the Preventive Conservation of Historic Silks, University of Southampton, UK, 2009.

[25] M.A. Koperska, DEGRADATION OF NATURAL FIBERS IN ARTEFACTS: MECHANISM AND INHIBITION, Jagiellonian University, 2015.

[26] Various, SAFESILK: Understanding, preventing and treating metal salt-induced silk degradation in heritage collections, (n.d.). https://www.uantwerpen.be/en/research-groups/arches/chemical-imaging/safesilk/ (accessed October 15, 2024).

[27] D. Badillo-Sanchez, D. Chelazzi, R. Giorgi, A. Cincinelli, P. Baglioni, Understanding the structural degradation of South American historical silk: A Focal Plane Array (FPA) FTIR and multivariate analysis, Sci Rep 9 (2019). https://doi.org/10.1038/s41598-019-53763-5.

[28] L. Geminiani, F.P. Campione, C. Corti, B. Giussani, G. Gorla, M. Luraschi, S. Recchia, L. Rampazzi, Historical silks: a novel method to evaluate their condition with ATR-FTIR spectroscopy and Principal Component Analysis, J Cult Herit 67 (2024) 9–22. https://doi.org/10.1016/j.culher.2024.01.015.

[29] L. Poletti, INVECCHIAMENTO ACCELERATO DI SETA TINTA: UNO STUDIO ANALITICO, Università dell'Insubria, 2024.

[30] L. Rampazzi, V. Brunello, F.P. Campione, C. Corti, L. Geminiani, S. Recchia, M. Luraschi, Non-invasive identification of pigments in Japanese coloured photographs, Microchemical Journal 157 (2020) 36–42. https://doi.org/10.1016/j.microc.2020.105017.

[31] A.L. Andrady, Wavelength Sensitivity in Polymer Photodegradation, in: Advances in Polymer Science, Springer, Berlin, Germany, 1997.

[32] R.L. Feller, Accelerated ageing - Photochemical and Thermal Aspects, The Getty Conservation Institute, Ann Arbor, Michigan (USA), 1994.

[33] A. Sionkowska, A. Planecka, The influence of UV radiation on silk fibroin, Polym Degrad Stab 96 (2011) 523–528. https://doi.org/10.1016/j.polymdegradstab.2011.01.001.

[34] A. Timar-Balazsy, D. Eastop, Materials, in: Chemical Principles in Textile Conservation, Third Edition, Routledge, New York, NY, USA, 1998: pp. 3–66.

[35] F. Civita, Le sete e le lacche vanno in battaglia: le armature giapponesi, in: M. Luraschi (Ed.), Il Samurai. Da Guerriero a Icona, Silvana Editoriale, Cinisello Balsamo, 2018: pp. 80–87.

[36] M. Arami, S. Rahimi, L. Mivehie, F. Mazaheri, N.M. Mahmoodi, Degumming of persian silk with mixed proteolytic enzymes, J Appl Polym Sci 106 (2007) 267–275. https://doi.org/10.1002/app.26492.

[37] T. Aguayo, M. Carolina Araya, T. Mónica Icaza, M. Campos-Vallette, A vibrational approach for the study of historical weighted and dyed silks, J Mol Struct 1075 (2014) 471–478. https://doi.org/10.1016/j.molstruc.2014.07.016.

[38] D. Sargunamani, N. Selvakumar, A study on the effects of ozone treatment on the properties of raw and degummed mulberry silk fabrics, Polym Degrad Stab 91 (2006) 2644–2653. https://doi.org/10.1016/j.polymdegradstab.2006.05.001.

[39] R. Mossotti, R. Innocenti, M. Zoccola, A. Anghileri, G. Freddi, The degumming of silk fabrics: A preliminary near infrared spectroscopy study, J Near Infrared Spectrosc 14 (2006) 201–208. https://doi.org/10.1255/jnirs.615.

[40] W. Wang, Y. Pan, K. Gong, Q. Zhou, T. Zhang, Q. Li, A comparative study of ultrasonic degumming of silk sericin using citric acid, sodium carbonate and papain, Coloration Technology 135 (2019) 195–201. https://doi.org/10.1111/cote.12392.

[41] R. Chen, M. Hu, H. Zheng, H. Yang, L. Zhou, Y. Zhou, Z. Peng, Z. Hu, B. Wang, Proteomics and immunology provide insight into the degradation mechanism of historic and artificially aged silk, Anal Chem 92 (2020) 2435–2442. https://doi.org/10.1021/acs.analchem.9b03616.

[42] M.M.R. Khan, M. Tsukada, Y. Gotoh, H. Morikawa, G. Freddi, H. Shiozaki, Physical properties and dyeability of silk fibers degummed with citric acid, Bioresour Technol 101 (2010) 8439–8445. https://doi.org/10.1016/j.biortech.2010.05.100.

[43] D. Tamburini, Investigating Asian colourants in Chinese textiles from Dunhuang (7th-10th century AD) by high performance liquid chromatography tandem mass spectrometry – Towards the creation of a mass spectra database, Dyes and Pigments 163 (2019) 454–474. https://doi.org/10.1016/j.dyepig.2018.12.025.

[44] D. Tamburini, J. Dyer, Fibre optic reflectance spectroscopy and multispectral imaging for the non-invasive investigation of Asian colourants in Chinese textiles from Dunhuang (7th-10th century AD), Dyes and Pigments 162 (2019) 494–511. https://doi.org/10.1016/j.dyepig.2018.10.054.

[45] L. LI, M. Yu Yao, T. Liu, A review of silk ageing: mechanism and stimulation methods, Journal of Historical Archaeology & Anthropological Sciences 5 (2020) 151–154. https://doi.org/10.15406/jhaas.2020.05.00229.

[46] J.H. Hofenk de Graaff, W.G. Th Roelofs, M.R. van Bommel SK, The Colourful Past Origins, Chemistry and Identification of Natural Dyestuffs, n.d.

[47] A. Casoli, D. M.E., S. L., I COLORANTI NELL'ARTE, (2009).

[48] J. Lee, M.H. Kang, K.B. Lee, Y. Lee, Characterization of natural dyes and traditional korean silk fabric by surface analytical techniques, Materials 6 (2013) 2007–2025. https://doi.org/10.3390/ma6052007.

[49] K. Kato, B. Doherty, I. Degano, F. Sabatini, C. Miliani, A. Romani, K. Ito, B.G. Brunetti, An SERS analytical protocol for characterizing native Japanese plant extracts, Journal of Raman Spectroscopy 51 (2020) 892–902. https://doi.org/10.1002/jrs.5856.

[50] E. Yi, J.Y. Cho, Color analysis of natural colorant-dyed fabrics, Color Res Appl 33 (2008) 148–157. https://doi.org/10.1002/col.20390.

[51] R. Nakamura, Y. Tanaka, A. Ogata, M. Naruse, Dye analysis of Shosoin textiles using excitation-emission matrix fluorescence and ultraviolet-visible reflectance spectroscopic techniques, Anal Chem 81 (2009) 5691–5698. https://doi.org/10.1021/ac900428a.

[52] C.K.K. Choo, K.S. Lau, Y.E. Lee, Analysis of dyeings produced by traditional Korean methods using colorants from plant extracts, Coloration Technology 118 (2002) 35–45. https://doi.org/10.1111/j.1478-4408.2002.tb00135.x.

[53] K. Lech, J. Nawała, S. Popiel, Mass Spectrometry for Investigation of Natural Dyes in Historical Textiles: Unveiling the Mystery behind Safflower-Dyed Fibers, J Am Soc Mass Spectrom 32 (2021) 2552–2566. https://doi.org/10.1021/jasms.1c00195.

[54] X. Zhang, K. Corrigan, B. MacLaren, M. Leveque, R. Laursen, Characterization of yellow dyes in nineteenth-century Chinese textiles, Studies in Conservation 52 (2007) 211–220. https://doi.org/10.1179/sic.2007.52.3.211.

[55] X. Luo, N. Fang, W. Zhang, Y. Du, Influence of environment on the stability of Chinese traditional colorants, Studies in Conservation 61 (2016) 305–307. https://doi.org/10.1080/00393630.2016.1182689.

[56] J. Liu, L. Ji, L. Chen, K. Pei, P. Zhao, Y. Zhou, F. Zhao, Identification of yellow dyes in two wall coverings from the Palace Museum: Evidence for reconstitution of artifacts, Dyes and Pigments 153 (2018) 137–143. https://doi.org/10.1016/j.dyepig.2018.01.057.

[57] C. Chavanne, A. Verney, C. Paquier-Berthelot, M. Bostal, P. Buléon, P. Walter, Bayeux Tapestry: First use of early synthetic dyes for the restoration of a masterpiece, Dyes and Pigments 208 (2022). https://doi.org/10.1016/j.dyepig.2022.110798.

[58] A. Manhita, V. Ferreira, H. Vargas, I. Ribeiro, A. Candeias, D. Teixeira, T. Ferreira, C.B. Dias, Enlightening the influence of mordant, dyeing technique and photodegradation on the colour hue of textiles dyed with madder - A chromatographic and spectrometric approach, Microchemical Journal 98 (2011) 82–90. https://doi.org/10.1016/j.microc.2010.12.002.

[59] A. Jahangiri, S.M. Ghoreishian, A. Akbari, M. Norouzi, M. Ghasemi, M. Ghoreishian, E. Shafiabadi, Natural Dyeing of Wool by Madder (Rubia tinctorum L.) Root Extract Using Tannin-based Biomordants: Colorimetric, Fastness and Tensile Assay, Fibers and Polymers 19 (2018) 2139–2148. https://doi.org/10.1007/s12221-018-8069-3.

[60] A. Gilchrist, J. Nobbs, Colorimetry, Theory, Encyclopedia of Spectroscopy and Spectrometry (1999) 337–343.

[61] M.R. Luo, G. Cui, B. Rigg, The development of the CIE 2000 colour-difference formula: CIEDE2000, Color Res Appl 26 (2001) 340–350. https://doi.org/10.1002/col.1049.

[62] Y. Gong, G. Zhou, C. Qiao, Y. Pan, Study on the photodegradation behaviors of thermal-aged silk, Herit Sci 12 (2024). https://doi.org/10.1186/s40494-024-01270-w.

[63] S. Lee, S.H. Kim, Y.Y. Jo, W.T. Ju, H.B. Kim, H. Kweon, Effects of ultraviolet light irradiation on silk fibroin films prepared under different conditions, Biomolecules 11 (2021) 1–11. https://doi.org/10.3390/biom11010070.

[64] J. Tocháček, Z. Vrátníčková, Polymer life-time prediction: The role of temperature in UV accelerated ageing of polypropylene and its copolymers, Polym Test 36 (2014) 82–87. https://doi.org/10.1016/j.polymertesting.2014.03.019.

[65] X. Zhang, D. Gong, Y. Gong, Insight into the orientation behavior of thermal-aged and historic silk fabrics by polarized FTIR microspectroscopy, J Cult Herit 38 (2019) 53–63. https://doi.org/10.1016/j.culher.2019.02.007.

[66] A.M. Coats, D.W.L. Hukins, C.T. Imrie, R.M. Aspden, Polarization artefacts of an FTIR microscope and the consequences for intensity measurements on anisotropic materials, J Microsc 211 (2003) 63–66. https://doi.org/10.1046/j.1365-2818.2003.01198.x.

[67] D.S. Bakirtzis, V.C. Tsapara, K.G. Kolovos, S.E. Liodakis, Assessment of the impact of fire retardants on the combustion of natural polymers employing DTG and LOI, Fire Mater 39 (2015) 109–118. https://doi.org/10.1002/fam.2232.

[68] D. Pawcenis, M. Smoleń, M.A. Aksamit-Koperska, T. Łojewski, J. Łojewska, Evaluating the impact of different exogenous factors on silk textiles deterioration with use of size exclusion chromatography, Appl Phys A Mater Sci Process 122 (2016). https://doi.org/10.1007/s00339-016-0052-5.

[69] Y. Gong, Z. Li, J. Hu, G. Zhou, G. Xu, W. Yang, J. Zhang, Insight into the measurements for determining the ageing degree of ancient silk, Polym Degrad Stab 196 (2022). https://doi.org/10.1016/j.polymdegradstab.2022.109833.

[70] J. Zhou, X. Zhou, L. Pan, Y. Deng, H. Zheng, Z. Peng, J. Wan, Y. Zhou, B. Wang, Molecular Evidence of Structural Changes in Silk Using Unlimited Degradation Mass Spectrometry, ACS Omega 8 (2023) 34410–34419. https://doi.org/10.1021/acsomega.3c02254.

[71] L.F. Drummy, D.M. Phillips, M.O. Stone, B.L. Farmer, R.J. Naik, Thermally induced α-helix to β-sheet transition in renegated silk fibers and films, Biomacromolecules 6 (2005) 3328–3333. https://doi.org/10.1021/bm0503524.

[72] M.A. Koperska, D. Pawcenis, J. Bagniuk, M.M. Zaitz, M. Missori, T. Łojewski, J. Łojewska, Degradation markers of fibroin in silk through infrared spectroscopy, Polym Degrad Stab 105 (2014) 185–196. https://doi.org/10.1016/j.polymdegradstab.2014.04.008.

[73] Y. Chai, H. Yang, L. Zhao, Data unfolding PCA modelling and monitoring of multiphase batch processes, in: IFAC Proceedings Volumes (IFAC-PapersOnline), IFAC Secretariat, 2013: pp. 569-574. https://doi.org/10.3182/20130708-3-CN-2036.00058.

3.5 Results – Undyed Silk

Undyed silk samples were studied through time to evaluate changes occurring due to light ageing. Different lamps were used to simulate different ageing conditions. The study was also functional to select the ageing conditions which could infer a significant degradation to the samples.

The ageing indicators which were considered in this part of the study were the following:

- Colour change, by means of colorimetric measurements;
- Structural change dependent on secondary structure, by means of ATR-FTIR analysis and XRD analysis;
- Oxidative change associated with hydrolysis, by means of ATR-FTIR analysis;
- Amide II change associated to the conversion of tyrosine into dopamine, by means of ATR-FTIR analysis;
- Depolymerization by means of thermogravimetric analysis.

Eventually, the kinetics of degradation of the three lamps were compared.

3.5.1 Colour change

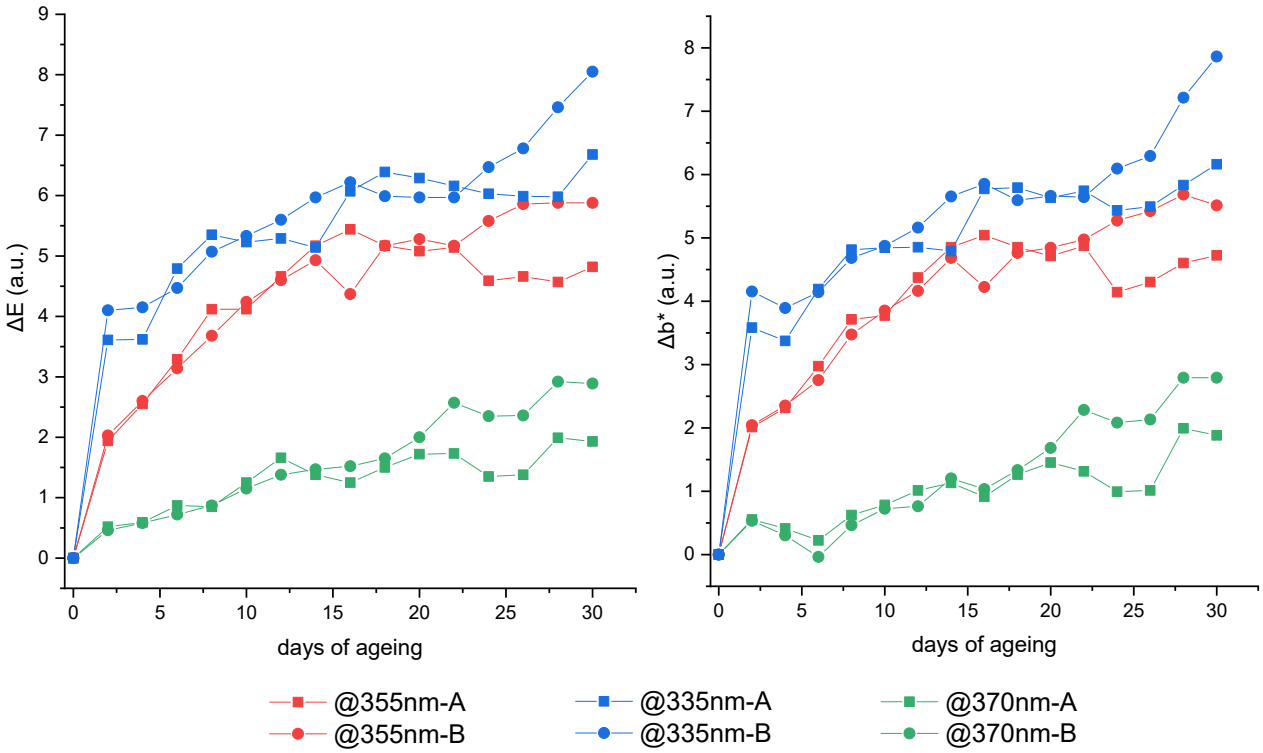

Figure 17. On the left, variation in E values (ΔE); on the right, variationd in b values (Δb*)*

Figure 17 shows the trends for ΔE and Δb* values for each set of samples aged 30 days under different lamps. For each trend, the values of ΔE and Δb* appear very similar because the Δb* value is the major factor contributing to the ΔE value. It can be seen that the two replicates for each lamp (A and B) show very similar values until day 20, then they start to diverge.

Assuming ΔE=3 as the threshold for the occurring of a visible variation in the colour, both UVA355nm and UVA335nm do exceed this limit. UVA335nm reaches the higher values. The rise in Δb* values for UVA335nm and UVA355nm shows an exponential asymptotic growth, with the most dramatic yellowing obtained in the first days of ageing. Similar data were obtained by other authors [1–3].

Δb* trend of UVA370nm is characterized by a slow linear increase, similar to the trend reported by Dang obtained with visible lamps [4].

3.5.2 Structural change

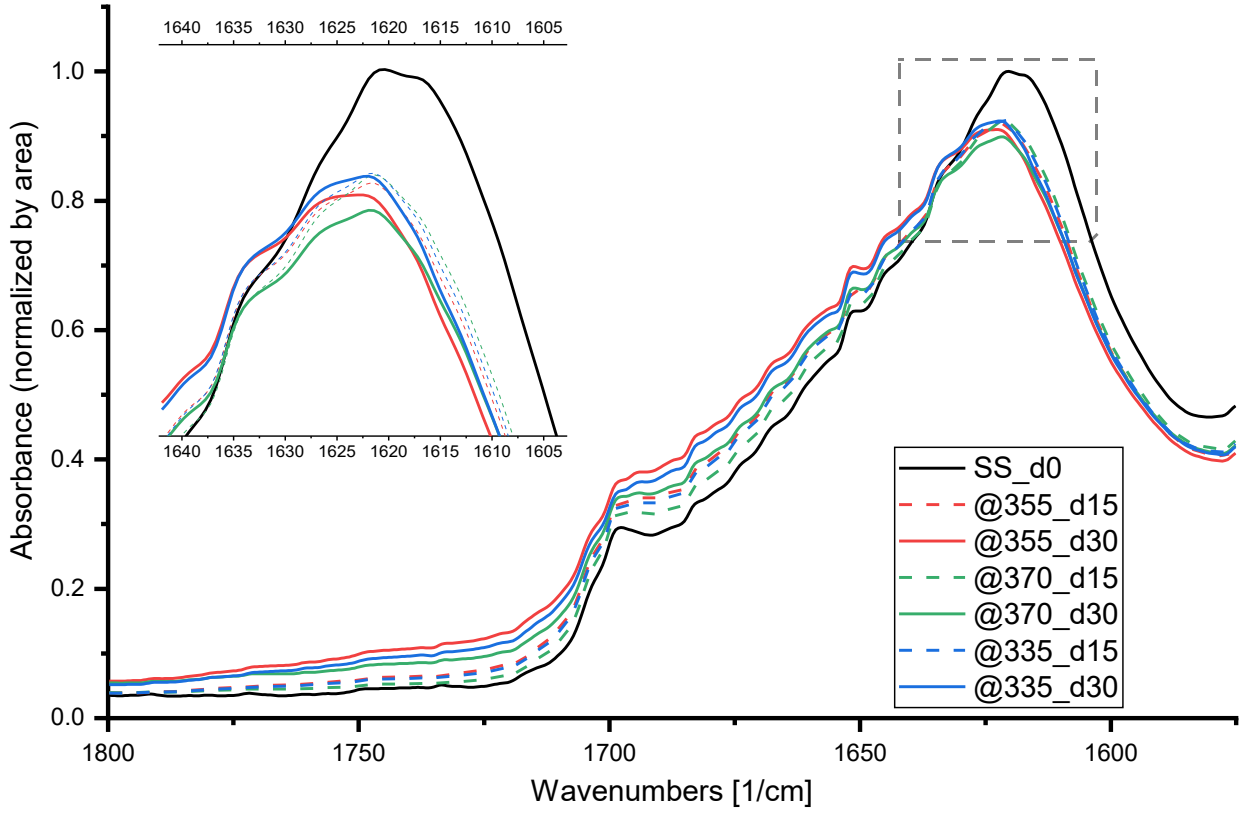

Figure 18. ATR-FTIR spectra for SET B samples (range 1800-1575 cm^{-1}). The region where the shift takes place is highlighted.

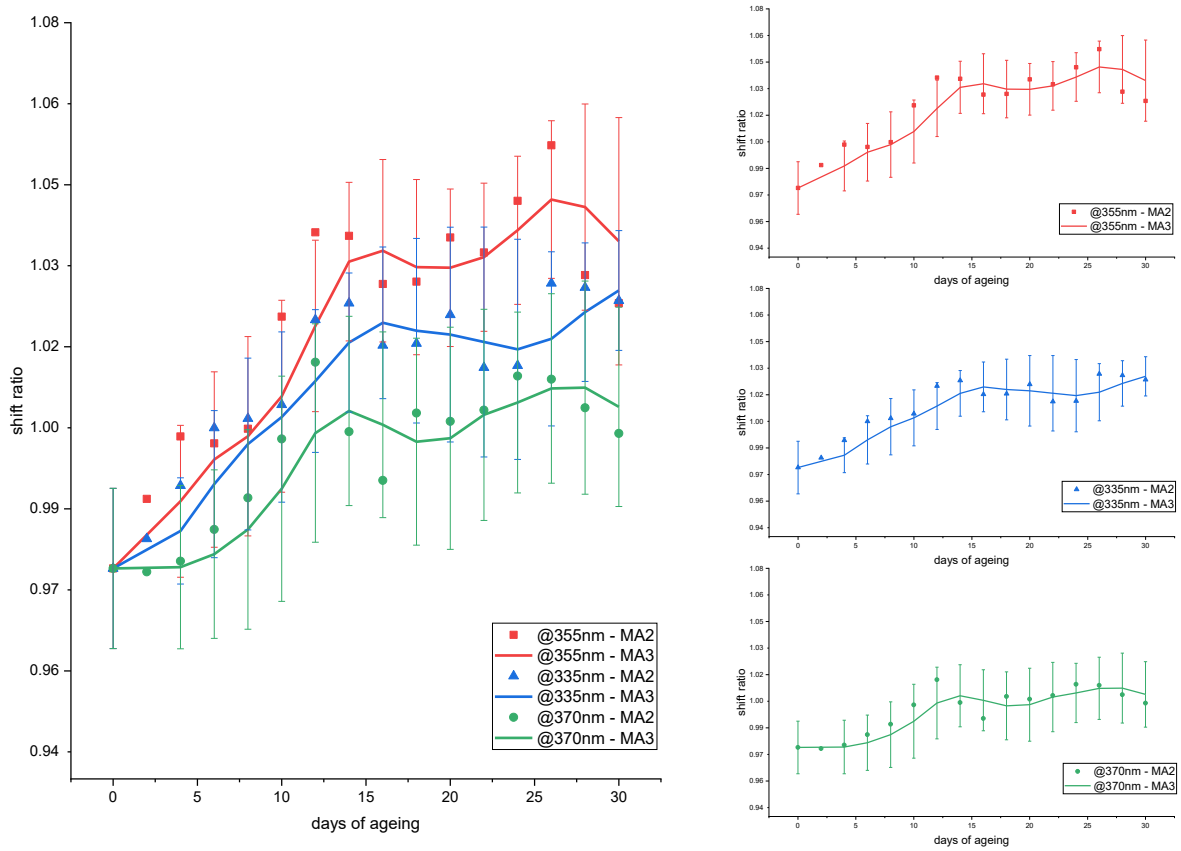

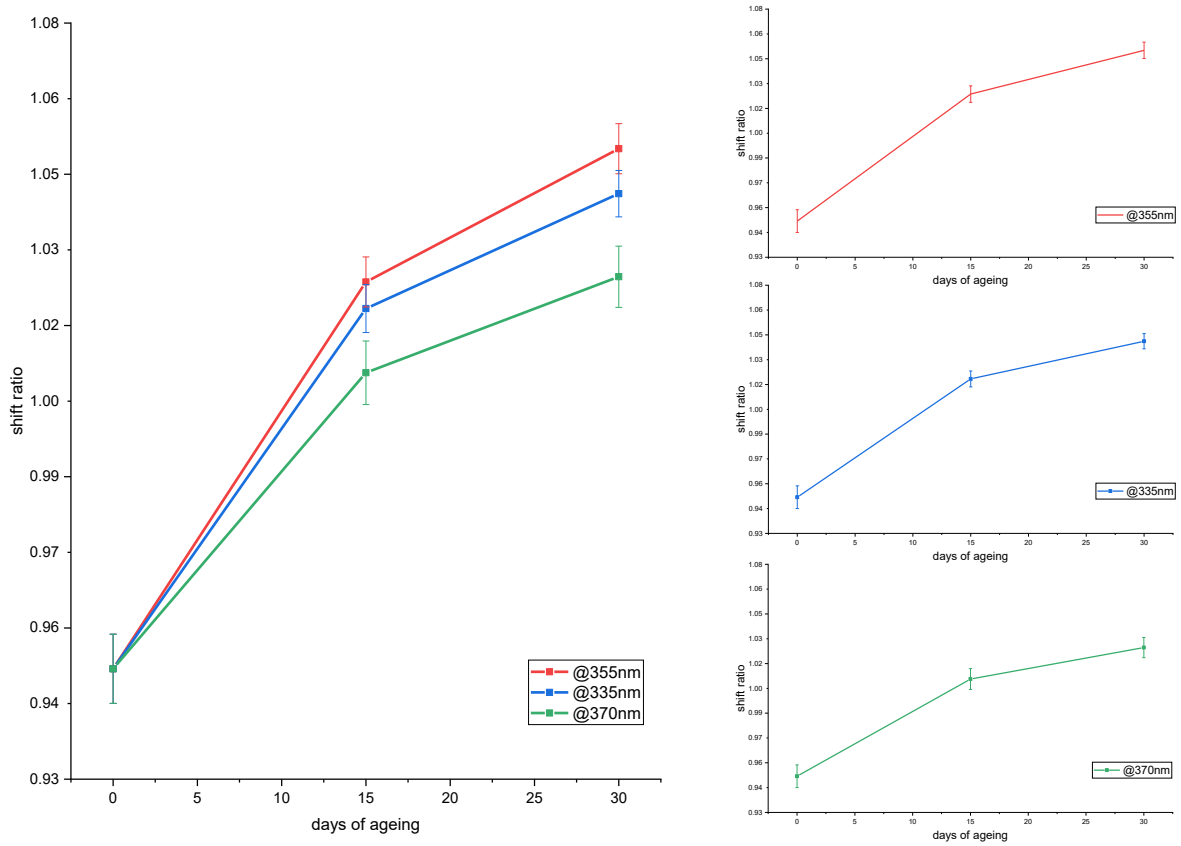

Figure 19. Upper image: Shift ratio values of SET A plotted against days of ageing; Lower image: Shift ratio values of SET B plotted against days of ageing

Figure 18 shows the averaged ATR-FTIR spectra for the samples of SET B. It can be appreciated that the intensity of aged samples is far lower than the intensity of silk in pristine condition (SS_d0), as reported in literature [5].

Several indicators of structural changes can be identified. Firstly, there is a shift of the maximum of peak of amide I from 1617 cm^{-1} to 1625 cm^{-1}. The blueshift has been attributed to the consumption of extended chain and random coil structures surrounding the crystalline domains of silk fibroin [6]. The peak maximum at 1620 cm^{-1} or lower is an indicator of the high content of intermolecular β-sheets and β-strands. As such structures are destroyed by light, absorption maximum shifts to blue owing to the emergence of β-sheet signals at 1625-30 cm^{-1}. Secondly, in the aged samples there is a rise in the intensity values between 1700-1650 cm^{-1}. The reason is due to the increase of non-crystalline domains, including α-helix, random coil and β-turn conformations.

Shift ratio represents the shift of the peak of amide I from 1617 cm^{-1} to 1625 cm^{-1}, which can be related to the structural change. Figure 19 shows the calculated shift ratios plotted against the days of ageing. The data taken from the SET A show high variability, as confirmed by the standard error (95%). To better visualize the trend, moving averages are shown instead of data points by creating a series of averages of different selections (2 or 3) of the original data.

To get more precise data, original data from SET B are presented as well. In this case, the standard error (95%) calculated over 32 replicates is much lower.

In both cases, the trends appear to be asymptotic exponential. After 15 days of ageing, the shift values of the SET A data reach a high value followed by a period of slower increase. Lamps UVA@355nm and UVA@335nm produce a change that is significantly different from the non-aged samples.

This trend is consistent with the proposed mechanism. The consumption of extended chain and random coil structures surrounding the crystalline domains of silk fibroin increases linearly in the first 15 days and then rate of consumption decreases as all the external material is virtually degraded. There is not a decrease of the ratio as the light degrades highly crystalline domains into lower crystalline structures (aggregated β-strand) and into non-crystalline domain, such as α-helix, random coil and β-turn conformations, whose signals appear in the spectra (Figure 18).

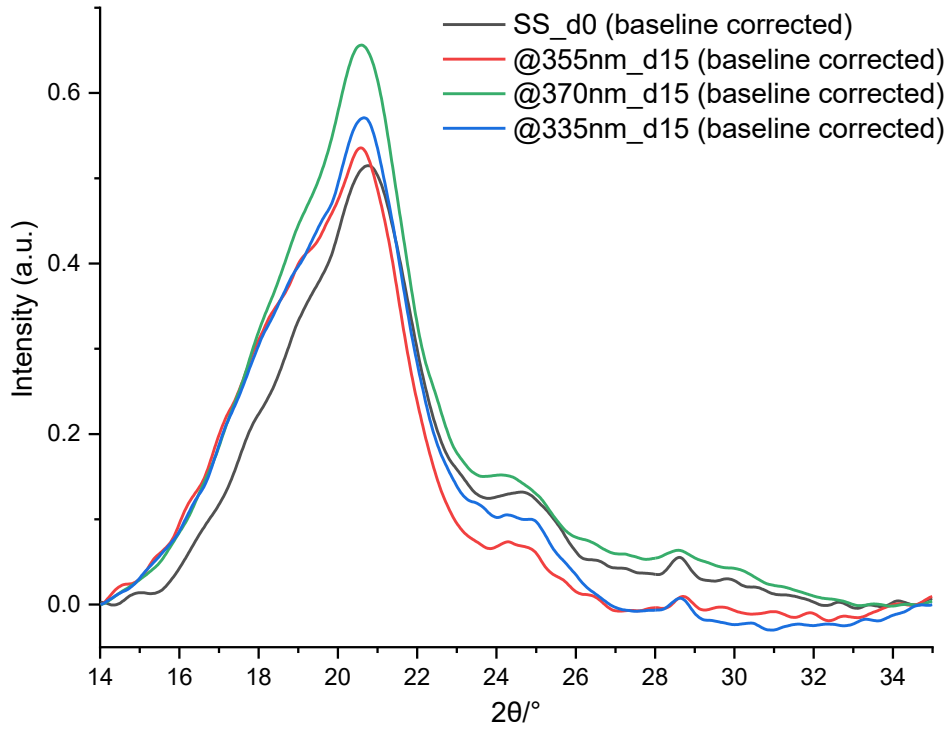

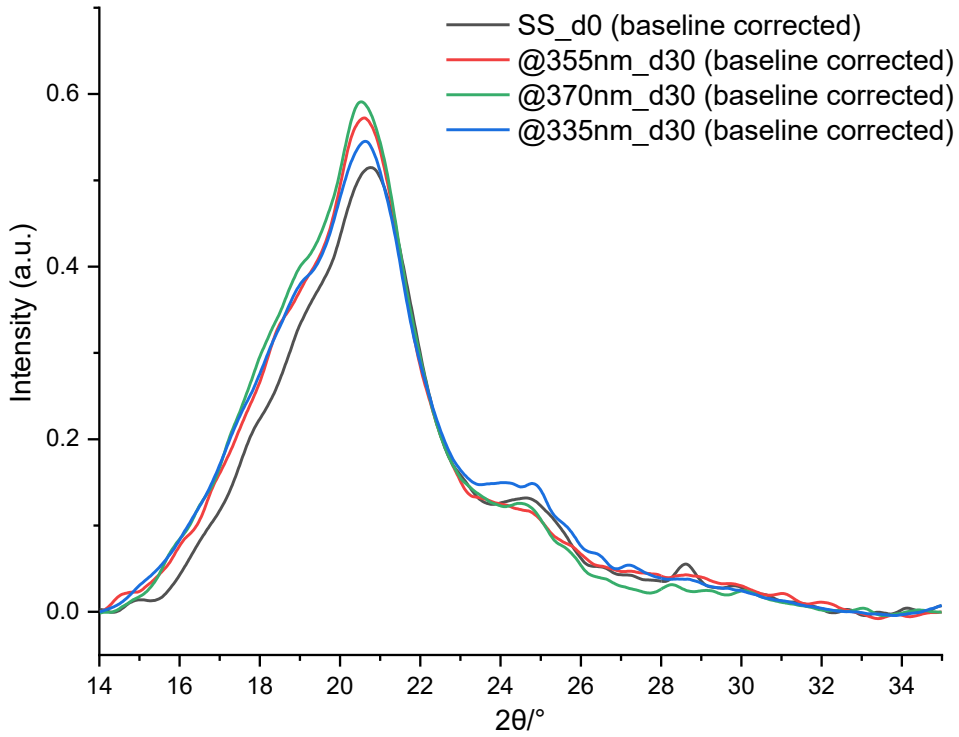

Figure 20. X-ray diffractograms for SET B samples

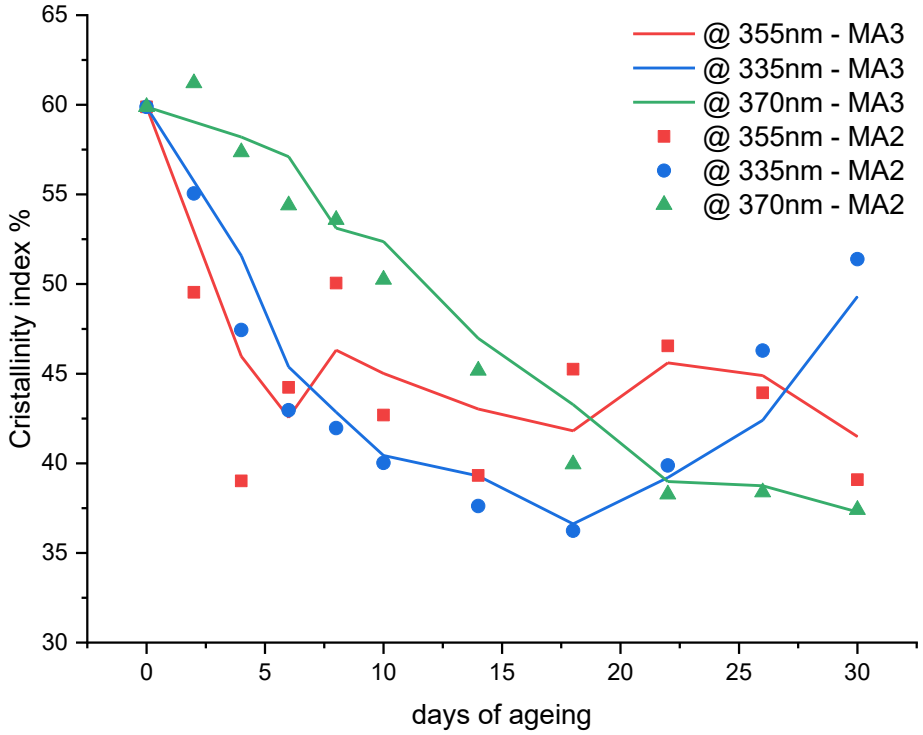

Figure 21. Cristallinity index calculated for SET A samples

Figure 20 shows the X-ray diffractograms for the samples of SET B. From the upper plots, it can be appreciated that the intensity of aged samples is higher than the intensity of silk in pristine condition (SS_d0) This could be related to the rise of the amorphous halo [7–9], which can be quantified according to the fitting procedure explained in the *Experimental parameters* section.

Several indicators of structural changes can be identified. Firstly, there is a shift of the maximum diffraction figure from 20.78° to 20.57°. This is an indicator of the decrease of the area attributed to the index (210), which corresponds to the β-sheet crystallites. Similarly, the rise of the intensity of the diffraction peaks attributed to α-helix and random coil (15.8°, 18.93°, 19.87°) [10], evidences that the non-crystalline domains have been raised by the light exposure.

Figure 21 shows the trends of the crystallinity index values calculated as explained in the *Experimental parameters* section. The data taken from the SET A show high variability, so moving averages are shown instead of data points to better visualize the trend. Pristine silk shows a crystallinity index equal to 60%, that is consistent with the data found in literature [11]. For all the aged samples, the crystallinity index has decreased with respect to the pristine silk, as reported by literature [2,12]. The rate of decrease is slower for samples aged under UVA@370nm, and faster for the others. However, after 30 days of ageing all the samples reached the same value of crystallinity, and unexpectedly there is a rise in crystallinity in samples aged under UVA 335nm after they reached the minimum value at day 18.

Figure 22 shows the trends of the percentages of α-helix, β-sheet and random coil in the samples of SET A calculated as explained in the *Experimental parameters* section. In pristine silk, the total percentage of β-sheets and α-helix is near to 50% of the total, that is consistent with the literature [13–15]. It should be noted that the percentage attributed to random coil also contains up to 22 % each of distorted β-turn and distorted β-sheets [15]. For all the aged samples, the random coil percentage has increased with respect to the pristine silk, while the α-helix has remained constant. The rate of decrease is slower for samples aged under UVA@370nm, and faster for the others, but after 30 days of ageing the UVA@370nm showed the highest values of random coil. The other lamps show an inversion of the trend after they reached the maximum value of random coil percentage at day 20.

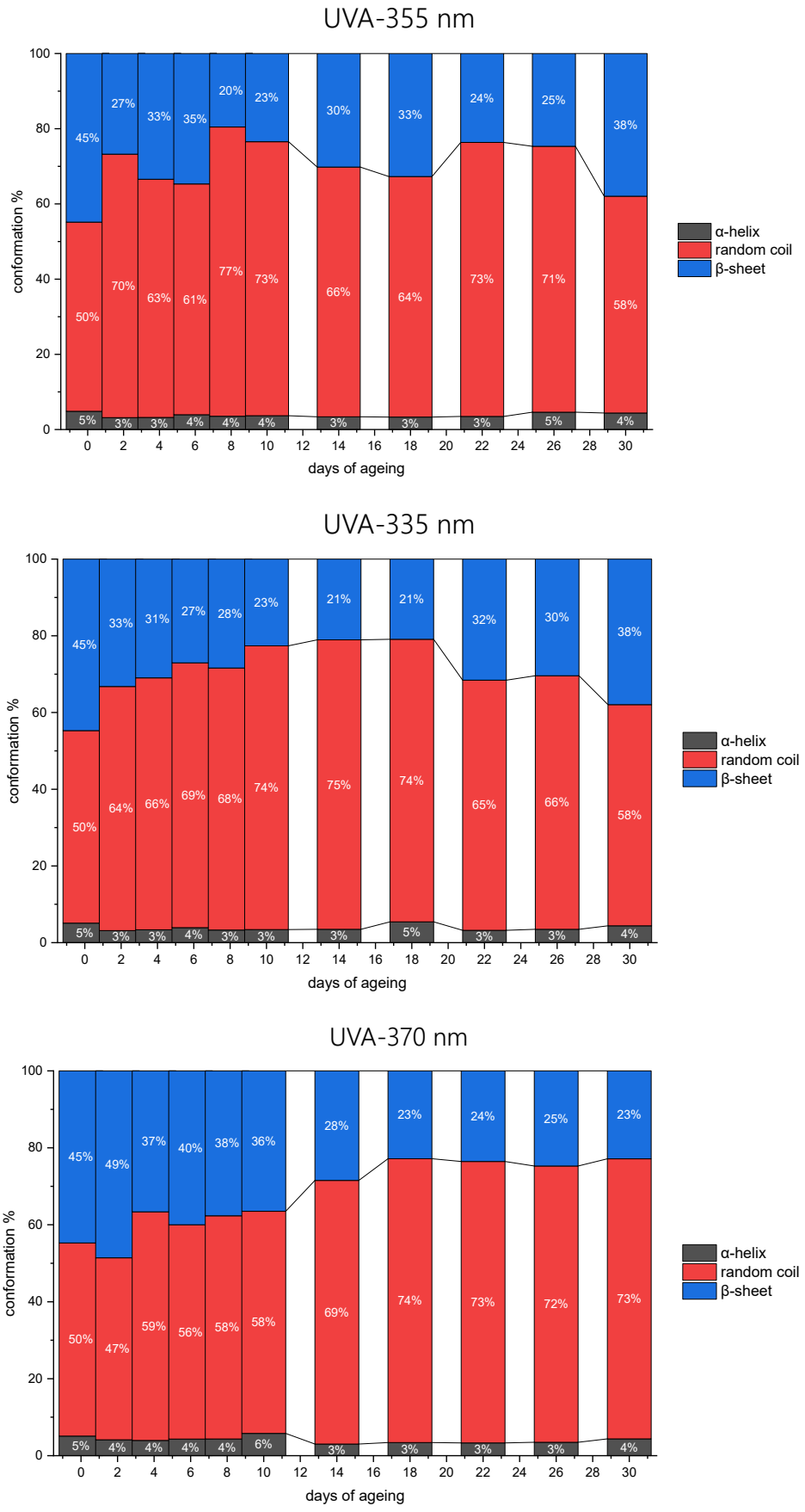

Figure 22. Barplots showing the percentages of α-helix, β-sheet and random coil in the samples of SET A

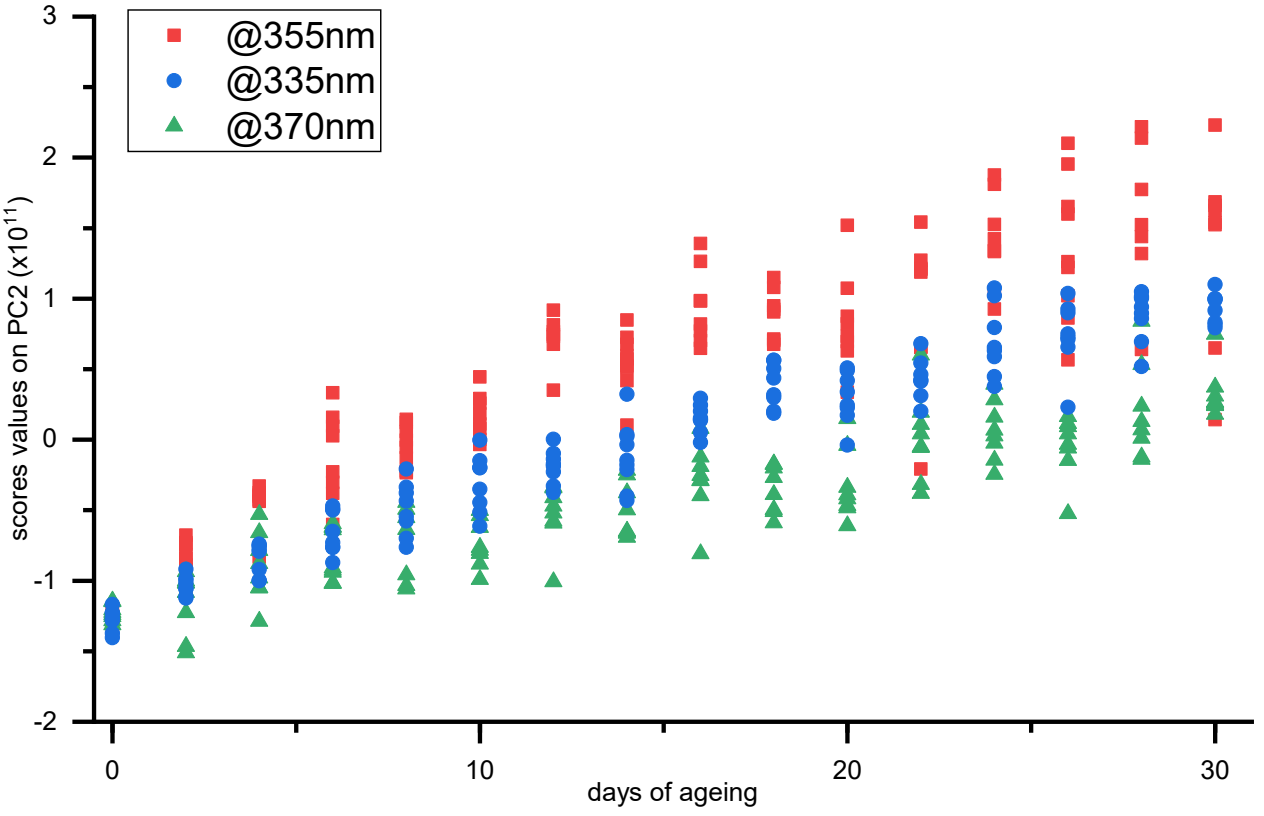
@355nm
@335nm
@370nm
scores values on PC2 (x10^11)
days of ageing

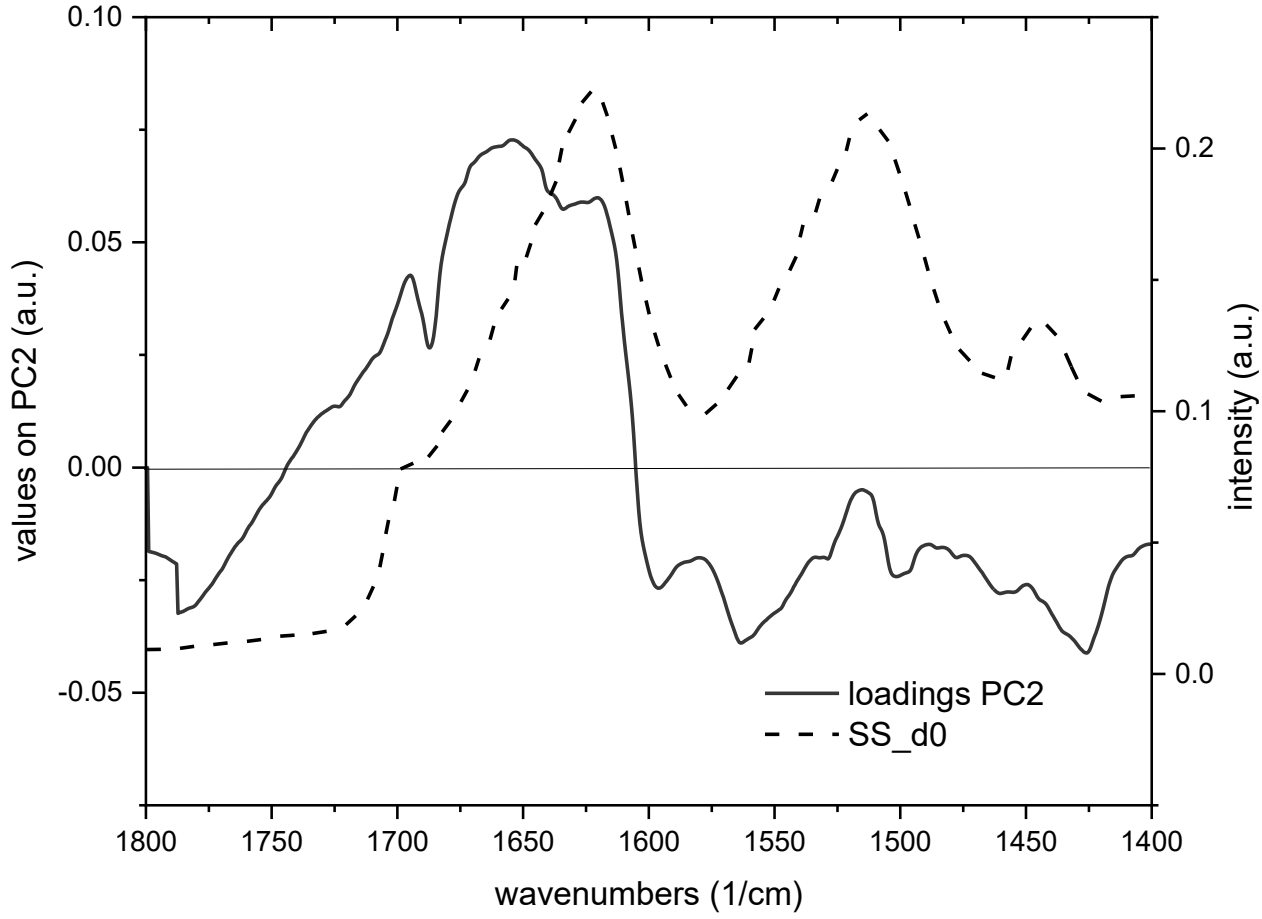
values on PC2 (a.u.)
intensity (a.u.)
loadings PC2
SS_d0
wavenumbers (1/cm)

Figure 23. Upper: scores values against days of ageing; lower: loadings values for PC2 (solid line) plotted with the spectrum of SS_d0 (dashed line)

ATR-FTIR data were elaborated with principal component analysis, as already done in previous works [6,16,17]. The resulting model is characterized by PC1 accounting for 74.3% of the total variance and by PC2 accounting for 21.6% of the total variance (Figure 23). The scores of PC1 are not considered as apparently they don't correlate to the ageing (refer to Supporting Material). The scores of PC2, inversely, nicely correlate to the ageing, as shown in Figure 23, together with the loadings of PC2. PCA loadings are the coefficients of the linear combination of the original variables from which the principal components (PCs) are constructed. They can be associated with the wavenumbers to identify the part of the original spectrum which has the greatest role in the calculation of the PCA. It appears that the signals of the amide I peak are essential. In particular, the peak at 1620 cm^{-1} and the broad band at 1650 cm^{-1} have a major role in the differentiation of the extent of ageing of the samples. This finding is consistent with the observed blueshift in the peak at 1620 cm^{-1} and with the rise of α-helix and random coil conformations related to the band at 1650 cm^{-1}.

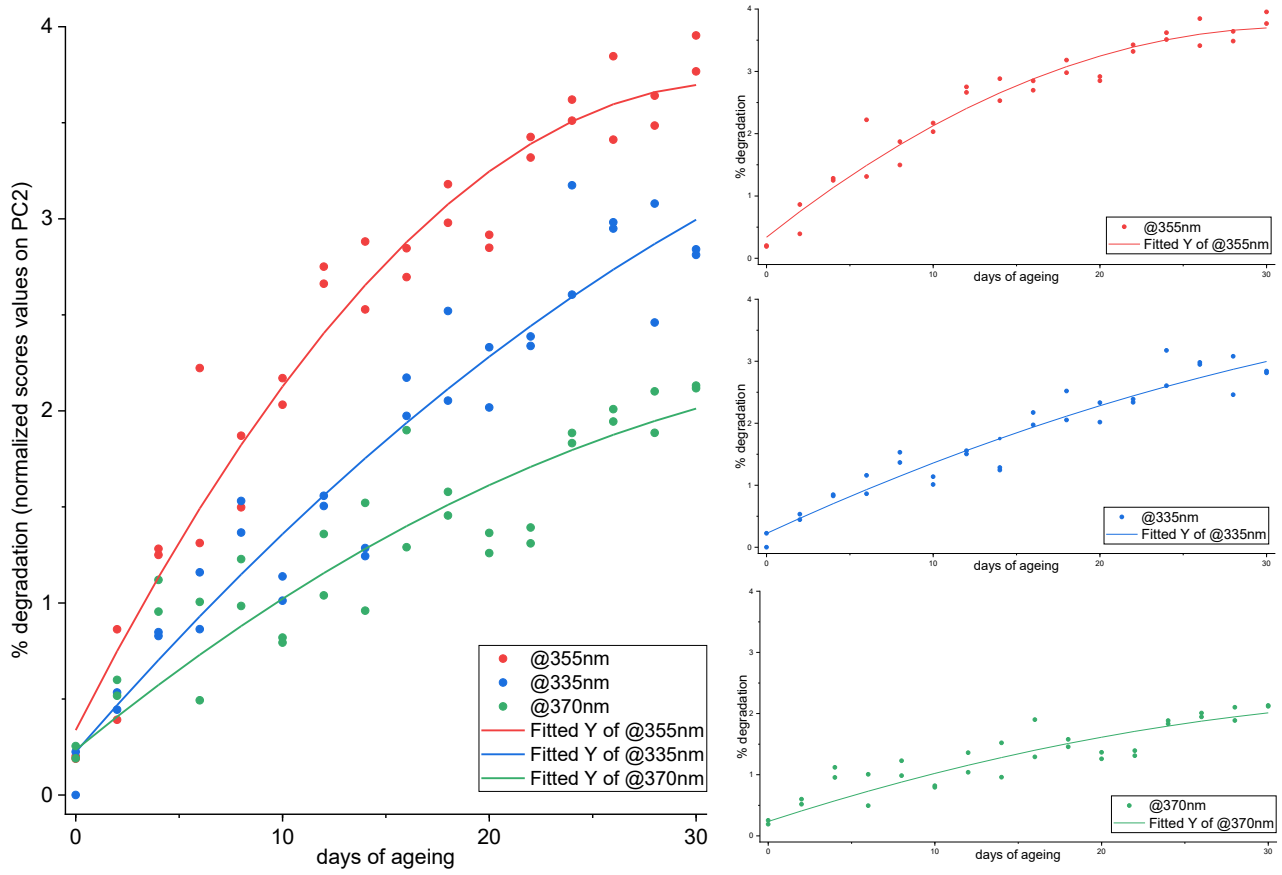

Figure 24. Normalized scores values against days of ageing

The normalized scores values of PC2, which can be considered an indicator of extent of degradation, are plotted against the days of ageing in Figure 24. For the sake of clarity, a reduced number of samples is shown. The trends for the 3 lamps are asymptotic exponential,

with the UVA355nm lamp showing the highest values of degradation %, followed by UVA335nm. The slope of the trend corresponding to UVA370nm is not as deep.

3.5.3 Oxidative change

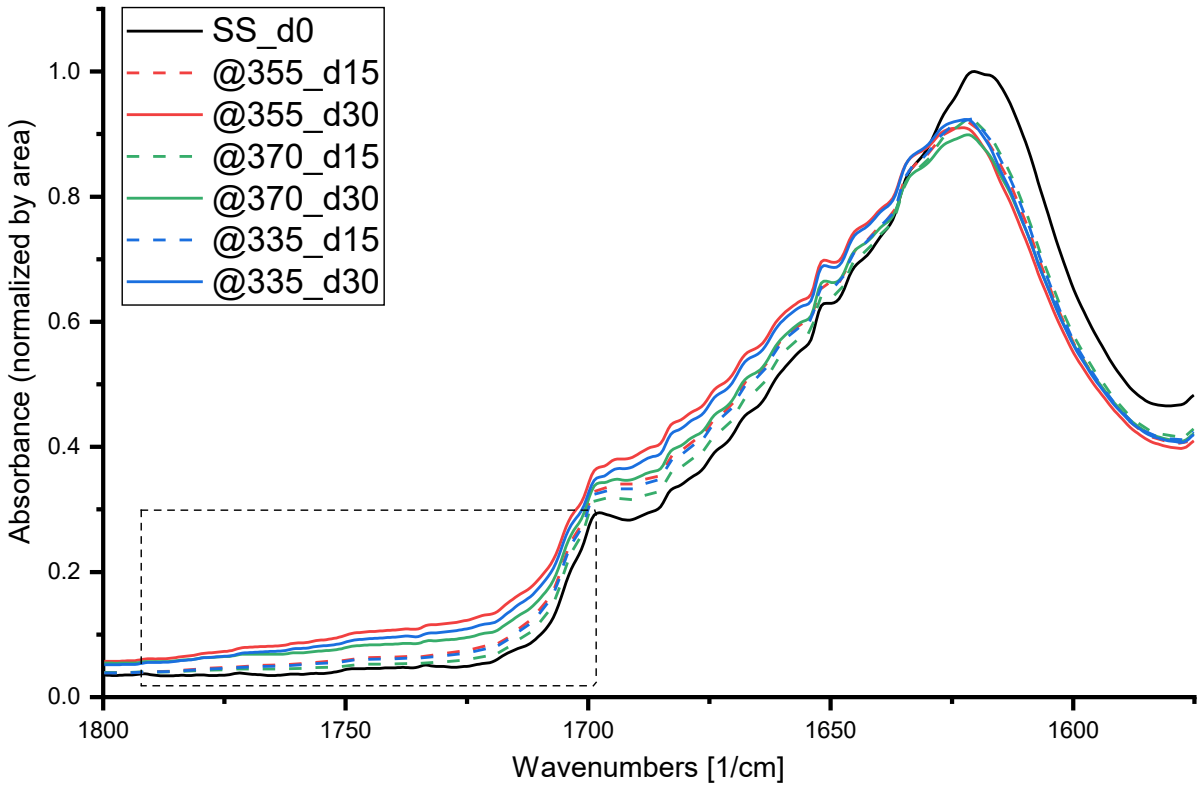

Figure 25. ATR-FTIR spectra for SET B samples (range 1800-1575 cm^{-1}). The oxidation products region is highlighted.

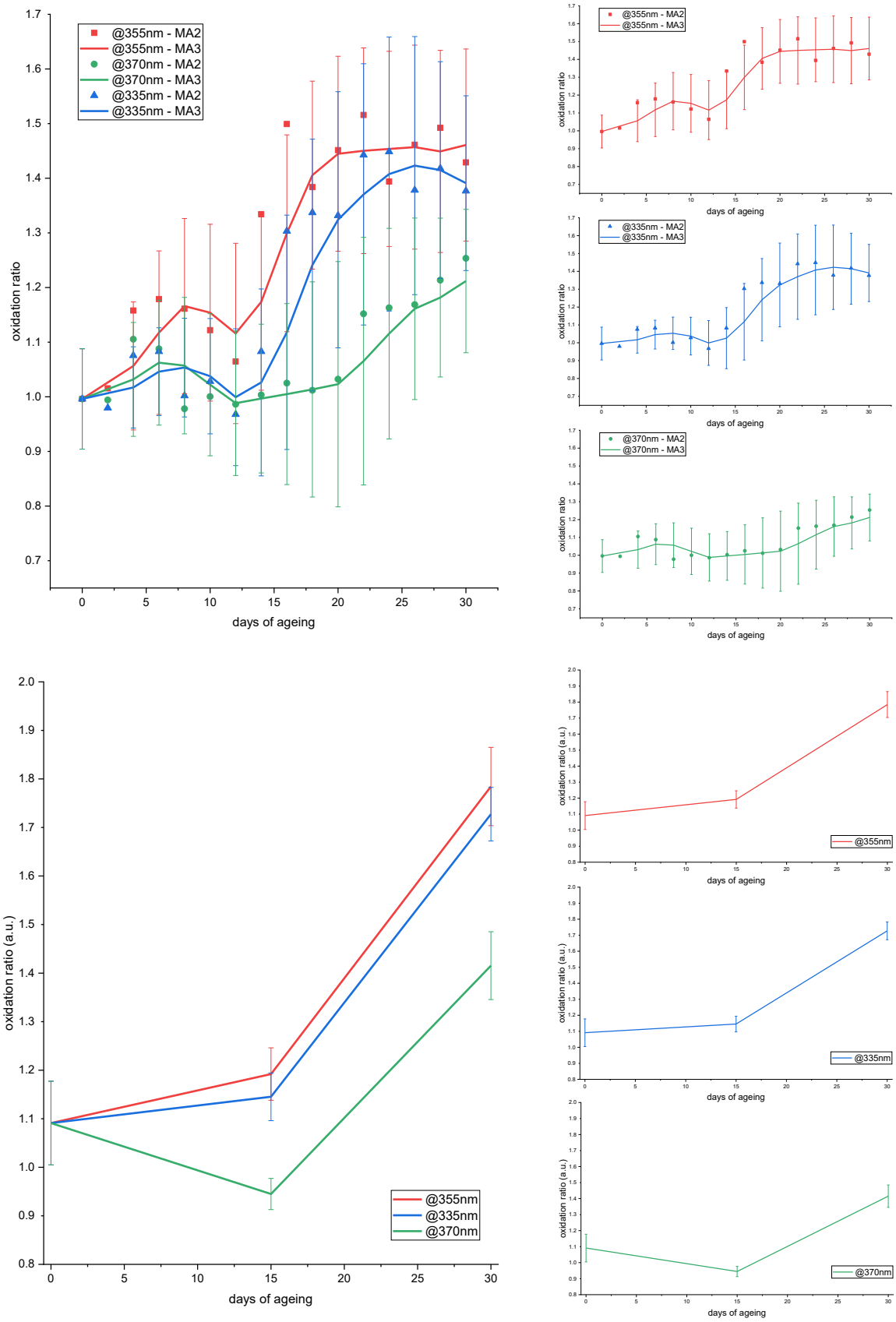

Figure 26. Upper image: Oxidation ratio values of SET A plotted against days of ageing; Lower image: Oxidation ratio values of SET B plotted against days of ageing

Figure 25 shows the averaged ATR-FTIR spectra for the samples of SET B. The region corresponding to C=O bond in oxidation products is highlighted. Oxidation products encompass dityrosine, dicarboxylic aminoacids and α-ketoacids [18]. In particular, α-ketoacids exhibit three overlapping signals at 1736 cm^{-1}, 1720 cm^{-1}, and 1704 cm^{-1} which correspond to carboxylgroups that participate in 0, 1, or 2 hydrogen bonds [19]. Thus, the formation of α-ketoacids due to light ageing can explain the rise of the intensities in the region 1800-1700 cm^{-1}, as clearly appear in the plots.

Several studies have proposed indicators of oxidation in this region [18,20–23]. In this work, the ratio between the intensity at 1725 cm^{-1}, representing the concentration of α-ketoacids, and the intensity at 1900 cm^{-1}, which is considered constant, are considered. Thus, oxidation ratio represents the rise of the oxidation products at 1725 cm^{-1}. Figure 26 shows the calculated oxidation ratios plotted against the days of ageing. The data taken from the SET A show high variability, as confirmed by the standard error (95%). To better visualize the trend, moving averages are shown instead of data points by creating a series of averages of different selections (2 or 3) of the original data.

To get more precise data, original data from SET B are presented as well. In this case, the standard error (95%) calculated over 32 replicates is much lower.

In both cases, the trends slowly increase in the first 15 days of ageing, and then appear to be asymptotic exponential reaching a plateau in samples aged under UVA355nm and UVA335nm. The rate of rising of the UVA 370nm trend is slower and quite linear. In Baltova's and Vilaplana's works, the rise of the index is deeper in the first days of ageing [1,20]. However, their study is limited to few days, so it can be consistent with the trend shown by UVA355nm, where a local maximum appears before day 10.

A two-stages trend can be assumed. For the first part, the presence of an induction period [22] can be hypothesized. For the asymptotic exponential trend, a different mechanism can be proposed [1]. The trend reaches a plateau because the rate of α-ketoacyl group formation is retarded. The cause cannot be the exhaustion of the polymer. The reason should be related to the accumulation of α-keto acids on the surface of the fibre. As they strongly absorb in the range 270-330 nm [1,24], they are competing with the polymer, so that the photochemical reaction rate leading to their formation is decreased. This 'filtration effect' due to the accumulation of the degradation products on the surface layer of the polymer can protect the bulk polymer slowing down the oxidation rate.

3.5.4 Amide II change

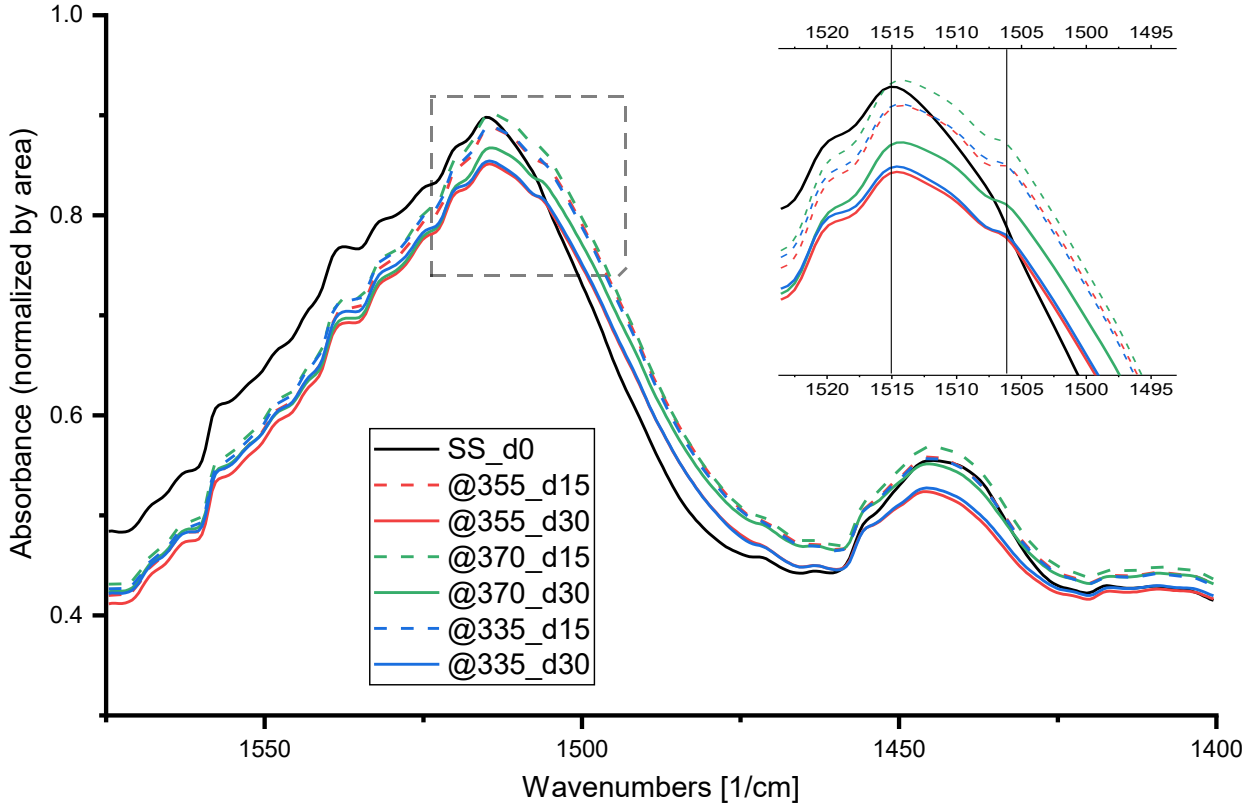

Figure 27. ATR-FTIR spectra for SET B samples (range 1575-1400 cm^{-1}). The region where the signals of tyrosine and dopamine is highlighted.

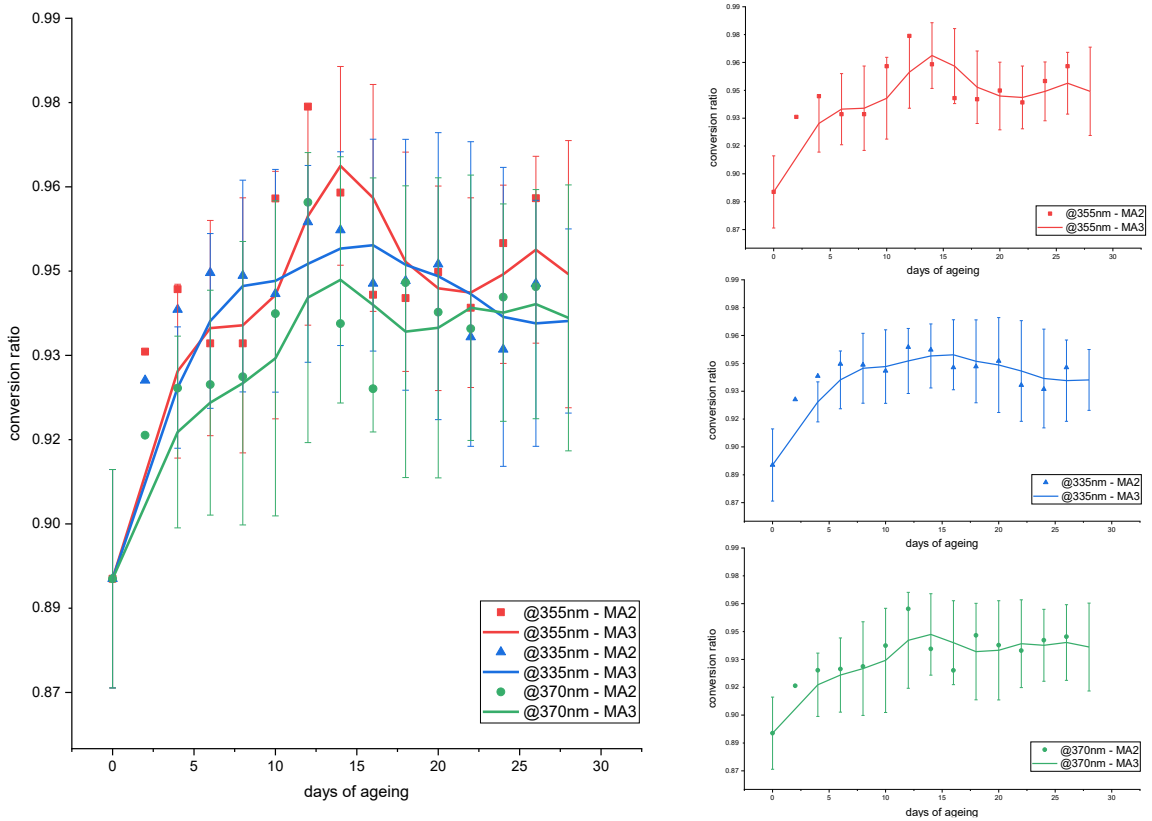

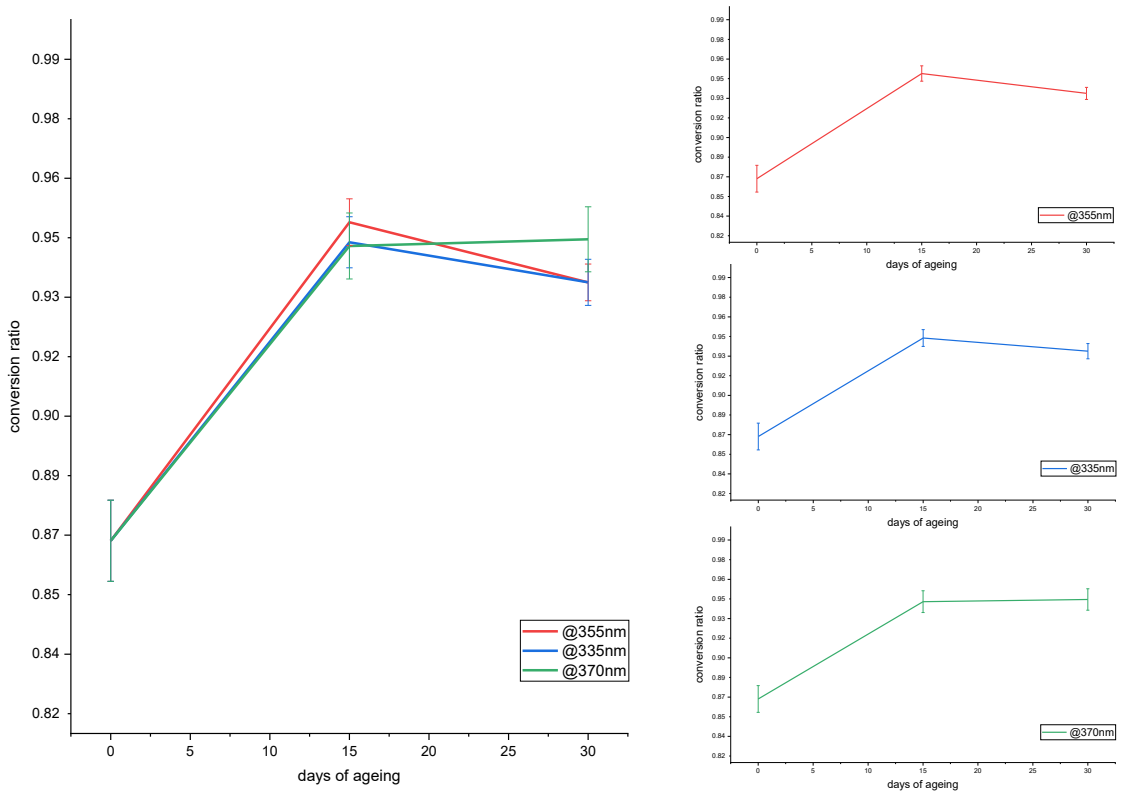

Figure 28. Upper image: Conversion ratio values of SET A plotted against days of ageing; Lower image: Conversion ratio values of SET B plotted against days of ageing

Figure 27 shows the averaged ATR-FTIR spectra for the samples of SET B. The region where the signals of tyrosine and of its degradation product dopamine is highlighted. Tyrosine shows in this region two absorption bands, one at 1555 cm^{-1} which is broad and weak, and the other at 1516 cm^{-1} which is very intense [6]. The amide II peak which appears at around 1510 cm^{-1} originates from the overlapping of the β-sheets signal at 1508 $cm^{-}1$, of the tyrosine peak at 1516 cm^{-1} and of the signals from tyrosine oxidation products, mainly dopamine (DOPA) [25,26], which shows a strong peak at 1506 cm^{-1} and o-quinone derivatives which forms from DOPA [27]. The highlighted area in the plot shows that, as degradation takes place, the peak at 1506 cm^{-1} grows while the peak at 1516 cm^{-1} decreases. Thus, the conversion ratio represents the conversion of tyrosine into dopamine.

Figure 28 shows the calculated conversion ratios plotted against the days of ageing. The data taken from the SET A show high variability, as confirmed by the standard error (95%). To better visualize the trend, moving averages are shown instead of data points by creating a series of averages of different selections (2 or 3) of the original data. To get more precise data, original data from SET B are presented as well. In this case, the standard error (95%) calculated over 32 replicates is much lower.

In all cases, the trends are asymptotic exponential, as the maximum value is reached after the first 15 days of ageing. Tyrosine is known to be very sensitive to light, so it is not surprising that its conversion is very fast, as reported by various authors [8,20,26,28–30]. In particular, the

shape of the trend is consistent with a previous work [27] measuring the oxygen uptake of a solution of fibroin.

3.5.5 Thermal analysis

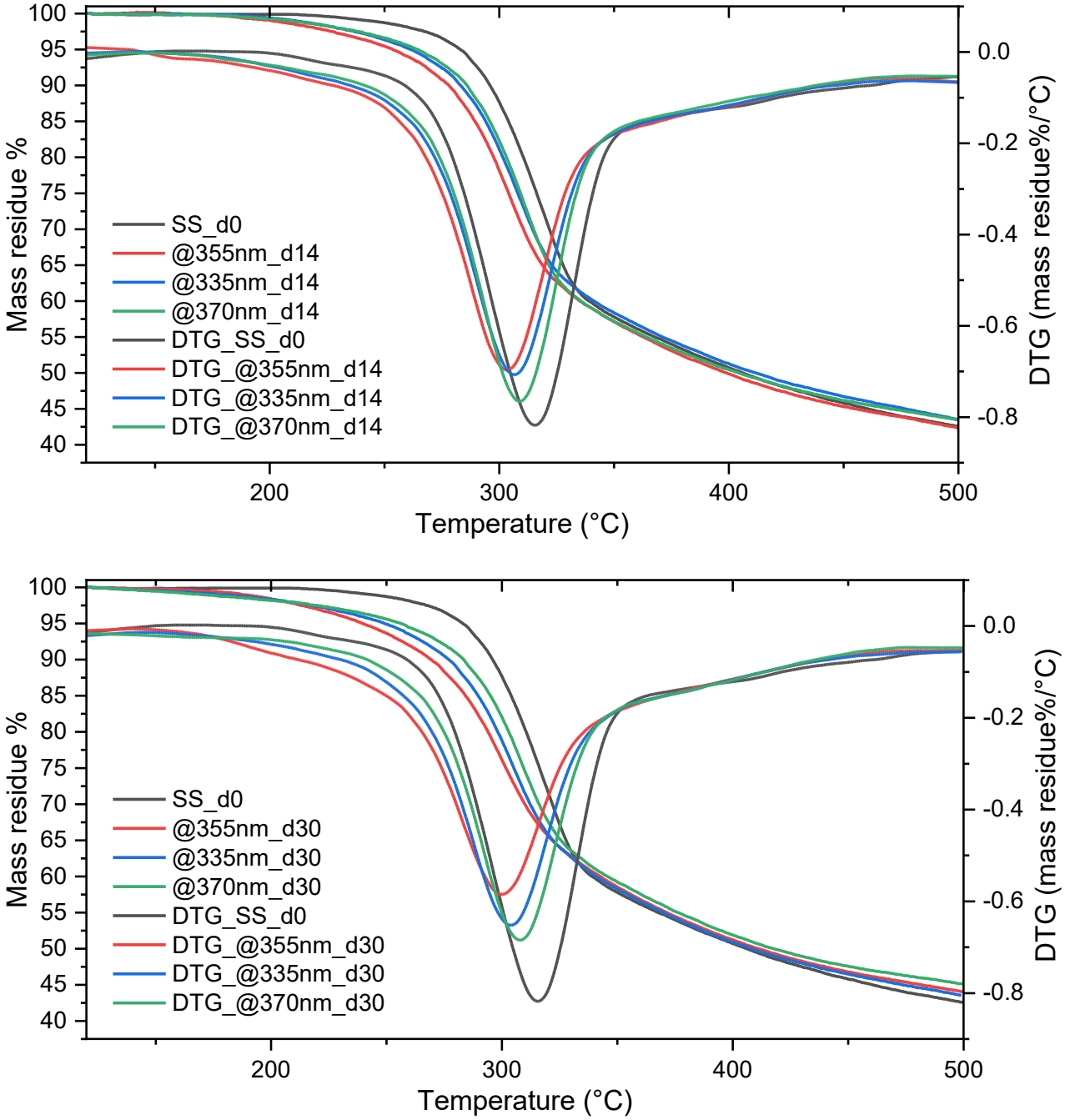

Figure 29. TG and DTG plot for SET A samples (days of ageing: 0, 14, 30)

Figure 29 depicts the plots obtained from thermogravimetric analysis. According to the TGA curves, thermal decomposition of pristine silk displays three main decomposition stages: the first step, a slight mass decrease due to the loss of moisture, from 25°C to 120°C (not shown); the second, an abrupt decomposition step from 260 to 350°C; and the third, from 350 to 500°C,

attributed to thermal degradation of a well-oriented β-sheet crystalline conformation [31–33]. The differential weight loss (DTG) curves provide clear evidence for the main degradation step.

According to specific literature [8,17,30,34], aged silk shows a shift of the temperature corresponding to the maximum decomposition rate of silk, from 315°C to lower temperatures. Kweon [32] demonstrated that such changes in the thermal decomposition behavior are not related to the modifications in conformation during ageing. However, the decomposition temperature was found to correlate with crystallinity and molecular orientation [8,33,35]. The higher the crystallinity and the degree of molecular orientation were, the higher the decomposition temperature. In the present analyses, the shift in T_{max} correlates nicely with the data available about the crystallinity index.

The primary and rapid decomposition event (260–350 °C) corresponds to the thermal breakdown of amino acids. During this stage, condensation, deamination, and decarboxylation reactions occur simultaneously, resulting in the cleavage of polypeptide bonds [36]. For instance, glycine begins to decompose at approximately 260 °C, releasing H_2O, NH_3, and CO_2, with the maximum decomposition rate occurring at 308 °C - closely aligning with the decomposition temperature of silk [37]. The overall thermal stability of silk is influenced by its amino acid composition, as individual amino acids exhibit slightly different thermal stabilities [38]. Notably, the side-chain groups of amino acid residues within the amorphous regions of silk are believed to decompose first [36].

Between 120°C and 260°C, silk mainly undergoes structural modification. The rise in temperature above 200 °C gives to the polypeptide chains sufficient mobility for various processes to occur, such as melting, chain rearrangement and crystallization. These modifications are detectable by DSC studies [36], but no mass loss occurs in pristine silk. The onset of weight loss starts at about 210 °C, with a mass loss of around 2.5% at 260 °C. Previous studies showed that in these temperature range only low molecular weight gases, such as water, carbon dioxide and ammonia are produced [36]. We can define this stage as slow decomposition event. As ageing proceeds, the mass loss values at 260 °C increases to 6% for @355nm_d14 and 8% for @355nm_d30. As a separate mass loss stage cannot be identified in this range, the decomposition of a number of different compounds evidently takes place. Based on literature [18,39–41], this distribution includes fragments from degraded amino acids and hydroperoxides, which are the proteins main degradation products due to the combined action of UV light and oxygen. The work of Vagkidis [41] demonstrated that hydroperoxides formed as a result of the UV action from peptides easily decompose upon heat treatment. The accumulation of a wide variety of oxidation products can explain why aged samples show increased mass loss before 260 °C. The hypothesis is supported by a previous thermal study of aged leather, which behaves similarly to silk [42]. The decomposition of aged samples starts at lower temperature than the new one, indicating the decreased thermal stability of aged leather. In particular, evolved gases are analyzed during the thermogravimetric analysis under inert conditions, revealing that a considerable amount of CO_2 is produced before 260°C. The

increased production of CO_2 is attributed to the partial oxidation of the samples during the natural and artificial ageing.

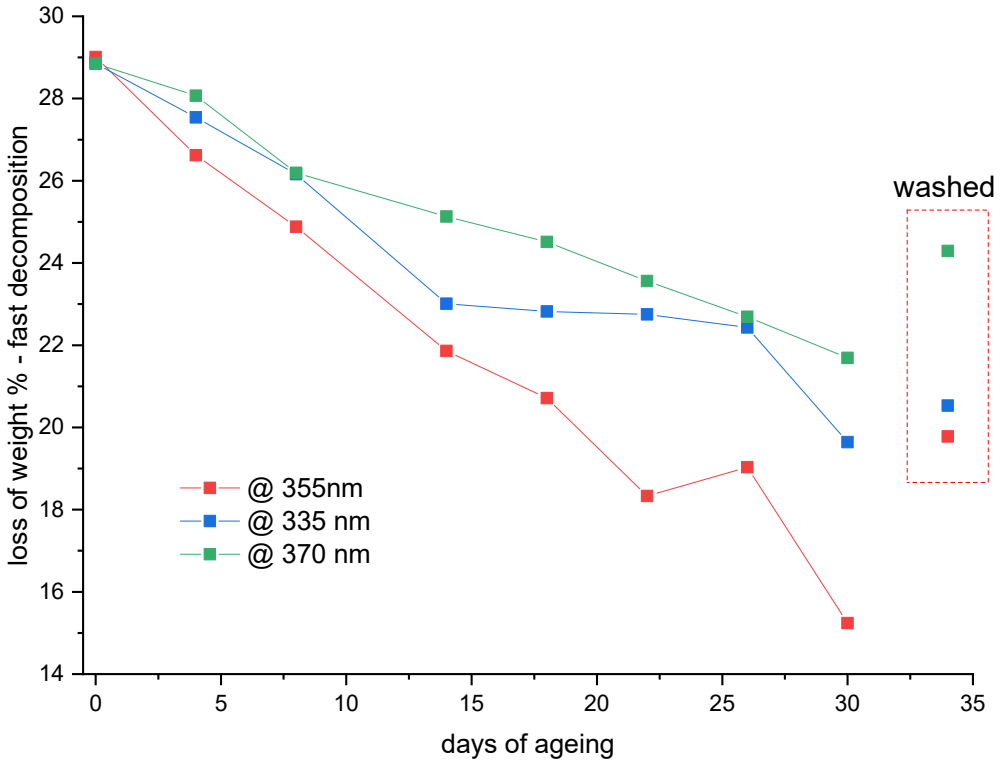

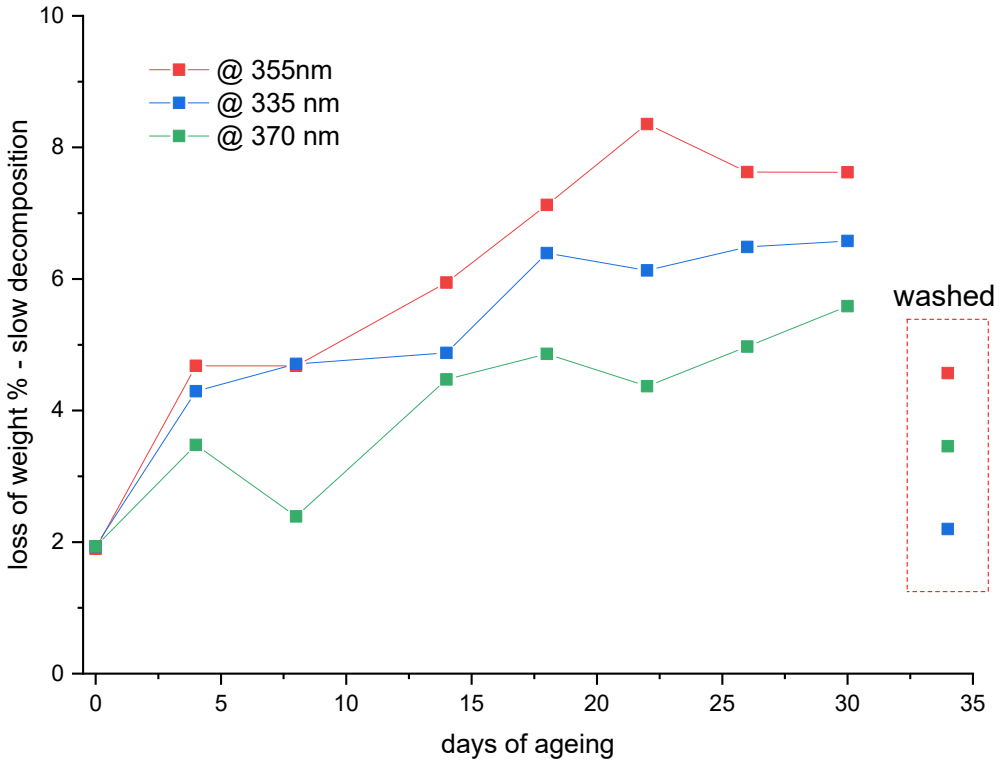

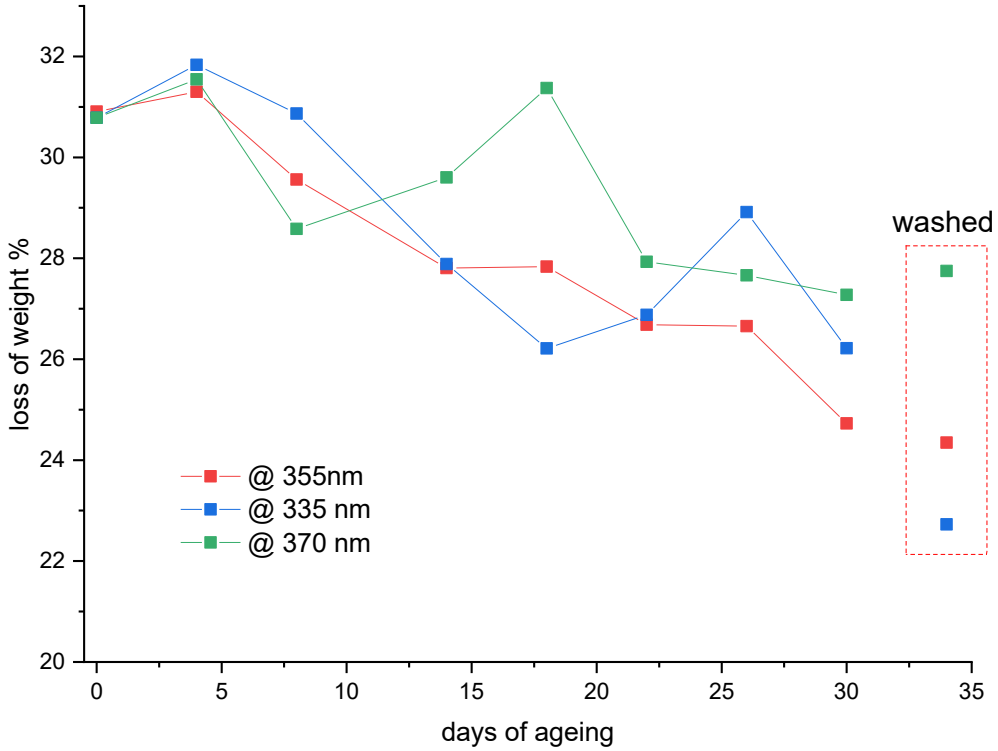

Figure 30. Trends of the weight loss % for the fast decomposition event (260-350°C) (upper); for the slow decomposition event (120-260°C) (central); for the whole range (120-350°C) (lower)

Temperature is not the only parameter affected by ageing. The percentage weight loss corresponds to the area under the DTG peak, calculated using the method described in the *Experimental Parameters* section. In Figure 30 (upper image), the trends of weight loss percentage during the fast decomposition event (260–350 °C) are reported. Notably, weight loss decreases as ageing progresses, with different light sources causing varying degrees of mass loss. In contrast, the slow decomposition event (120–260 °C) exhibits opposite trends (Figure 30, central image). Despite the total residue mass being similar across all samples (Figure 29), the combined weight loss from both the fast and slow decomposition events declines with ageing (Figure 30, lower image). Although the slow decomposition phase partially compensates through mass gain, the overall balance still indicates a net mass decrease. This observation suggests that the thermal stability of aged silk increases with respect to pristine silk. An explanation can involve the modification of amino acid composition of silk over prolonged exposure to light - a hypothesis consistent with previous studies reporting alterations in pristine silk's amino acid profile [28,35,43].

As irradiation time increases, mass loss is associated with the release of ammonia gas resulting from photochemical reactions. Amino acids with hydroxylated and ionizable side chains - such as serine, phenylalanine, and tyrosine - undergo significant reduction during UV ageing. These amino acids are partially converted into oxidized by-products, like DOPA, or volatile compounds such as ammonia [28,35]. Consequently, the amino acid composition of aged silk differs substantially from that of pristine silk, with a relative increase in aliphatic amino acids,

which exhibit greater thermal stability. Therefore, the observation of lower total mass loss in aged samples compared to pristine silk is expected, because in aged samples selective destruction of amino acids makes them not available for thermal decomposition.

The increasing trend in mass loss during the slow decomposition event is attributed to the accumulation of oxidized products as ageing progresses. A plateau appears to be reached after approximately 20 days, consistent with the previously discussed filtration effect [1]. As α-keto acids - strongly absorbing in the 270–330 nm range [1,24] - accumulate on the fibre surface, they compete with the polymer for incident radiation, thus decreasing the photochemical reaction rate responsible for their formation.

A further test was set up, where the extraction of silk samples was carried out in deionized water. Previous studies have shown that aging silk makes it more soluble in water, ethanol and urea solutions [17,28]. It is expected that the process results in the extraction of degradation products. 30-day aged silk was soaked in deionized water, drained and left to dry. As hypothesized, washed silk behaves similarly to less-aged silk, as demonstrated by the loss of weight % values shown in Figure 30. In previous studies [17,28], the recovered residues were studied and showed broad molecular weight distribution profiles and amino acid composition consistent with silk. Both are evidence for the cleavage of the peptide bonds. Other works using SEC and SDS-PAGE experiments showed that silk degradation is characterized by the formation of a wide distribution of peptides [3,28,44,45]. As a result, oxidation and depolymerization are correlated and both take place during the ageing of silk.

Data coming from DTG curves are rationalized using an equation proposed by Bakyrtzis [46]. He used a mathematical technique based on the observation that the DTG profile peaks become less pronounced and are shifted to lower temperatures when a fire retardant is added to a lignocellulosic polymer. As the behavior is similar to the trend observed during the ageing of silk, the same equation was employed, using the following parameters: the depth of the main peak; (ii) the main decomposition peak temperature; (iii) the temperature range of the DTG curve; and (iv) the area above the curve. The details of the calculation are reported in the *Experimental parameters* section. The result of the computation is the extent of degradation (E%), which is reported against days of ageing in Figure 31. All the lamps are characterized by a linear trend, where the slope is greater for UVA355nm, followed by UVA335nm and eventually UVA370nm.

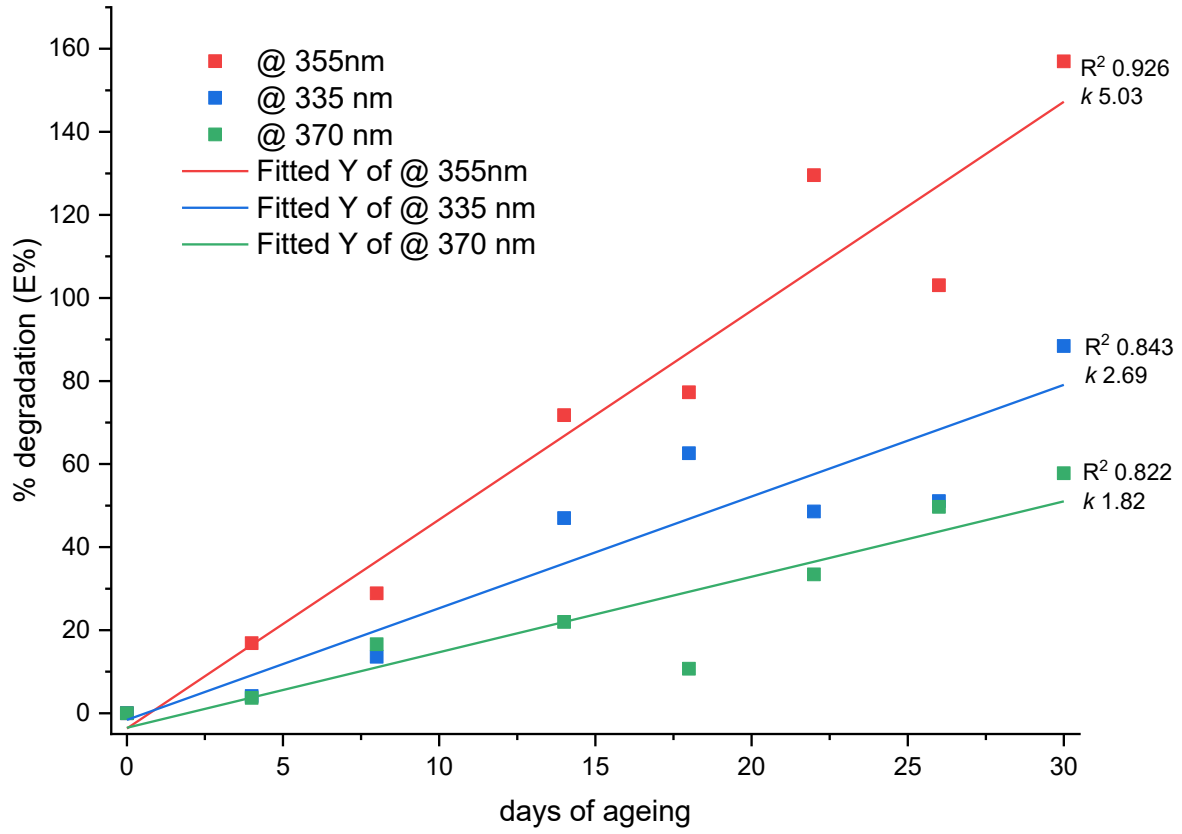

Figure 31. Degradation % obtained from TGA data against days of ageing.

3.5.6 Ageing trends versus colour change

In this section, the goal is to evaluate which lamp causes the most significant damage to silk fibers during accelerated aging procedures. One common method for comparing the effects of different aging procedures is to correlate the rate of change of a specific degradation indicator (like yellowing or tensile strength) with chemical or structural processes within the material, rather than simply tracking time [47].

This approach is widely used in scientific studies to assess material degradation. For example, it is common to correlate changes in tensile strength or yellowing to the percentage of tyrosine present in the silk, as explored by some authors [26,29,48].

In this case, yellowing—measured by b* values—was selected as a key indicator of aging due to its visual prominence. Figure 32 shows correlation plots of yellowing against various indicators, revealing that UVA355nm causes the most significant degradation, even though yellowing is more pronounced under UVA 335 nm. Both UVA 355 nm and UVA 335 nm exhibit similar exponential trends, with high R^2 values, indicating strong correlations. On the other hand, UVA 370 nm displays a more gradual, almost linear trend with a much lower R^2 value, suggesting that it is less effective in accelerating silk degradation.

Interestingly, there is a clear linear correlation between the conversion ratio and yellowing, suggesting that the formation of dopamine is strongly associated with the yellowing process in silk. This observation aligns with previous findings [26,29,48], the conclusion that dopamine formation is a significant factor in silk fibre degradation.

YELLOWING (B VALUES) VS SHIFT RATIO*

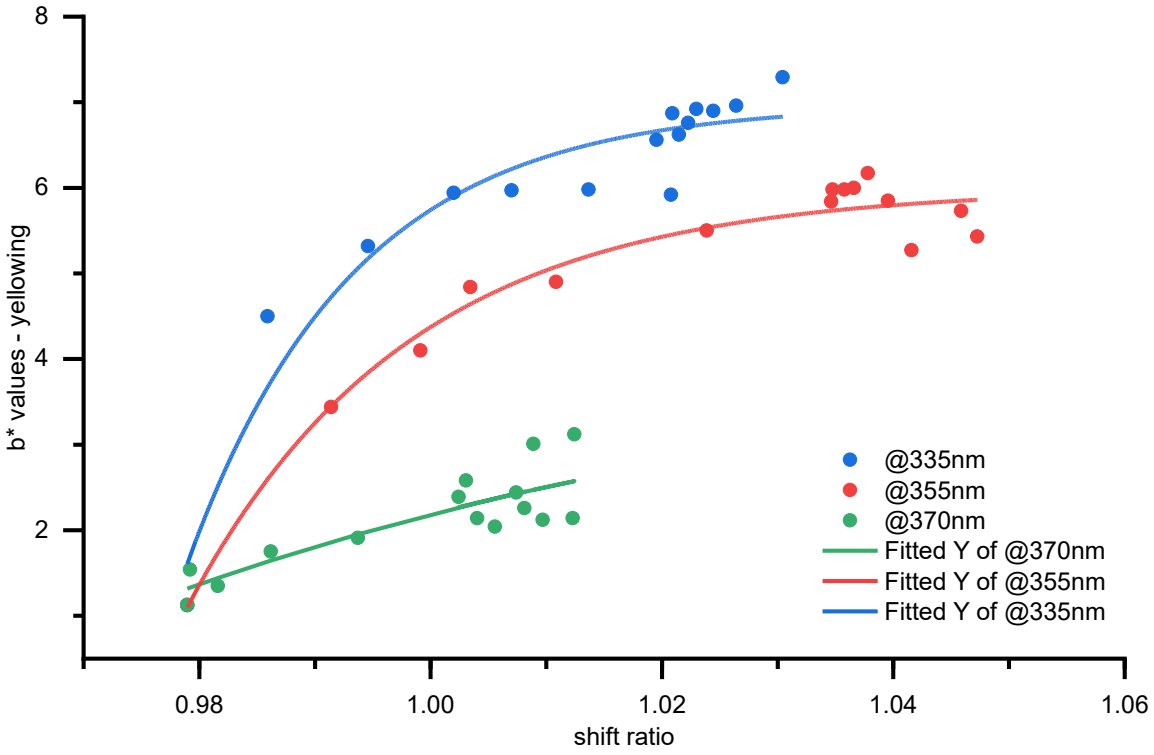

YELLOWING (B* VALUES) VS OXIDATION RATIO

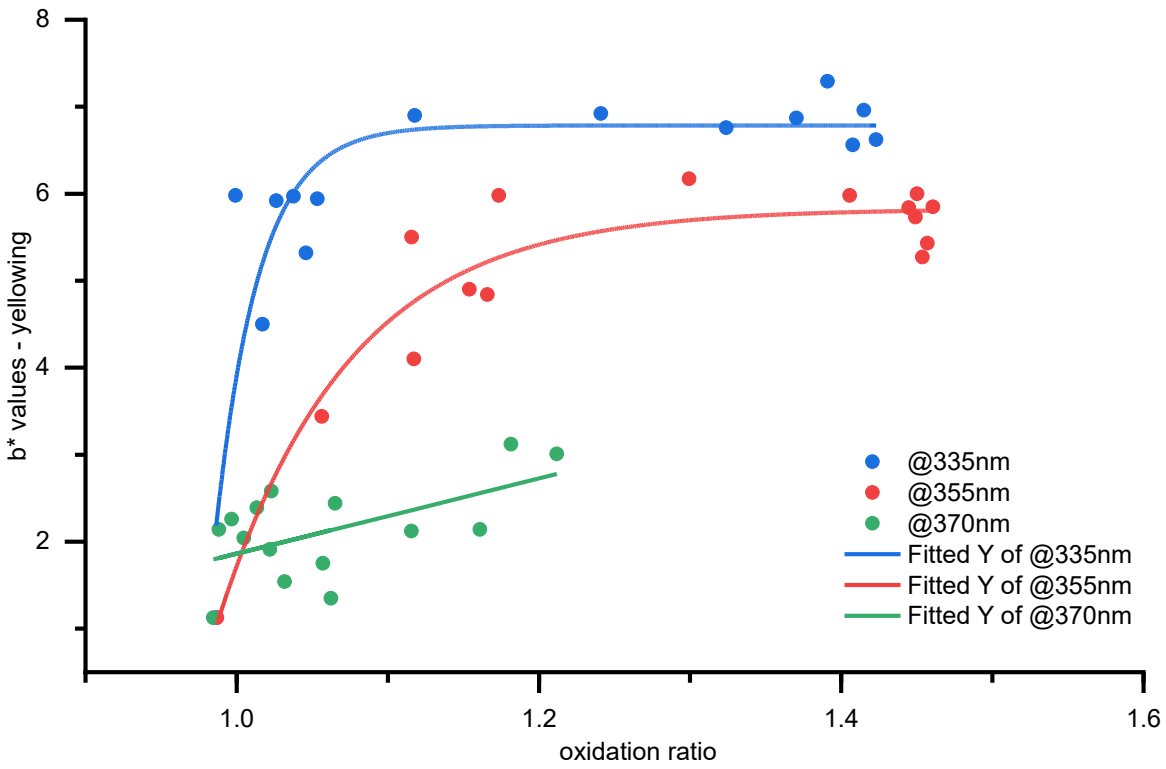

YELLOWING (B* VALUES) VS CONVERSION RATIO

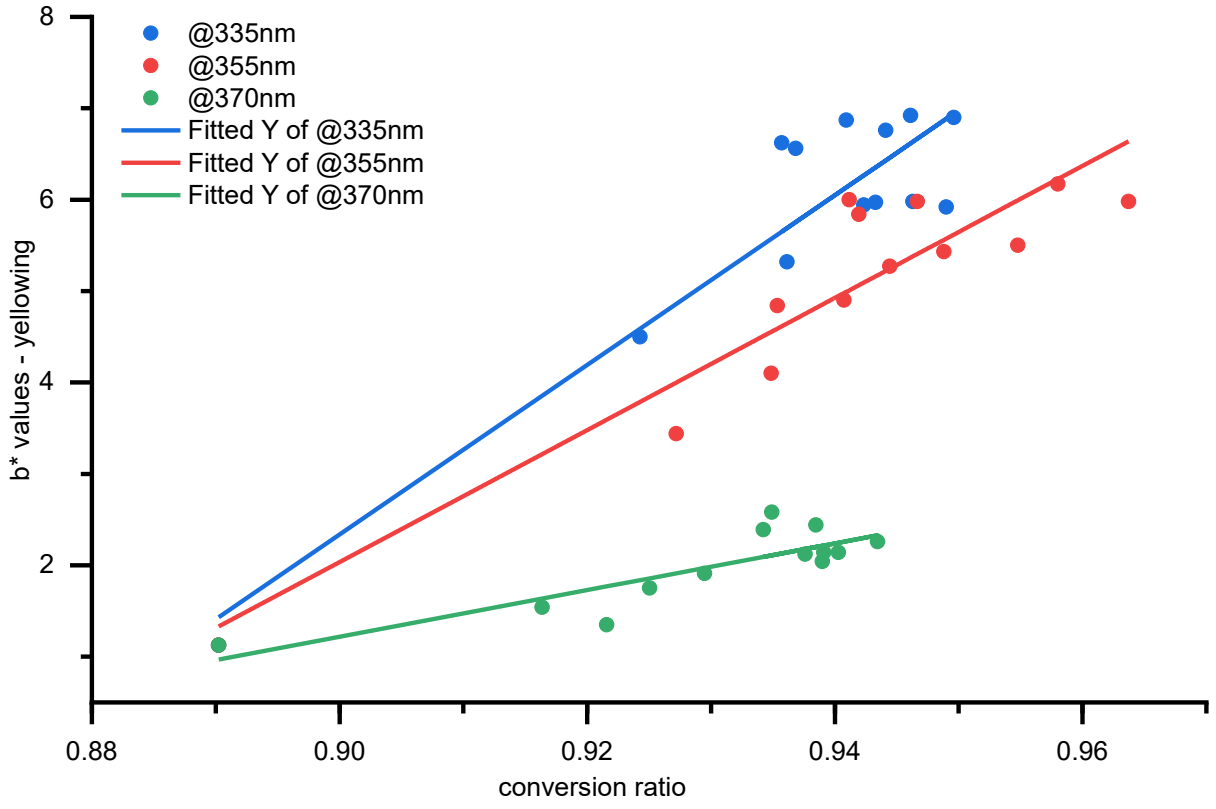

YELLOWING (B VALUES) VS % DEGRADATION (SCORES PC2)*

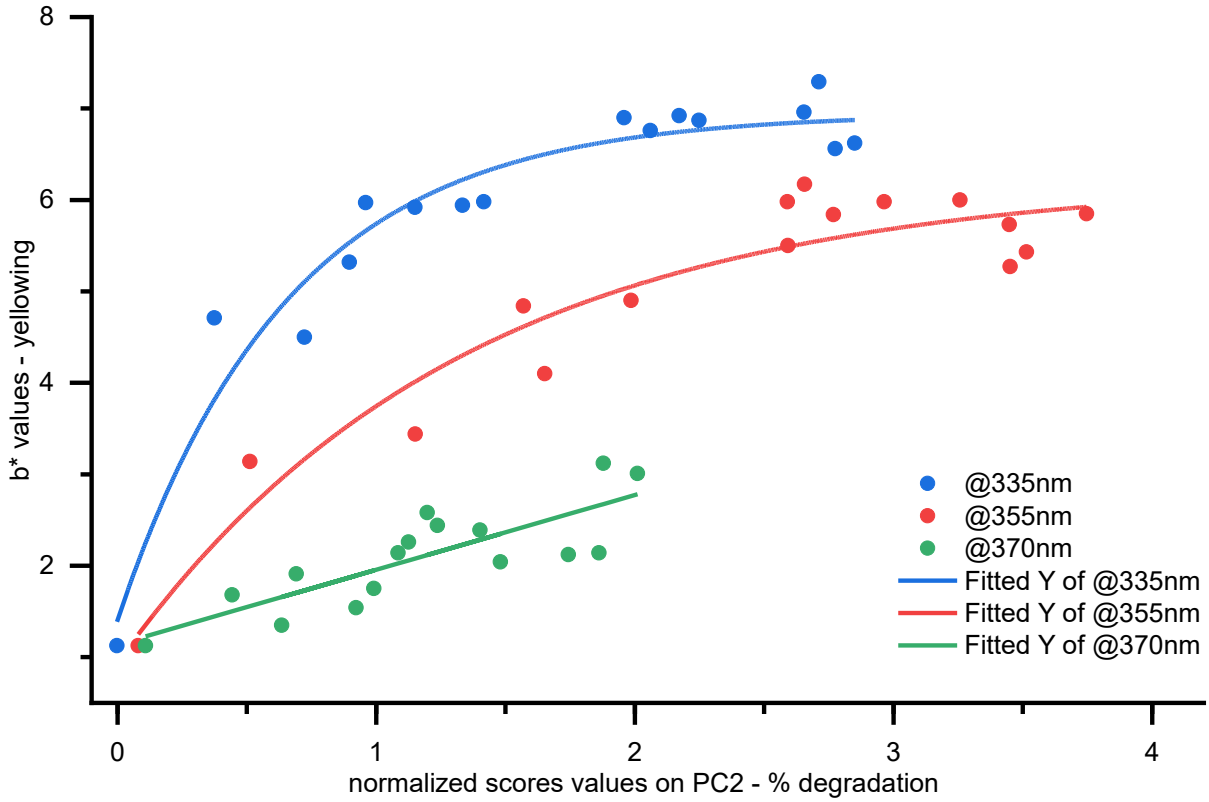

YELLOWING (B VALUES) VS EXTENT OF DEGRADATION (E%)*

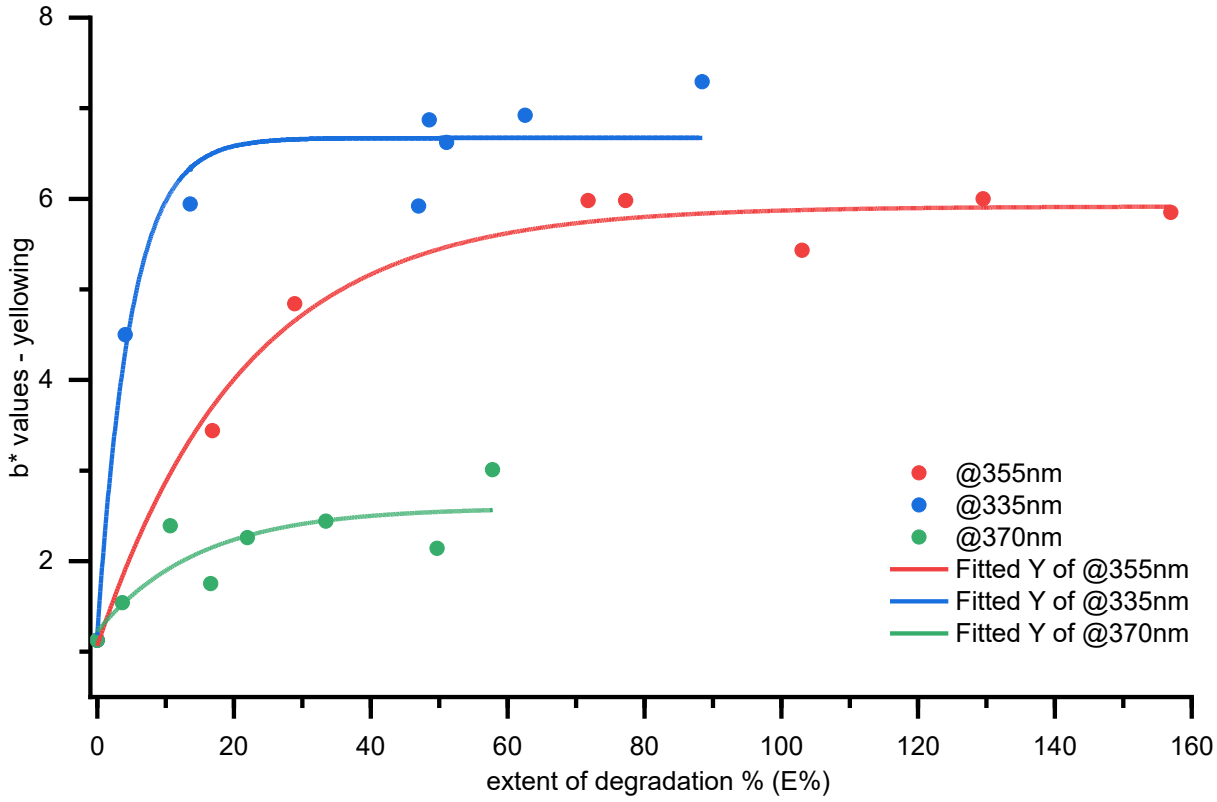

Figure 32. Correlation plots of yellowing (b values) against different indicators: shift ratio, oxidation ratio, conversion ratio, degradation % obtained from PC2 scores, extent of degradation % obtained from TGA (E%).*

3.5.7 Conclusion

Colour Change and Yellowing

The results from colorimetric analysis indicate that both UVA355nm and UVA335nm lamps induce significant yellowing of the silk samples, as demonstrated by the ΔE and Δb* values. These lamps exceeded the ΔE threshold of 3, indicating visible changes in colour after ageing. Notably, UVA335nm caused the most pronounced yellowing, with the data suggesting an initial rapid change, followed by slower increases as ageing progressed. This trend is consistent with previous studies and highlights the significant role of UV exposure in accelerating yellowing process.

Structural Changes

The structural changes observed through ATR-FTIR spectroscopy and X-ray diffraction support the notion that UV exposure leads to the breakdown of silk's crystalline and non-crystalline domains. The shift in the amide I peak from 1617 cm-1 to 1625 cm-1, along with the increased intensity between 1700-1650 cm-1, indicates a loss of crystalline β-sheet structures and an increase in random coil and α-helix conformations. XRD data further corroborates these findings, with a decrease in crystallinity index and a shift in diffraction peaks suggesting the transformation of silk's structural domains. These changes highlight how UV ageing degrades the silk's molecular structure, accelerating the breakdown of its extended chain and

random coil structures, while simultaneously reducing its crystallinity. This mechanism appears to be the same for all the lamps, as their trends are quite similar. UVA355nm induces the highest shift ratio values, followed by UVA335nm and finally UVA370nm.

Oxidative Degradation

The ATR-FTIR data indicates that UV exposure promotes oxidation in silk fibres, particularly under UVA355nm and UVA335nm wavelengths. Initially, there is a slow rise in oxidation over the first 15 days, followed by a stage of rapid increase until a plateau is reached. This pattern suggests that as degradation products like α-ketoacids accumulate on the surface, further oxidation slows down. The conversion of tyrosine into dopamine also follows a similar trend, but it occurs much faster, with the maximum conversion happening within the first 15 days. This behavior suggests a two-stage mechanism for UV-induced degradation: first, UV light triggers the rapid oxidation of tyrosine, and once the readily accessible sites for this oxidation are depleted, the rate of backbone oxidation increases, leading to the formation of α-ketoacids. This competitive process sheds light on the photooxidative pathway that significantly contributes to silk aging under UV exposure.

Thermal Analysis

TGA and DTG results indicate that UV-induced ageing leads to a shift in decomposition temperature towards lower values, correlating with a reduction in the mass of amino acids with hydroxylated and ionizable side chains, such as serine, phenylalanine, and tyrosine. They partially transform into volatile gases (H_2O, NH_3, CO_2) and oxidation products such as DOPA and hydroperoxides. The observed decrease in the weight loss percentage during the fast decomposition event (260-350°C) and the increase in weight loss during the slow decomposition event (120-260°C) further support this conclusion. The degradation trends are linear across all UV lamps, with UVA355nm causing the most significant degradation, followed by UVA335nm and UVA370nm.

Comparative Damage by UV Lamps

Overall, comparing the different UV lamps, it is evident that UVA355nm causes the most severe damage to both the structure and appearance of silk fibres, followed closely by UVA335nm. These two lamps show accelerated degradation, as evidenced by colour change, structural breakdown, and oxidative and depolymerization processes. UVA370nm, while still causing measurable damage, induces less significant changes and at a slower rate. Overall, the findings suggest that UVA355nm is the most aggressive in terms of ageing silk, while UVA370nm appears to be the least harmful among the tested UV sources.

The results were unexpected, as exposure to UVA355nm - representing typical indoor aging conditions - proved to be more harmful to silk than UVA335nm, which is commonly used to simulate outdoor aging. Contrary to the general assumption that lower wavelengths induce greater damage, this relationship does not hold in this case, except in terms of silk yellowing. These findings demonstrate that silk degradation is strongly wavelength dependent.

Additionally, when exposed to UVA370nm, the rates of degradation indicator modifications were significantly slower, particularly for oxidation-related markers. While the overall

degradation trends followed a similar trajectory, the UVA370nm lamp proved ineffective for rapid accelerated aging.

3.5.8 References

[1] S. Baltova, V. Vassileva, E. Valtcheva, Photochemical behaviour of natural silk-I. Kinetic investigation of photoyellowing, 1998.

[2] Y. Gong, G. Zhou, C. Qiao, Y. Pan, Study on the photodegradation behaviors of thermal-aged silk, Herit Sci 12 (2024). https://doi.org/10.1186/s40494-024-01270-w.

[3] M.A. Koperska, D. Pawcenis, J.M. Milczarek, A. Blachecki, T. Łojewski, J. Łojewska, Fibroin degradation - Critical evaluation of conventional analytical methods, Polym Degrad Stab 120 (2015) 357–367. https://doi.org/10.1016/j.polymdegradstab.2015.07.006.

[4] R. Dang, F. Zhang, D. Yang, W. Guo, G. Liu, Spectral damage model for lighting paper and silk in museum, J Cult Herit 45 (2020) 249–253. https://doi.org/10.1016/j.culher.2020.03.001.

[5] M.A. Koperska, T. Łojewski, J. Łojewska, Evaluating degradation of silk's fibroin by attenuated total reflectance infrared spectroscopy: Case study of ancient banners from Polish collections, Spectrochim Acta A Mol Biomol Spectrosc 135 (2015) 576–582. https://doi.org/10.1016/j.saa.2014.05.030.

[6] L. Geminiani, F.P. Campione, C. Corti, B. Giussani, G. Gorla, M. Luraschi, S. Recchia, L. Rampazzi, Historical silks: a novel method to evaluate their condition with ATR-FTIR spectroscopy and Principal Component Analysis, J Cult Herit 67 (2024) 9–22. https://doi.org/10.1016/j.culher.2024.01.015.

[7] Y. Gong, Z. Li, J. Hu, G. Zhou, G. Xu, W. Yang, J. Zhang, Insight into the measurements for determining the ageing degree of ancient silk, Polym Degrad Stab 196 (2022). https://doi.org/10.1016/j.polymdegradstab.2022.109833.

[8] X. Zhang, D. Gong, Y. Gong, Insight into the orientation behavior of thermal-aged and historic silk fabrics by polarized FTIR microspectroscopy, J Cult Herit 38 (2019) 53–63. https://doi.org/10.1016/j.culher.2019.02.007.

[9] J. Zhou, X. Zhou, L. Pan, Y. Deng, H. Zheng, Z. Peng, J. Wan, Y. Zhou, B. Wang, Molecular Evidence of Structural Changes in Silk Using Unlimited Degradation Mass Spectrometry, ACS Omega 8 (2023) 34410–34419. https://doi.org/10.1021/acsomega.3c02254.

[10] L.F. Drummy, D.M. Phillips, M.O. Stone, B.L. Farmer, R.J. Naik, Thermally induced α-helix to β-sheet transition in renegated silk fibers and films, Biomacromolecules 6 (2005) 3328–3333. https://doi.org/10.1021/bm0503524.

[11] A. Sinsawat, S. Putthanarat, Y. Magoshi, R. Pachter, R.K. Eby, X-ray diffraction and computational studies of the modulus of silk (Bombyx mori), Polymer (Guildf) 43 (2002) 1323–1330. www.elsevier.com/locate/polymer.

[12] J. Shao, J. Zheng, J. Liu, C.M. Carr, Fourier transform Raman and Fourier transform infrared spectroscopy studies of silk fibroin, J Appl Polym Sci 96 (2005) 1999–2004. https://doi.org/10.1002/app.21346.

[13] T. Asakura, Conformation Characterization of Bombyx mori Silk Fibroin in the Solid State by High-Frequency 13C Cross Polarization-Magic Angle Spinning NMR, X-ray Diffraction, and Infrared Spectroscopy, Macromolecules 18 (1985) 1841–1845.

[14] T. Asakura, J. Yao, 13 C CP/MAS NMR study on structural heterogeneity in Bombyx mori silk fiber and their generation by stretching , Protein Science 11 (2002) 2706–2713. https://doi.org/10.1110/ps.0221702.

[15] T. Asakura, M.P. Williamson, A review on the structure of Bombyx mori silk fibroin fiber studied using solid-state NMR: An antipolar lamella with an 8-residue repeat, Int J Biol Macromol 245 (2023). https://doi.org/10.1016/j.ijbiomac.2023.125537.

[16] X. Luo, J. Wu, A. Intisar, J. Geng, L. Wu, K. Zheng, Y. Du, Study on Light Aging of Silk Fabric by Fourier Transform Infrared Spectroscopy and Principal Component Analysis, Anal Lett 45 (2012) 1286–1296. https://doi.org/10.1080/00032719.2012.673098.

[17] D. Badillo-Sanchez, D. Chelazzi, R. Giorgi, A. Cincinelli, P. Baglioni, Understanding the structural degradation of South American historical silk: A Focal Plane Array (FPA) FTIR and multivariate analysis, Sci Rep 9 (2019). https://doi.org/10.1038/s41598-019-53763-5.

[18] M.A. Koperska, D. Pawcenis, J. Bagniuk, M.M. Zaitz, M. Missori, T. Łojewski, J. Łojewska, Degradation markers of fibroin in silk through infrared spectroscopy, Polym Degrad Stab 105 (2014) 185–196. https://doi.org/10.1016/j.polymdegradstab.2014.04.008.

[19] A.M. Deal, A.E. Smith, K.M. Oyala, G.H. Campolo, B.E. Rugeley, T.A. Mose, D.L. Talley, C.B. Cooley, R.J. Rapf, Infrared Reflection-Absorption Spectroscopy of α-Keto Acids at the Air-Water Interface: Effects of Chain Length and Headgroup on Environmentally Relevant Surfactant Films, Journal of Physical Chemistry A 127 (2023) 4137–4151. https://doi.org/10.1021/acs.jpca.3c01266.

[20] F. Vilaplana, J. Nilsson, D.V.P. Sommer, S. Karlsson, Analytical markers for silk degradation: comparing historic silk and silk artificially aged in different environments, Anal Bioanal Chem 407 (2015) 1433–1449. https://doi.org/10.1007/s00216-014-8361-z.

[21] S. Baltova, V. Vassileva, Photochemical behaviour of natural silk-II. Mechanism of fibroin photodestruction, 1998.

[22] J. Tocháček, Z. Vrátníčková, Polymer life-time prediction: The role of temperature in UV accelerated ageing of polypropylene and its copolymers, Polym Test 36 (2014) 82–87. https://doi.org/10.1016/j.polymertesting.2014.03.019.

[23] X. Zhou, Y. Guo, X. Luo, L. Zhang, M. Wu, W. Zhang, Systematic assessment of the silk deterioration behaviors for silk aging prediction, Polym Degrad Stab 218 (2023). https://doi.org/10.1016/j.polymdegradstab.2023.110532.

[24] R. Dang, Y. Kang, H. Tan, Y. Yang, Color Damage of Visible Light on Plain-Woven Silk in Different Conservation States of Paintings and Calligraphy in Collections, Fibers and Polymers 25 (2024) 235–242. https://doi.org/10.1007/s12221-023-00414-2.

[25] C. Giulivi, N.J. Traaseth, K.J.A. Davies, Tyrosine oxidation products: Analysis and biological relevance, Amino Acids 25 (2003) 227–232. https://doi.org/10.1007/s00726-003-0013-0.

[26] C. Solazzo, J.M. Dyer, S. Deb-Choudhury, S. Clerens, P. Wyeth, Proteomic profiling of the photo-oxidation of silk fibroin: Implications for historic tin-weighted silk, Photochem Photobiol 88 (2012) 1217–1226. https://doi.org/10.1111/j.1751-1097.2012.01167.x.

[27] G.D. Kang, K.H. Lee, Crosslinking reaction of Phenolic Side Chains in silk fibroin by Tyrosinase, Fibers and Polymers 5 (2004) 234–238.

[28] M.A. Becker, N. Tuross, Initial Degradative Changes Found in Bombyx mori Silk Fibroin , (1993) 252–269. https://doi.org/10.1021/bk-1994-0544.ch022.

[29] X. Zhang, I. Vanden Berghe, P. Wyeth, Heat and moisture promoted deterioration of raw silk estimated by amino acid analysis, J Cult Herit 12 (2011) 408–411. https://doi.org/10.1016/j.culher.2011.03.002.

[30] D. Gong, X. Zhang, Y. Gong, Insight Into the Crystallinity of Chinese Ancient Silk by Synchrotron Radiation-Based and Conventional X-ray Diffraction Methods, Journal of Conservation Science 36 (2020). https://doi.org/10.12654/JCS.2020.

[31] A. Motta, L. Fambri, C. Migliaresi, Regenerated Silk Fibroin Films: Thermal and Dynamic Mechanical Analysis, Macromol Chem Phys 203 (2002).

[32] H. Kweon, Y.H. Park, Dissolution and characterization of regenerated Antheraea pernyi silk fibroin, J Appl Polym Sci 82 (2001) 750–758. https://doi.org/10.1002/app.1901.

[33] M. Tsukada, G. Freddi, P. Monti, A. Bertoluzza, N. Kasai, Structure and Molecular Conformation of Tussah Silk Fibroin Films: Effect of Methanol, Journal of Polymer Science 33 (1995) 1995–2001.

[34] M.Y. Li, Y. Zhao, T. Tong, X.H. Hou, B.S. Fang, S.Q. Wu, X.Y. Shen, H. Tong, Study of the degradation mechanism of Chinese historic silk (Bombyx mori) for the purpose of conservation, Polym Degrad Stab 98 (2013) 727–735. https://doi.org/10.1016/j.polymdegradstab.2012.12.021.

[35] Y. Yanagi, Y. Kondo, K. Hirabayashi, Deterioration of silk fabrics and their crystallinity, Textile Res. J 10 (2000) 871–875.

[36] G. Freddi, P. Monti, M. Nagura, Y. Gotoh, M. Tsukada, Structure and molecular conformation of Tussah silk fibroin films: Effect of heat treatment, J Polym Sci B Polym Phys 35 (1997) 841–847. https://doi.org/10.1002/(SICI)1099-0488(19970415)35:5<841::AID-POLB13>3.0.CO;2-A.

[37] J. Li, Z. Wang, X. Yang, L. Hu, Y. Liu, C. Wang, Evaluate the pyrolysis pathway of glycine and glycylglycine by TG-FTIR, J Anal Appl Pyrolysis 80 (2007) 247–253. https://doi.org/10.1016/j.jaap.2007.03.001.

[38] T. Wanjun, W. Cunxin, C. Donghua, An investigation of the pyrolysis kinetics of some aliphatic amino acids, J Anal Appl Pyrolysis 75 (2006) 49–53. https://doi.org/10.1016/j.jaap.2005.04.003.

[39] F. Basile, S. Zhang, S.K. Kandar, L. Lu, Mass spectrometry characterization of the thermal decomposition/digestion (TDD) at cysteine in peptides and proteins in the condensed phase, J Am Soc Mass Spectrom 22 (2011) 1926–1940. https://doi.org/10.1007/s13361-011-0222-9.

[40] A. Ballistreri, P. Maravigna, G. Montaudo, Direct Mass Spectrometry of Polymers. XII.* Thermal Fragmentation Processes in Poly-a-Aminoacids, Journal of Polymer Science 23 (1985) 1145–1161.

[41] N. Vagkidis, L. Li, J.M. Marsh, V. Chechik, Synergy of UV light and heat in peptide degradation, J Photochem Photobiol A Chem 439 (2023). https://doi.org/10.1016/j.jphotochem.2023.114627.

[42] Z. Sebestyén, Z. Czégény, E. Badea, C. Carsote, C. Şendrea, E. Barta-Rajnai, J. Bozi, L. Miu, E. Jakab, Thermal characterization of new, artificially aged and historical leather and parchment, J Anal Appl Pyrolysis 115 (2015) 419–427. https://doi.org/10.1016/j.jaap.2015.08.022.

[43] K. Setoyama, Effect of Water on the Heat-Yellowing of Silk and Changes in Amino Acid Composition Due to Heat-Yellowing, Journal of Sericultural Science of Japan 51 (1982) 365–369.

[44] M.A. Becker, Y. Magoshi, T. Sakai, N.C. Tuross, Chemical and Physical Properties of Old Silk Fabrics, Studies in Conservation 42 (1997) 27–37.

[45] D. Pawcenis, M. Smoleń, M.A. Aksamit-Koperska, T. Łojewski, J. Łojewska, Evaluating the impact of different exogenous factors on silk textiles deterioration with use of size exclusion chromatography, Appl Phys A Mater Sci Process 122 (2016). https://doi.org/10.1007/s00339-016-0052-5.

[46] D.S. Bakirtzis, V.C. Tsapara, K.G. Kolovos, S.E. Liodakis, Assessment of the impact of fire retardants on the combustion of natural polymers employing DTG and LOI, Fire Mater 39 (2015) 109–118. https://doi.org/10.1002/fam.2232.

[47] R.L. Feller, Accelerated ageing - Photochemical and Thermal Aspects, The Getty Conservation Institute, Ann Arbor, Michigan (USA), 1994.

[48] I. Vanden Berghe, Towards an early warning system for oxidative degradation of protein fibres in historical tapestries by means of calibrated amino acid analysis, J Archaeol Sci 39 (2012) 1349–1359. https://doi.org/10.1016/j.jas.2011.12.033.

3.5.9 Supporting material

The data obtained from the PCA of ATR-FTIR dataset are presented.

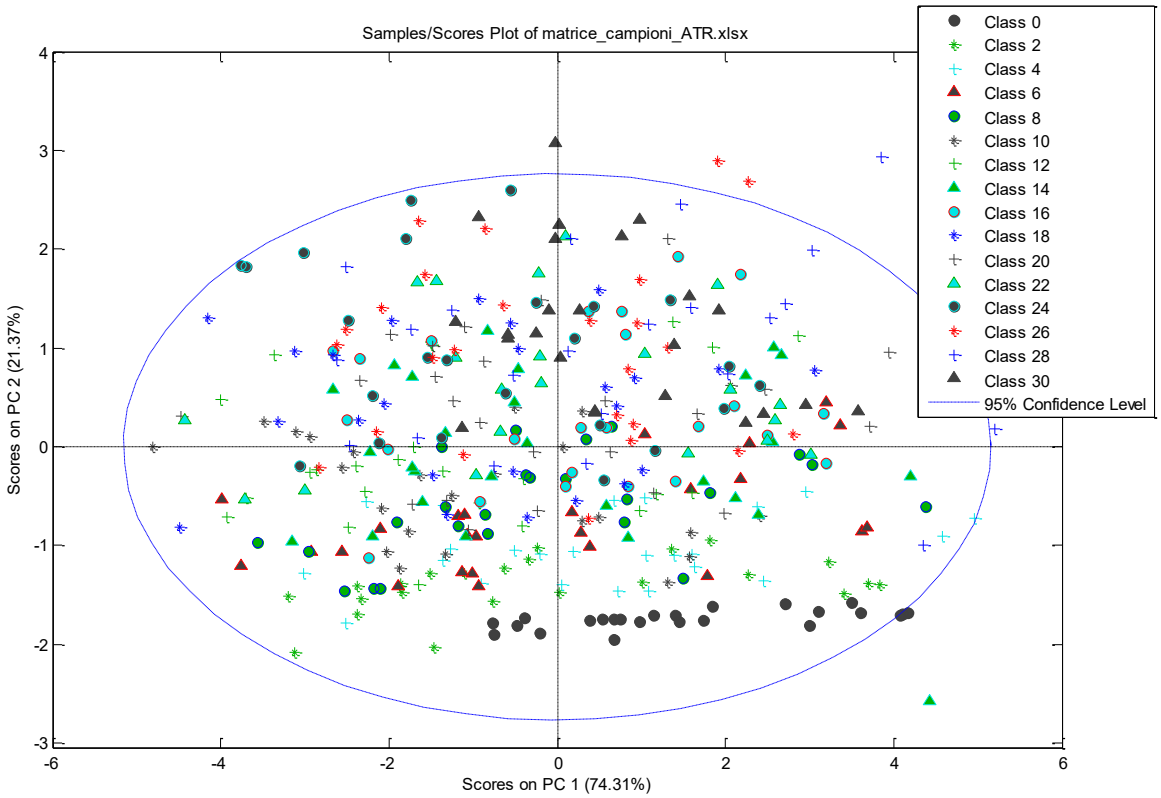

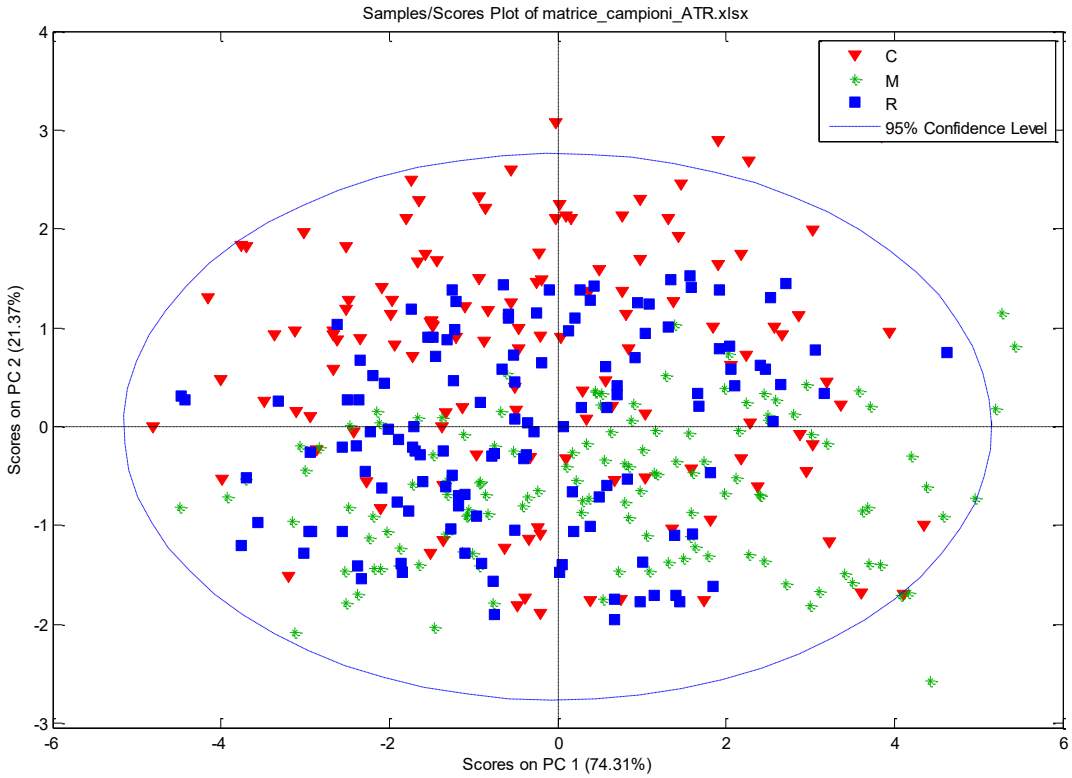

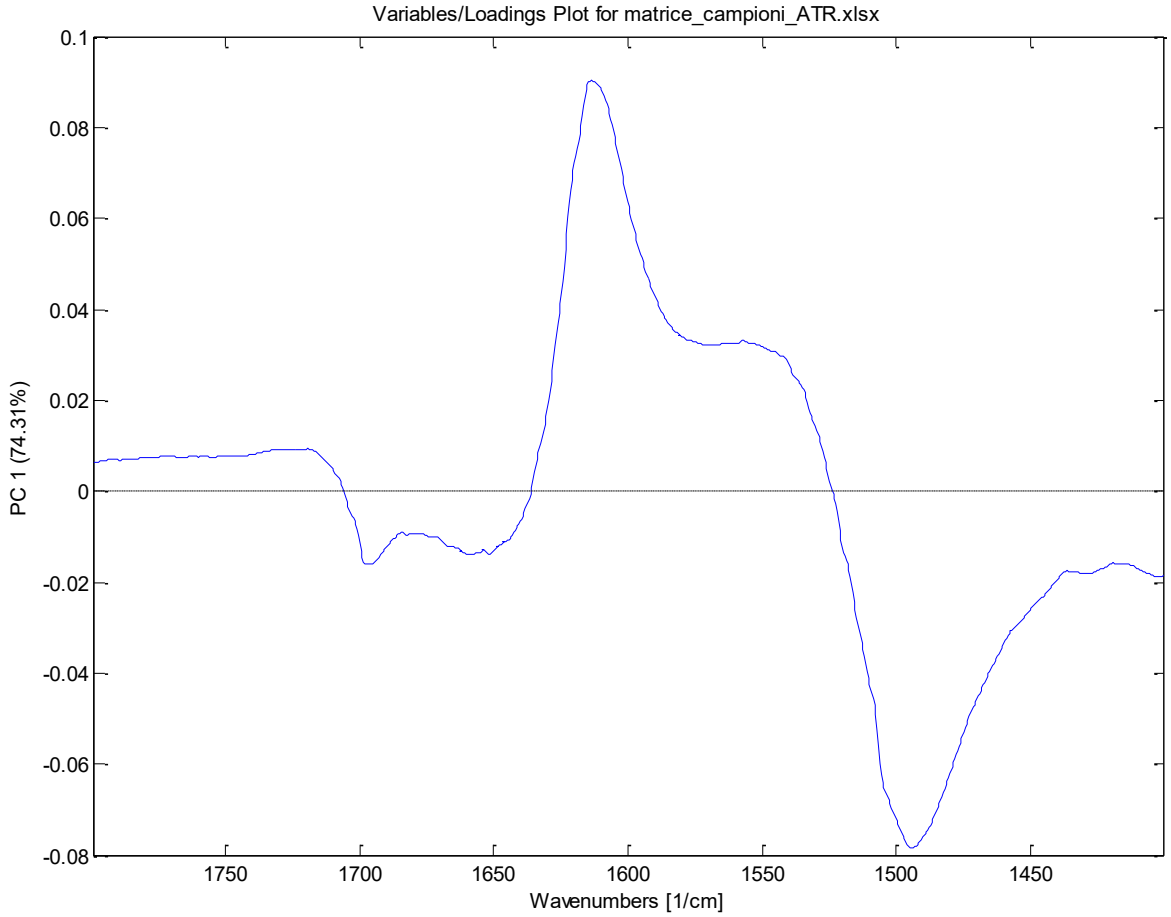
Variables/Loadings Plot for matrice_campioni_ATR.xlsx
PC 1 (74.31%)
Wavenumbers [1/cm]
0.1
0.08
0.06
0.04
0.02
0
-0.02
-0.04
-0.06
-0.08
1750
1700
1650
1600
1550
1500
1450

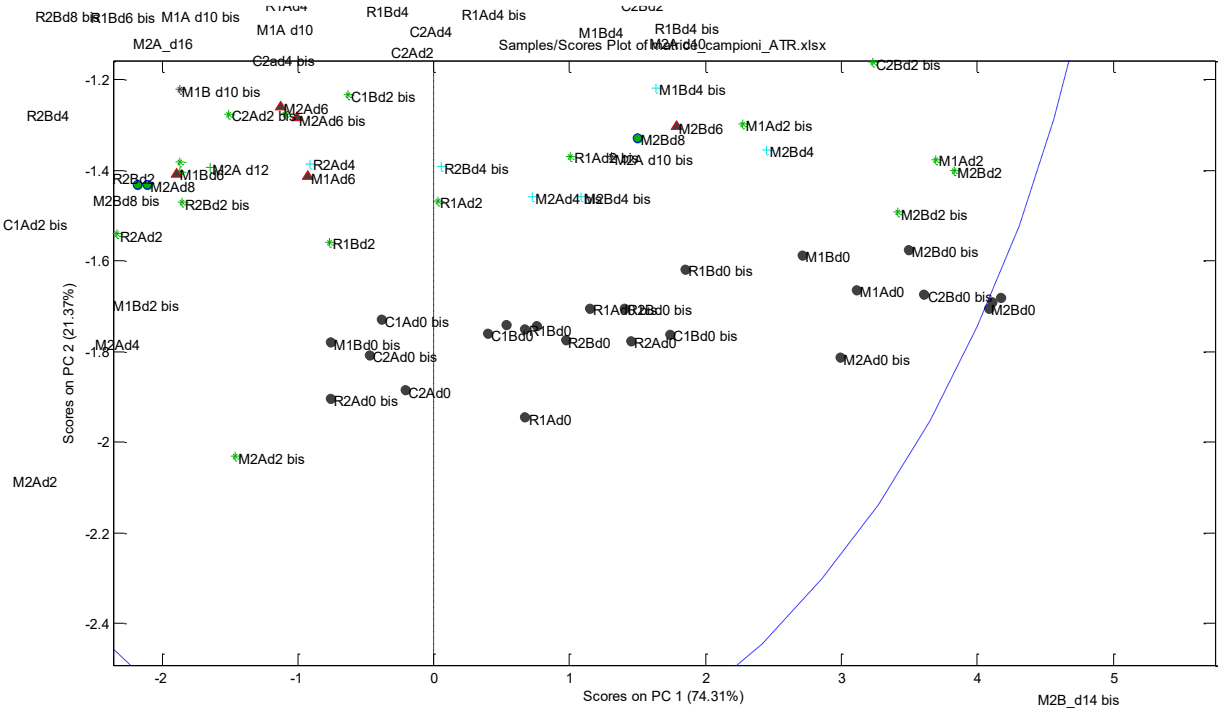
Samples/Scores Plot of matrice_campioni_ATR.xlsx
Scores on PC 1 (74.31%)
Scores on PC 2 (21.37%)
M2B_d14 bis
M1B d10 bis
C1Bd2 bis
C2Ad2 bis
M2Ad6
M2Ad6 bis
M2A d12
R2Ad4
M1Ad6
R2Bd2 bis
R1Bd2
C1Ad0 bis
M1Bd0 bis
C2Ad0 bis
C2Ad0
R2Ad0 bis
R1Ad0
M2Ad2 bis
M1Bd4 bis
M2Bd6
M1Ad2 bis
M2Bd8
M2Bd4
M2A d10 bis
R2Bd4 bis
R1Ad2
M2Bd4 bis
R1Bd0 bis
M1Bd0
M2Bd0 bis
M1Ad0
C2Bd0 bis
M2Bd0
C1Bd0
R2Bd0
R2Ad0
C1Bd0 bis
M2Ad0 bis
C2Bd2 bis
M1Ad2
M2Bd2
M2Bd2 bis
R2Bd4
M1Bd2 bis
M2Ad4
C1Ad2 bis
M2Bd8 bis
M2Ad2

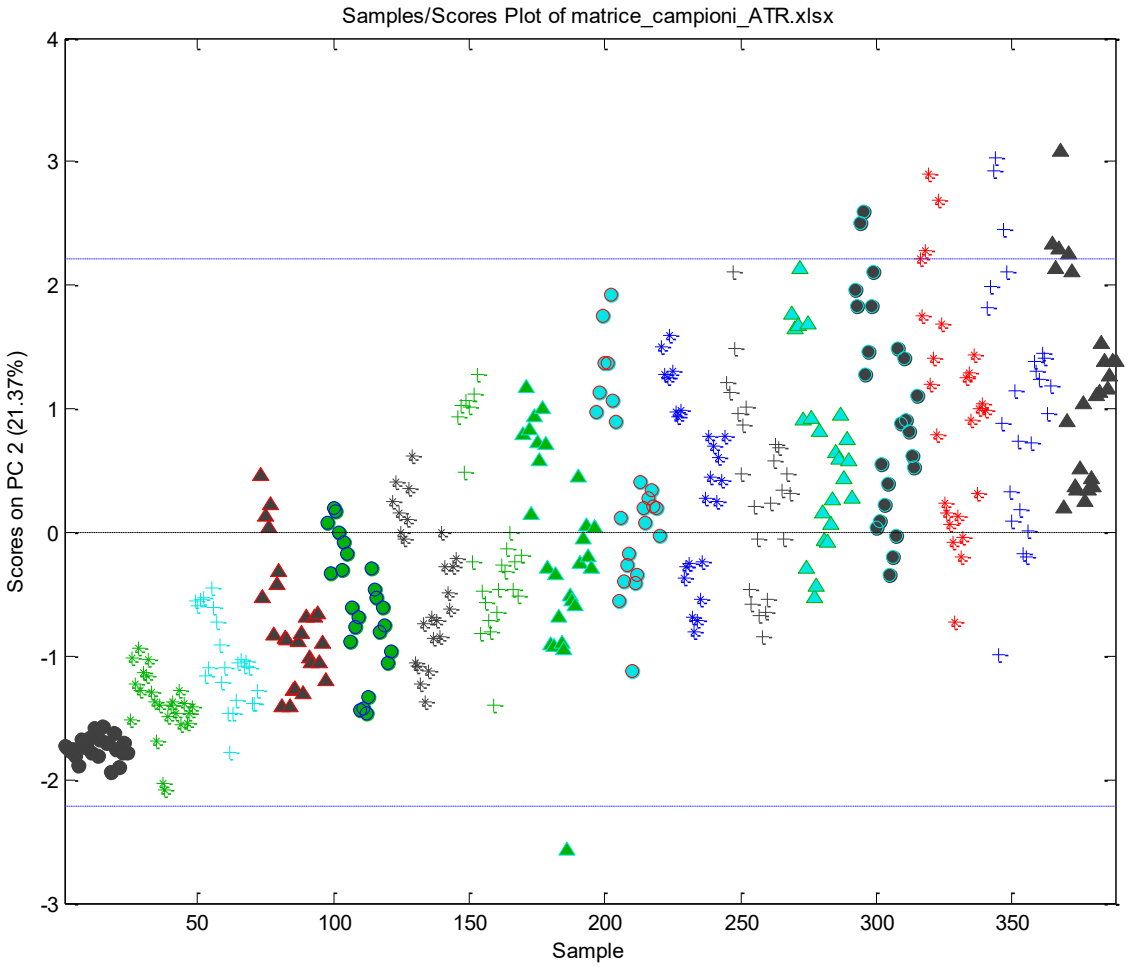
Samples/Scores Plot of matrice_campioni_ATR.xlsx
Scores on PC 2 (21.37%)
Sample
4
3
2
1
0
-1
-2
-3
50
100
150
200
250
300
350

3.6 Results - Mordanted Silk

The samples considered in this section were mordanted and aged under UVA355nm and visible light.

The samples were analysed after different ageing times (0, 15, 30 days).

3.6.1 Colorimetry

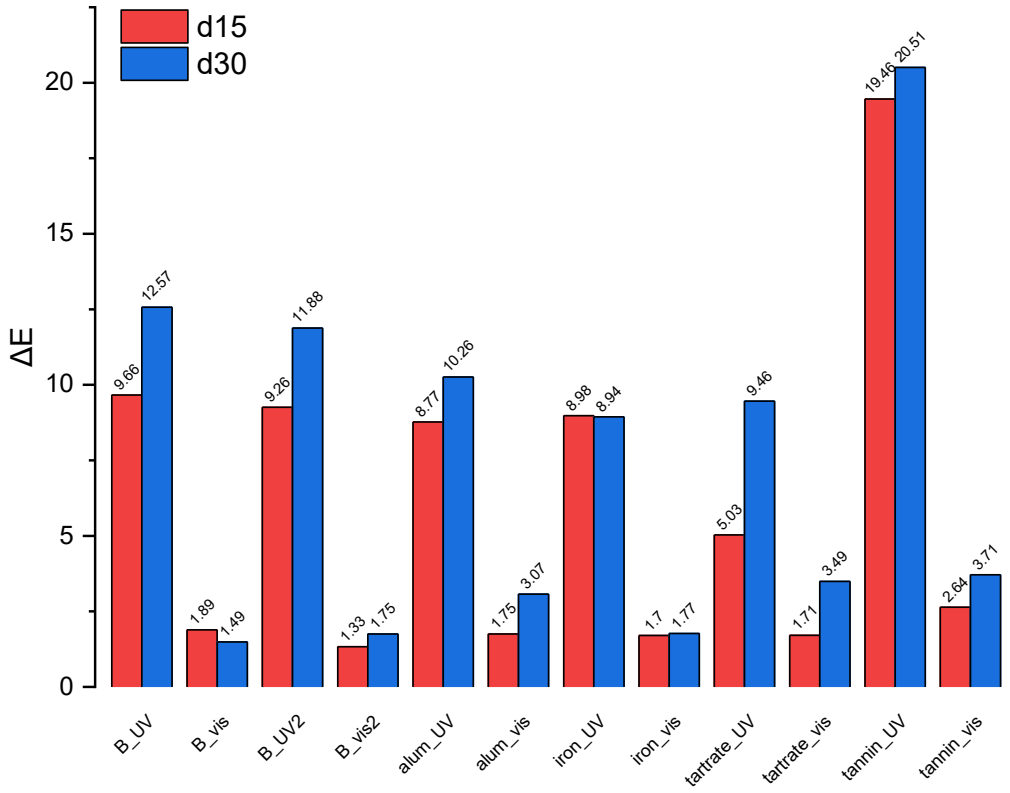

Figure 33. ΔE values for white silk (B) and mordanted silk aged under UVA355nm and Vis light

Figure 33 depicts the ΔE values for undyed silk samples subjected to accelerated aging with visible light and ultraviolet light. The bars refer to the aged silk after 15 and 30 days. ΔE values are calculated with respect to each sample before ageing. It emerges that most of the colour change happens in the first 15 days and that UV light creates much more effect with respect to visible light.

Figure 34 depicts La*b* coordinates for undyed and mordanted silk aged under UVA355nm and Vis light. It can be appreciated that mordanting with tannin, alum and iron affects the original colour of silk.

Visible	undyed silk	alum	tannin	tartrate	iron
Day 0	93.355 0.44 3.25	89.24 2.42 5.64	87.75 3.08 10.91	90.68 1.87 4.44	85.89 2.36 19.35
Day 15	92.04 0.34 2.47	90.33 0.92 6.38	87.21 1.66 10	91.64 0.59 2.97	83.99 2.6 20.79
Day 30	94.44 0.35 1.88	91.68 0.37 6.25	89.27 1.28 10.31	93.7 0.42 1.99	84.57 3.02 23.06

UVA355nm	undyed silk	alum	tannin	tartrate	iron
Day 0	93.355 0.44 3.25	89.24 2.42 5.64	87.75 3.08 10.91	90.68 1.87 4.44	85.89 2.36 19.35
Day 15	90.07 -0.44 12.11	88.66 -0.85 13.78	78.59 5.3 28.15	89.54 -0.38 9.38	79.93 2.99 24.78
Day 30	91.42 -1.1 14.86	90.9 -0.99 15.17	81.85 4.96 30.47	91.43 -0.96 13.44	80.83 2.68 26.72

*Figure 34. La*b* coordinates for undyed and mordanted silk aged under UVA355nm and Vis light. The background of the cells is coloured according to the La*b* coordinates.*

3.6.2 UV-VIS Spectroscopy

Figure 35 shows the UV-Vis spectra of undyed silk samples subjected to accelerated aging with visible light (Figure 35a) and ultraviolet light (Figure 35b). The spectra refer to the unaged silk and after 15 and 30 days of aging.

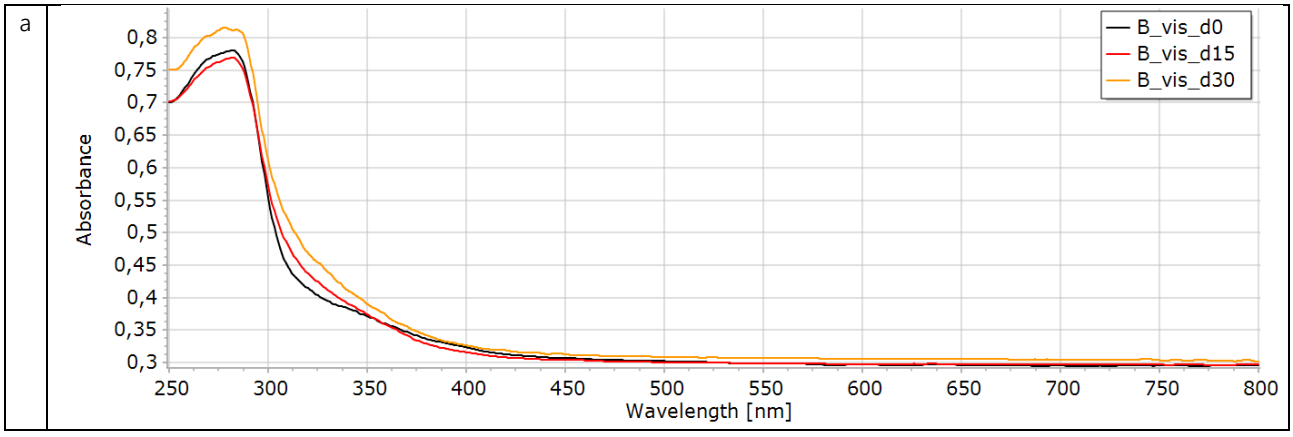

b

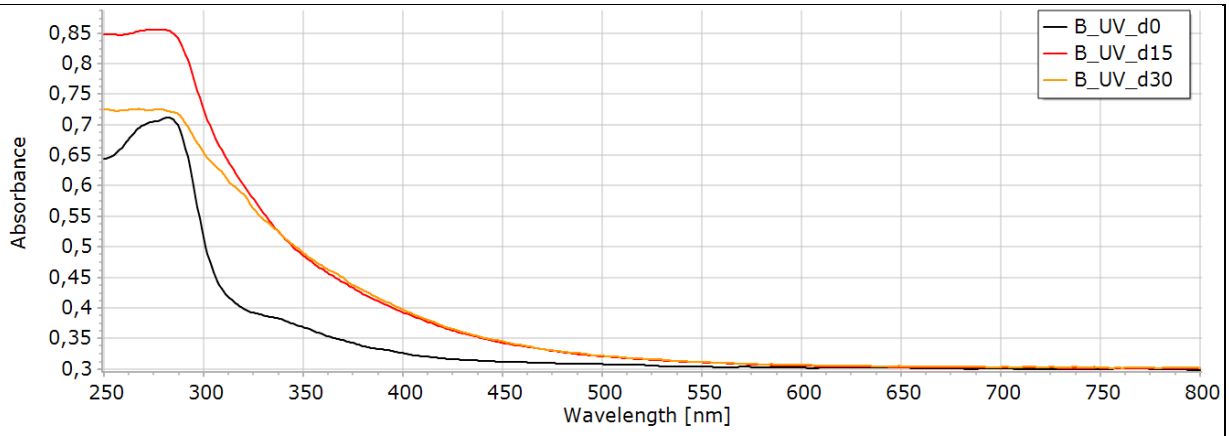

Figure 35. UV-Vis spectra of unaged silk and after 15 and 30 days of aging, a) with visible light lamp, b) with ultraviolet light lamp.

The peptide groups of the protein main chain are known to absorb light in the high energy UV range (180-230 nm) [1]. The band centered at 280 nm, visible in Figure 3, is due to aromatic amino acids, namely tyrosine, tryptophane, phenylalanine, which absorb respectively at 275, 280, 258 nm.

The signals in the 270-330 nm range should be attributed to the presence of a small quantity of α-keto-acids groups and dicarboxylic amino groups [2], but also to o-quinone residues and p-cross-linked quinone, which show absorption band at 306 and 360 nm [3]. The presence of these chromophores should be attributed to a slight oxidation of the substrate due to its processing.

Upon aging, the plots of the silk aged with visible light show minimal absorption variation in the 300-400 nm wavelength range, unlike the silk aged with ultraviolet light. A significant growth can be seen both in the bands attributed to quinone and to α-keto-acids. The rise of the plot in the region above 400 nm turns into the yellowing of the sample. The findings are consistent with the literature [1,3–5].

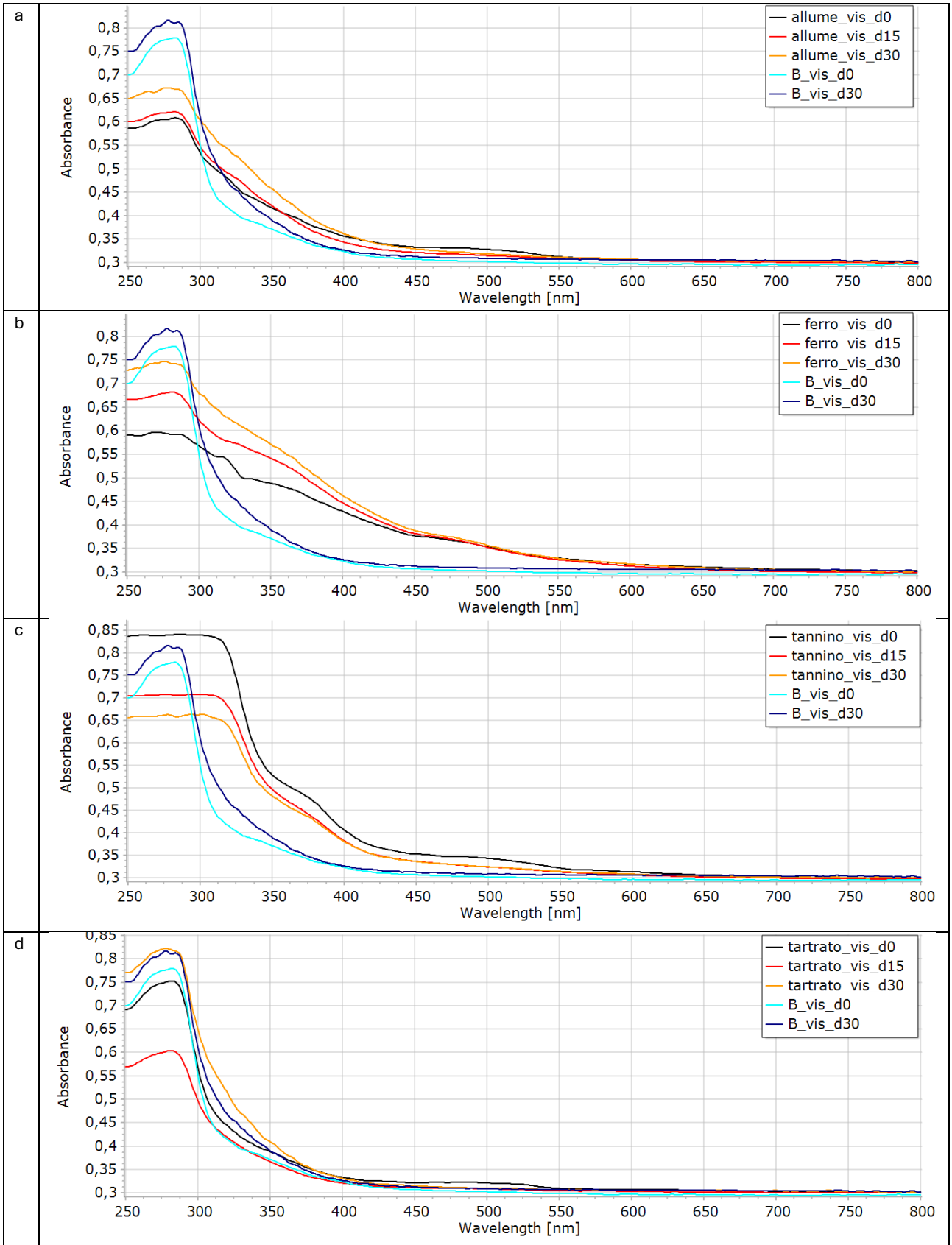

Figure 36. a) UV-Vis spectra of silk samples mordanted with potassium alum, b) UV-Vis spectra of silk samples mordanted with iron sulfate, c) UV-Vis spectra of silk samples mordanted with tannic acid, d) UV-Vis spectra of silk samples mordanted with potassium bitartrate. All graphs are compared with references of unmordanted white silk, both unaged and aged for 30 days. All spectra refer to aging with visible light.

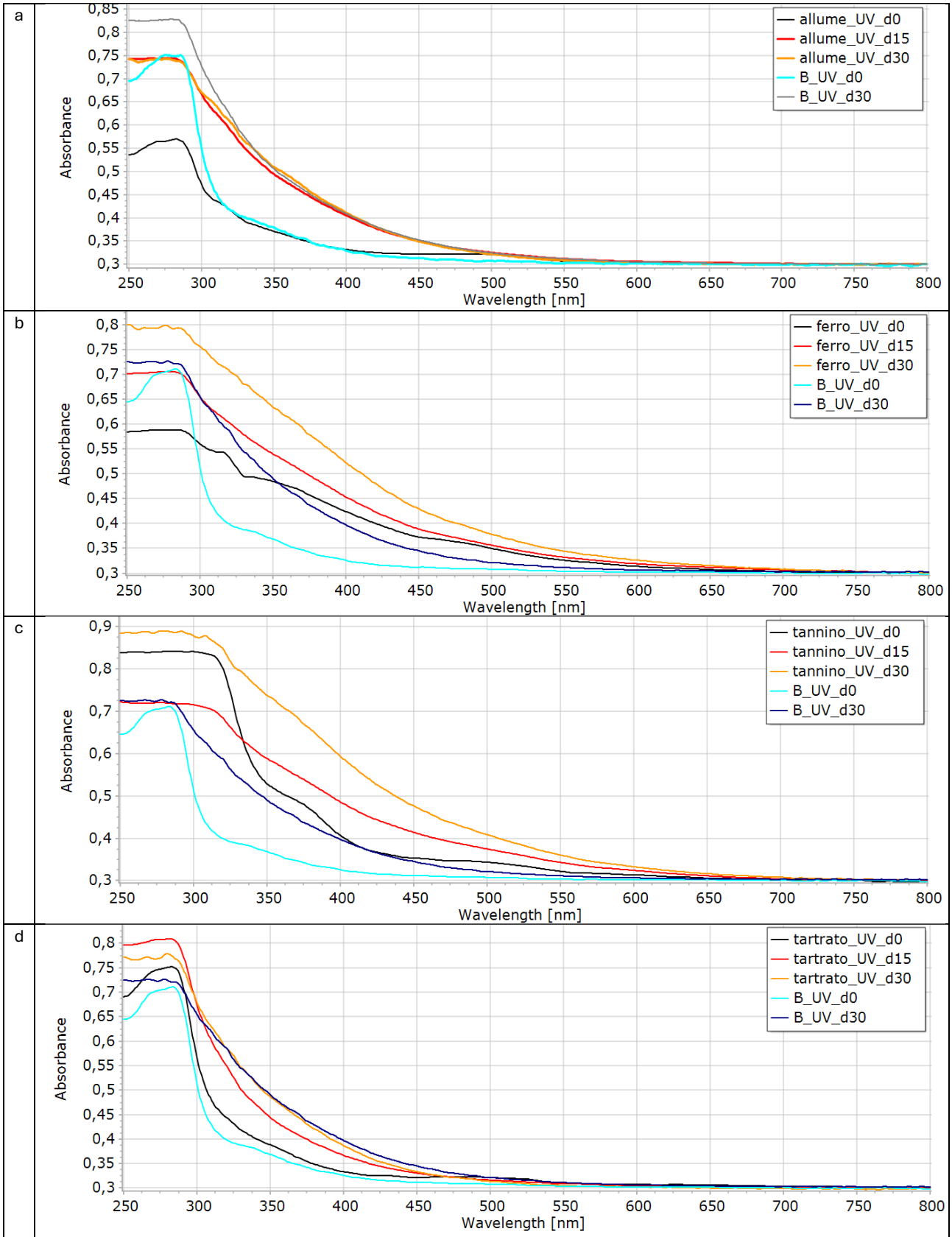

Figure 37. a) UV-Vis spectra of silk samples mordanted with potassium alum, b) UV-Vis spectra of silk samples mordanted with iron sulfate, c) UV-Vis spectra of silk samples mordanted with tannic acid, d) UV-Vis spectra of silk samples mordanted with potassium bitartrate. All graphs are compared with references of unmordanted white silk, both unaged and aged for 30 days. All spectra refer to aging with UV light.

Figure 36 shows the plots of silk treated only with mordant and subjected to aging with visible light. To facilitate the evaluation of the graphs, in addition to the spectra at different ageing times (0, 15, and 30 days) for each mordant, references of untreated white silk at 0 and 30 days have also been included. The results can be resumed as follows:

- Silk mordanted with potassium alum does not undergo significant changes during aging with visible light. Compared to unmordanted silk, it shows an absorption band between 300 and 350 nm.
- Silk mordanted with iron sulfate shows a similar trend over time, but compared to white silk, it absorbs a fraction of visible radiation (400-550 nm).
- Silk mordanted with tannic acid does not undergo significant changes over time. Compared to white silk, it shows light absorption between 300 and 550 nm.
- Silk mordanted with potassium bitartrate has a very similar trend over time to white silk. No particular absorption zones are noticeable.

Figure 37 shows the graphs of silk treated only with mordant and subjected to aging with UV light. To facilitate the evaluation of the graphs, in addition to the spectra at three time points (0, 15, and 30 days) for each mordant, references of untreated white silk at 0 and 30 days have been included.
The results can be resumed as follows:

- During aging with ultraviolet light, no significant changes are observed in the spectra for silk mordanted with potassium alum. Compared to unmordanted silk, it has an absorption between 300 and 350 nm.
- Silk mordanted with iron sulfate absorbs in the 300-550 nm range; before aging, an absorption band appears between 325 and 400 nm, and after 15 days, the shape of the curve changes. By 30 days, no marked differences are observed.
- The graphs of silk mordanted with tannic acid show an absorption band at around 375 nm, which widens to the 325-450 nm range during aging.
- Potassium bitartrate does not show evident differences over time. After 30 days of aging, the trace of mordanted silk is mostly superimposable with the white silk aged for 30 days as well.

3.6.3 ATR-FTIR spectroscopy and thermogravimetric analysis

All the ATR spectra shown were trimmed to the 1800-1400 cm^{-1} range and normalized to the peak with the highest intensity to make differences more evident.

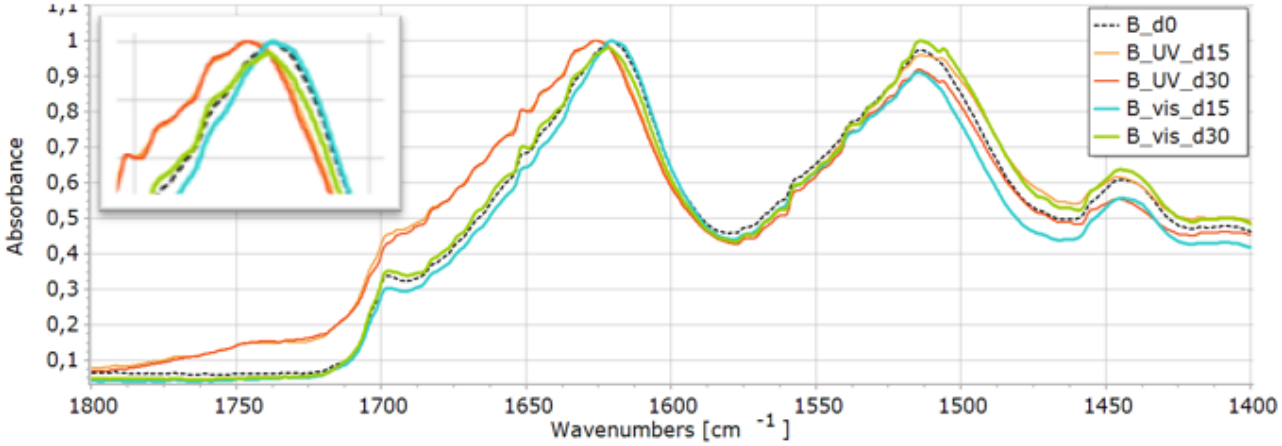

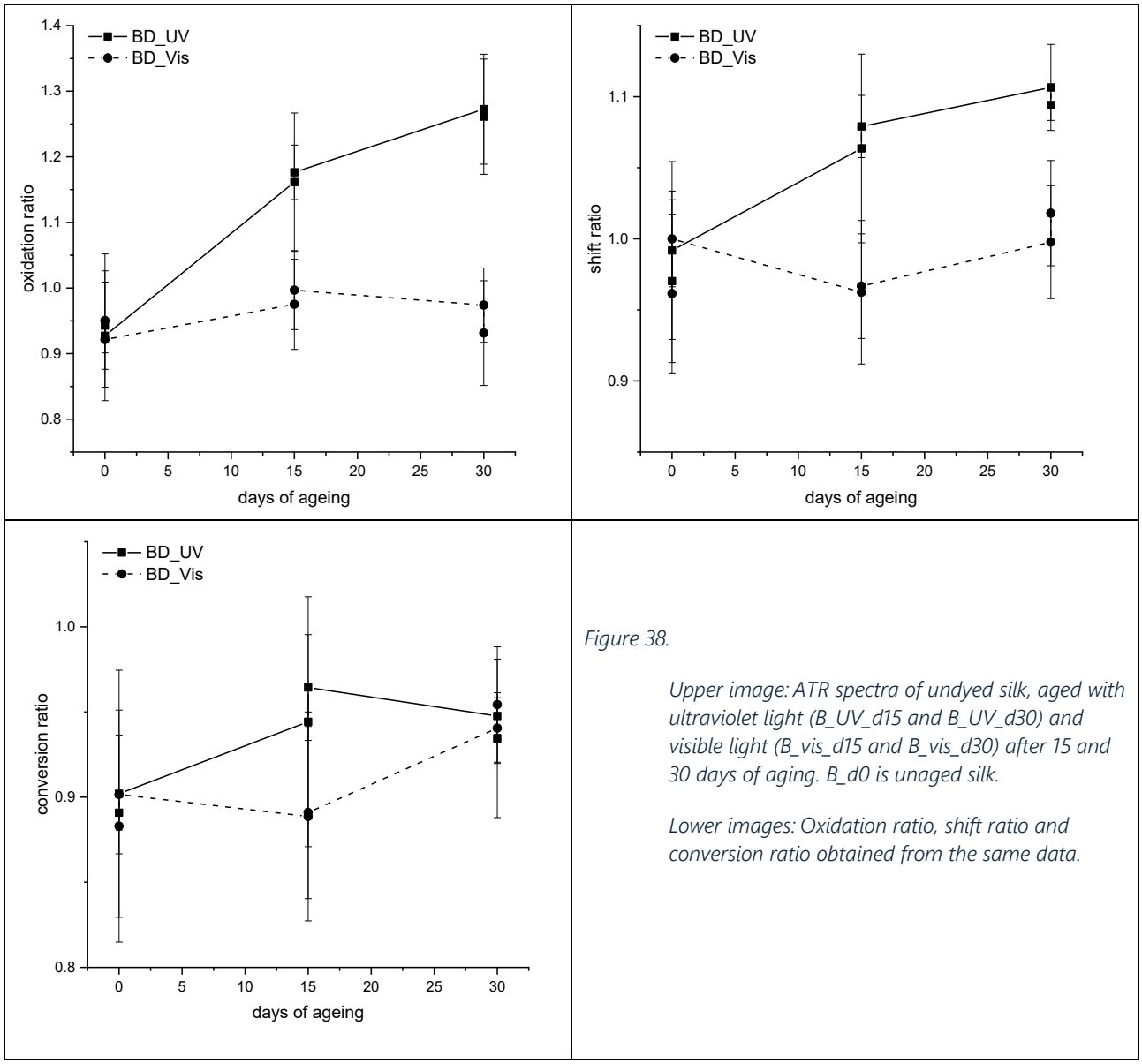

Figure 38.

Upper image: ATR spectra of undyed silk, aged with ultraviolet light (B_UV_d15 and B_UV_d30) and visible light (B_vis_d15 and B_vis_d30) after 15 and 30 days of aging. B_d0 is unaged silk.

Lower images: Oxidation ratio, shift ratio and conversion ratio obtained from the same data.

Figure 38 shows the ATR spectra of white silk samples subjected to accelerated aging with visible (Vis) and ultraviolet (UV) light. The spectrum of unaged silk (B_d0) is provided for comparison.
After just 15 days of aging with ultraviolet light (B_UV_d15), a shift in the Amide I signal toward higher wavenumbers is observed (from 1617 cm^{-1} to 1625 cm^{-1}). Significant differences are also noted in the 1720-1760 cm^{-1} region, typical of oxidation products. However, for aging with visible light, the spectra do not show a marked variation over time.

Figure 38 also summarizes the differences between the ageing under visible and UV light for white silk. Oxidation ratio, shift ratio and conversion ratio were calculated from the ATR-FTIR data.

The oxidation ratio shows that a significant increase of the oxidative extent of silk is caused by the ageing under UV light. Visible light does not seem to affect silk oxidation.

The shift ratio is increased by the UV ageing, and not by visible ageing.

The conversion ratio of UV-aged silk shows the typical maximum after 15 days, followed by a decrease, which has been attributed to the exhaustion of accessible sites of tyrosine for oxidation. Visible light shows a different trend, characterized by a long induction period. However, after 30 days it reaches the same value of conversion of UV-aged silk.

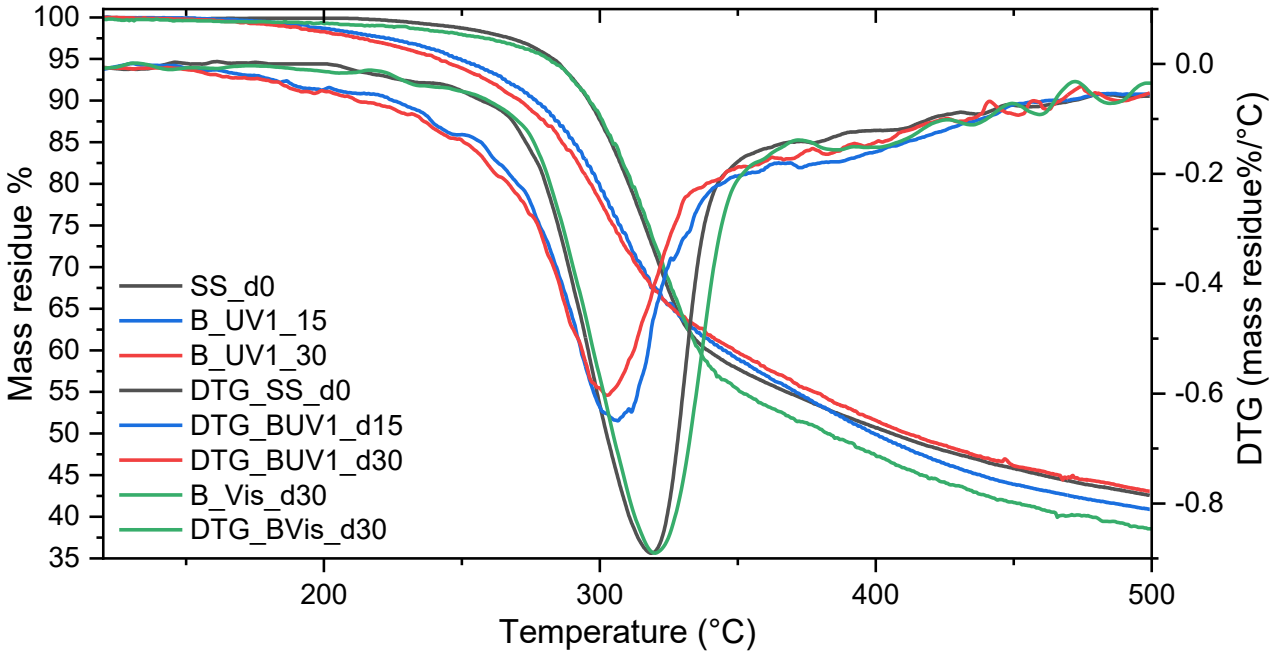

Figure 39. TG and DTG plots of the unmordanted samples under different ageing conditions: SS_d0 (unaged), BUV1_d15 (aged 15 days under UV light), BUV1_d30 (aged 30 days under UV light), BVis_d30 (aged 30 days under visible light)

Figure 39 shows the TG and DTG plots of the unmordanted samples under different ageing conditions. The trend of the UV aged silk is in accordance with the results found in the previous experiment, that is the T_{max} peak shifts towards lower temperatures as the ageing goes further. Similarly, the area under the curve becomes smaller. In the case of visible-aged silk, the curve does not show significant changes respect to non-aged silk.

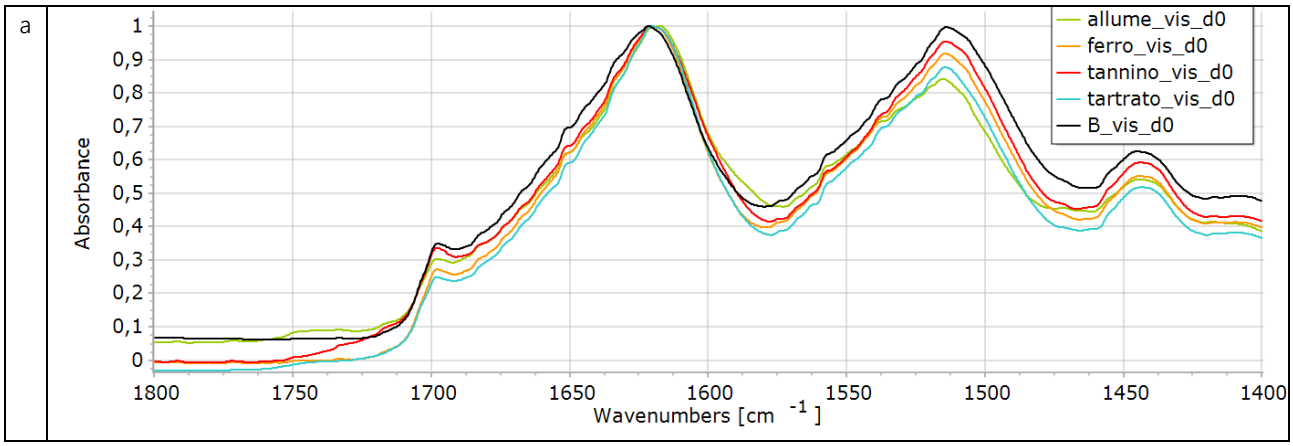

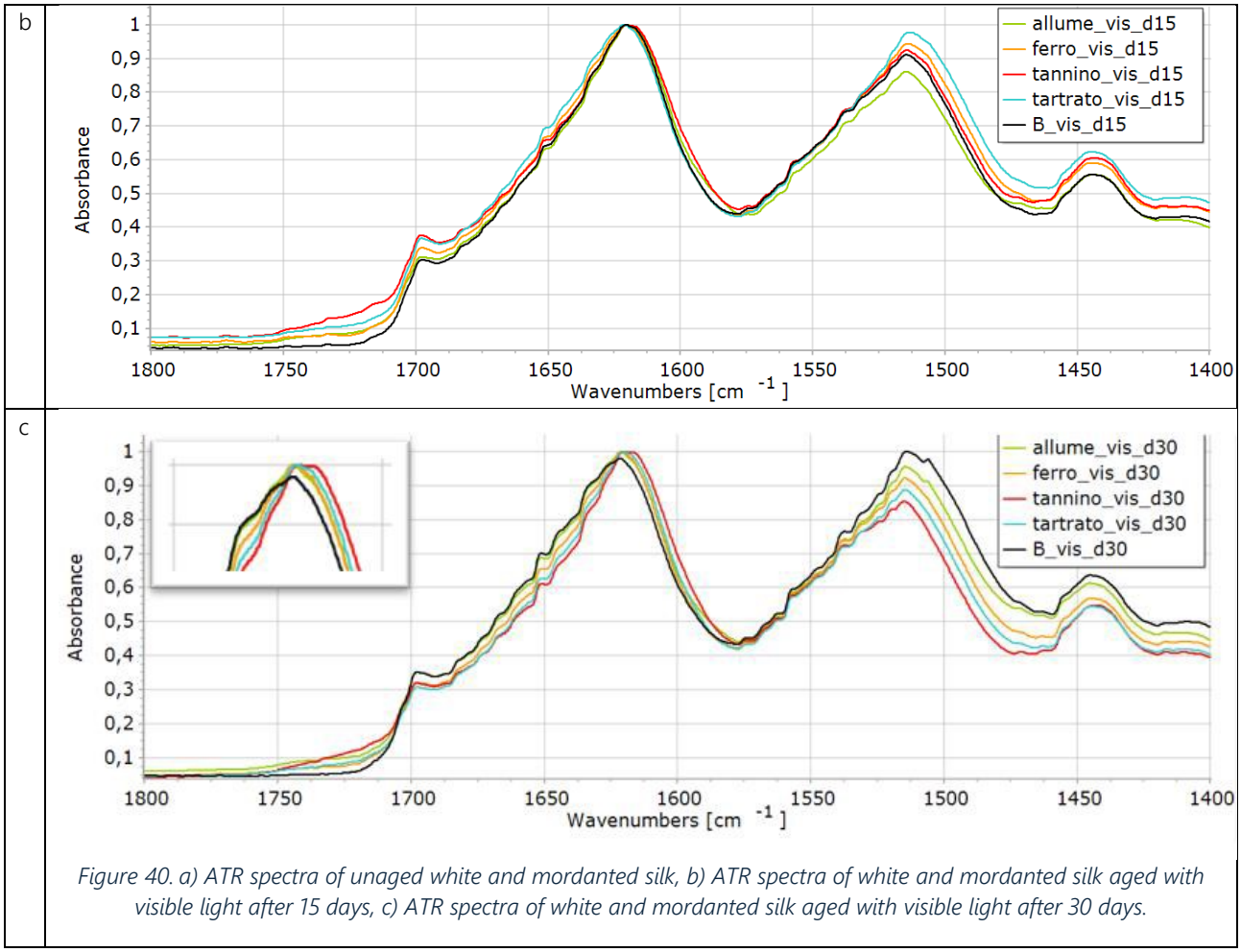

Figure 40. a) ATR spectra of unaged white and mordanted silk, b) ATR spectra of white and mordanted silk aged with visible light after 15 days, c) ATR spectra of white and mordanted silk aged with visible light after 30 days.

A comparison was made between the spectra of white silk and mordanted silk. The comparison was made at all analysis times (d_0, d_15, and d_30) and with all mordants (potassium alum, iron sulfate, potassium bitartrate, and tannic acid). Figure 40 shows the spectra of the samples aged under visible light. During aging, oxidation products are observed in the 1720-1760 cm^{-1} region, predominant in the samples with tannic acid (red spectra). After 30 days of aging (Figure 40c), the peak related to Amide I in white silk is shifted to lower wavenumbers compared to the mordanted samples.

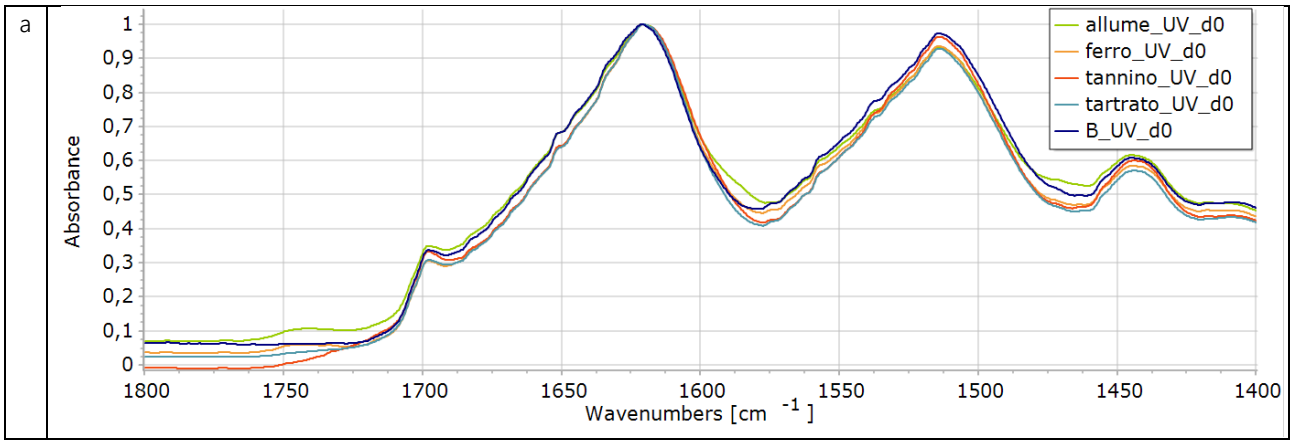

b

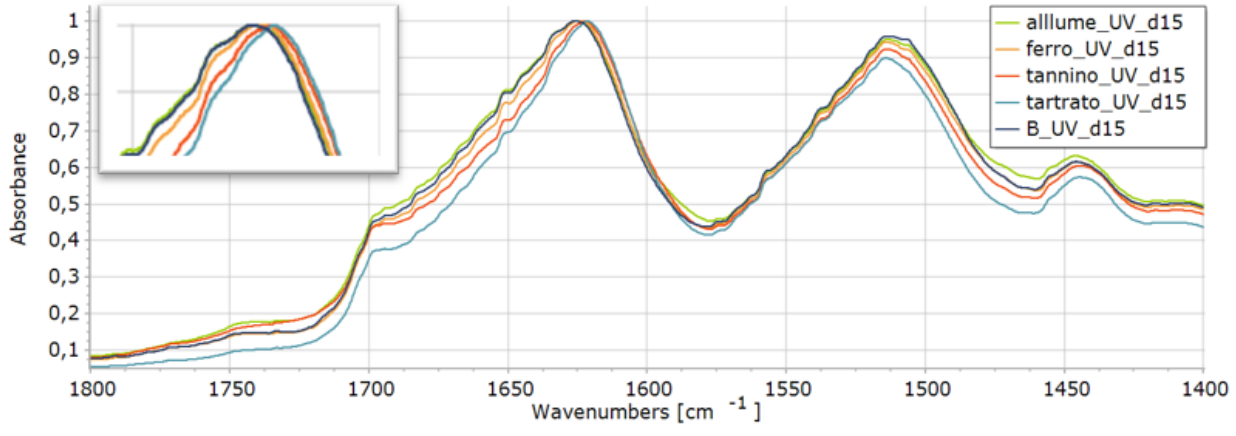

c

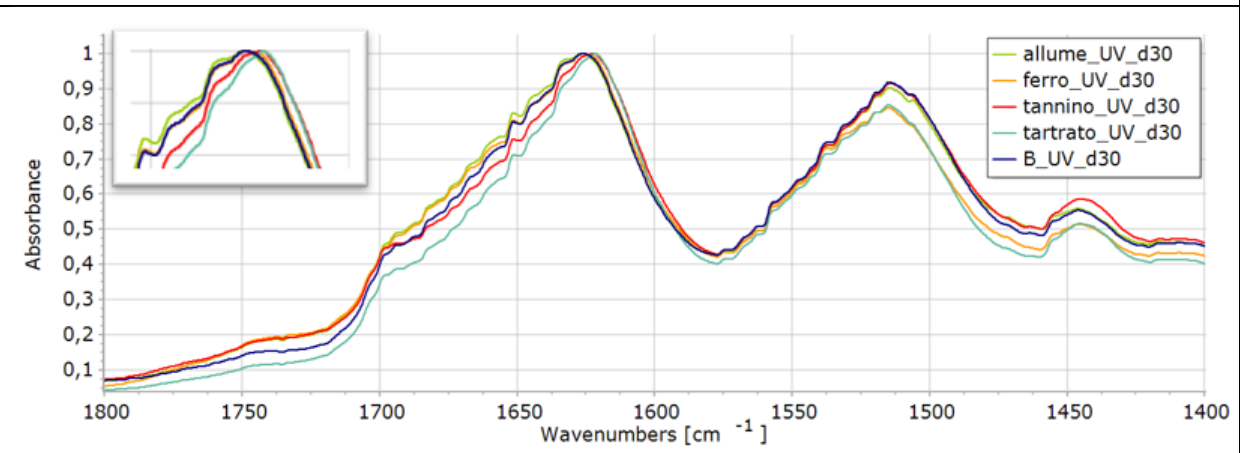

Figure 41. a) ATR spectra of unaged white and mordanted silk, b) ATR spectra of white and mordanted silk aged with ultraviolet light after 15 days, c) ATR spectra of white and mordanted silk aged with ultraviolet light after 30 days.

Regarding mordanted silk subjected to accelerated aging with ultraviolet light (Figure 41), before aging, all samples show almost superimposable spectra, without significant differences. However, after 15 days of aging, the traces widen between the different samples, and the alum_UV_d15 sample shows a marked shift toward 1625 cm^{-1} compared to the tartrate_UV_d15 and tannin_UV_d15 samples. Additionally, after 30 days, the white sample B_UV_d30 is superimposable with alum_UV_d30 in the Amide I region (1625 cm^{-1}), but diverges in the oxidation product region (1720-1760 cm^{-1}), where greater intensity is observed in the spectra related to alum and tannic acid.

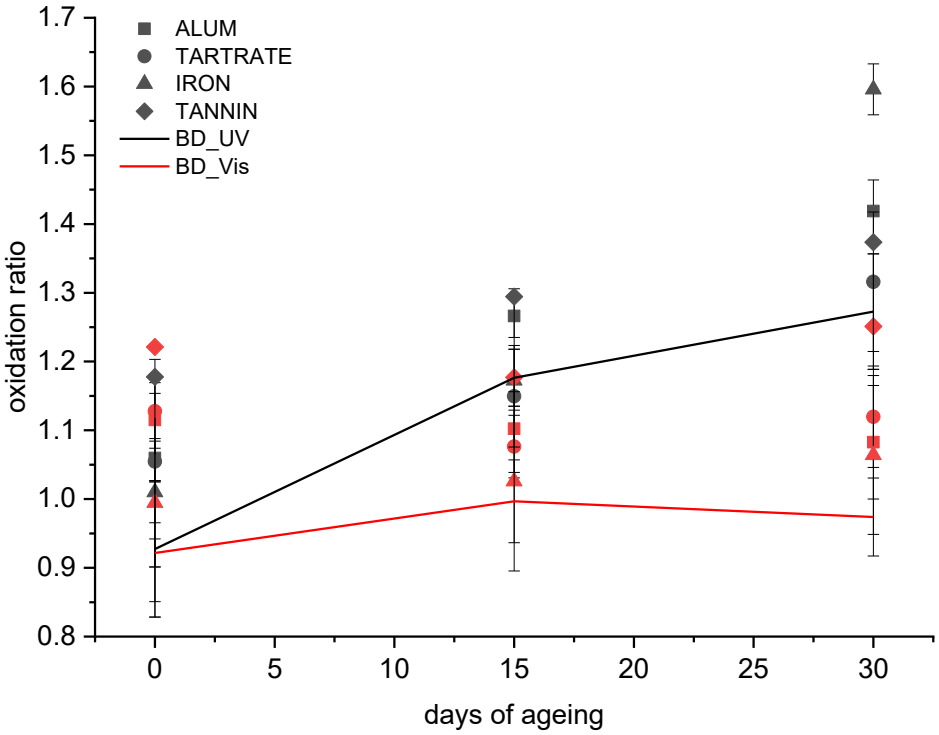
ALUM
TARTRATE
IRON
TANNIN
BD_UV
BD_Vis
oxidation ratio
1.7
1.6
1.5
1.4
1.3
1.2
1.1
1.0
0.9
0.8
0
5
10
15
20
25
30
days of ageing

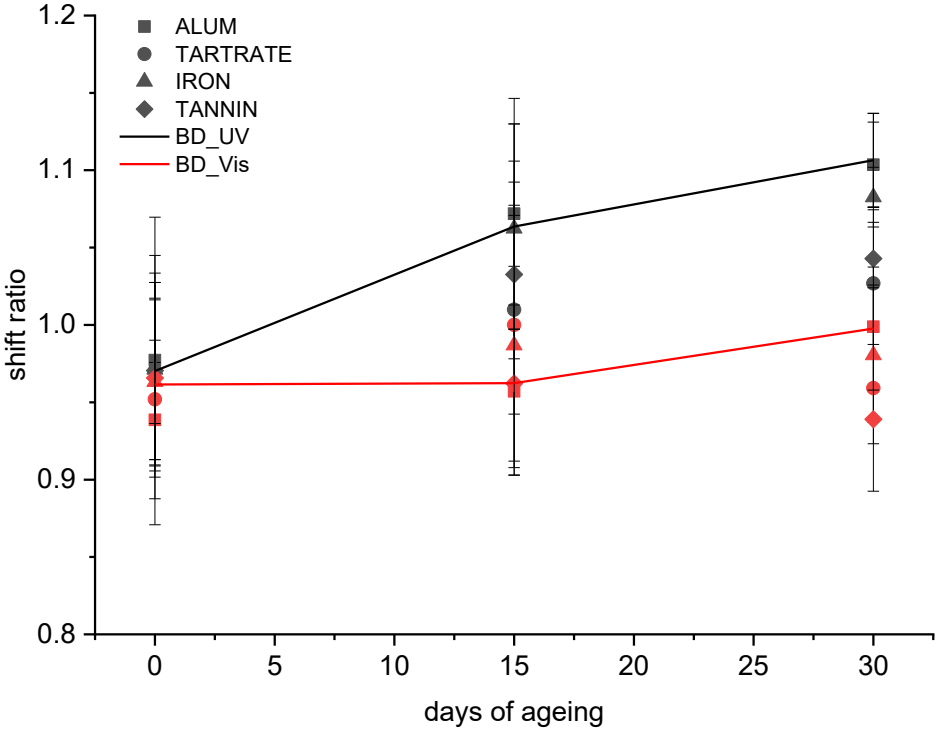
ALUM
TARTRATE
IRON
TANNIN
BD_UV
BD_Vis
shift ratio
1.2
1.1
1.0
0.9
0.8
0
5
10
15
20
25
30
days of ageing

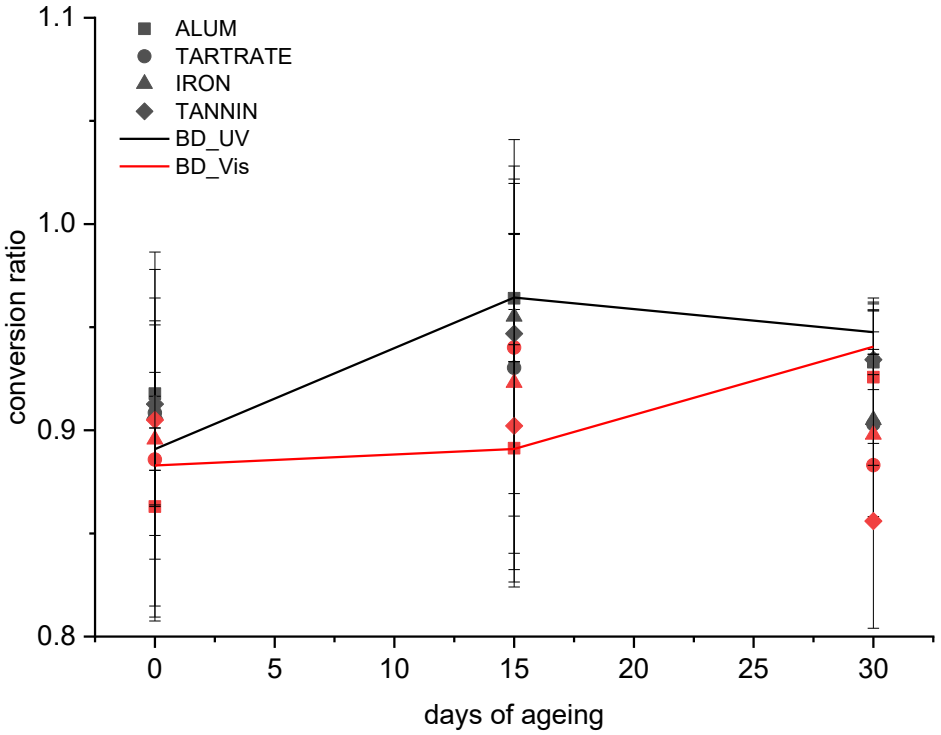

Figure 42. Oxidation ratio, shift ratio and conversion ratio calculated for white silk and mordanted silk. All analysis times (d_0, d_15, and d_30) and all mordants (potassium alum, iron sulfate, potassium bitartrate, and tannic acid) are considered. Red symbols stand for ageing with visible light, black symbols for ageing with UVA355nm. The lines represent the ageing trend for white silk.

Figure 42 summarizes the differences between white silk (BD) and mordanted silk. Oxidation ratio, shift ratio and conversion ratio were calculated from the ATR-FTIR data. The presence of a mordant deeply modifies the ageing behavior of silk.

The oxidation ratio shows that a significant increase of the oxidative extent of silk is caused by the treatment of a mordant, also before ageing. Tannin mordanted silk is the most deeply affected. The extent of oxidation of mordanted silk is significantly increased after 30 days of UV ageing, with iron mordanted silk appearing as the most deeply affected.

The shift ratio is not modified by the treatment with mordants. A slight decrease of the shift is observed for mordanted silk with respect to white silk, especially for tannin-mordanted and tartrate-mordanted silk.

The conversion ratio is minimally affected by the treatment with mordants. Similarly to what happens with white silk, the ratio reaches a maximum in 15 days and then decreases, probably due to the exhaustion of accessible sites of tyrosine. The trend of white silk under visible light behaves differently, but not when silk is treated with mordants. In this condition, the ageing under visible and UV light is the same.

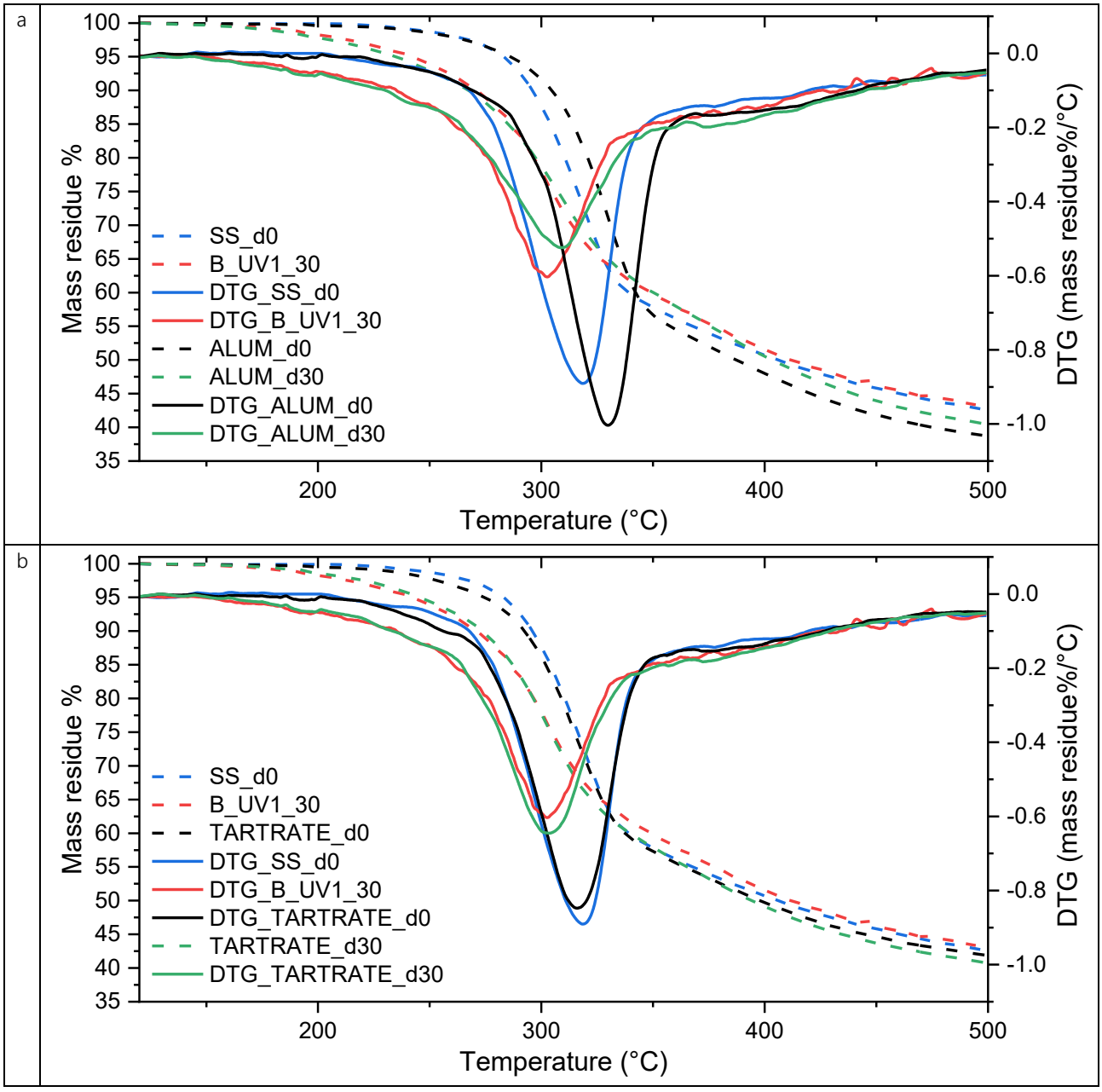
a
Mass residue %
DTG (mass residue%/°C)
Temperature (°C)
SS_d0
B_UV1_30
DTG_SS_d0
DTG_B_UV1_30
ALUM_d0
ALUM_d30
DTG_ALUM_d0
DTG_ALUM_d30
b
Mass residue %
DTG (mass residue%/°C)
Temperature (°C)
SS_d0
B_UV1_30
TARTRATE_d0
DTG_SS_d0
DTG_B_UV1_30
DTG_TARTRATE_d0
TARTRATE_d30
DTG_TARTRATE_d30

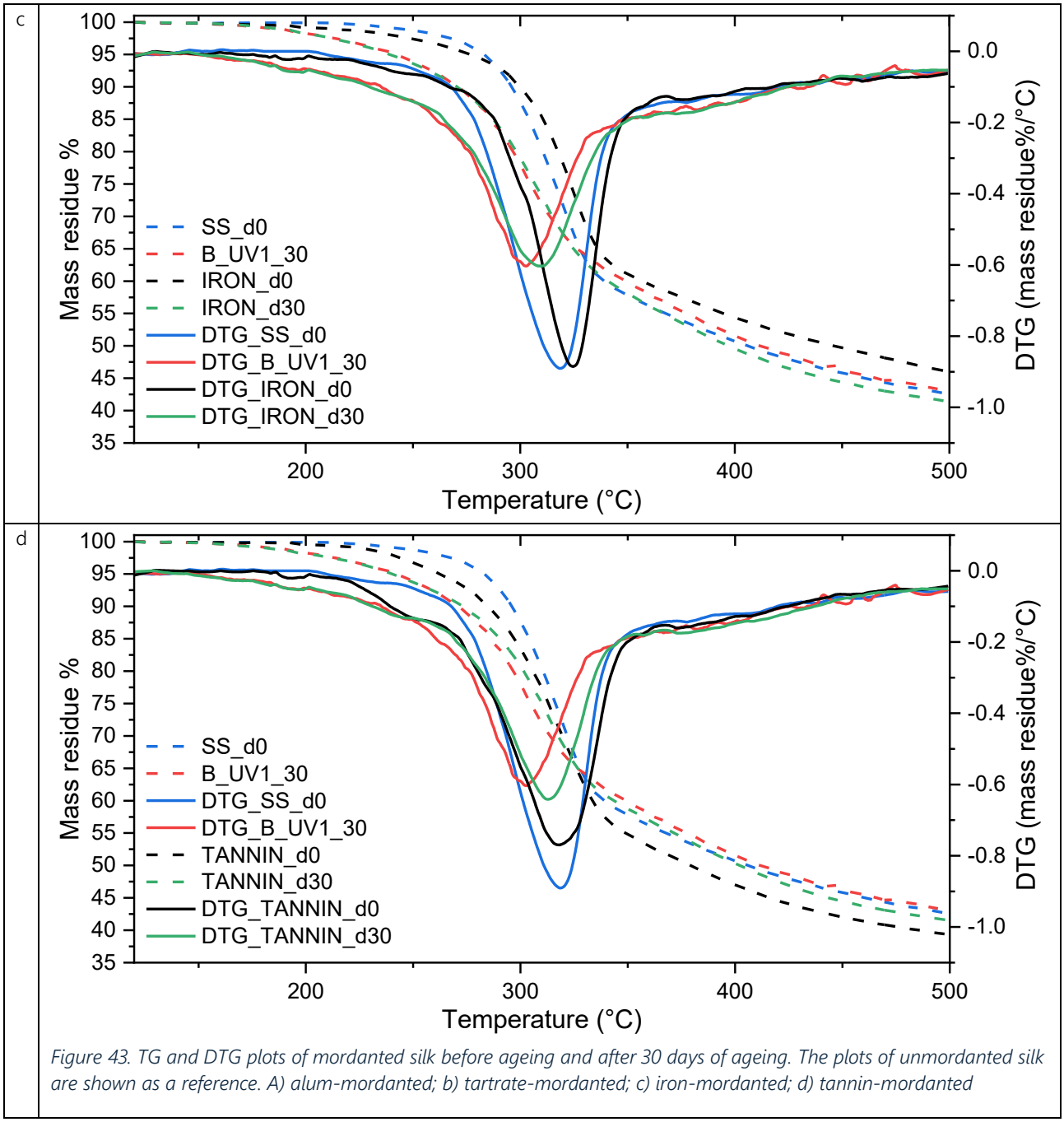

Figure 43. TG and DTG plots of mordanted silk before ageing and after 30 days of ageing. The plots of unmordanted silk are shown as a reference. A) alum-mordanted; b) tartrate-mordanted; c) iron-mordanted; d) tannin-mordanted

Figure 43 shows TG and DTG plots of mordanted silk before ageing and after 30 days of ageing. The treatment with mordants gives rise to important differences with respect to the plots of unmordanted silk.

The main decomposition event for alum-mordanted silk before ageing occurs at higher temperatures and the total mass loss is higher as well. This behaviour can be related to the fire-retardant properties shown by potassium alum [6]. After 30 days of UV ageing, the peak of the decomposition is still at slightly higher temperatures, but the area of the curve is consistent with the area of unmordanted silk.

In the case of tartrate-mordanted silk, the curves are comparable.

Iron-mordanted silk plots are slightly shifted at higher temperatures with respect to unmordanted silk, probably for the same fire-retardant properties. The areas are comparable.

Tannin-mordanted silk plot before ageing has the same peak temperature, but the area under the curve is smaller, indicating a higher extent of degradation. After 30 days, the area of the curve is similar to the area of unmordanted silk, but the peak is shifted to higher temperatures, indicating that tannins give flame-retardant properties to the silk.

The features of the DTG curves for mordanted and white silk are summarized in Table 10, together with the values of the E% factor, calculated according to the *Experimental parameters* section.

Sample	Area (A)	T_{max}	d_{max}	A	E% (vs B_UV1_30)
SS_d0 - 1st derivative	-29.5	319	0.895	0.010686	-66.0689
B_UV1_30 - 1st derivative	-15.54	302	0.608	0.031541	0
B_VIS_30 - 1st derivative	-29.69	320	0.9	0.010525	-66.5781
ALUM_d0 - 1st derivative	-24.53	330	-1.01	-0.01101	-134.954
ALUM_30 - 1st derivative	-14.21	308	0.527	0.03902	23.90206
IRON_d0 - 1st derivative	-23.85	325	0.895	0.012973	-58.8055
IRON_30 - 1st derivative	-17.7	308	0.605	0.027287	-13.3528
TANNIN_d0 - 1st derivative	-24.92	318	0.77	0.014749	-53.1653
TANNIN_30 - 1st derivative	-18.43	313	0.65	0.024003	-23.7832
TARTRATE_30 - 1st derivative	-18.53	302	0.648	0.024819	-21.1909
TARTRATE_d0 - 1st derivative	-26.93	315	0.85	0.012482	-60.366

Table 10. Features of the DTG curves for mordanted and white silk, shown together with the values of the E% factor

The extent of degradation (E%) was calculated with respect to sample B_UV1_30, which is set to zero. As a consequence, the other samples exhibit positive values if they show bigger levels of degradation and negative values if they show lower levels of degradation. Non-aged silk and visible-aged silk show obviously negative values. The only mordanted sample which exhibits an increase of the degradation level is the alum-mordanted sample aged 30 days.

3.7 Results – Dyed Silk

3.7.1 Colorimetry

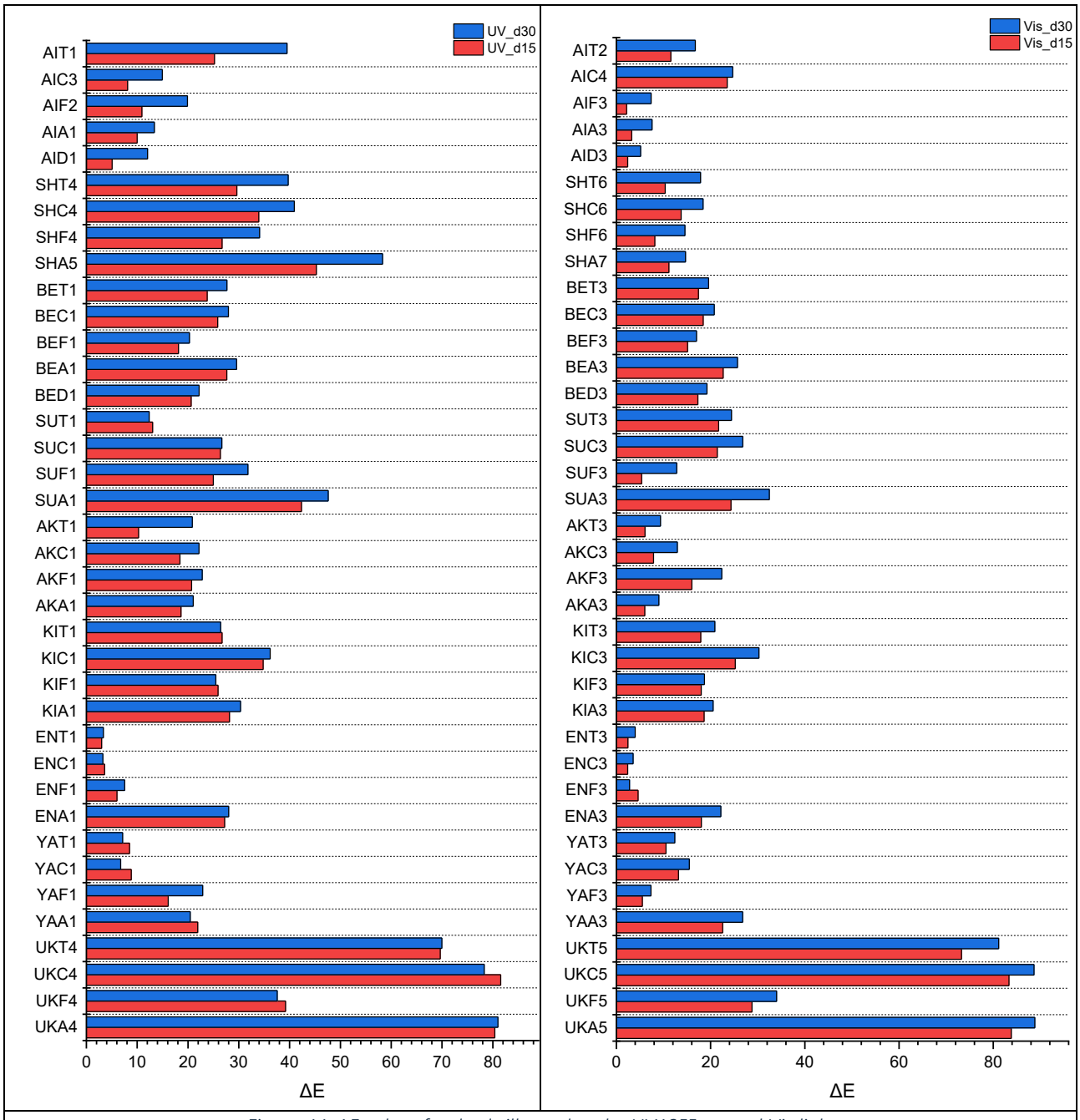

Figure 44. ΔE values for dyed silk aged under UVA355nm and Vis light

Figure 44 depicts the ΔE values for dyed silk samples subjected to accelerated aging with visible light and ultraviolet light. The bars refer to the aged silk after 15 and 30 days. ΔE values are calculated with respect to each sample before ageing. It emerges that most of the colour change happens in the first 15 days and that UV light creates much more effect with respect to visible light.

3.7.2 UV-Vis spectroscopy

The UV-Vis spectra of the dyed samples, unaged (d0), after 15 and 30 days of aging with visible and UV light, are presented in Figures 45-62. The spectra are shown divided by the dye/mordant combination over time. For each spectrum, the comparison with the reference mordant, unaged and after 30 days of aging under the same conditions as the dyed samples, is shown. For each mordant, references for mordanted silk at only 0 and 30 days are provided.

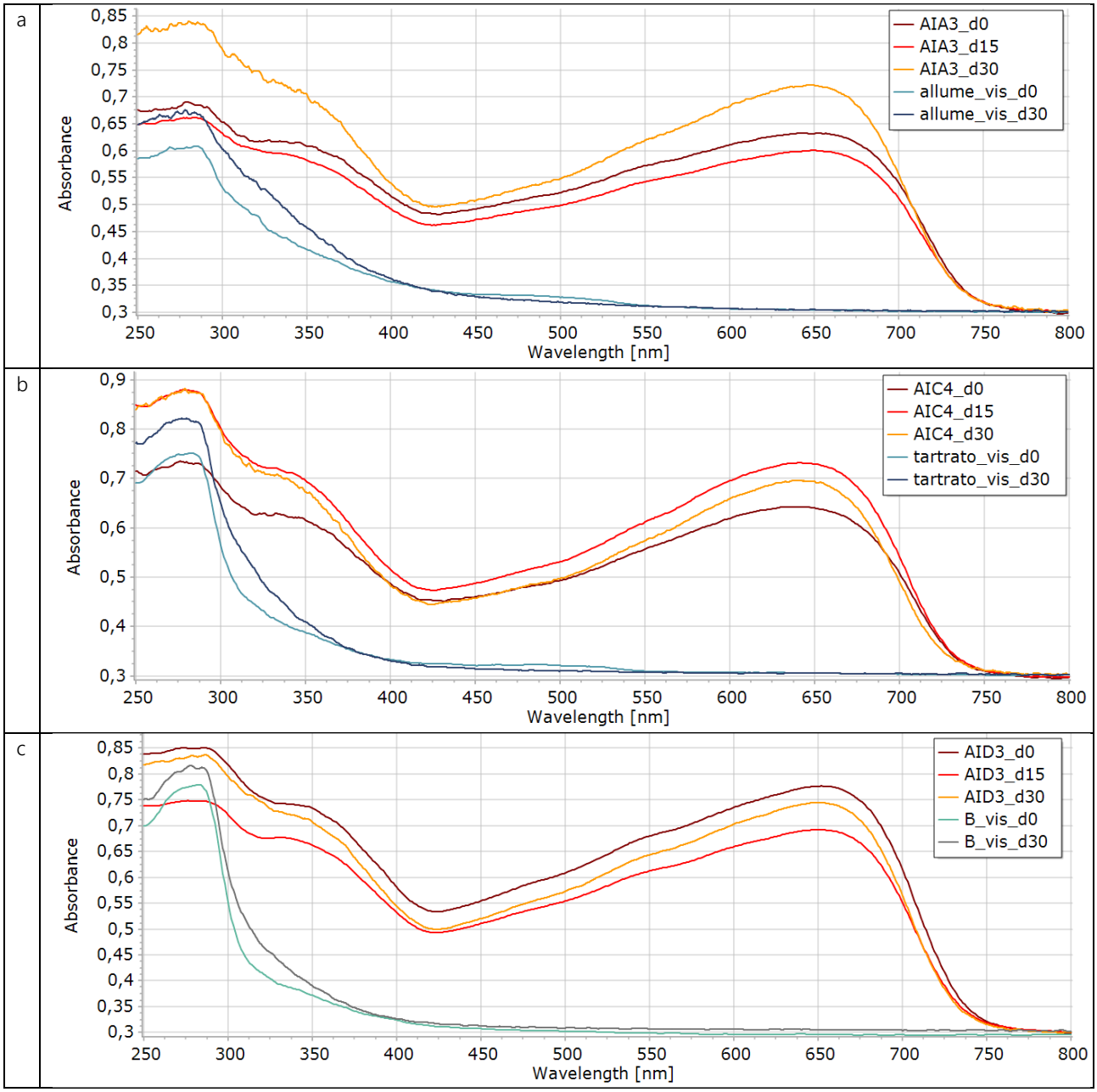

d

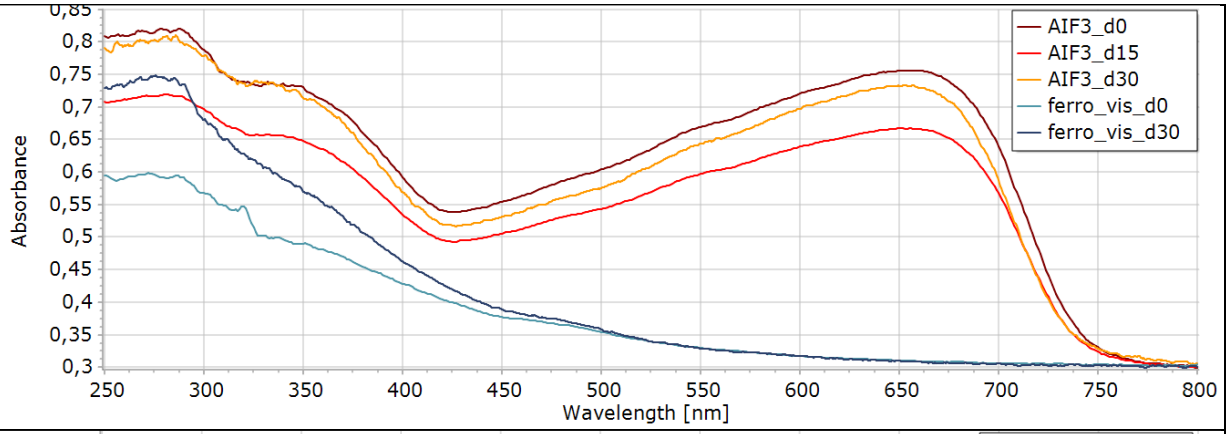

e

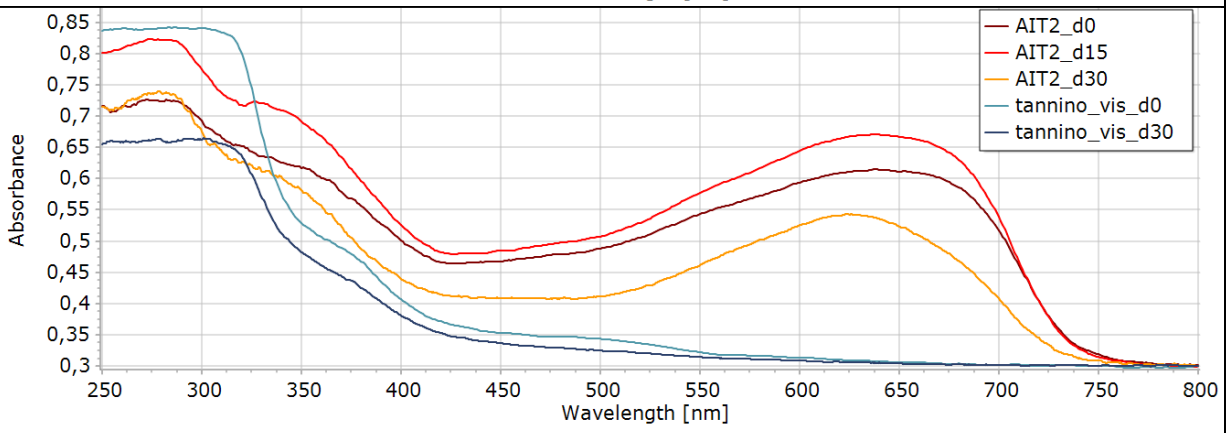

Figure 45. UV-Vis spectra of silk samples dyed with ai and aged with visible light. a) silk samples mordanted with potassium alum, b) silk samples mordanted with potassium bitartrate, c) directly dyed silk samples, d) silk samples mordanted with iron sulfate, e) silk samples mordanted with tannic acid.

a

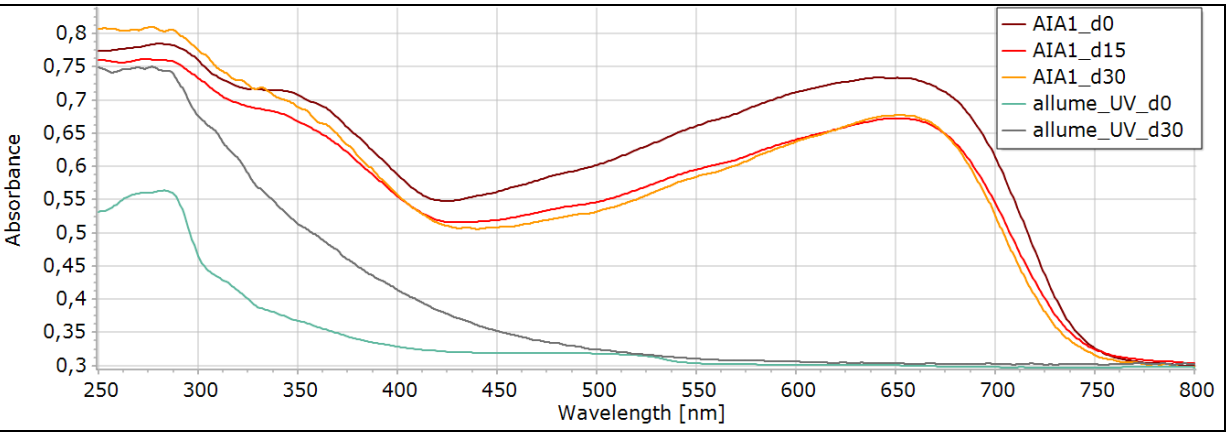

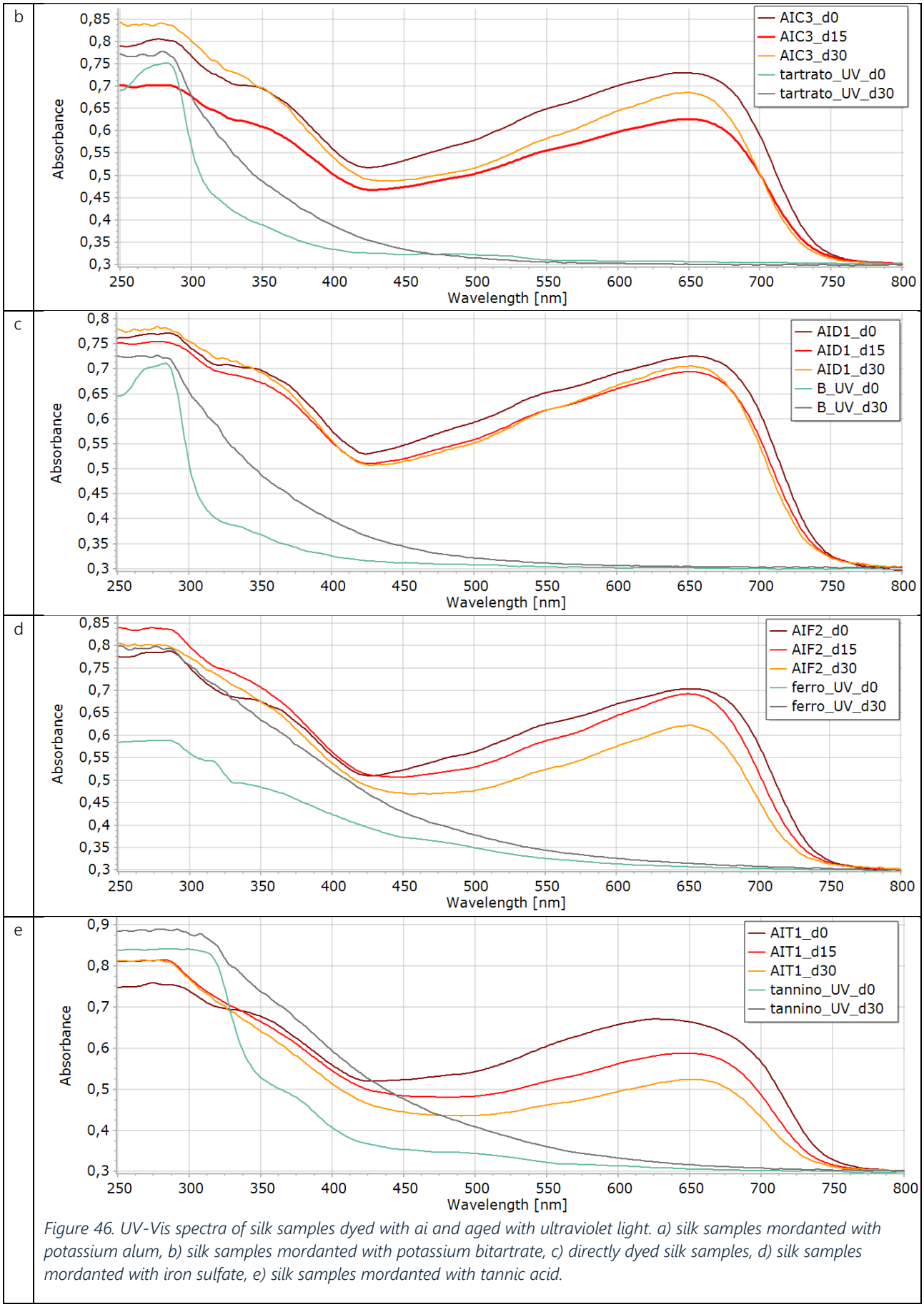

Figure 46. UV-Vis spectra of silk samples dyed with ai and aged with ultraviolet light. a) silk samples mordanted with potassium alum, b) silk samples mordanted with potassium bitartrate, c) directly dyed silk samples, d) silk samples mordanted with iron sulfate, e) silk samples mordanted with tannic acid.

The silk dyed with *ai* in all dye/mordant combinations shows no significant changes during visible ageing (Figure 45) and UV ageing (Figure 46). There is strong absorption in the visible region (450-750 nm) and a band appears in the range 325-400 nm, which does not seem to be significantly affected by the ageing.

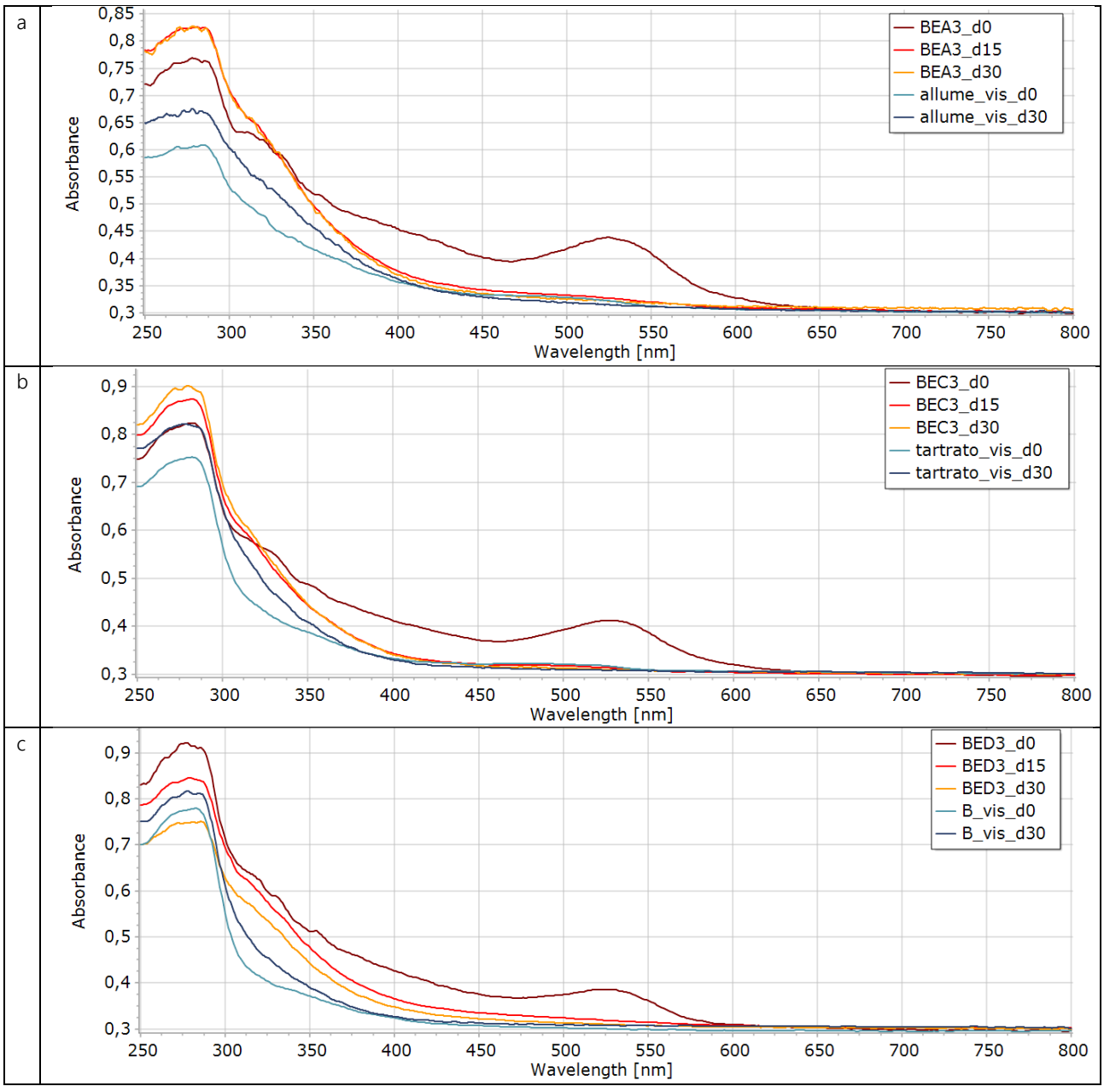

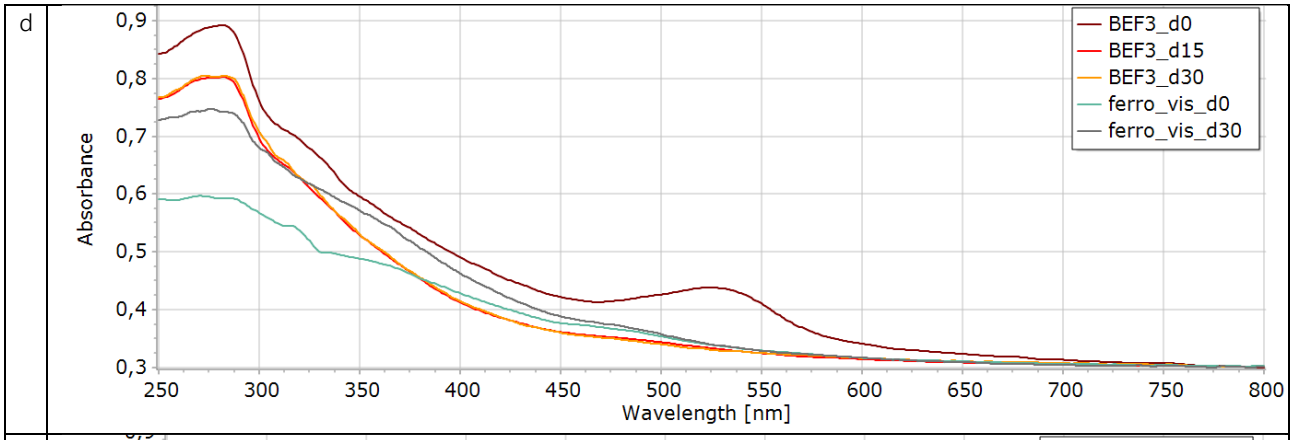

Figure 47. UV-Vis spectra of silk samples dyed with beni and aged with visible light. a) silk samples mordanted with potassium alum, b) silk samples mordanted with potassium bitartrate, c) directly dyed silk samples, d) silk samples mordanted with iron sulfate, e) silk samples mordanted with tannic acid.

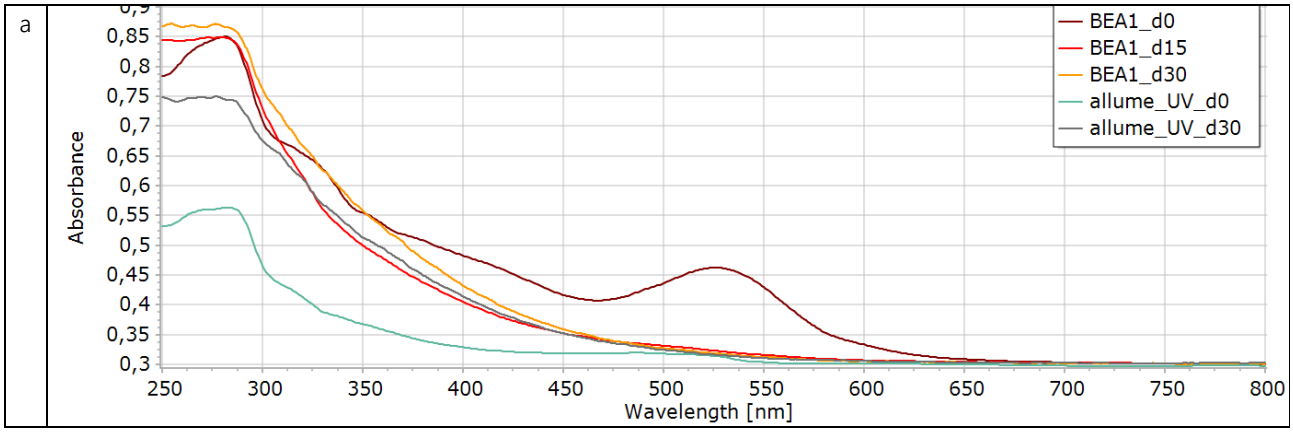

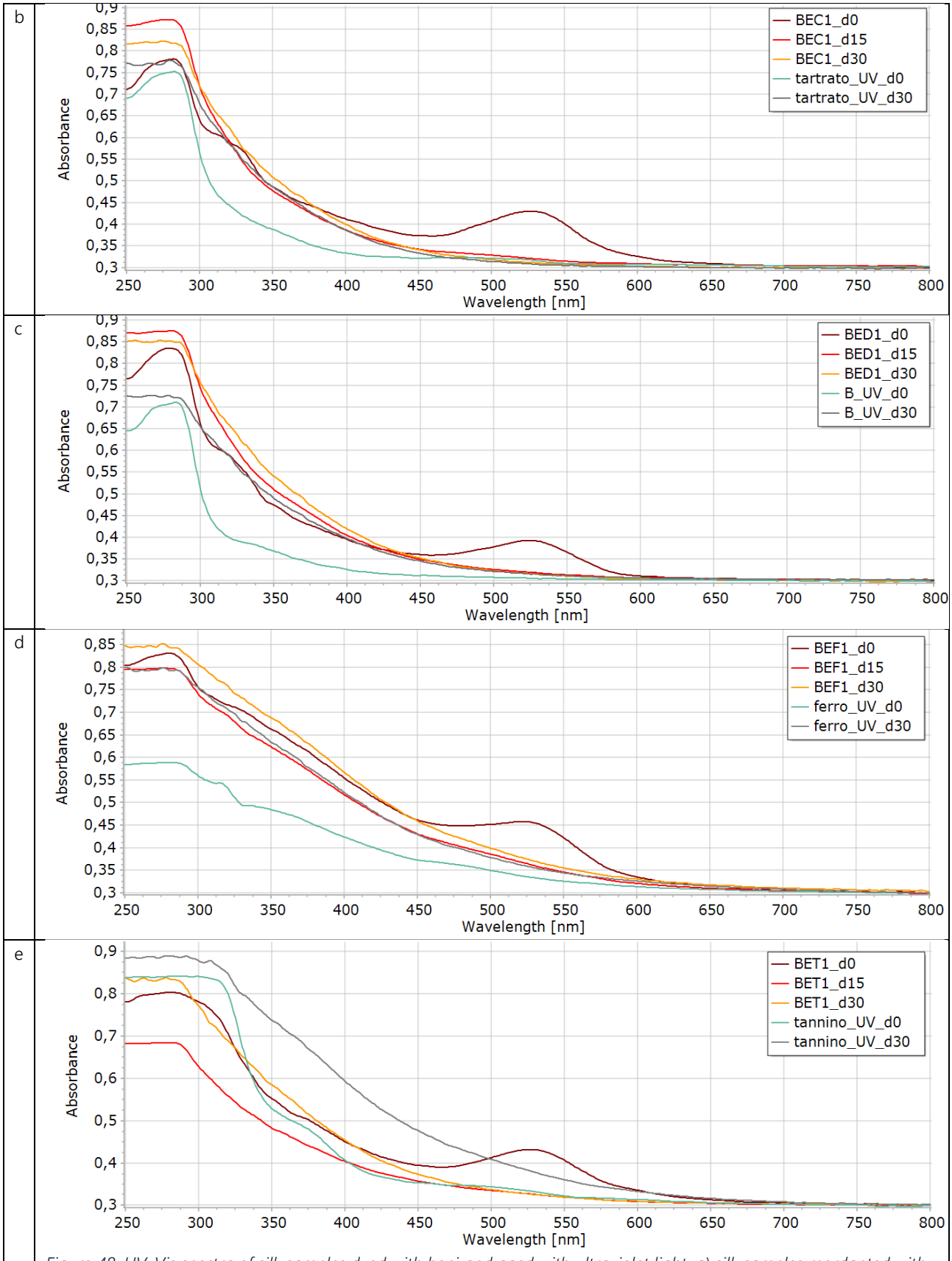

Figure 48. UV-Vis spectra of silk samples dyed with beni and aged with ultraviolet light. a) silk samples mordanted with potassium alum, b) silk samples mordanted with potassium bitartrate, c) directly dyed silk samples, d) silk samples mordanted with iron sulfate, e) silk samples mordanted with tannic acid.

Silk dyed with *beni* in all combinations with mordants and as a direct dye shows an absorption band centered at 525 nm before visible aging. After just 15 days of aging, the absorption band disappears under both visible (Figure 47) and UV ageing (Figure 48). The absorption bands at lower wavelengths (250-300 nm) are comparable to the absorption of the reference mordanted silk.

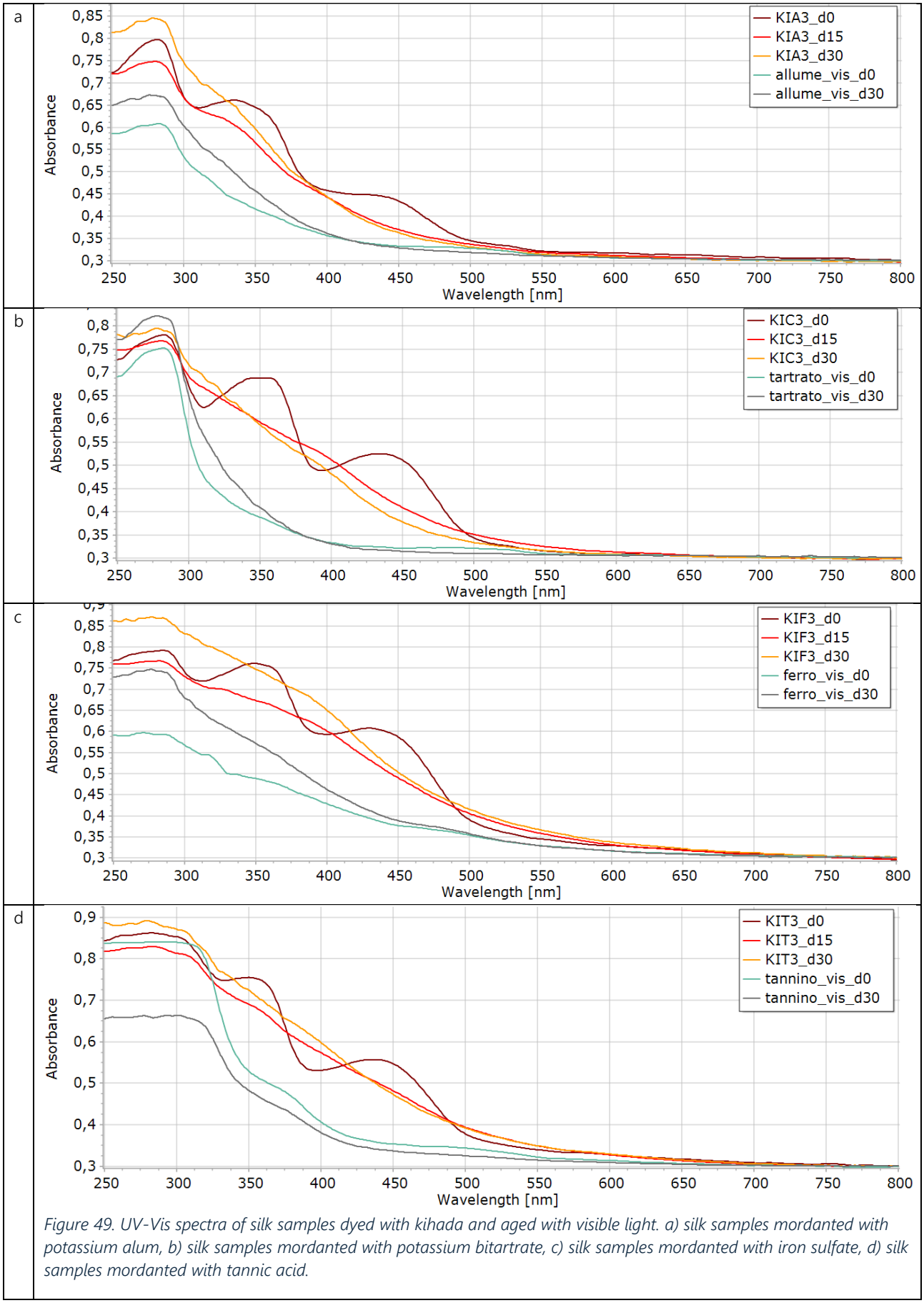

Figure 49. UV-Vis spectra of silk samples dyed with kihada and aged with visible light. a) silk samples mordanted with potassium alum, b) silk samples mordanted with potassium bitartrate, c) silk samples mordanted with iron sulfate, d) silk samples mordanted with tannic acid.

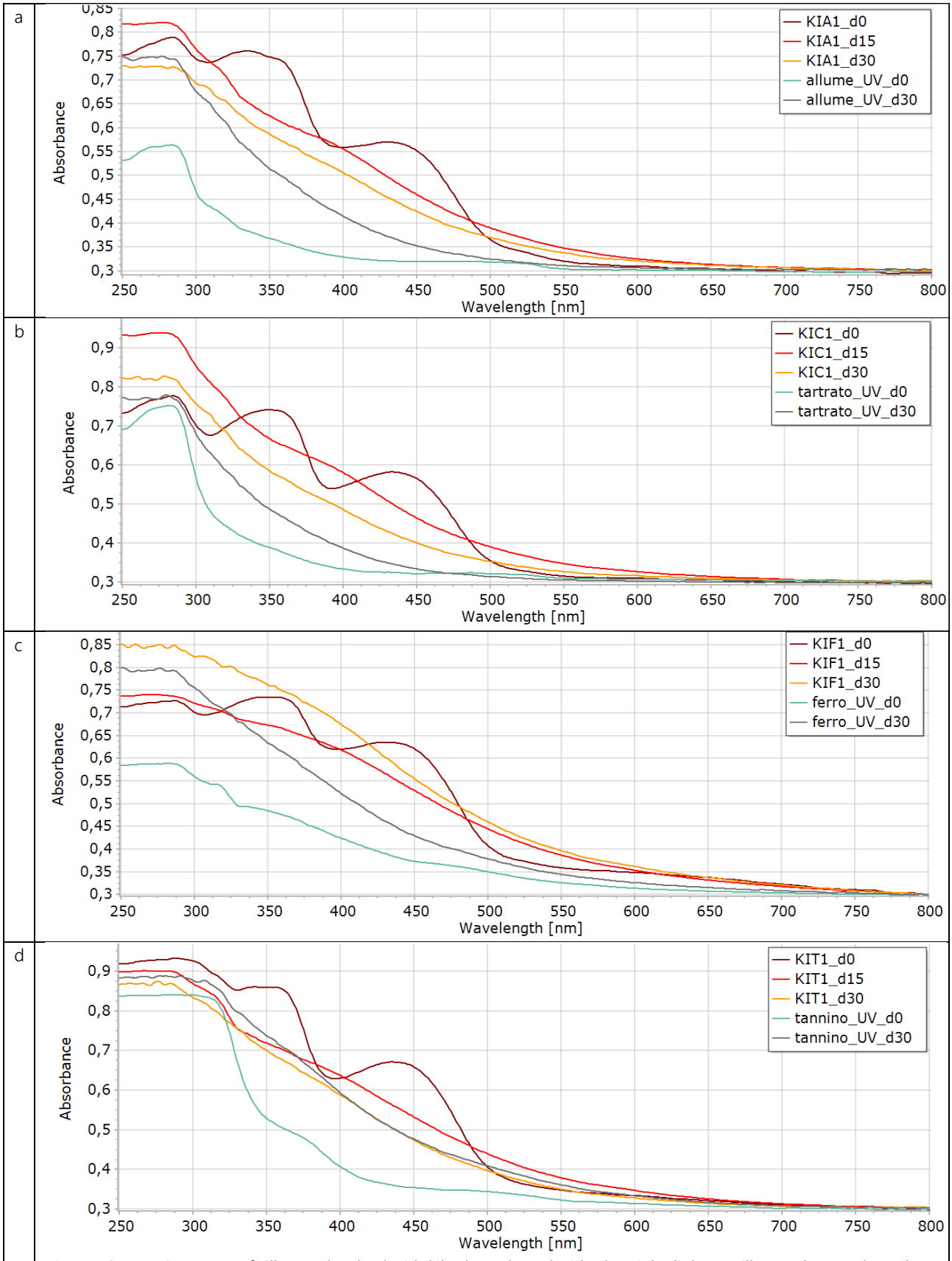

Figure 50. UV-Vis spectra of silk samples dyed with kihada and aged with ultraviolet light. a) silk samples mordanted with potassium alum, b) silk samples mordanted with potassium bitartrate, c) directly dyed silk samples, d) silk samples mordanted with iron sulfate, e) silk samples mordanted with tannic acid.

The spectra of silk samples dyed with *kihada* and the different mordants reveal two absorption regions, between 300-350 nm and 400-500 nm (Figure 49 and 50). The absorption bands at lower wavelengths (250-300 nm) are comparable to the absorption of the reference mordanted silk. After 15 days of aging (both visible and UV), the intensity of the bands decreases, with two peaks no longer distinguishable, but a continuous band between 300 and 450 nm.

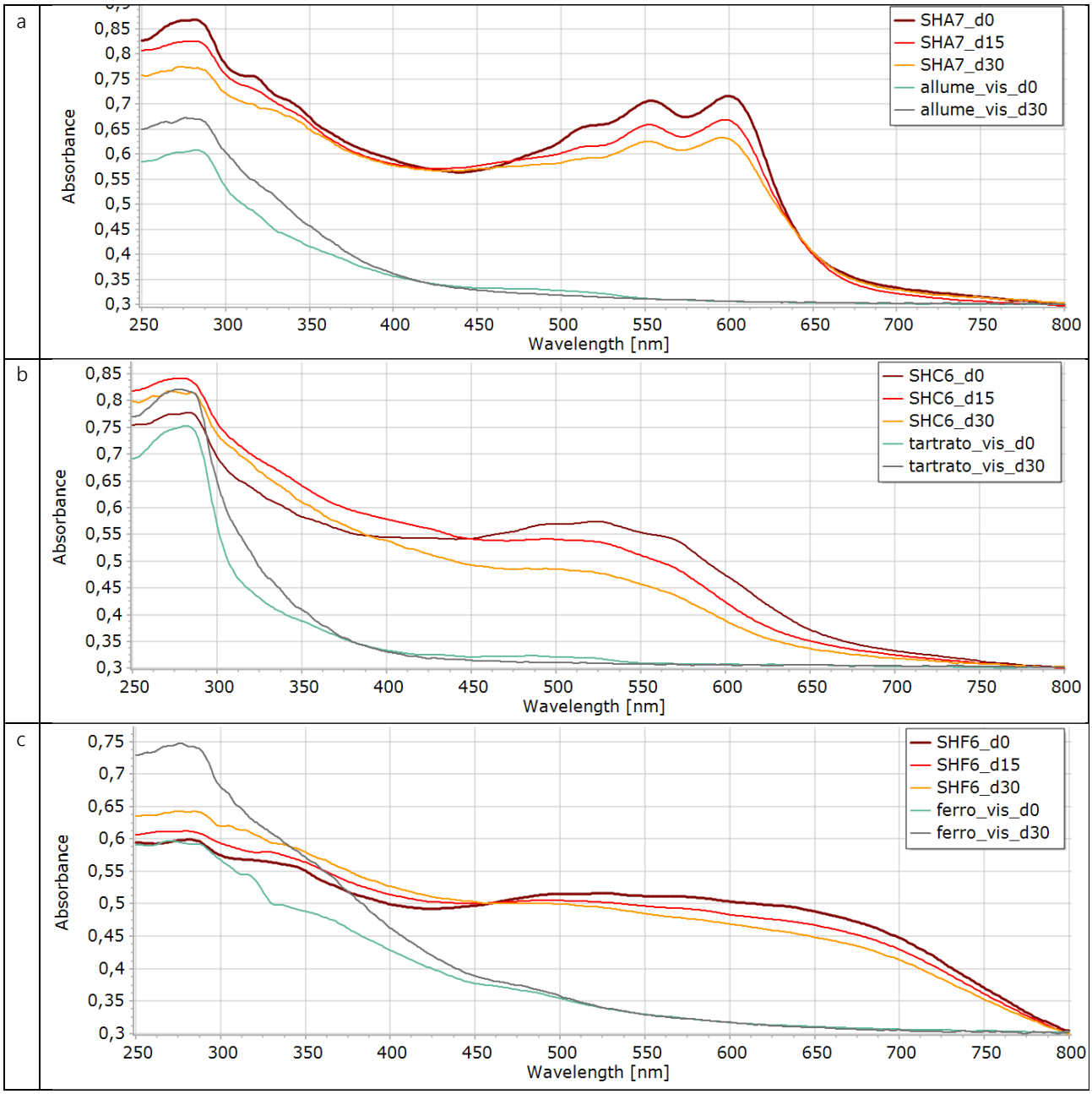

d

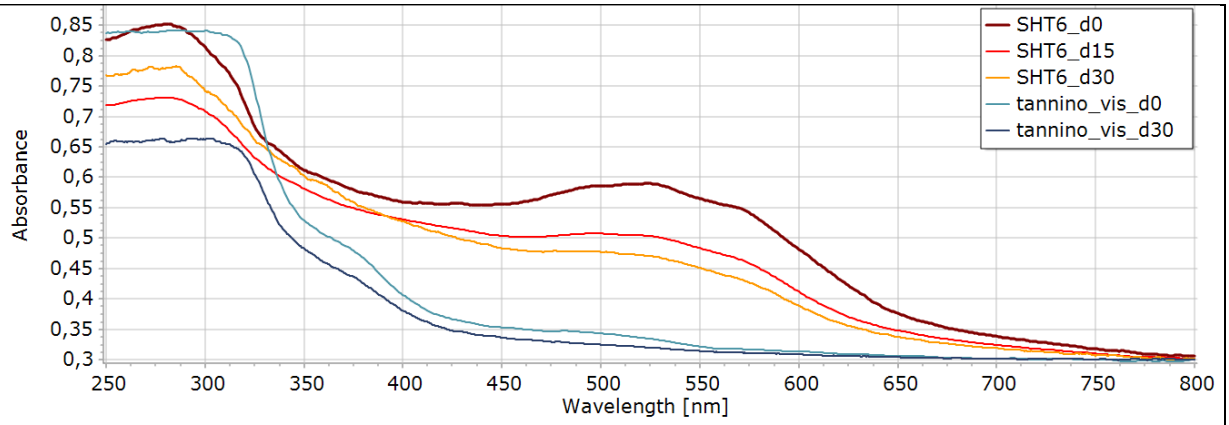

Figure 51. UV-Vis spectra of silk samples dyed with shikon and aged with visible light. a) silk samples mordanted with potassium alum, b) silk samples mordanted with potassium bitartrate, c) silk samples mordanted with iron sulfate, d) silk samples mordanted with tannic acid.

a

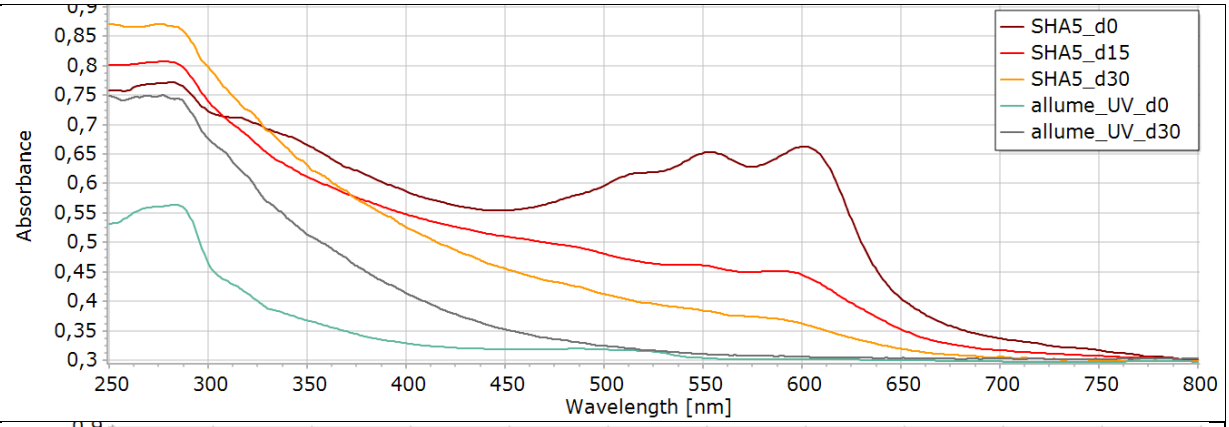

b

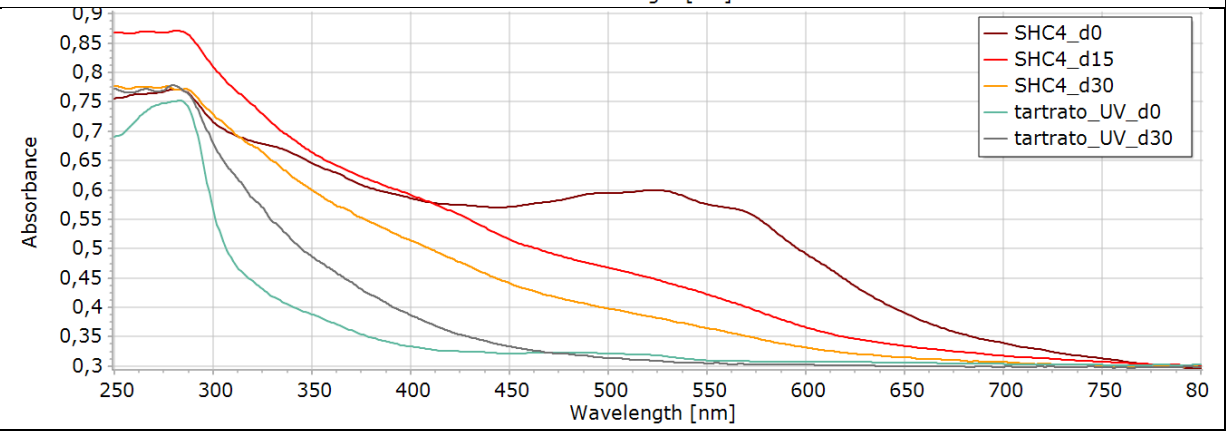

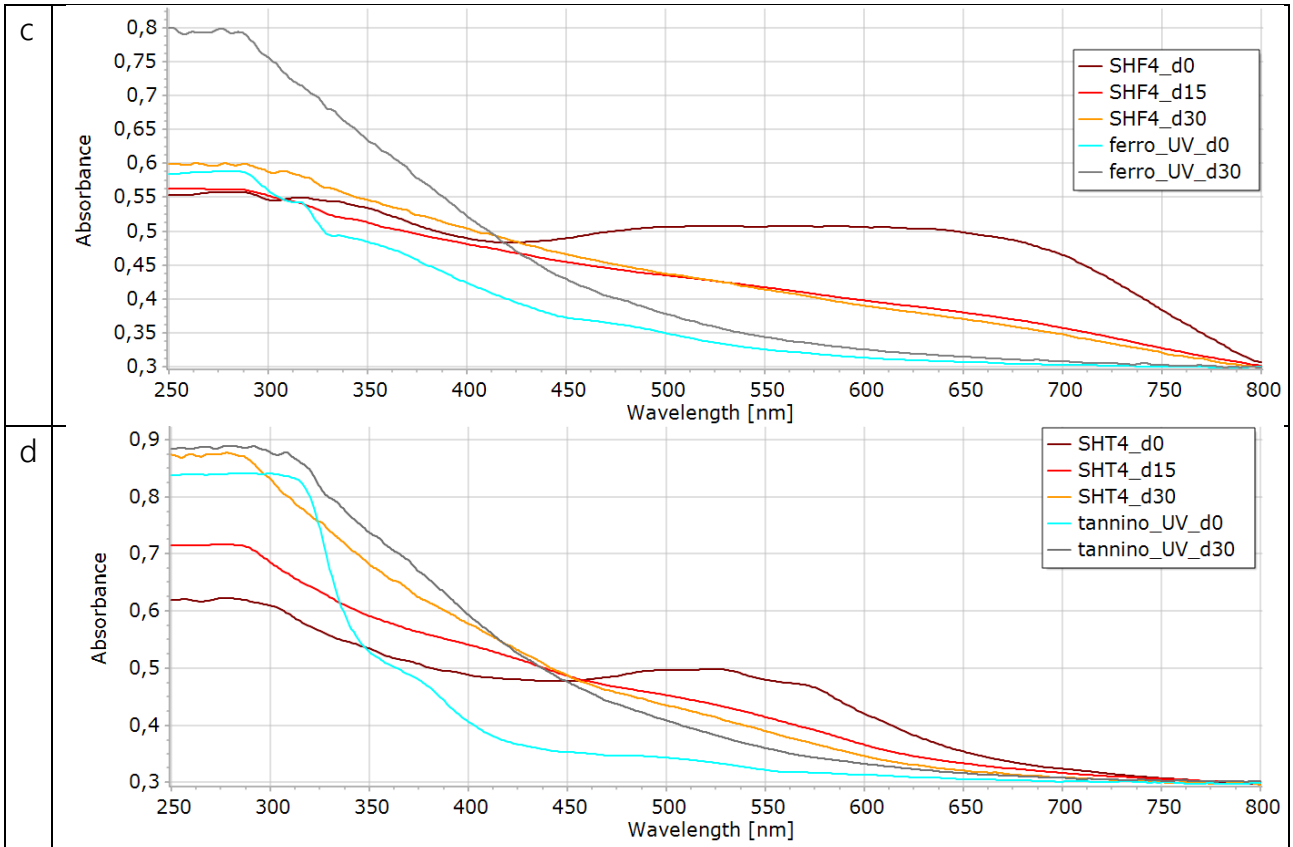

Figure 52. UV-Vis spectra of silk samples dyed with shikon and aged with ultraviolet light. a) silk samples mordanted with potassium alum, b) silk samples mordanted with potassium bitartrate, c) directly dyed silk samples, d) silk samples mordanted with iron sulfate, e) silk samples mordanted with tannic acid.

The dye *shikon*, associated with the four different mordants, shows significant absorption changes due to the interaction of the dye with each mordant (Figure 51-52). Strong absorption occurs in the 325-750 nm range for samples dyed and mordanted with potassium alum (SHA5) and potassium bitartrate (SHC4). With iron sulfate (SHF5), broad absorption is observed covering the 400-800 nm range. The sample dyed and mordanted with tannic acid (SHT4) absorbs in the 450-700 nm range. The trends do not change over time due to visible light, except for slight intensity differences compared to unaged dyed silk.

After UV aging, all samples show a drastic reduction in absorption in the visible region, especially in SHC4 and SHT4 samples. The ultraviolet region absorptions are attributable to the reference mordant.

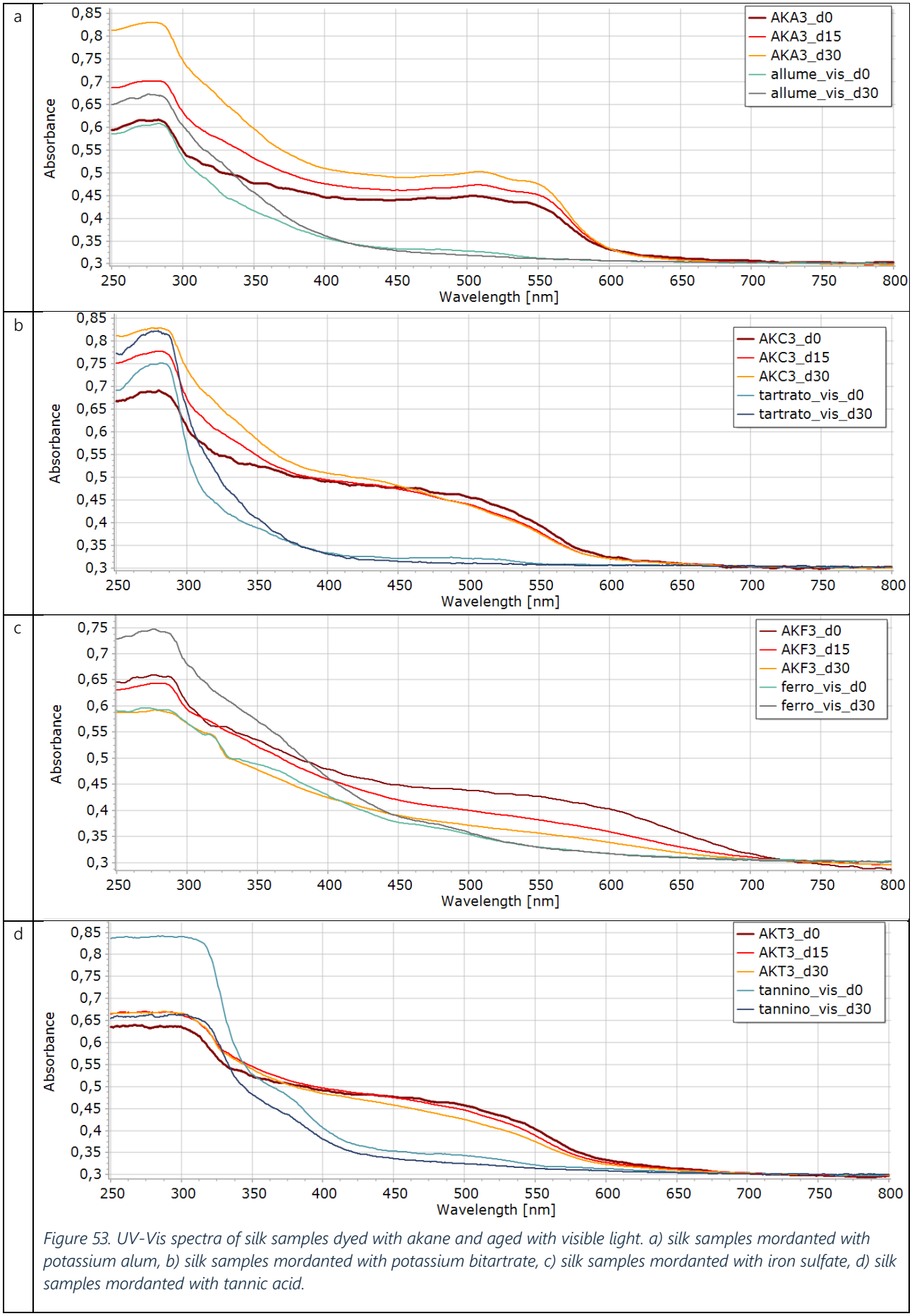

Figure 53. UV-Vis spectra of silk samples dyed with akane and aged with visible light. a) silk samples mordanted with potassium alum, b) silk samples mordanted with potassium bitartrate, c) silk samples mordanted with iron sulfate, d) silk samples mordanted with tannic acid.

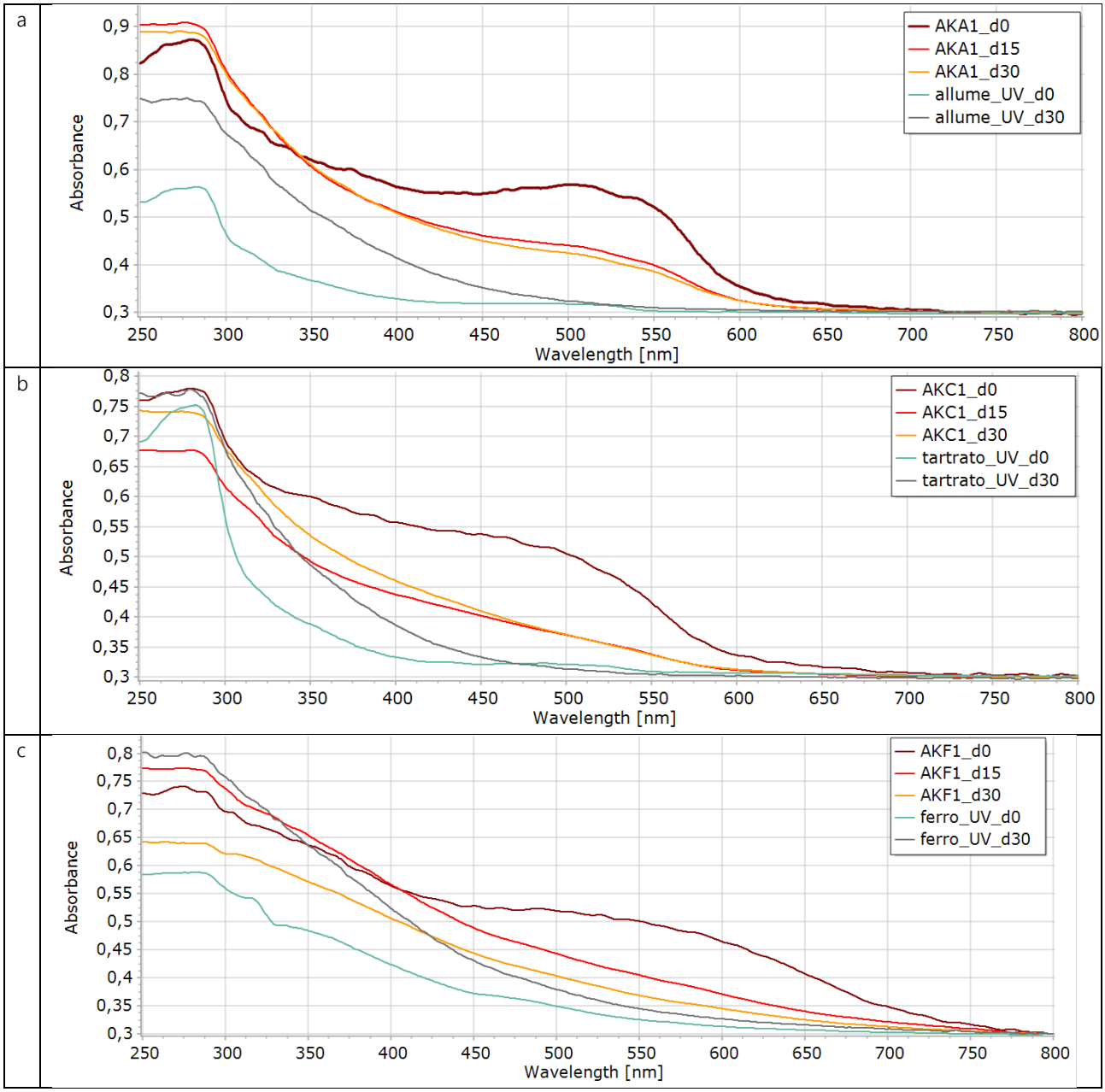
a
Absorbance
Wavelength [nm]
AKA1_d0
AKA1_d15
AKA1_d30
allume_UV_d0
allume_UV_d30
b
Absorbance
Wavelength [nm]
AKC1_d0
AKC1_d15
AKC1_d30
tartrato_UV_d0
tartrato_UV_d30
c
Absorbance
Wavelength [nm]
AKF1_d0
AKF1_d15
AKF1_d30
ferro_UV_d0
ferro_UV_d30

d

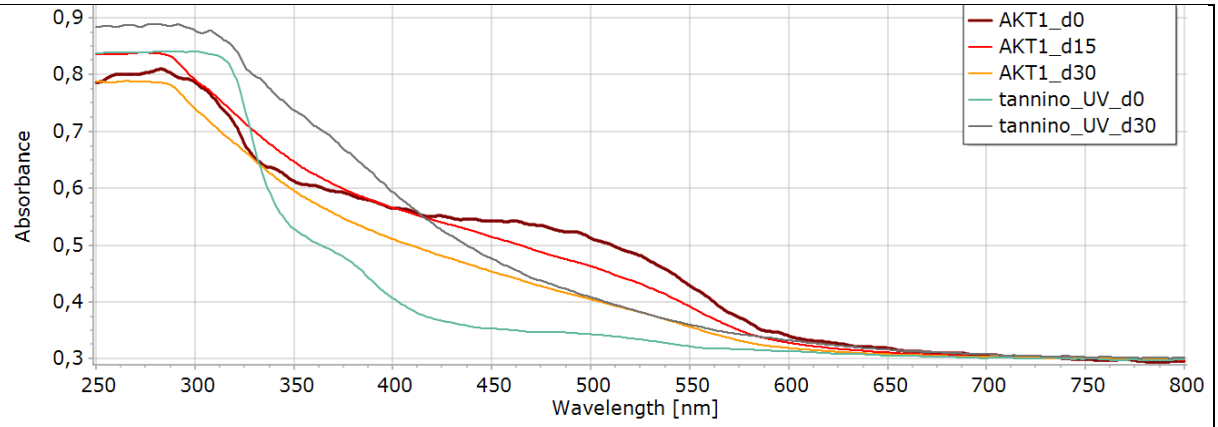

Figure 54. UV-Vis spectra of silk samples dyed with akane and aged with ultraviolet light. a) silk samples mordanted with potassium alum, b) silk samples mordanted with potassium bitartrate, c) silk samples mordanted with iron sulfate, d) silk samples mordanted with tannic acid.

The dye *akane*, associated with the four different mordants, shows significant absorption changes due to the interaction of the dye with each mordant (Figure 53-54). No significant changes occur over time due to visible light. The ultraviolet region absorptions are attributable to the reference mordant.

After 30 days of UV ageing, the samples mordanted with potassium alum and tannic acid still show absorption in the visible region, although with lower intensity than at zero time. For the other mordants, the absorption is much lower, with a trend mainly attributable to the curves of the reference mordants.

a

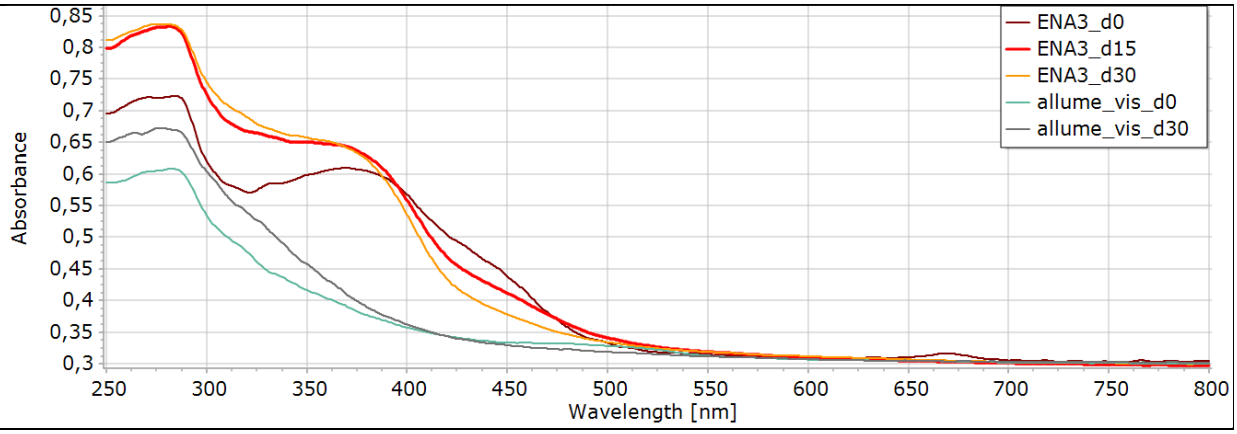

b

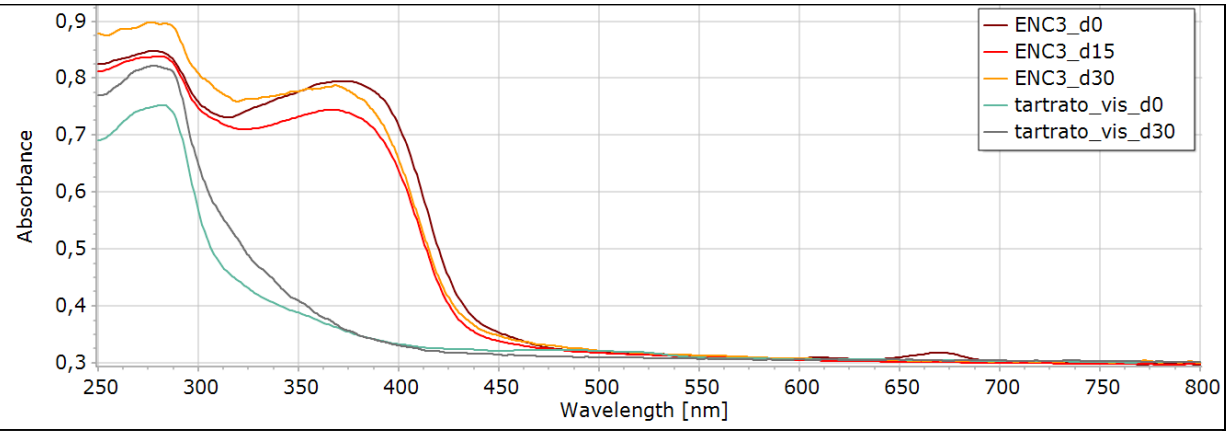

c

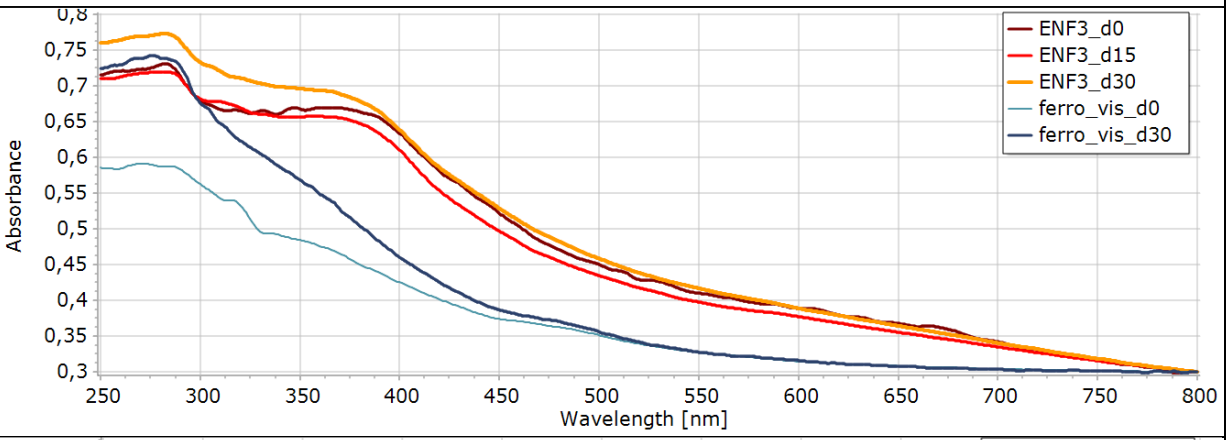

d

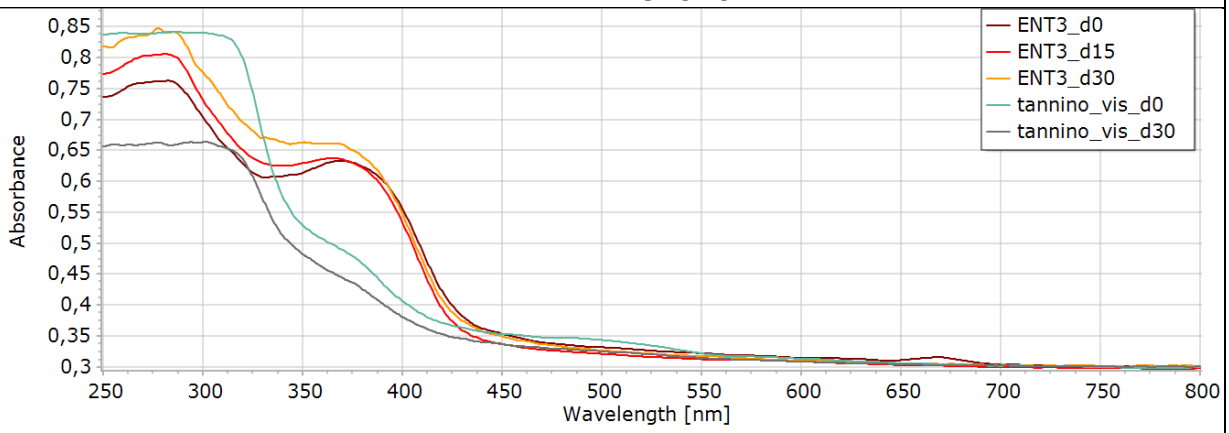

Figure 55. UV-Vis spectra of silk samples dyed with enju and aged with visible light. a) silk samples mordanted with potassium alum, b) silk samples mordanted with potassium bitartrate, c) silk samples mordanted with iron sulfate, d) silk samples mordanted with tannic acid.

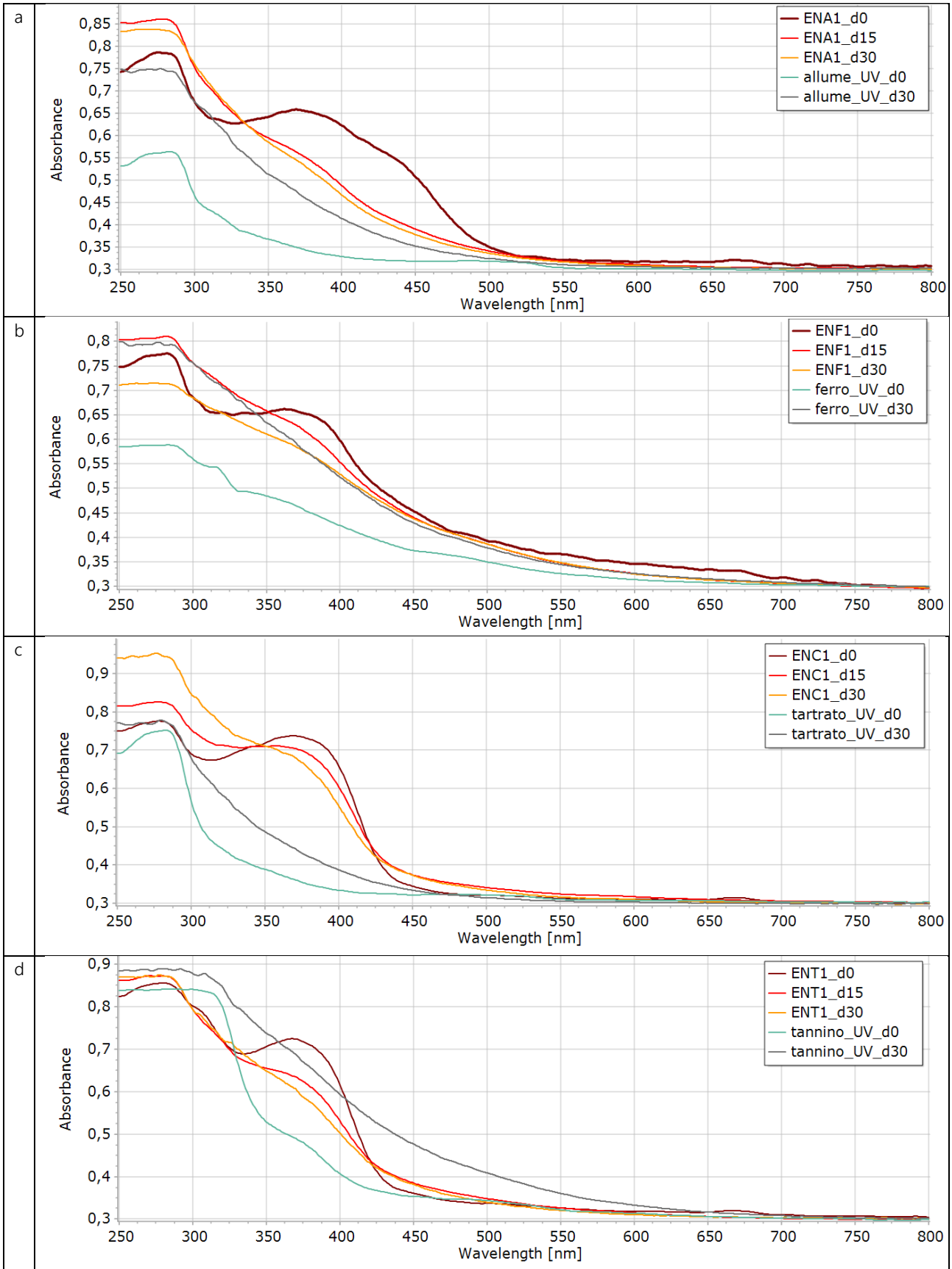

Figure 56. UV-Vis spectra of silk samples dyed with enju and aged with ultraviolet light. a) silk samples mordanted with potassium alum, b) silk samples mordanted with potassium bitartrate, c) silk samples mordanted with iron sulfate, d) silk samples mordanted with tannic acid.

The dye *enju*, associated with the four different mordants, shows significant absorption changes due to the interaction of the dye with each mordant (Figure 55-56). No significant changes during visible aging. The ultraviolet region absorptions are attributable to the reference mordant.

In the case of UV ageing, the samples showing absorption after 30 days of aging are ENC1 and ENT1, mordanted with potassium bitartrate and tannic acid, respectively. For ENA1 and ENF1, mordanted with potassium alum and iron sulfate, respectively, the intensity of the peaks decreases during aging. The ultraviolet region absorptions are attributable to the reference mordant.

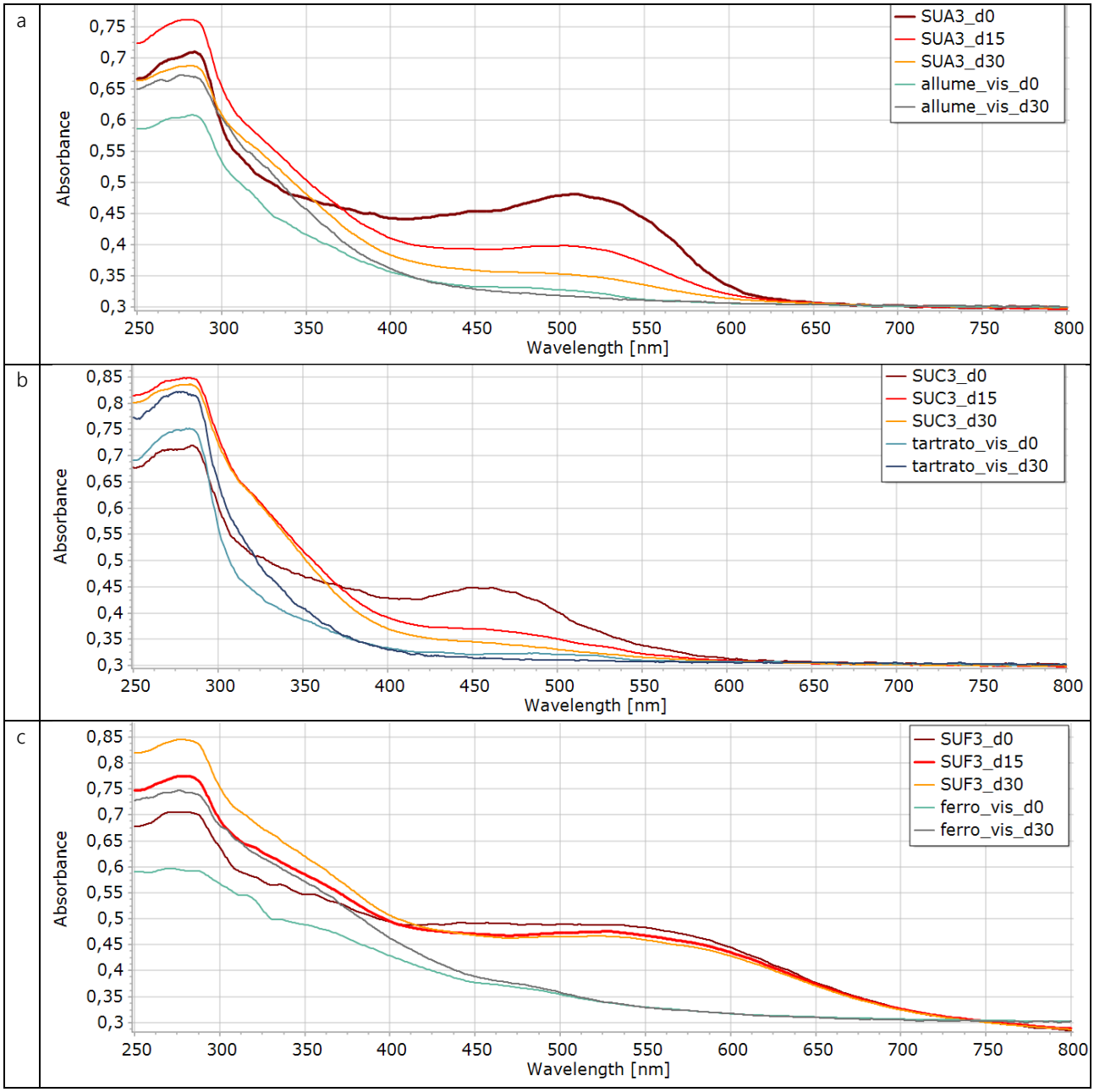

d

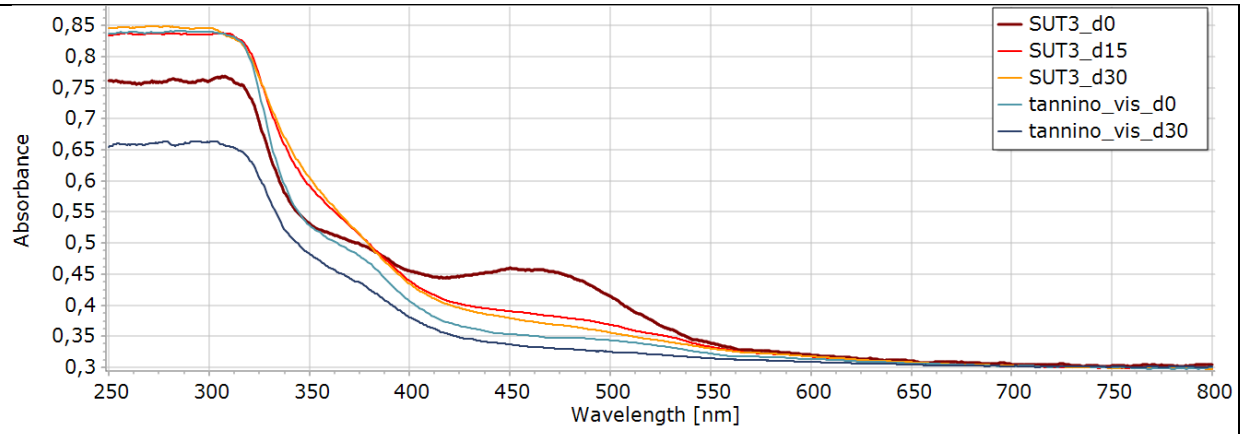

Figure 57. UV-Vis spectra of silk samples dyed with suo and aged with visible light. a) silk samples mordanted with potassium alum, b) silk samples mordanted with potassium bitartrate, c) silk samples mordanted with iron sulfate, d) silk samples mordanted with tannic acid.

a

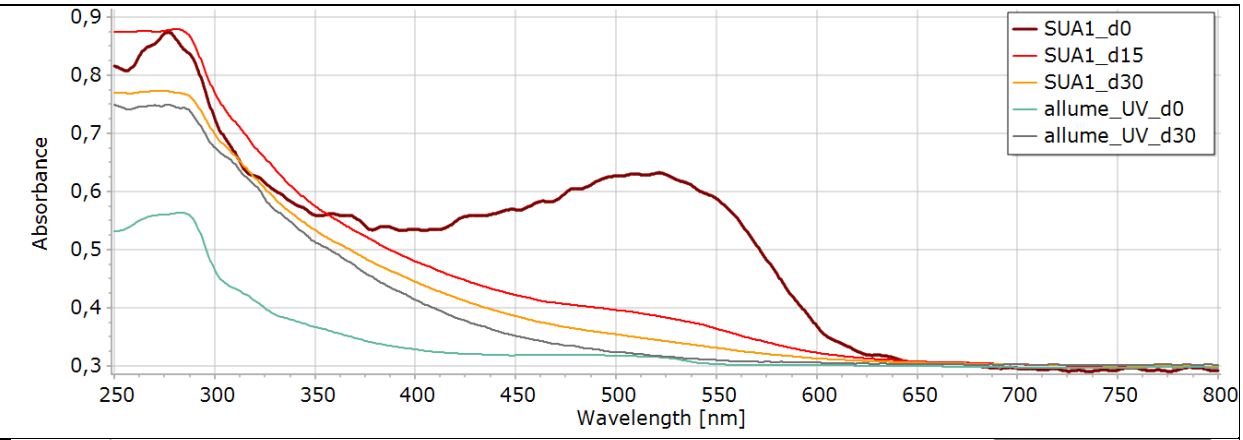

b

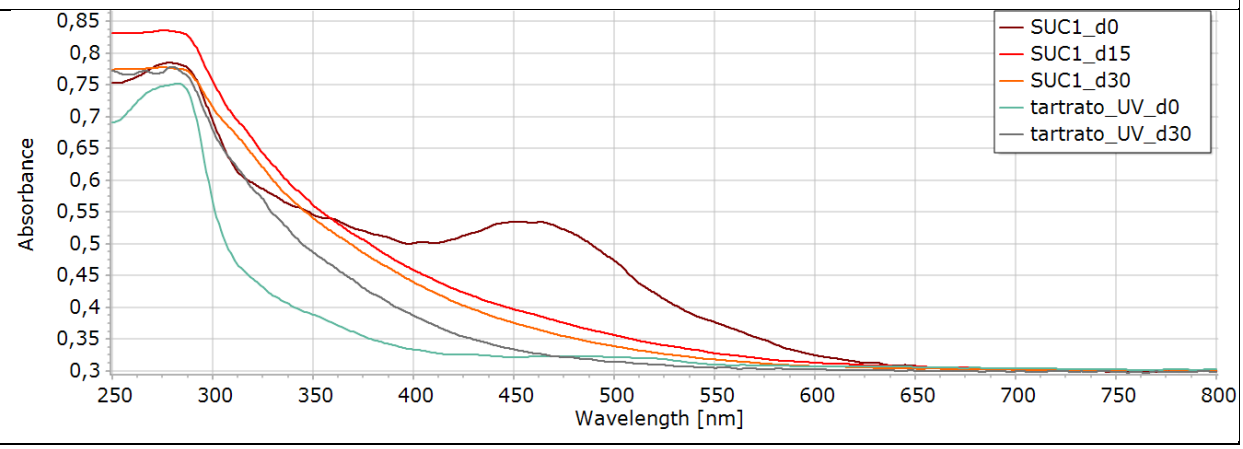

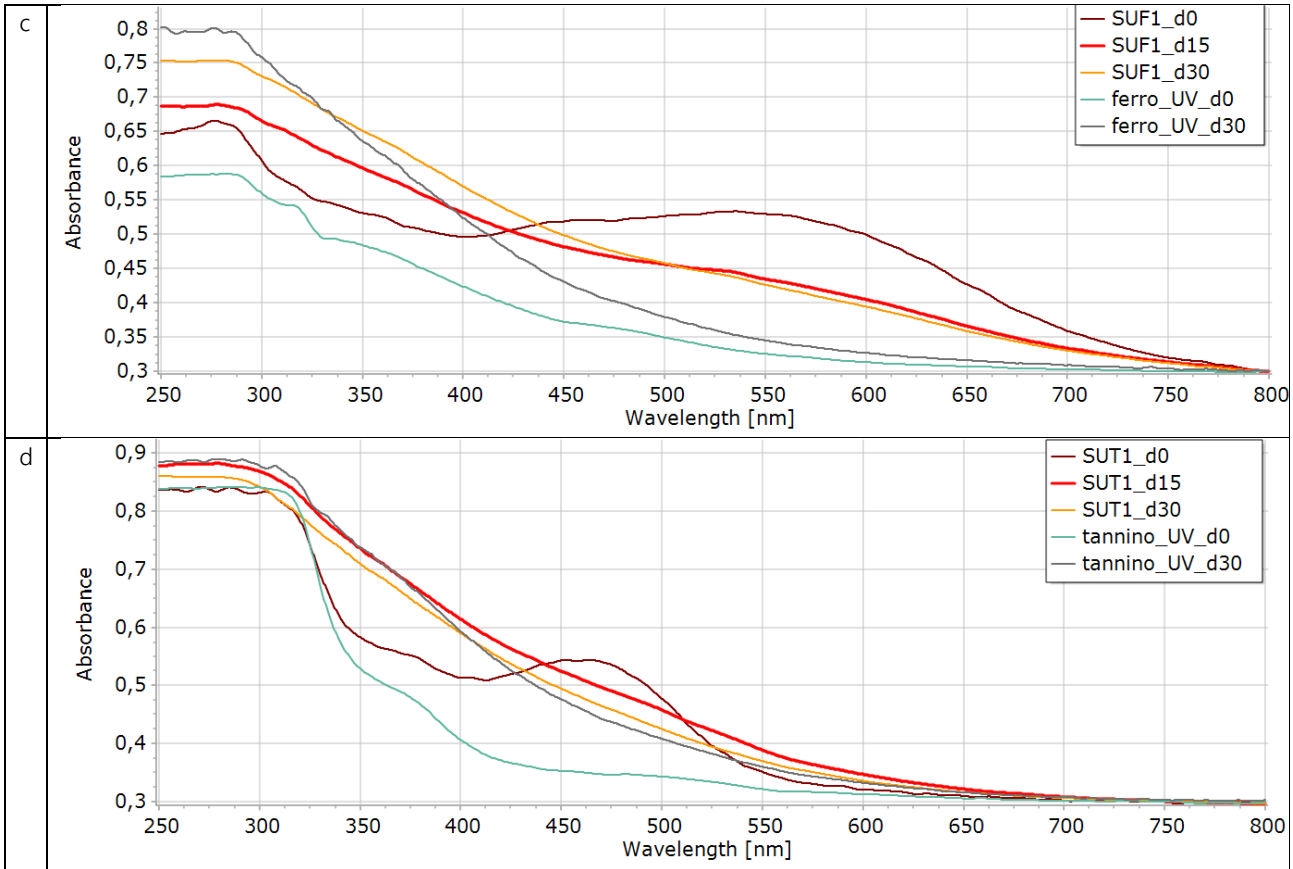

Figure 58. UV-Vis spectra of silk samples dyed with suo and aged with ultraviolet light. a) silk samples mordanted with potassium alum, b) silk samples mordanted with potassium bitartrate, c) silk samples mordanted with iron sulfate, d) silk samples mordanted with tannic acid.

The dye *suo*, associated with the four different mordants, shows significant absorption changes in the 350-600 nm range due to the interaction of the dye with each mordant (Figure 57-58). In particular, the sample dyed with iron sulfate absorbs over a larger spectral range (320-750 nm). Under visible light, the dye *suo* shows absorption changes over time, especially with potassium alum (with intensity differences over time), potassium bitartrate, and tannic acid. However, with iron sulfate, there are no significant absorption changes over time. Additionally, the ultraviolet region absorptions are attributable to the reference mordant.

After UV ageing, all samples, except the one with iron sulfate, show a drastic reduction in absorption in the visible region. The ultraviolet region absorptions are attributable to the reference mordant.

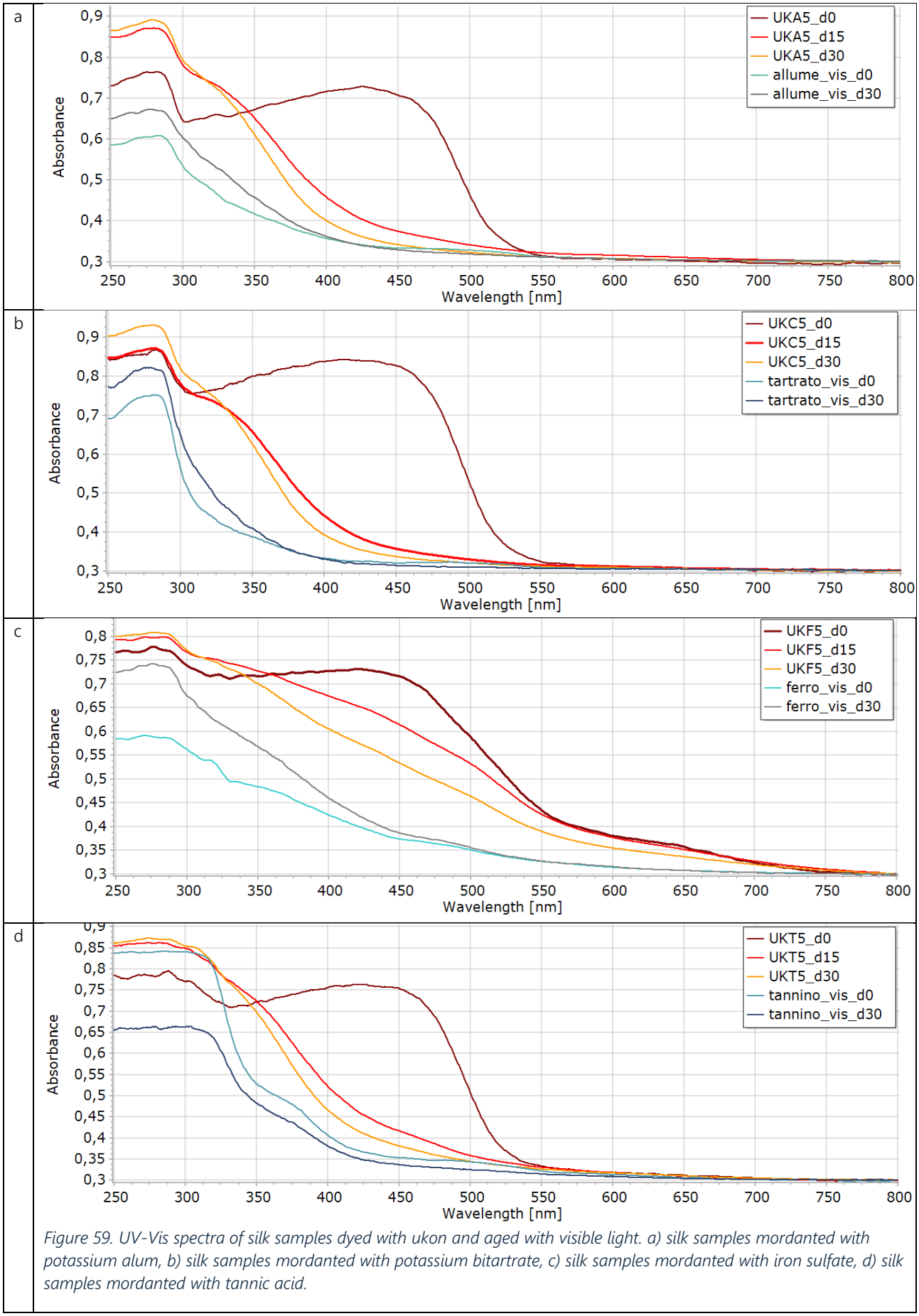

Figure 59. UV-Vis spectra of silk samples dyed with ukon and aged with visible light. a) silk samples mordanted with potassium alum, b) silk samples mordanted with potassium bitartrate, c) silk samples mordanted with iron sulfate, d) silk samples mordanted with tannic acid.

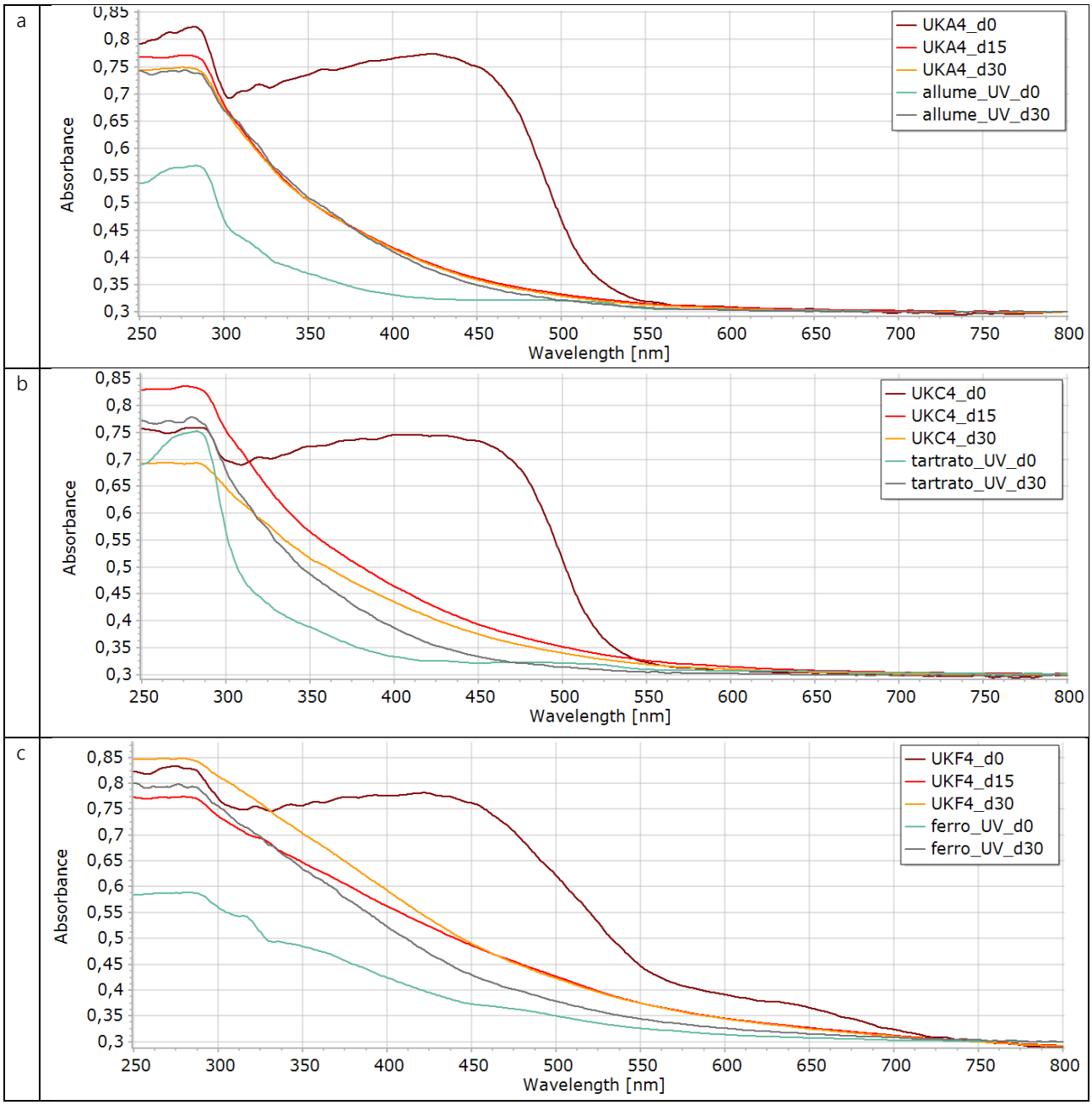
a
Absorbance
Wavelength [nm]
UKA4_d0
UKA4_d15
UKA4_d30
allume_UV_d0
allume_UV_d30
b
Absorbance
Wavelength [nm]
UKC4_d0
UKC4_d15
UKC4_d30
tartrato_UV_d0
tartrato_UV_d30
c
Absorbance
Wavelength [nm]
UKF4_d0
UKF4_d15
UKF4_d30
ferro_UV_d0
ferro_UV_d30

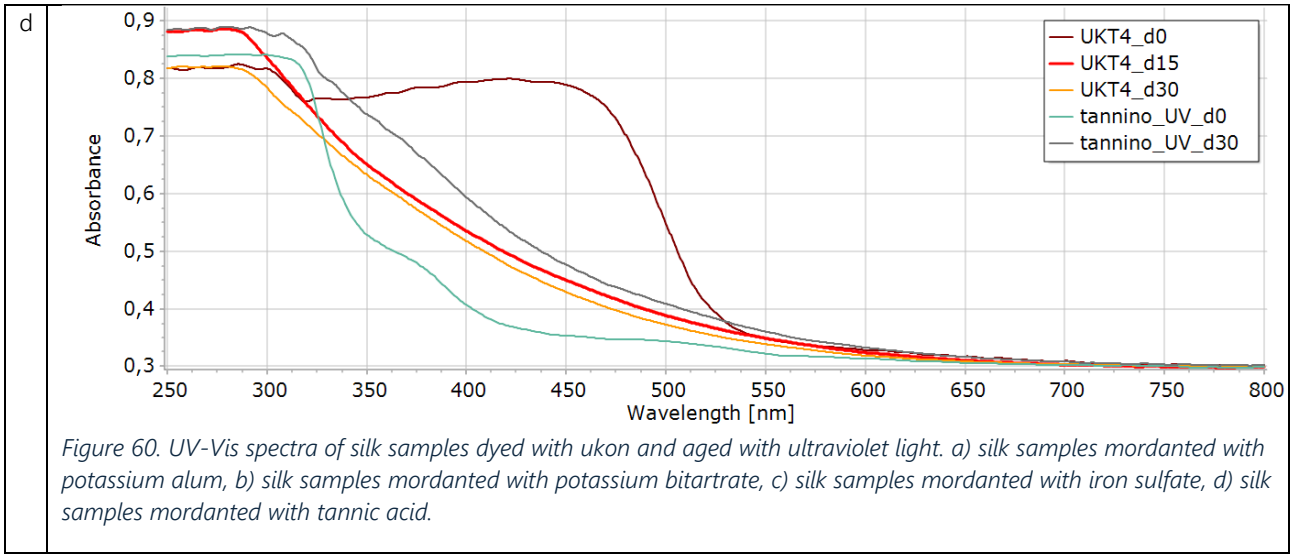

Figure 60. UV-Vis spectra of silk samples dyed with ukon and aged with ultraviolet light. a) silk samples mordanted with potassium alum, b) silk samples mordanted with potassium bitartrate, c) silk samples mordanted with iron sulfate, d) silk samples mordanted with tannic acid.

The dye *ukon* (Figure 59-60) associated with the four different mordants shows strong absorption before aging (300-550 nm, extending to 700 nm with iron sulfate). During visible aging, with all mordants except iron sulfate, a dramatic reduction in absorption is observed, creating a lower intensity band shifted to 300-400 nm. For the sample mordanted with iron sulfate (UKF5), absorption intensity changes over time are evident, although not as marked as with the other mordants. The ultraviolet region absorptions are attributable to the reference mordant.

During UV ageing, the absorption band is dramatically reduced. In the case of the sample associated with alum, the spectra at 15 and 30 days are superimposable to those of the reference mordant. Finally, the ultraviolet region absorptions for all dyed samples are attributable to the reference mordant.

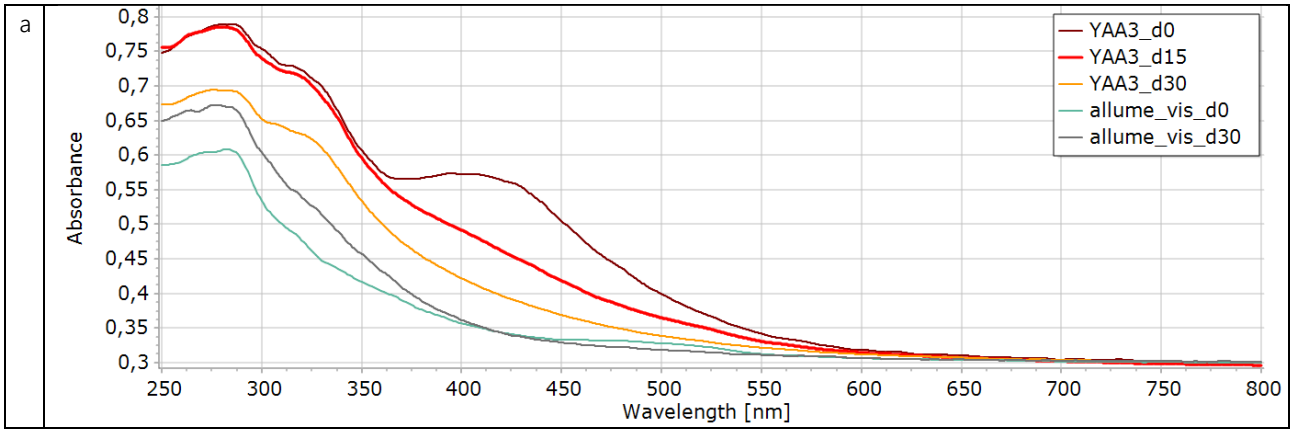

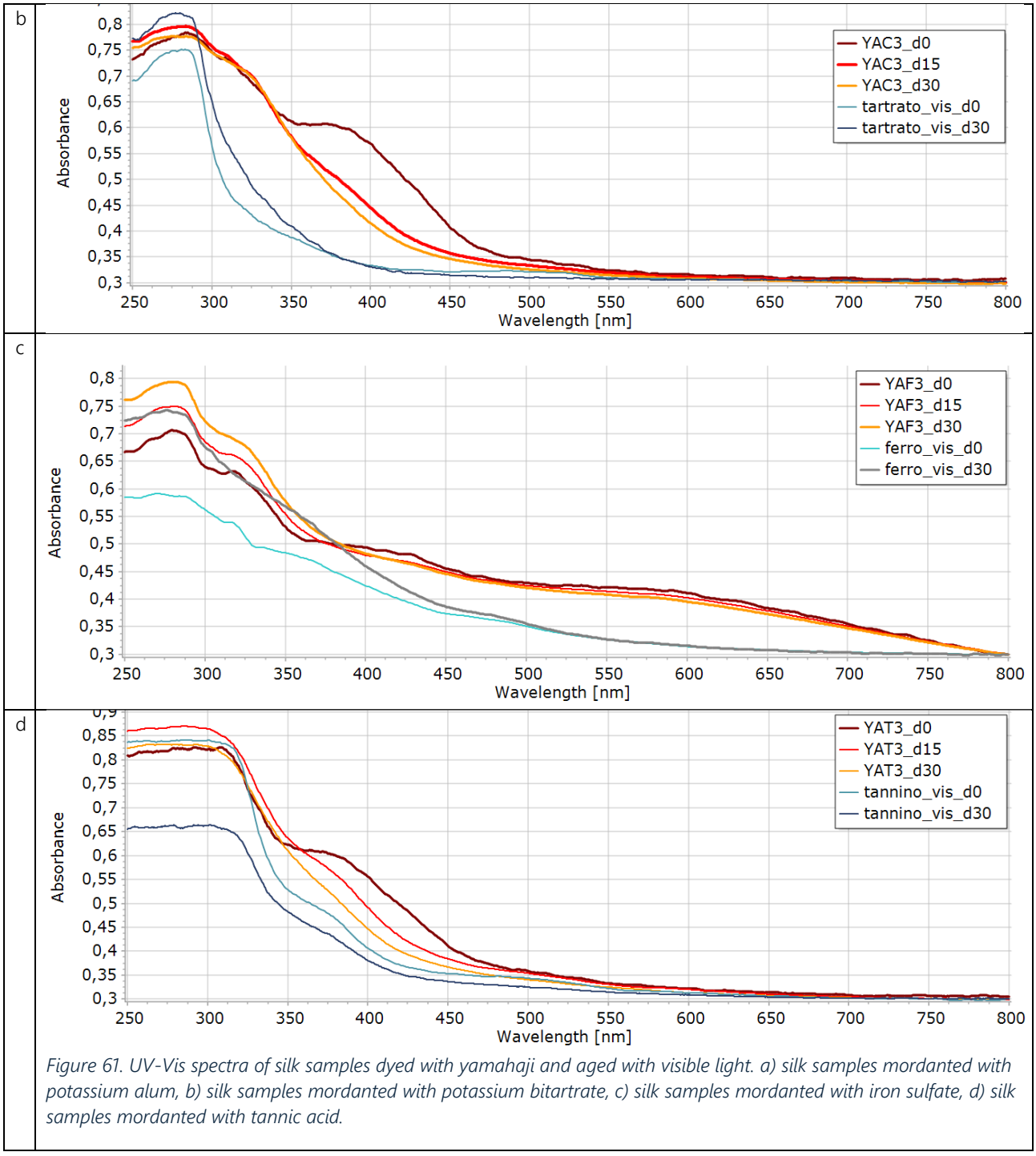

Figure 61. UV-Vis spectra of silk samples dyed with yamahaji and aged with visible light. a) silk samples mordanted with potassium alum, b) silk samples mordanted with potassium bitartrate, c) silk samples mordanted with iron sulfate, d) silk samples mordanted with tannic acid.

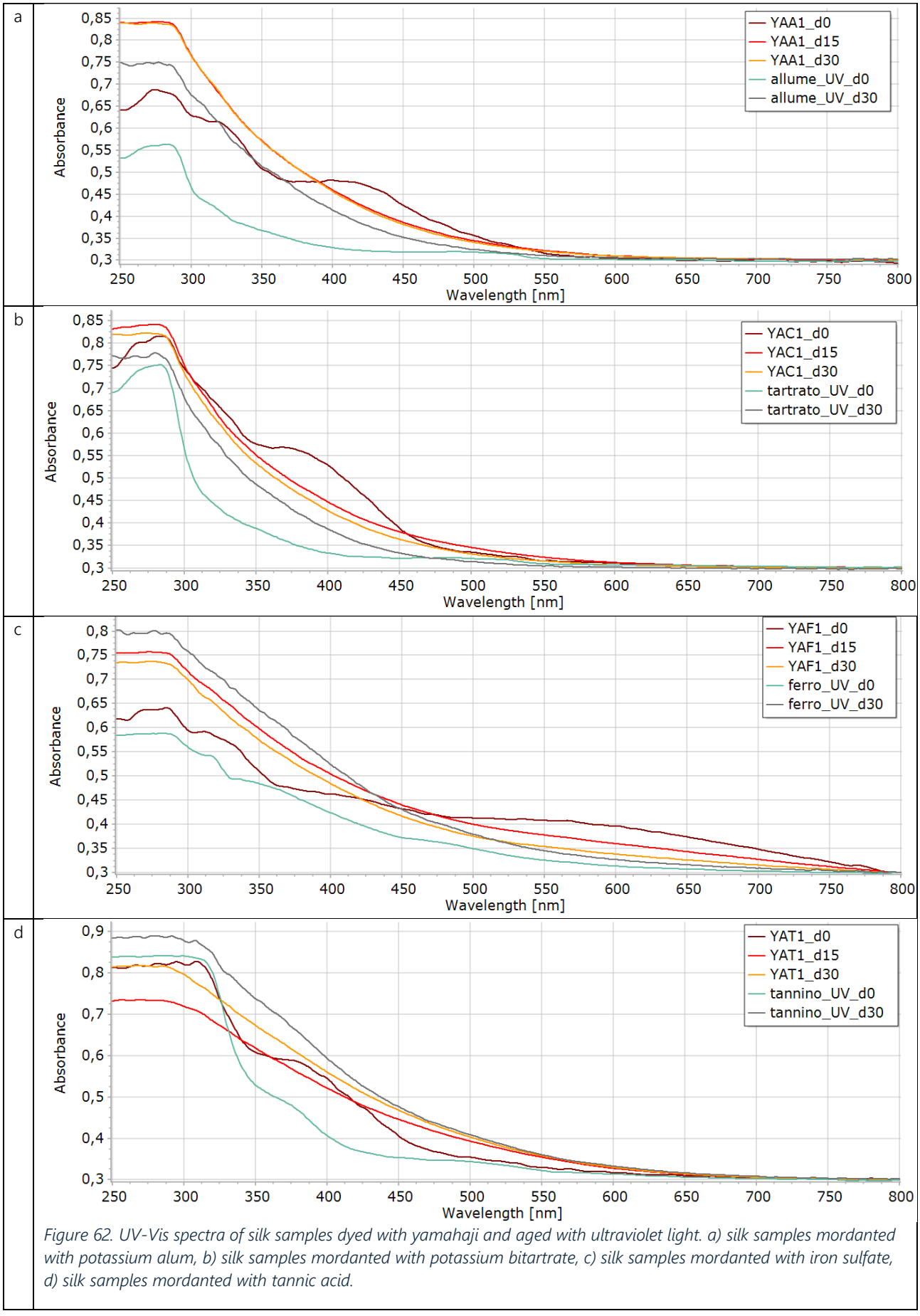

Figure 62. UV-Vis spectra of silk samples dyed with yamahaji and aged with ultraviolet light. a) silk samples mordanted with potassium alum, b) silk samples mordanted with potassium bitartrate, c) silk samples mordanted with iron sulfate, d) silk samples mordanted with tannic acid.

The dye *yamahaji* (Figure 61-62) associated with the mordants potassium alum, potassium bitartrate, and tannic acid shows absorption before aging in the 350-500 nm range, while with iron sulfate (YAF3), an extended band is present from 400 to 800 nm. For the first three combinations, during visible ageing, a significant reduction in absorption occurs. Compared to the mordanted-only samples, there is still absorption after 15 and 30 days of aging (350-400 nm). The YAF3 sample does not show significant changes during aging. The ultraviolet region absorptions are attributable to the reference mordant.

After UV aging, in all samples, the curves reflect those of the reference mordants.

3.7.3 ATR-FTIR spectroscopy

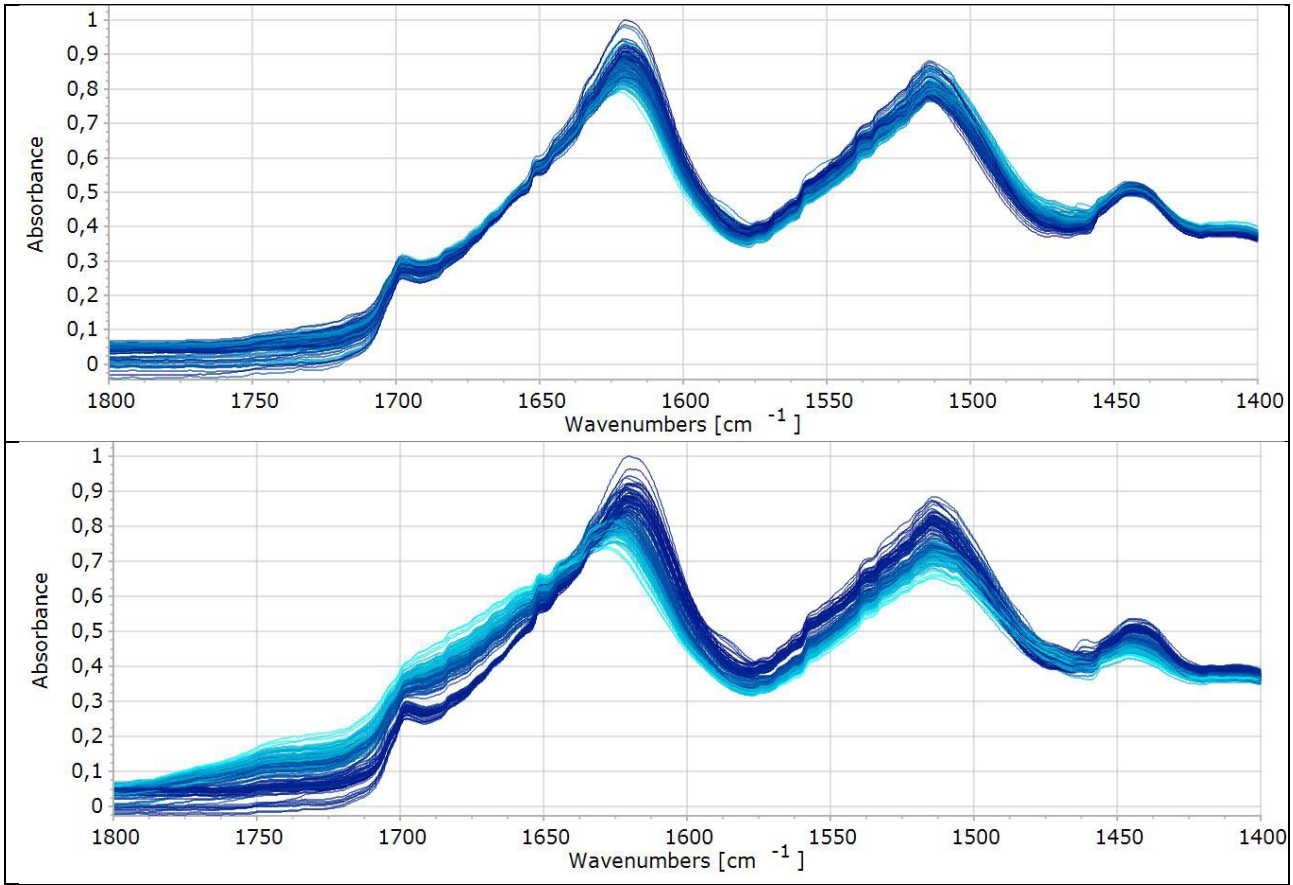

Figure 63. Superimposition of all the ATR-FTIR spectra obtained from dyed samples (region 1800-1400 cm^{-1}, normalized by area). Spectra are coloured based on the shift of amide I peak (deep blue: 1617cm^{-1}; light blue: 1625 cm^{-1}). The upper image refers to visible-aged samples, the lower image refers to UV-aged samples.

Figure 63 shows a superimposition of all the ATR-FTIR spectra obtained from dyed samples, for visible-aged samples (upper image) and UV-aged samples (lower image). Spectra are coloured based on the shift of amide I peak (deep blue: 1617cm^{-1}; light blue: 1625 cm^{-1}). The images visualize the general trends within the samples. It emerges visually that the changes in the visible-aged samples are limited, while deep modifications occur in UV-aged samples, especially in the oxidation band (1725 cm^{-1}), in the random-coil band (1650 cm^{-1}), in the amide I peak (1617-25 cm^{-1}) and in the amide II peak (1516-1505 cm^{-1}).

a

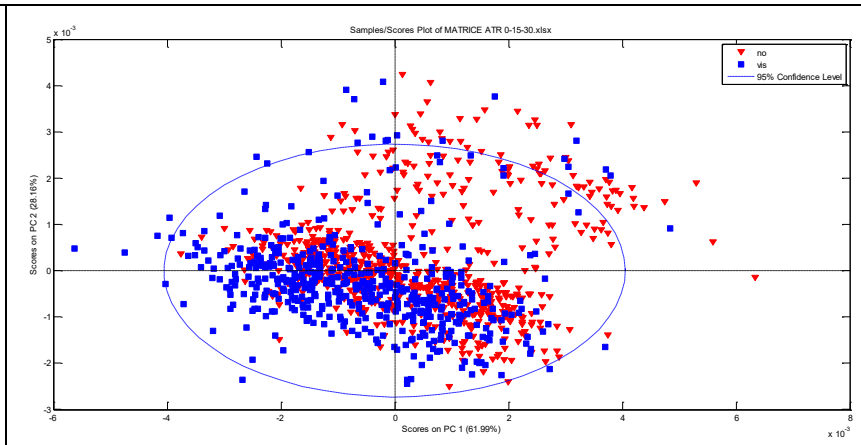

b

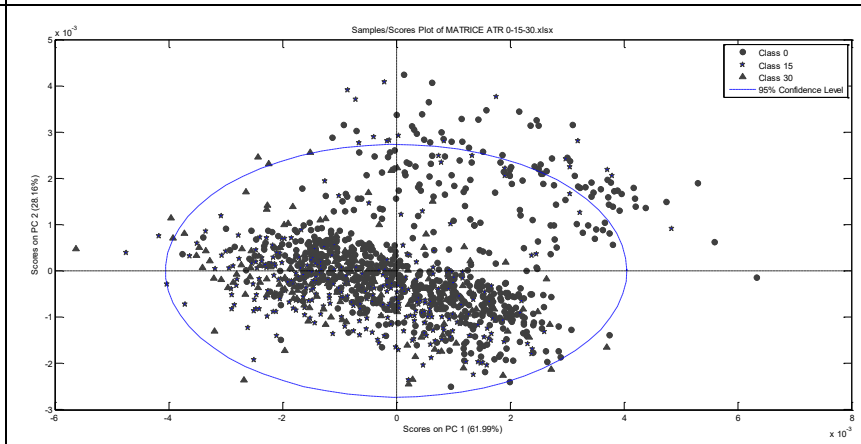

c

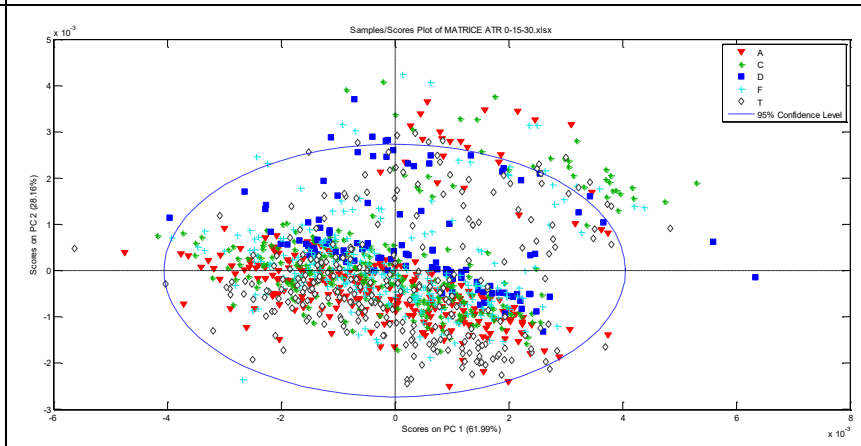

d

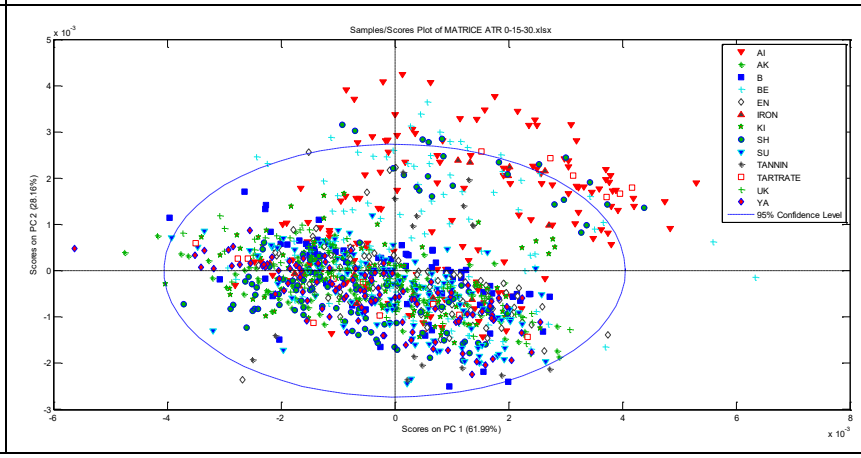

Figure 64. Score plots of the PCA model obtained from the dataset containing unaged and visible-aged samples.

a) Samples colored according to light source

b) Samples colored according to aging time

c) Samples colored according to mordant

d) Samples colored according to dye

Loadings plots of the PCA model obtained from the dataset containing unaged and visible-aged samples.

e) loadings plot for PC1

f) loadings plot for PC2

e

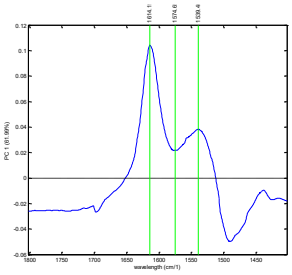

f

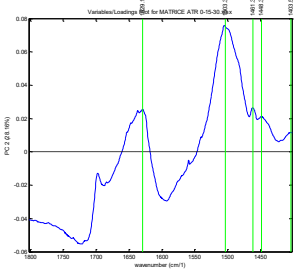

Figure 64 shows the score plots of the PCA calculated on the dataset containing the ATR-FTIR spectra of both unaged and visible-aged samples. The total variance of the model is 90.16%. A cluster centered around PC1 and PC2 can be distinguished, with a trend parallel to PC1. Other samples are positioned at high values of both PC1 and PC2, with an apparently random distribution. By coloring the points based on the type of ageing (Figure 64a), a random distribution is observed within the two aforementioned groupings. The same trend is observed in Figure 64b, where points representing different ageing times are marked with different symbols. In Figure 64c, the distribution of samples is shown, colored according to the mordant used. In this case, some categories show groupings explained along PC2. Finally, Figure 64d shows the samples colored by the type of dye. In the grouping at high values of PC1 and PC2, all samples dyed with *ai* are grouped together. In the same region, samples dyed with other dyes or only mordanted (beni, shikon, only tartrate, only tannin, only iron) also appear, though they also appear in the other group. Therefore, we can hypothesize that these samples share some characteristics with the samples dyed with *ai*.

a

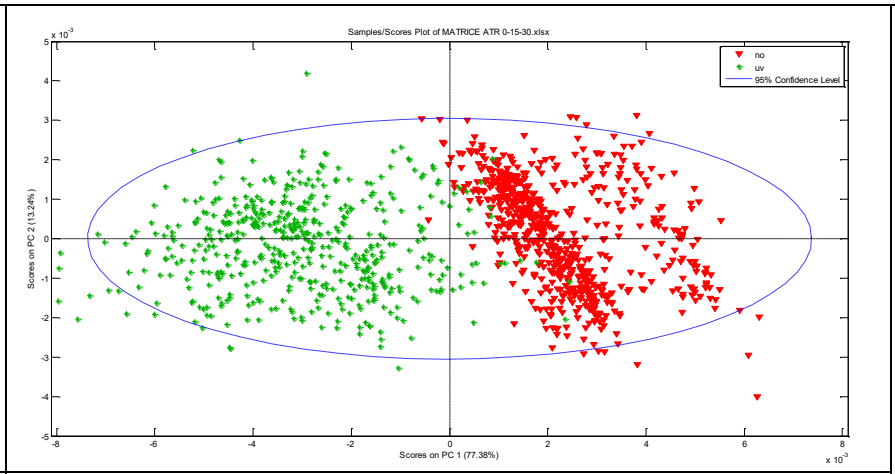

b

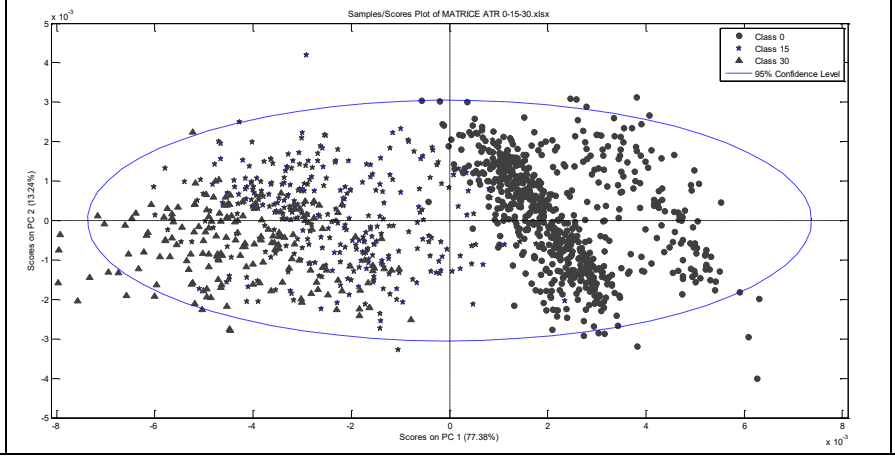

Figure 65. Score plots of the PCA model obtained from the dataset containing unaged and UV-aged samples.

a) Samples colored according to light source

b) Samples colored according to aging time

c) Samples colored according to mordant

d) Samples colored according to dye

Loadings plots of the PCA model obtained from the dataset containing unaged and UV-aged samples.

e) loadings plot for PC1

f) loadings plot for PC2

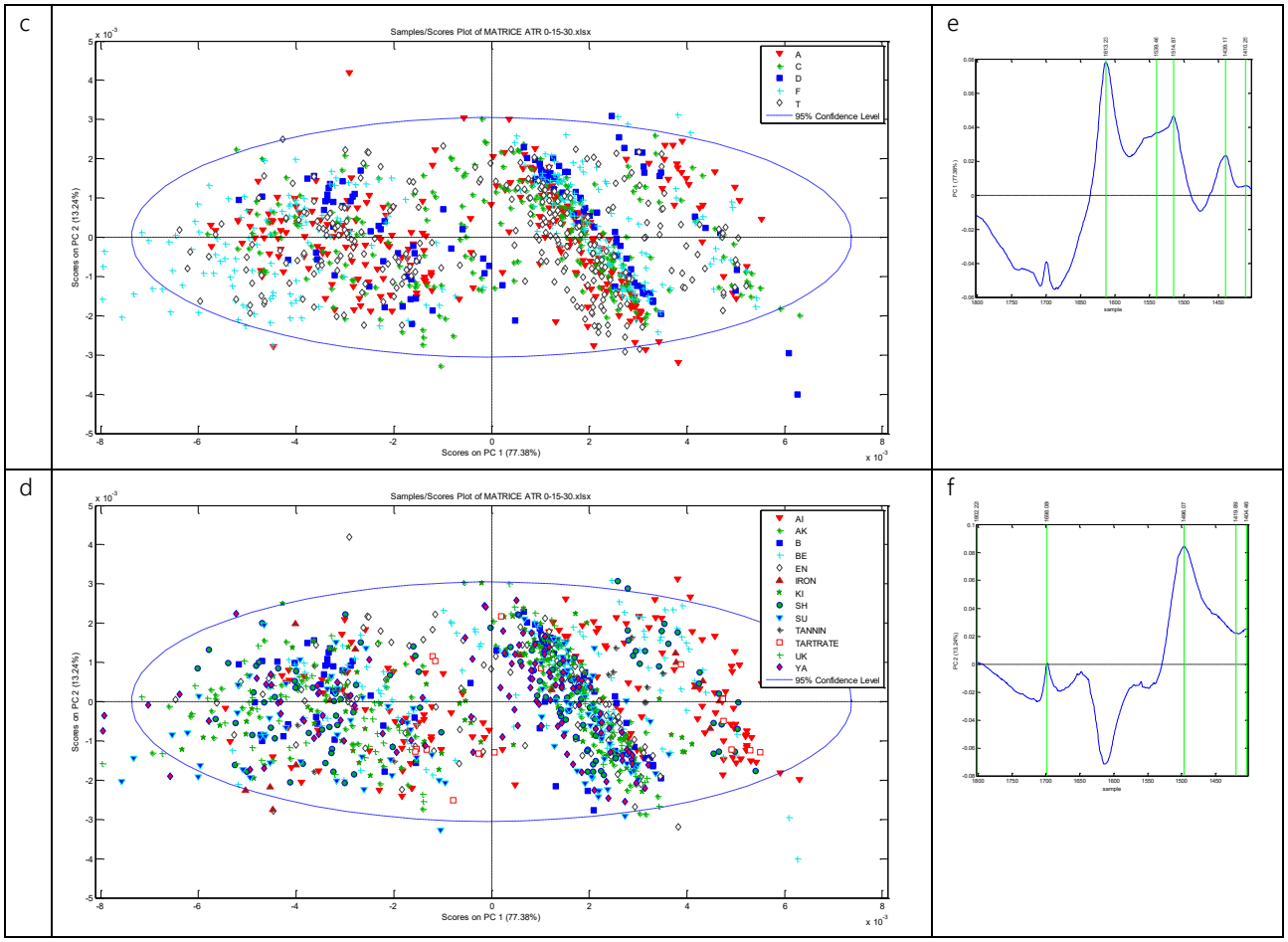

Figure 65 shows the score plots of the PCA calculated on the dataset containing the ATR spectra of both unaged and UV-aged samples. The total variance of the model is 90.62%. Three clusters can be distinguished along PC1. By colouring the points based on the type of ageing (Figure 65a), it is observed that the UV-aged samples are located at low PC1 values and are distributed along PC2, while the unaged samples are positioned at high PC1 values, following a linear trend parallel to PC2. The same trend is observed in Figure 65b, where points representing different ageing times are indicated with different symbols. Samples aged for 15 days are positioned at negative PC1 values, and samples aged for 30 days at even more negative values. Figure 65c shows the distribution of the samples colored according to the mordant used, and a random distribution is observed. The same trend is observed in Figure 65d, which shows the samples colored by the type of dye. In any case, since PC1 seems to be strongly correlated with the degree of aging of the sample, it is reasonable to assume that negative values correspond to samples containing dye/mordant combinations that cause greater fiber degradation.

a

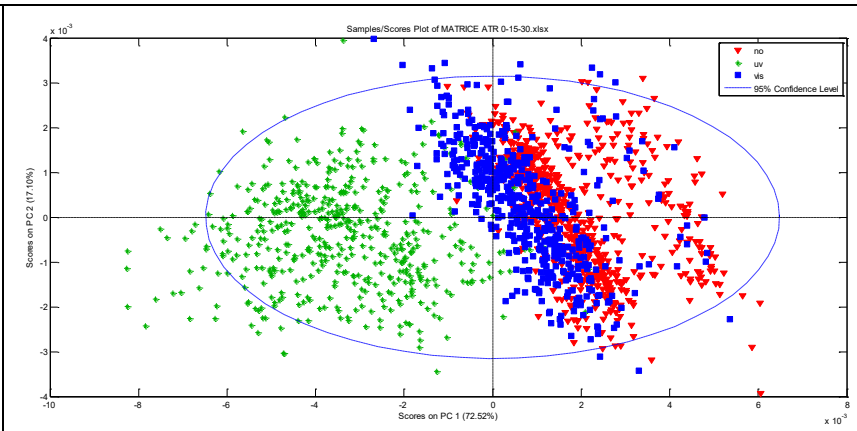

b

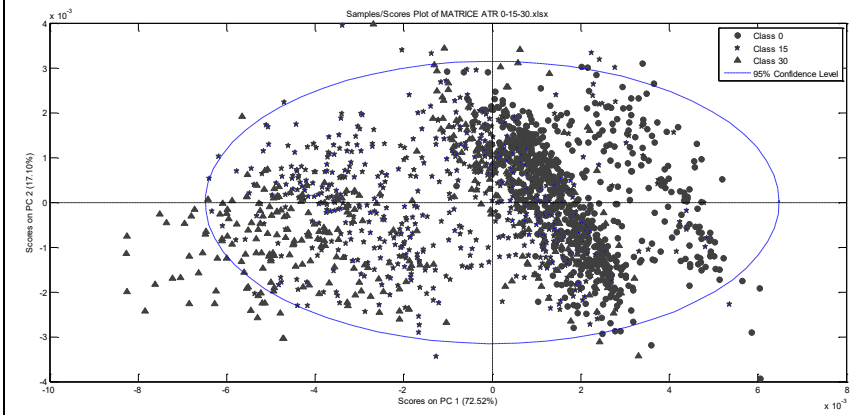

c

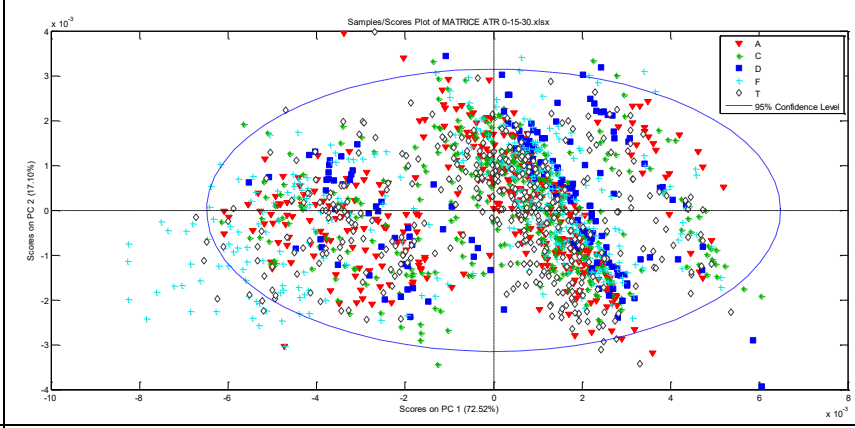

d

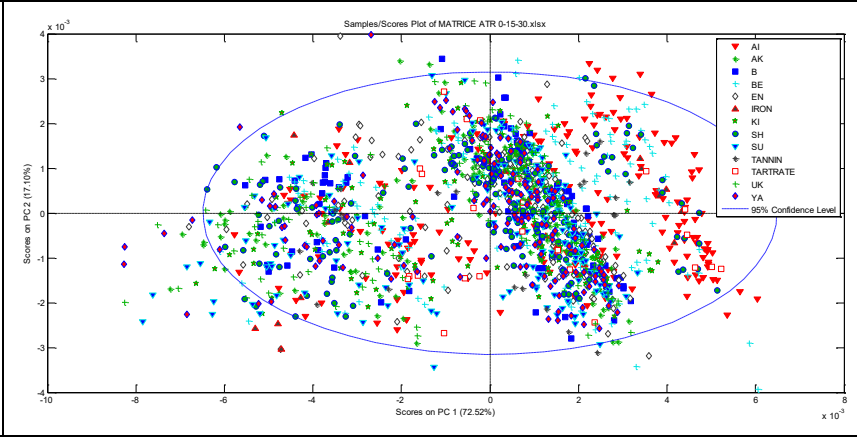

Figure 66. Score plots of the PCA model obtained from the dataset containing unaged, visible-aged and UV-aged samples.

a) Samples colored according to light source

b) Samples colored according to aging time

c) Samples colored according to mordant

d) Samples colored according to dye

Loadings plots of the PCA model obtained from the dataset containing unaged, visible-aged and UV-aged samples.

e) loadings plot for PC1

f) loadings plot for PC2

e

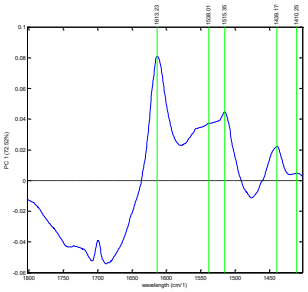

f

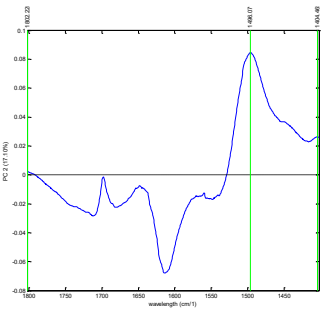

Figure 66 shows the score plots of the PCA calculated on the dataset containing the ATR-FTIR spectra of both unaged samples and those aged with UV and visible light. The total variance of the model is 89.62%. Three groupings can be distinguished along PC1, which appear very similar to those identified in Figure 65. By coloring the points based on the type of aging (Figure 66a), it is observed that the UV-aged samples are located at low PC1 values and are distributed along PC2, while the unaged samples and those aged with visible light are positioned at high PC1 values, following a linear trend parallel to PC2. The same trend is observed in Figure 66b, where points representing different ageing times are marked with different symbols. Samples aged with UV light for 15 days are positioned at negative PC1 values, and those aged with UV light for 30 days at even more negative values, while all samples aged with visible light partially overlap with the unaged ones. Figure 66c shows the distribution of the samples colored according to the mordant used, and a random distribution is observed. The same trend is observed in Figure 66d, which shows the samples colored by the type of dye. In any case, since PC1 seems to be strongly correlated with the degree of aging of the sample, it is reasonable to assume that negative values correspond to samples containing dye/mordant combinations that cause greater silk degradation.

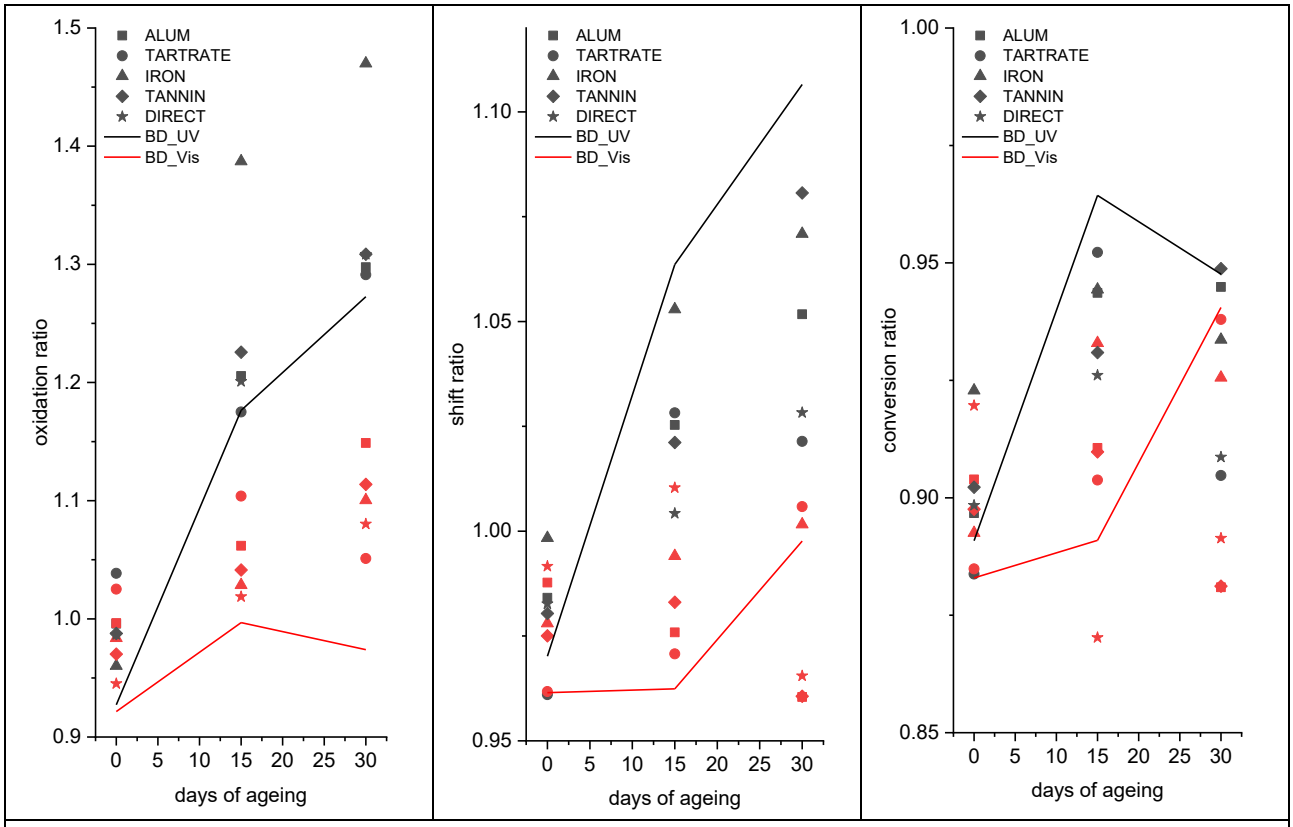

Figure 67. Oxidation ratio, shift ratio and conversion ratio calculated for ai-dyed samples are plotted for day 0, day 15 and day 30 of UV-ageing (black symbols) and visible ageing (red symbols). The same indicators calculated for unmordanted silk are shown as a reference (UV-ageing: black line; visible ageing: red line)

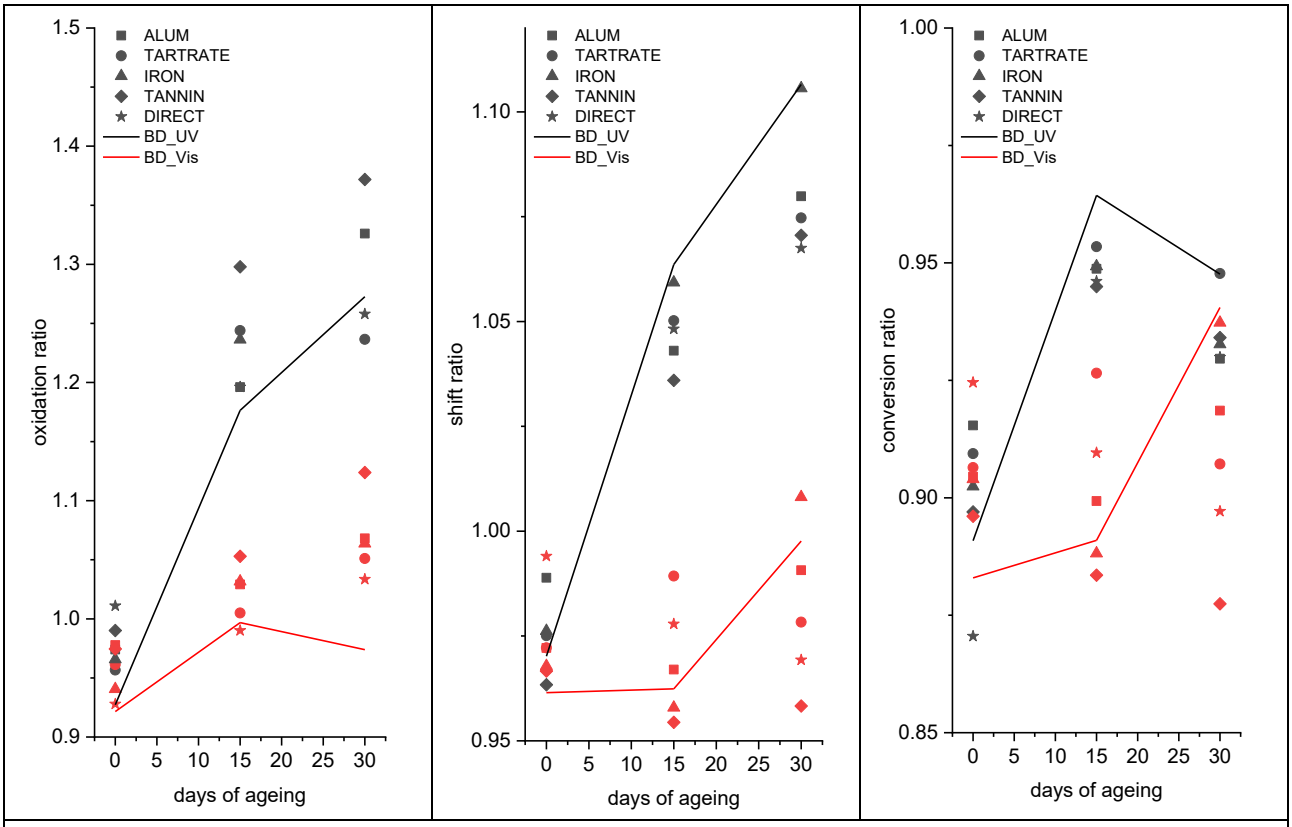

Figure 68. Oxidation ratio, shift ratio and conversion ratio calculated for beni-dyed samples are plotted for day 0, day 15 and day 30 of UV-ageing (black symbols) and visible ageing (red symbols). The same indicators calculated for unmordanted silk are shown as a reference (UV-ageing: black line; visible ageing: red line)

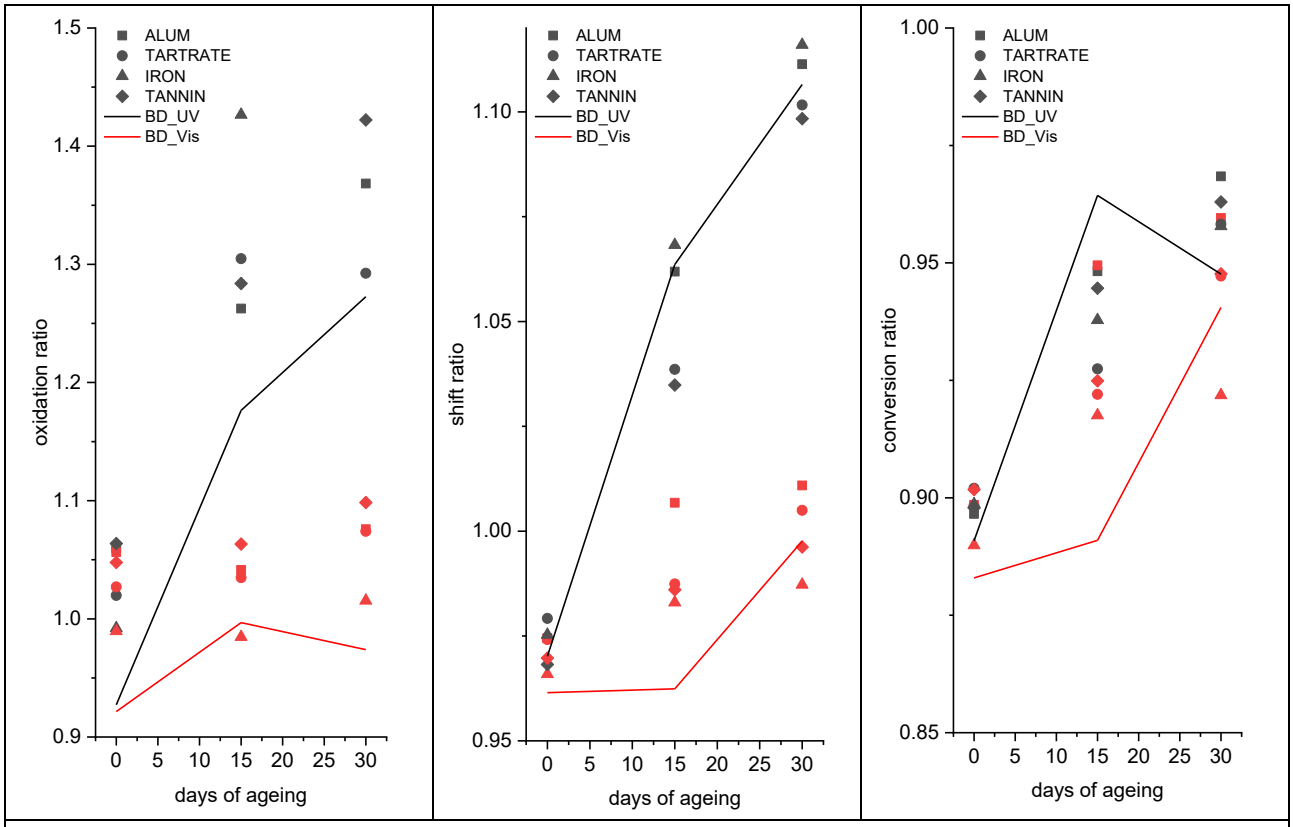

Figure 69. Oxidation ratio, shift ratio and conversion ratio calculated for akane-dyed samples are plotted for day 0, day 15 and day 30 of UV-ageing (black symbols) and visible ageing (red symbols). The same indicators calculated for unmordanted silk are shown as a reference (UV-ageing: black line; visible ageing: red line)

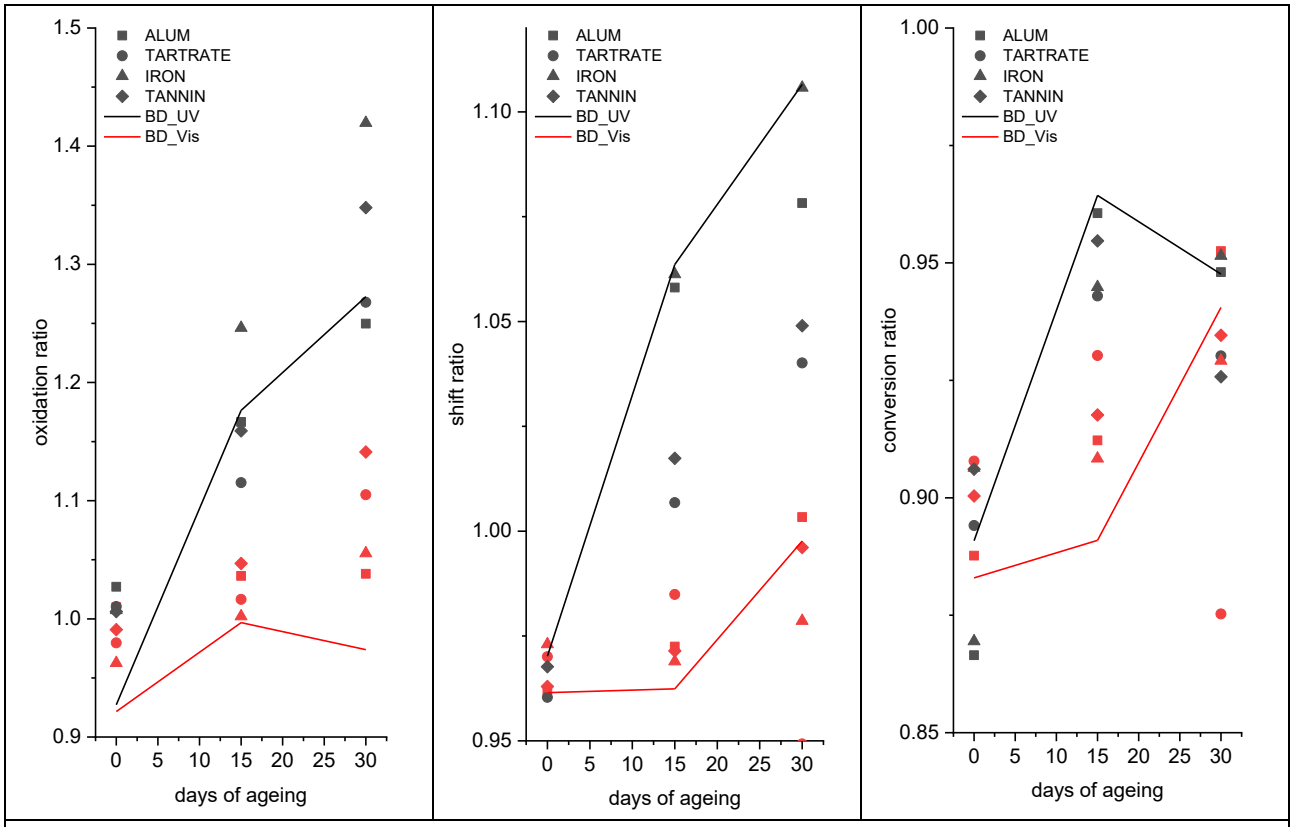

Figure 70. Oxidation ratio, shift ratio and conversion ratio calculated for enju-dyed samples are plotted for day 0, day 15 and day 30 of UV-ageing (black symbols) and visible ageing (red symbols). The same indicators calculated for unmordanted silk are shown as a reference (UV-ageing: black line; visible ageing: red line)

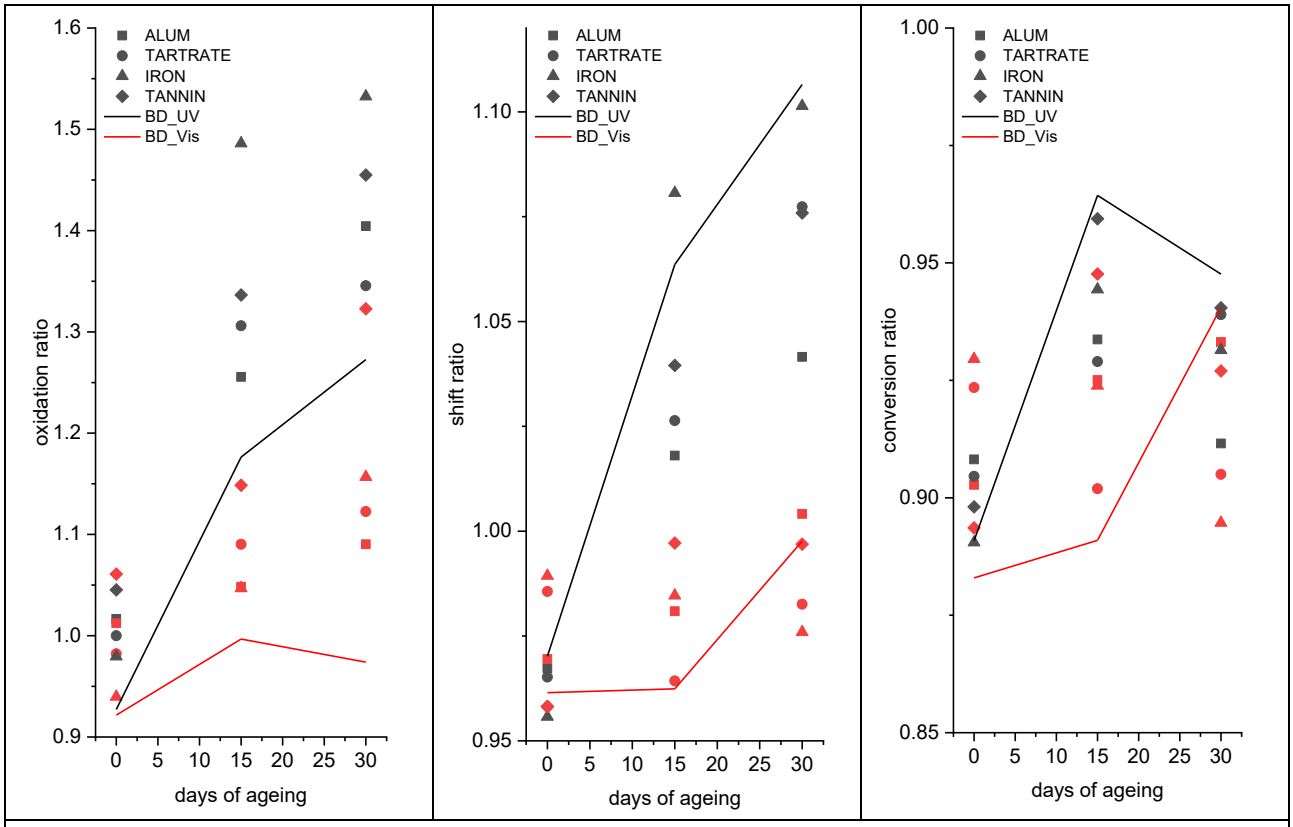

Figure 71. Oxidation ratio, shift ratio and conversion ratio calculated for kihada-dyed samples are plotted for day 0, day 15 and day 30 of UV-ageing (black symbols) and visible ageing (red symbols). The same indicators calculated for unmordanted silk are shown as a reference (UV-ageing: black line; visible ageing: red line)

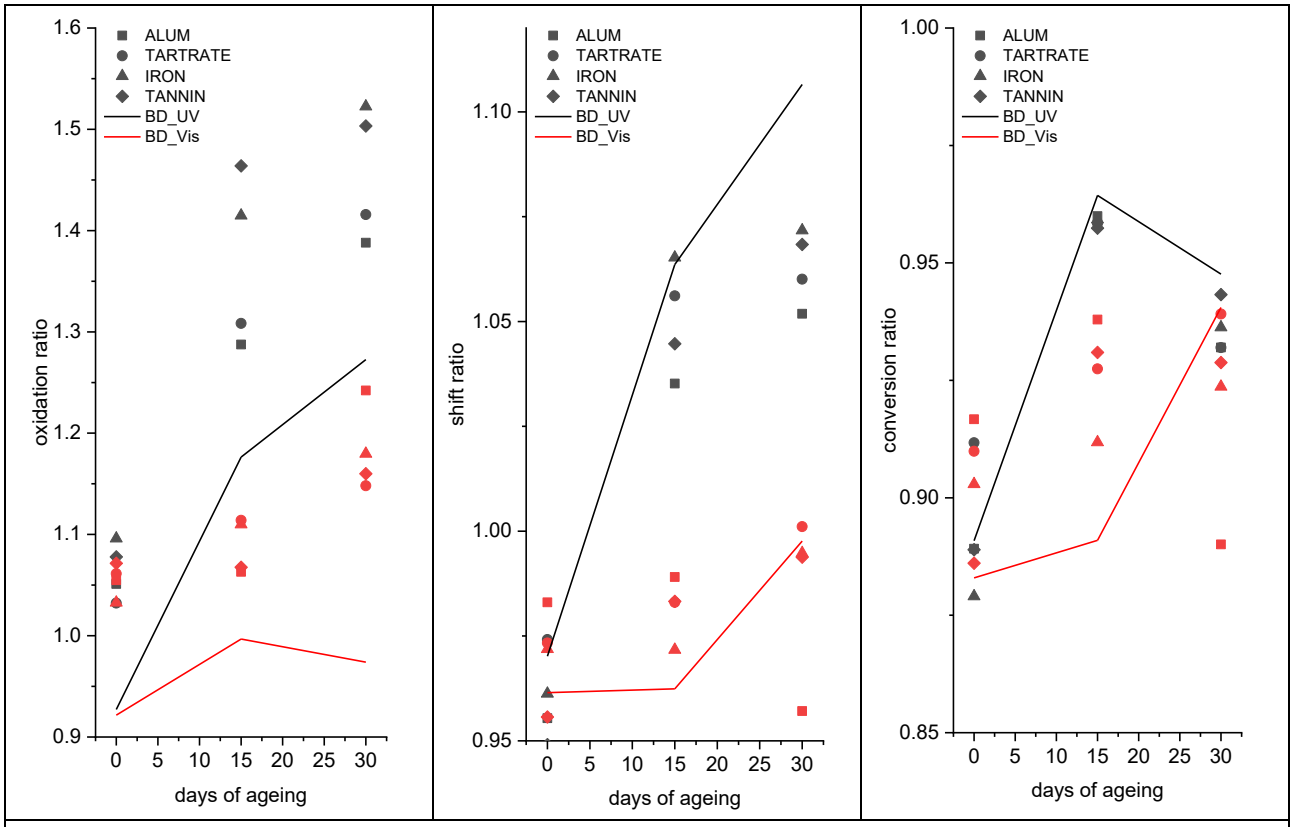

Figure 72. Oxidation ratio, shift ratio and conversion ratio calculated for shikon-dyed samples are plotted for day 0, day 15 and day 30 of UV-ageing (black symbols) and visible ageing (red symbols). The same indicators calculated for unmordanted silk are shown as a reference (UV-ageing: black line; visible ageing: red line)

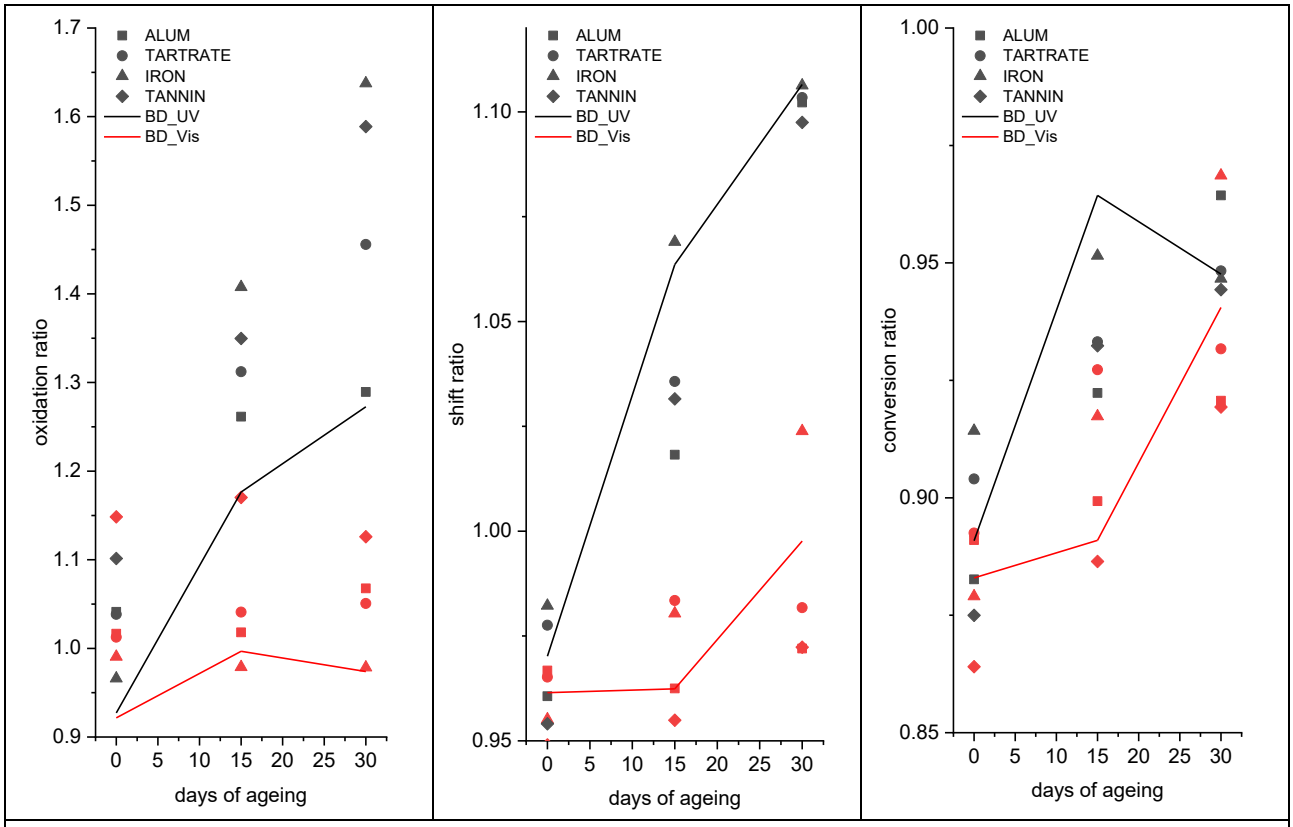

Figure 73. Oxidation ratio, shift ratio and conversion ratio calculated for suo-dyed samples are plotted for day 0, day 15 and day 30 of UV-ageing (black symbols) and visible ageing (red symbols). The same indicators calculated for unmordanted silk are shown as a reference (UV-ageing: black line; visible ageing: red line)

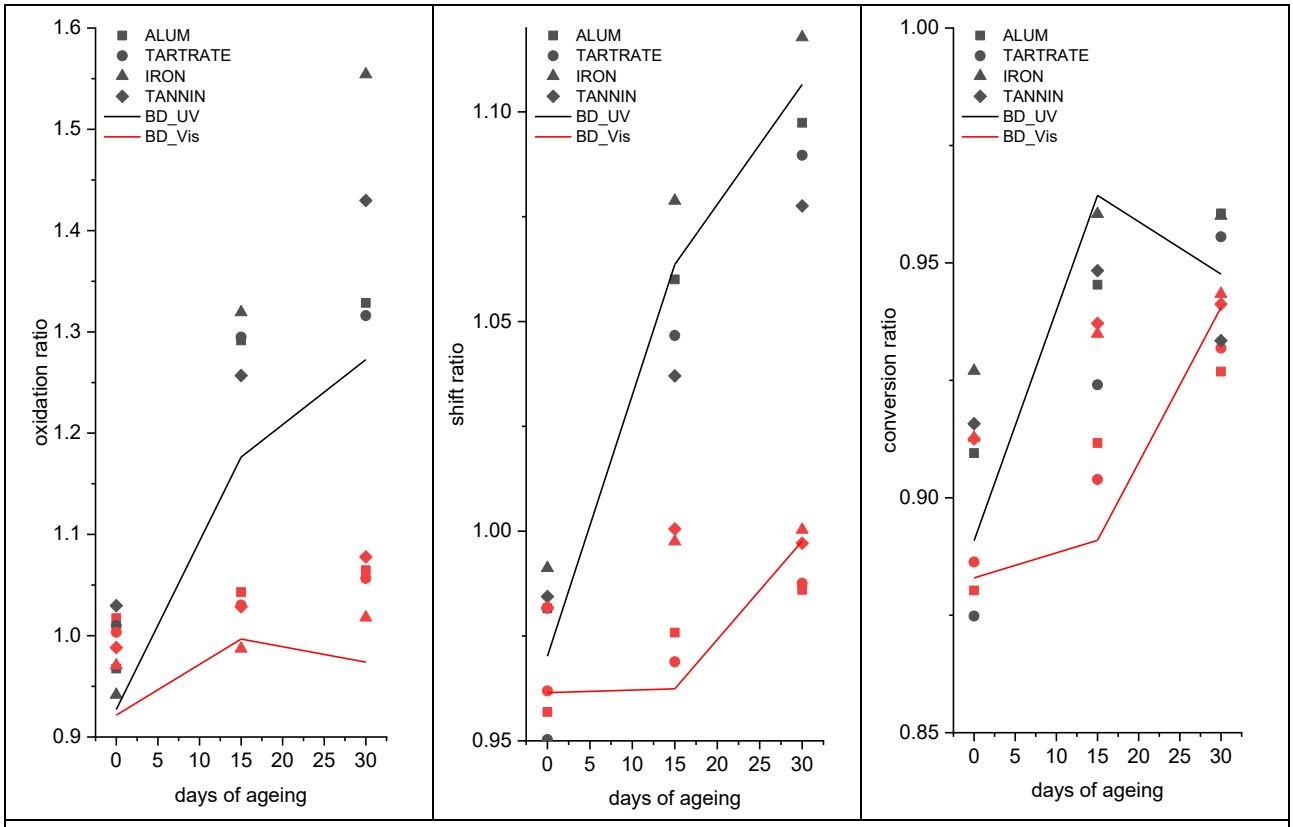

Figure 74. Oxidation ratio, shift ratio and conversion ratio calculated for ukon-dyed samples are plotted for day 0, day 15 and day 30 of UV-ageing (black symbols) and visible ageing (red symbols). The same indicators calculated for unmordanted silk are shown as a reference (UV-ageing: black line; visible ageing: red line)

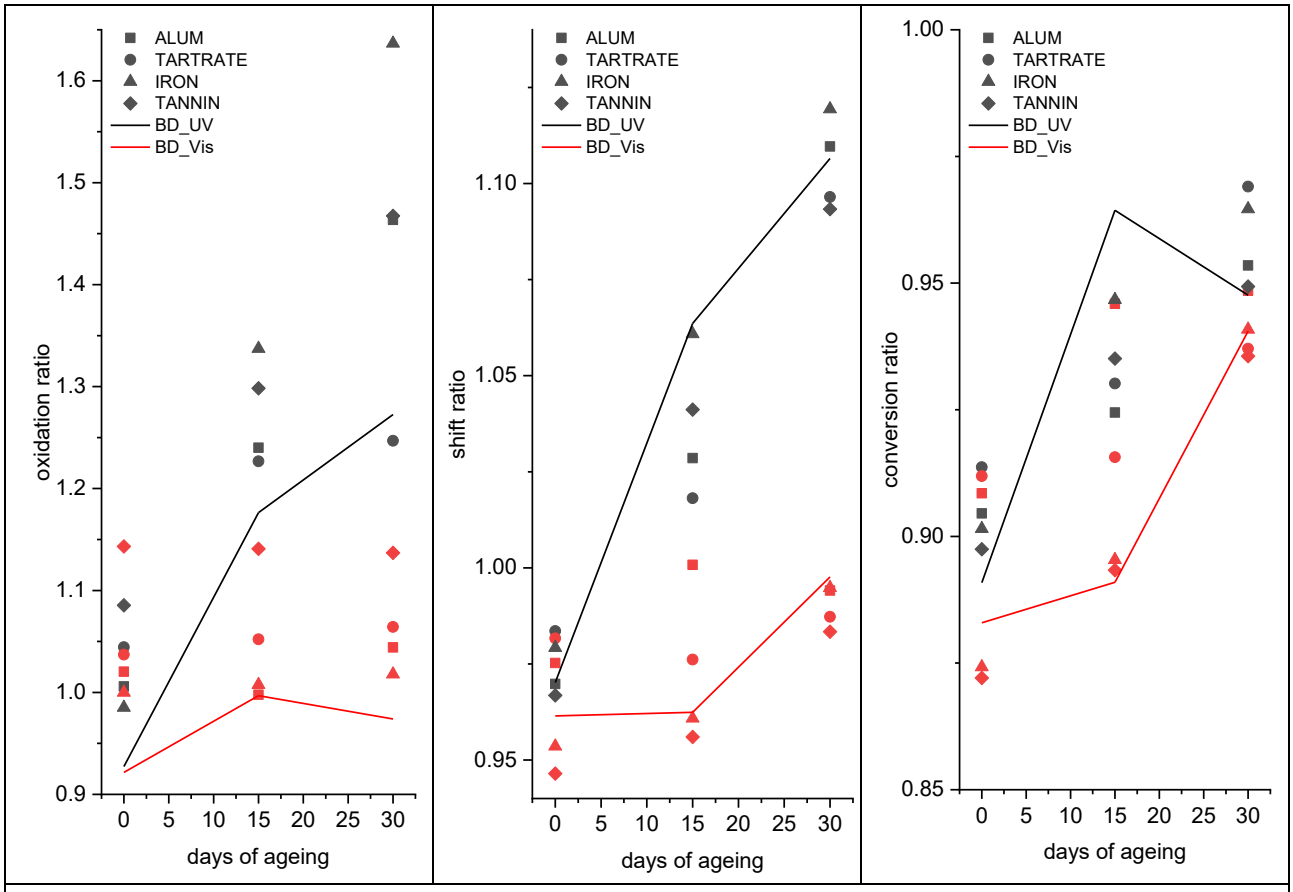

Figure 75. Oxidation ratio, shift ratio and conversion ratio calculated for yamahaji-dyed samples are plotted for day 0, day 15 and day 30 of UV-ageing (black symbols) and visible ageing (red symbols). The same indicators calculated for unmordanted silk are shown as a reference (UV-ageing: black line; visible ageing: red line)

To further investigate these changes, in Figures 67-75 oxidation ratio, shift ratio and conversion ratio calculated for each dye are plotted for day 0, day 15 and day 30 of UV-ageing (black symbols) and visible ageing (red symbols). The same indicators calculated for unmordanted silk are shown as a reference.

Each combination pf dye/mordant shows specific behaviour. Some general observations can be drawn. Visible-aged samples exhibit lower values of oxidation ratio and shift ratio with respect to UV-aged samples, while values for conversion ratio are consistent with those of UV-aged samples. While UV-aged samples always show values of oxidation and shift higher than white silk, visible-aged samples show higher values only for specific combinations.

When comparing UV-aged samples with respect to visible-aged and white samples, oxidation values are generally higher than shift values. So, the most important differences are found in the extent of oxidation of the fibre, while the influence of the presence of dyes or mordants is limited when considering the conversion ratio.

Figure 76 graphically summarizes the values of oxidation ratio, shift ratio and conversion ratio calculated for all the samples. The dashed lines, corresponding to the calculated values for sample B_UV_d30, fix a threshold. For each estimator, lower values stand for less damaged combinations, higher values indicate most damaged combinations.

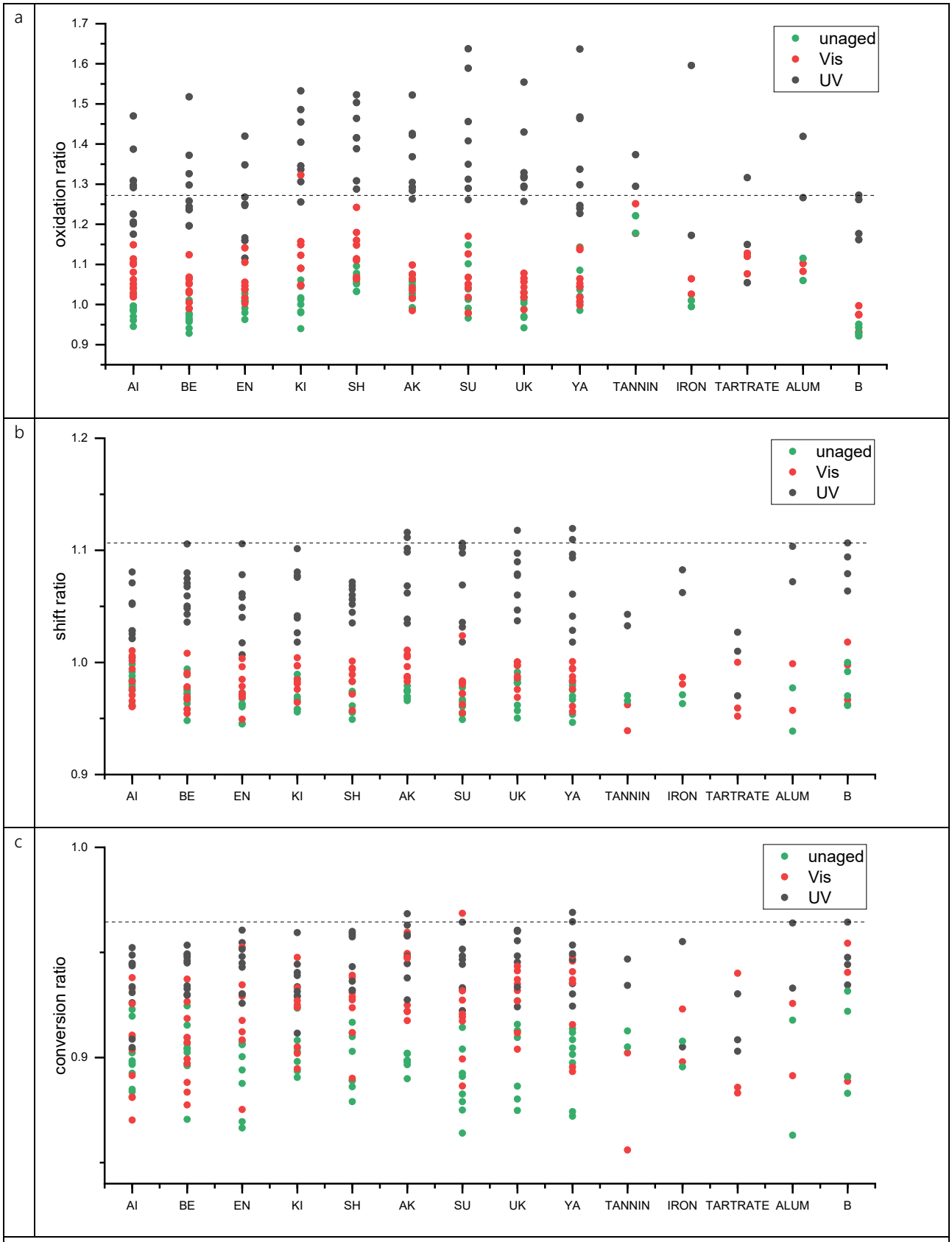

Figure 76. Oxidation ratio, shift ratio and conversion ratio calculated for all the samples are plotted and coloured according to unaged (green symbols), visible-aged after 30 days (red symbols) and UV-aged after 30 days (black symbols). The dashed line highlights the values of reference sample B_UV_d30.

3.7.4 Thermal analysis

The samples aged for 30 days under visible light (partially) and UV light underwent TGA analysis. The DTG plots were obtained from the TG curves, and the features of each DTG curve were calculated (T_{max}, d_{max}, area of the fast decomposition event, area of the slow decomposition event).

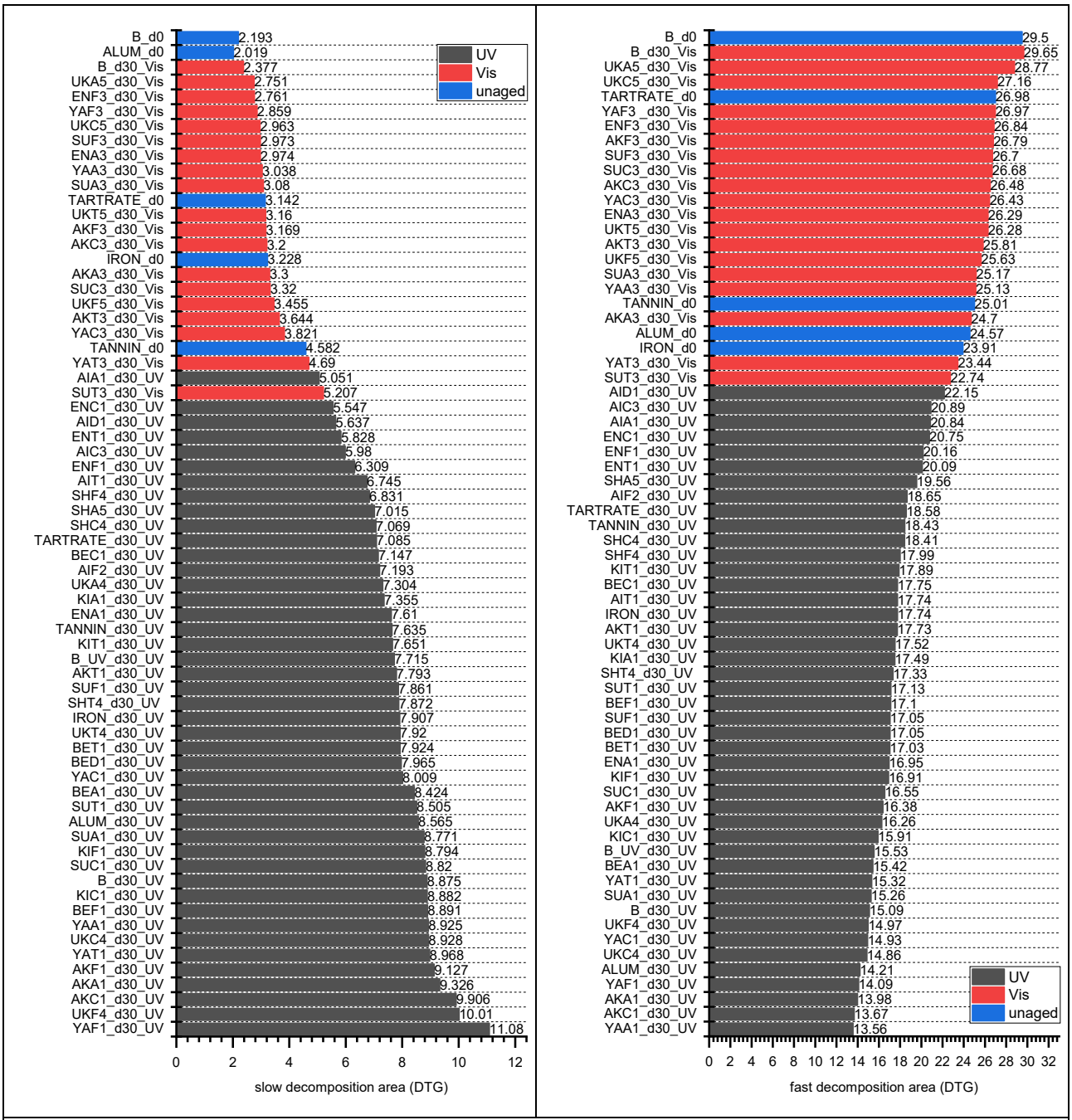

Figure 77. Areas calculated for the slow decomposition event and the fast decomposition event for the samples aged for 30 days under visible light and UV light. Low areas values for fast decomposition and high values for slow decomposition are indicators for silk degradation.

Figure 77 summarizes the area values calculated for the slow decomposition event and the fast decomposition event for the samples aged for 30 days under visible light and UV light. Both the areas correspond to the weight loss % which occurs during the event.

If the main, fast decomposition event (260-350°C) is explained with the thermal decomposition of silk, where the reduced weight loss % can be correlated to a reduced amount of amorphous/β-strand silk, which is lost during photooxidation. The loss of weight % which happens during the slow decomposition event can be associated with the increased amount of oxidation products. As already demonstrated before, it increases with ageing or degradation extent. So, low areas values for fast decomposition and high values for slow decomposition are indicators for silk degradation. It is not surprising that in this category there are UV-aged samples, while unaged and visible-aged show low degradation extent.

The features of the DTG curves for all the samples are summarized in Table 11, together with the values of the E% factor, calculated according to the *Experimental parameters* section.

The extent of degradation (E%) was calculated with respect to sample B_UV1_30, which is set to zero. As a consequence, the other samples exhibit positive values if they show bigger levels of degradation and negative values if they show lower levels of degradation. A large part of the combinations dye/mordant show negative values, but significantly some of them exhibit an increase of the degradation level.

Sample	Area (A)	Tmax	dmax	A	E% (with respect to B_UV_d30)
ALUM_d0 - 1st derivative	-24.53	330	-1.01	-0.01101	-135.0
UKT5 - 1st derivative	-26.37	325	9.87	0.001064	-96.6
UKA5 - 1st derivative	-29.45	325	0.91	0.010333	-67.2
B_VIS_30 - 1st derivative	-29.69	320	0.9	0.010525	-66.6
SS_d0 - 1st derivative	-29.5	319	0.895	0.010686	-66.1
ENA3 - 1st derivative	-26.29	326	0.96	0.010939	-65.3
SUA3 - 1st derivative	-25.25	330	0.97	0.011135	-64.6
YAF3 - 1st derivative	-27.06	326	0.9	0.011336	-64.0
AKF3 - 1st derivative	-26.99	323	0.91	0.011345	-64.0
UKC5 - 1st derivative	-27.08	324	0.9	0.011397	-63.8
SUC3 - 1st derivative	-26.67	327	0.89	0.011595	-63.2
SUF3 - 1st derivative	-26.7	326	0.89	0.011618	-63.1
ENF3 - 1st derivative	-26.86	323	0.88	0.011788	-62.6
YAA3 - 1st derivative	-25.05	330	0.92	0.011834	-62.4
AKA3 - 1st derivative	-24.67	327	0.94	0.011869	-62.3
AKC3 - 1st derivative	-26.37	322	0.89	0.011909	-62.2
UKF5 - 1st derivative	-25.75	325	0.88	0.012221	-61.2
TARTRATE_d0 - 1st derivative	-26.93	315	0.85	0.012482	-60.4
IRON_d0 - 1st derivative	-23.85	325	0.895	0.012973	-58.8
YAC3 - 1st derivative	-26.38	318	0.81	0.013245	-57.9
AKT3 - 1st derivative	-25.66	319	0.8	0.013744	-56.4
TANNIN_d0 - 1st derivative	-24.92	318	0.77	0.014749	-53.2

YAT3 - 1st derivative	-23.31	323	0.81	0.014757	-53.1
SUT3 - 1st derivative	-22.61	321	0.8	0.015501	-50.8
AID1_30 - 1st derivative	-22.13	316	0.722	0.017825	-43.4
AIA1_30 - 1st derivative	-20.78	318	0.735	0.01853	-41.2
AIC3_30 - 1st derivative	-20.88	314	0.705	0.019471	-38.2
ENC1_30 - 1st derivative	-20.67	313	0.69	0.020161	-36.0
ENT1_30 - 1st derivative	-20.03	314	0.704	0.020326	-35.5
ENF1 - 1st derivative	-19.94	313	0.7	0.0206	-34.6
SHA5_30 - 1st derivative	-19.48	314	0.685	0.02148	-31.8
AIF2_30 - 1st derivative	-18.59	311	0.65	0.023949	-24.0
TANNIN_30 - 1st derivative	-18.43	313	0.65	0.024003	-23.8
SHC4_30 - 1st derivative	-18.35	313	0.635	0.024677	-21.6
TARTRATE_30 - 1st derivative	-18.53	302	0.648	0.024819	-21.2
SHF4_30 - 1st derivative	-17.9	313	0.63	0.025498	-19.0
AIT1_30 - 1st derivative	-17.65	307	0.64	0.025953	-17.6
KIA1_30 - 1st derivative	-17.38	312	0.63	0.026345	-16.3
KIT1_30 - 1st derivative	-17.87	313	0.61	0.026378	-16.2
BEC1_30 - 1st derivative	-17.7	305	0.625	0.026674	-15.3
IRON_30 - 1st derivative	-17.7	308	0.605	0.027287	-13.4
SHT4_30 - 1st derivative	-17.26	314	0.6	0.027677	-12.1
BED1_30 - 1st derivative	-16.98	305	0.625	0.027805	-11.7
ENA1 - 1st derivative	-17	309	0.61	0.028087	-10.8
BET1_30 - 1st derivative	-16.98	307	0.61	0.028303	-10.1
KIF1_30 - 1st derivative	-16.86	311	0.585	0.029341	-6.8
BEF1_30 - 1st derivative	-17.06	307	0.575	0.029885	-5.1
UKT4 - 1st derivative	-17.48	312	0.5296	0.03116	-1.1
B_UV1_30 - 1st derivative	-15.54	302	0.608	0.031541	0.2
SUC1 - 1st derivative	-16.4	308	0.5585	0.031903	1.3
SUF1 - 1st derivative	-17.02	311	0.5299	0.032087	1.9
KIC1_30 - 1st derivative	-15.84	307	0.57	0.032469	3.1
UKA4 - 1st derivative	-15.92	308	0.5645	0.032515	3.2
AKF1 - 1st derivative	-16.4	310	0.5394	0.032819	4.2
SUA1 - 1st derivative	-15.45	309	0.5559	0.033912	7.7
UKF4 - 1st derivative	-15.17	308	0.5669	0.033978	7.9
AKT1 - 1st derivative	-17.7	315	0.4727	0.034149	8.4
BEA1_30 - 1st derivative	-15.32	304	0.55	0.035136	11.6
UKC4 - 1st derivative	-14.83	308	0.5567	0.035394	12.4
SUT1 - 1st derivative	-17.12	314	0.472	0.03547	12.6
YAT1 - 1st derivative	-15.36	312	0.528	0.035568	12.9
YAC1 - 1st derivative	-14.63	309	0.5491	0.036257	15.1
YAA1 - 1st derivative	-13.64	305	0.5888	0.036742	16.7
AKC1 - 1st derivative	-13.57	303	0.5953	0.036769	16.8
YAF1 - 1st derivative	-14.08	307	0.5646	0.036877	17.1
AKA1 - 1st derivative	-13.98	307	0.5651	0.037108	17.8
ALUM_30 - 1st derivative	-14.21	308	0.527	0.03902	23.9

Table 11. Features of the DTG curves for all the samples, shown together with the values of the E% factor. Samples are listed in increasing order.

3.7.5 Discussion

The samples aged with visible light show clear discoloration but almost no characteristics attributable to fibre degradation. No significant changes in the secondary structure conformation are observed, although an increase in the degree of oxidation is noted, possibly linked to dyeing conditions. The degree of oxidation of tyrosine is consistent with the level reached by UV ageing. Thermal analysis shows that the samples have not undergone significant ageing compared to the reference silk. The samples aged with UV light show degradation characteristics similar to those observed in aged white silk in the previous experiment. The degradation is more intense due to the higher irradiance conditions. Discoloration of the dye is very evident in most of the samples. ATR-FTIR analysis reveals a clear conformational change during ageing, as evidenced by the shift in Amide I to values of 1625 cm^{-1}, as well as very high oxidation ratio values, which attest to peptide oxidation. The degree of oxidation of tyrosine is consistent with the level reached by visible light ageing. The values differ based on the dye/mordant combination. Thermal analysis also shows that the samples have a higher or lower ageing factor than the aged white reference silk under the same conditions, depending on the dye/mordant combination. The graphs shown below summarize the correlation found between fibre degradation and the nature of the dye/mordant combination.

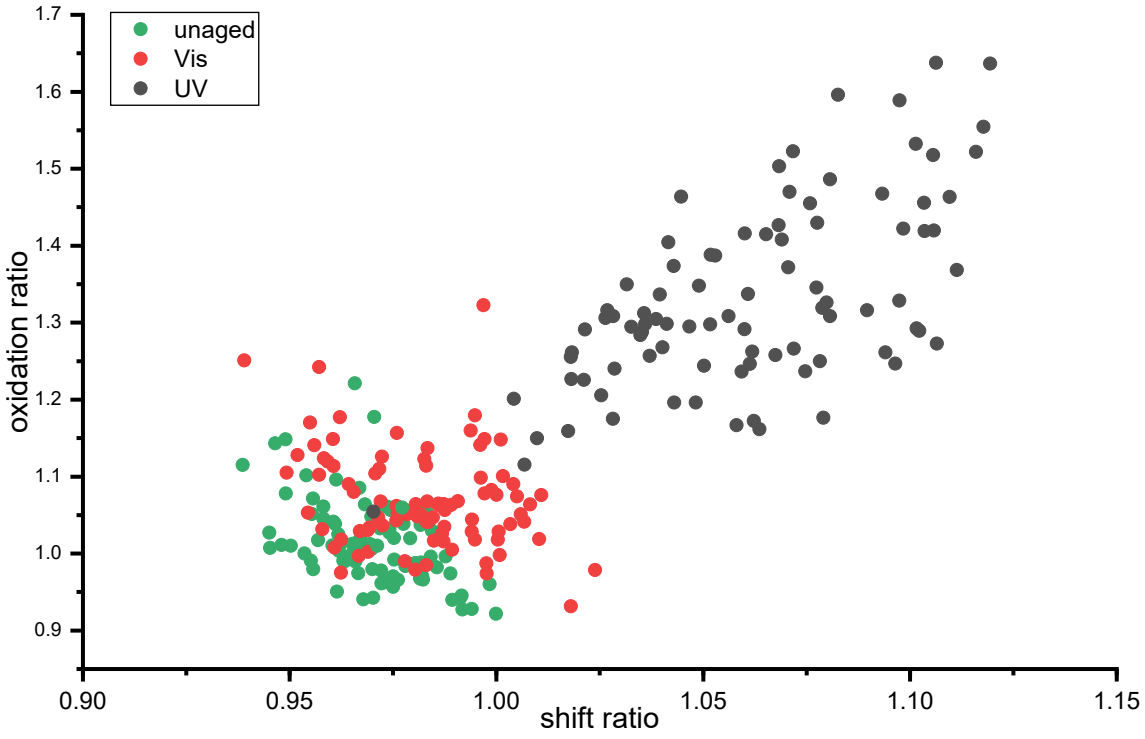

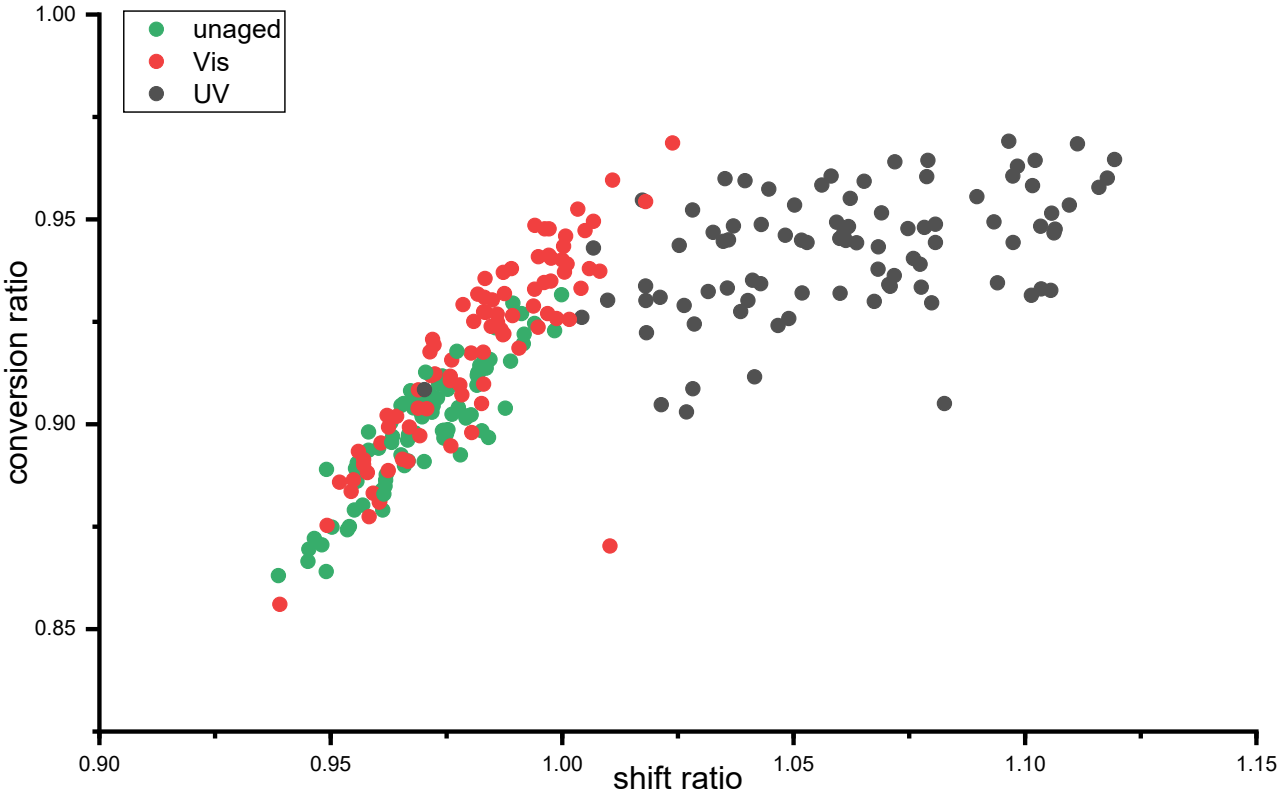

Figure 78. Shift ratio values plotted against oxidation ratio values (upper image) and conversion ratio values (lower plot) for samples aged with visible light after 15 and 30 days, with ultraviolet light after 15 and 30 days, and under unaged conditions.

Figure 78 shows Shift ratio values plotted against oxidation ratio values (upper image) and conversion ratio values (lower plot) for samples aged with both visible and ultraviolet light. The samples aged with visible light are located in the same region as the unaged samples. This suggests that visible light does not alter the secondary structure of silk nor the oxidation of the fibre, unlike UV light. In the case of conversion, all the sets of samples show similar values along the y-axis related to conversion, with those aged with UV light exhibit a much smaller range of shift values compared to the visible-aged samples. That means that conversion ratio is not decisive for the assessment of the extent of degradation. Given that shift ratio value is a decisive indicator of degradation together with oxidation ratio, it can be stated that the most degraded samples are those on the upper right side of the graphs.

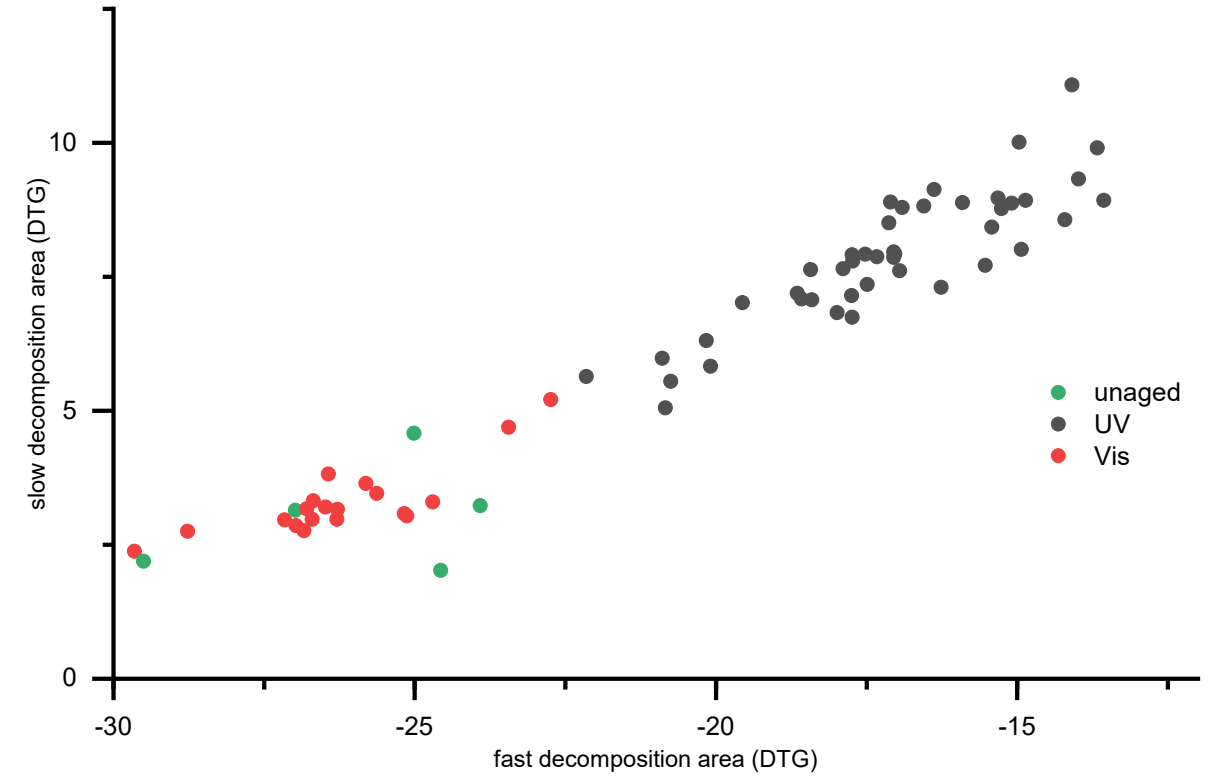

Figure 79. Fast decomposition area values plotted against slow decomposition area values for samples aged with visible light after 30 days, with ultraviolet light after 30 days, and under unaged conditions.

Figure 79 represents the areas obtained from thermal analysis. Compared to the plot of shift against oxidation ratios (Figure 78 upper), the same trend can be found, showing that only UV aged samples suffered from significant ageing.

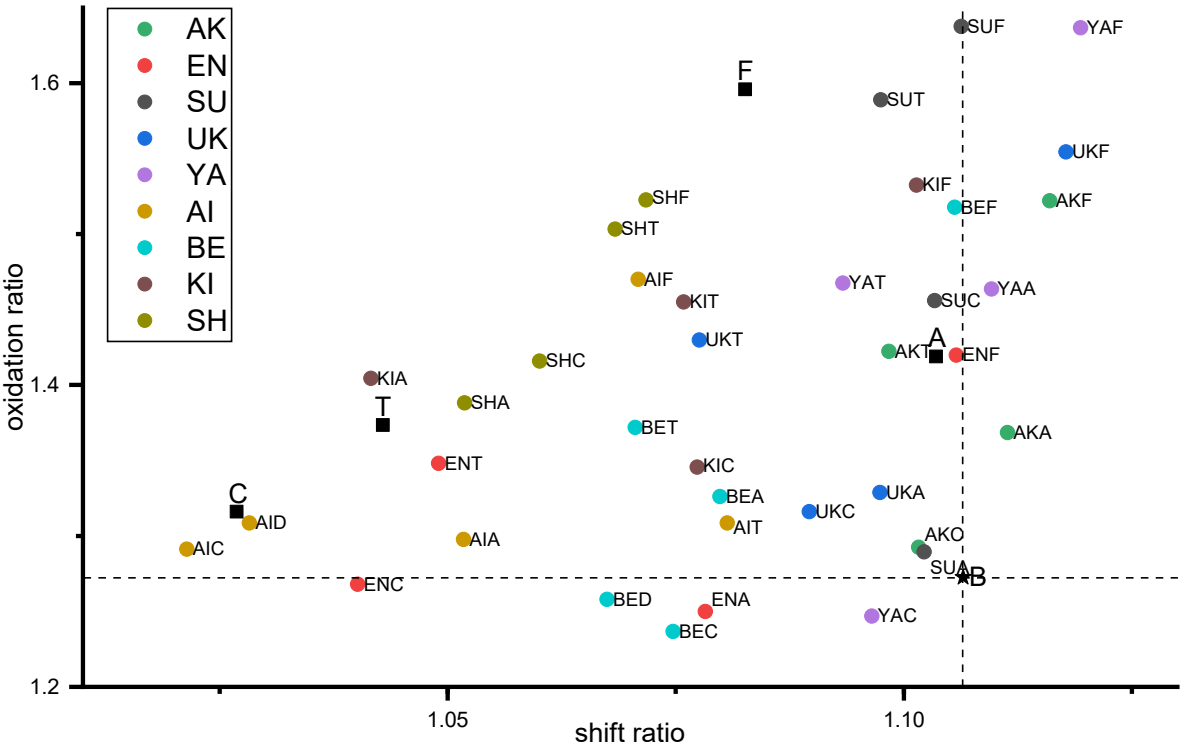

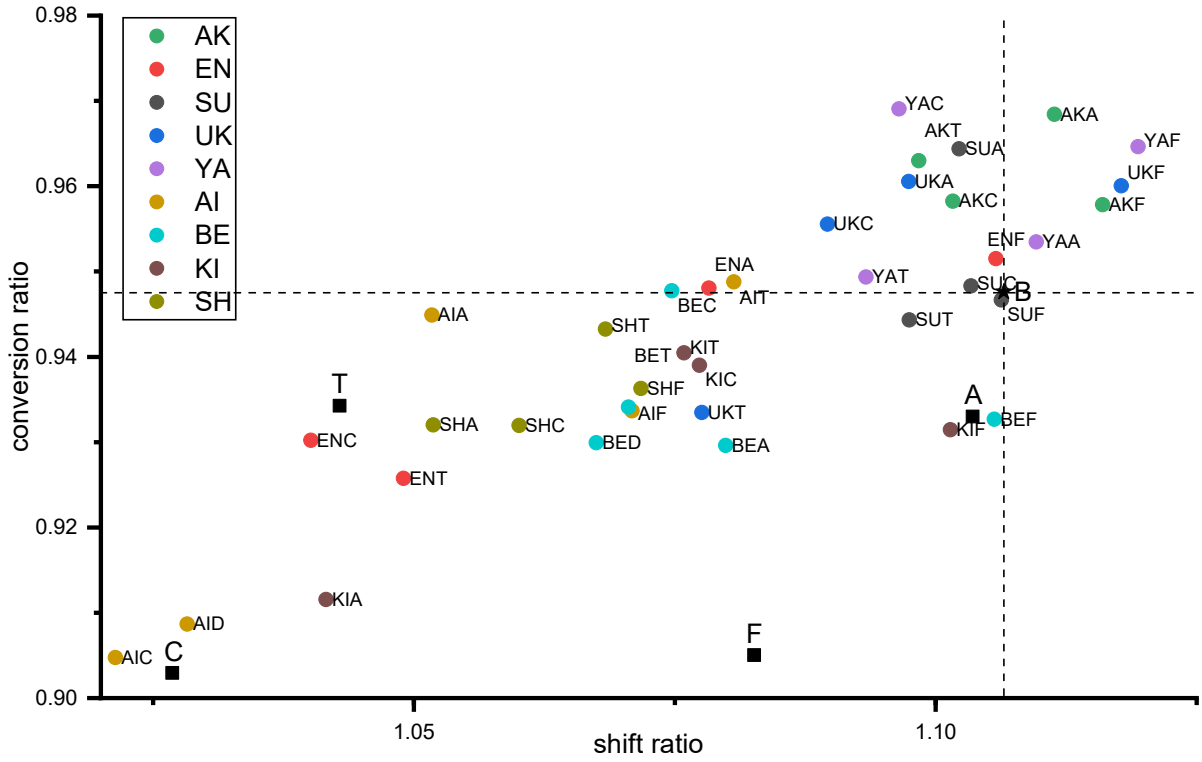

Figure 80. Shift ratio values against oxidation ratio values (upper plot) and against conversion ratio values (lower plot) are shown for dyed silk samples (circles), mordanted silk samples (black squares) and reference white silk B_UV_d30 (black star). All the values are referred to UV-aged specimens.

Figure 80 represents a close-up of the upper right parts of Figure 78 (upper). The most degraded samples appear in the upper right corner, including the samples dyed with *akane*, *yamahaji*, *ukon*, *suo*, *kihada*/iron, and *beni*/iron. Mordant-induced degradation can be inferred as well. They all show increased values of oxidation respect to the white sample, especially the iron-mordanted silk sample. This phenomenon can be explained by taking into account the occurrence of Fenton reactions [7]. Tannin and tartrate reduce the shift ratio with respect to white silk.

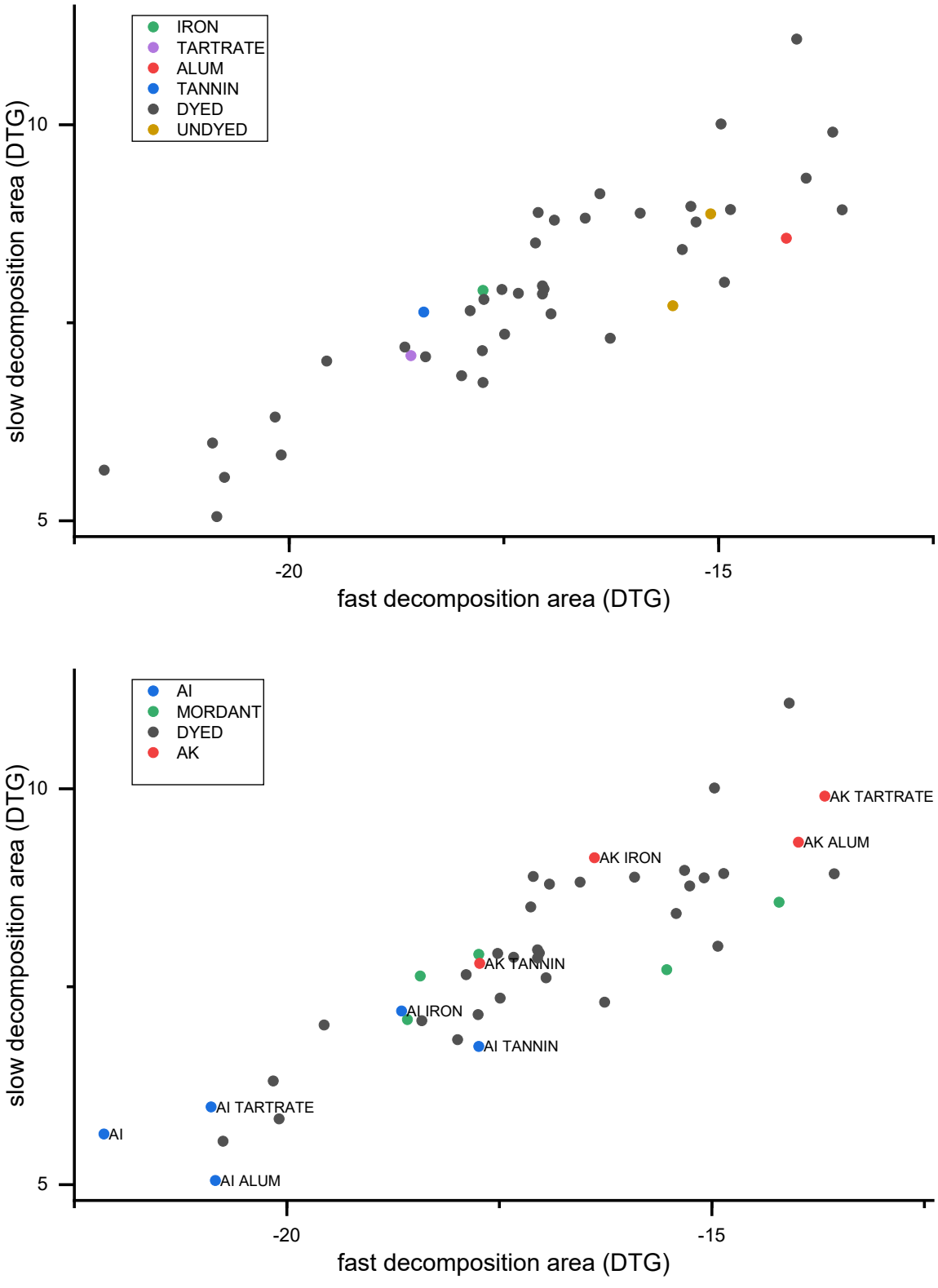

Figure 81. Fast decomposition area values plotted against slow decomposition area values for samples aged with ultraviolet light after 30 days.

When considering the same samples analyzed with TGA (Figure 81), the distribution of dyed samples is much wider with respect to the distribution of mordanted samples, whose area values are not very different from the values of the white silk. When considering the dyed

samples which stand at the limits of the distribution, it appears that all indigo-dyed samples regardless of the mordant show lower levels of degradation, while all the samples dyed with madder show higher levels of degradation. These findings exemplify the pivotal role of the dye compared to the role of the mordant in silk degradation.

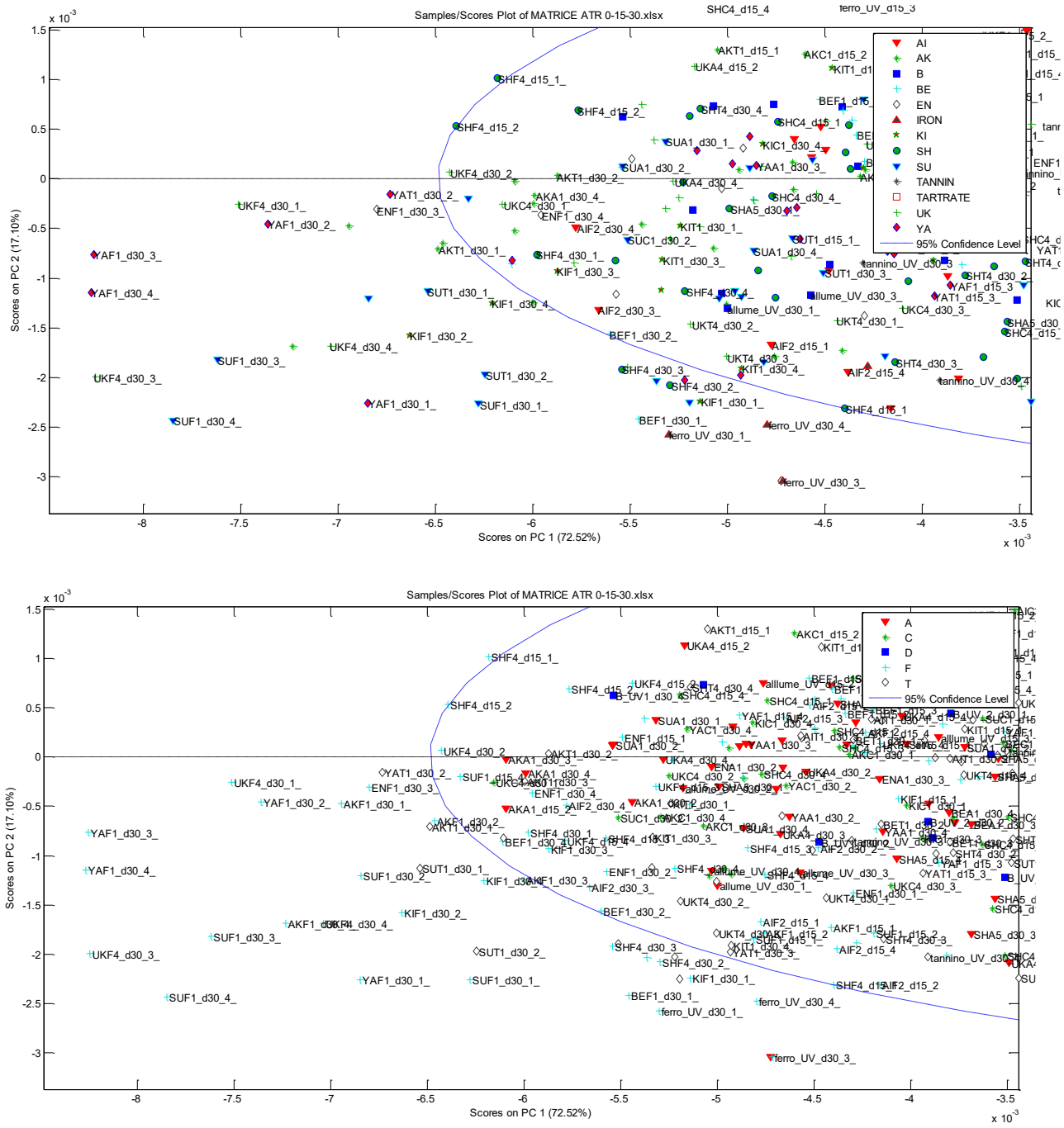

Figure 82. Scores plot of the PCA model obtained from the dataset containing all the samples. Close-up of the lower left part with samples coloured according to the dye (upper image); close-up of the lower left part with samples coloured according to the mordant (lower image)

Figure 82 shows a close-up of the PCA score plot presented in Figure 66. At low PC1 values, corresponding to high shift ratio values, the most degraded samples are found with small

differences, corresponding to those already mentioned above (*akane*, *suo*, *yamahaji*, *ukon*, *kihada*/iron, *beni*/iron). From the graphical representation of the PCA, where the samples are coloured based on the mordant used (Figure 82, lower), it appears that the most degraded samples are those dyed with the above-mentioned dyes and mordanted with iron sulfate and tannic acid. The samples dyed and mordanted with potassium alum, potassium bitartrate, and those dyed without mordant appear at less negative PC1 values and are thus likely less degraded.

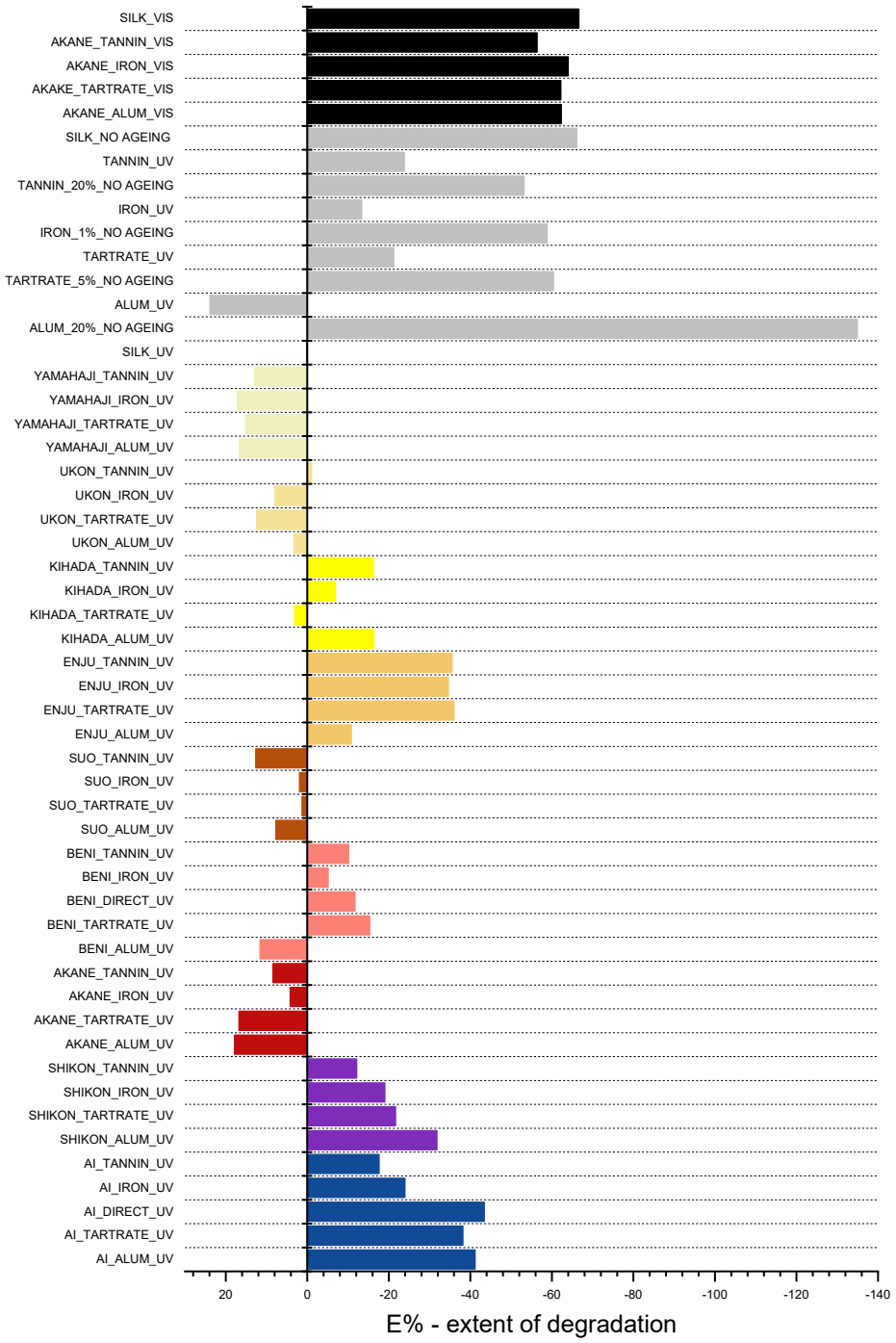

Figure 83. Extent of degradation, E%, derived from the DTG curves of the samples aged 30 days

Figure 83 shows the extent of degradation, E%, derived from the DTG curves of the samples aged for 30 days. All values are shown relative to 30-day UV-aged white silk (Silk_UV), which has a degradation value of 0. To the left of 0, positive E% values are shown, indicating samples that have undergone more degradation than Silk_UV, while to the right are samples that are less degraded than Silk_UV. Starting from the top, only a limited set of samples aged with visible light for 30 days is shown, as they all exhibit similar behavior. These include the white silk samples (Silk_vis) and the samples dyed with *akane* associated with various mordants, indicated by black bars. It is noted that the *akane*-dyed samples do not significantly differ from the undyed silk sample. All samples in this category show a lower degradation factor than the UV-aged white silk sample.

Further down the graph, the gray bars represent mordanted silk samples with various mordants, both unaged (no ageing) and UV-aged for 30 days. All these samples, except for the one mordanted with alum, have a lower degradation extent than Silk_UV, indicating that, during the ageing process, their combination dye/mordant seems to slow down fibre degradation. The dyes that have a protective function on the fibre, as they seem to slow down the degradation process, are *beni* with iron sulfate, direct *beni*, *beni* with potassium bitartrate and tannic acid, *enju*, *shikon*, and *ai* associated with all mordants. On the other hand, the samples dyed with *yamahaji* and *ukon* seem to accelerate degradation, as do the samples dyed with the *kihada/*tartrate (potassium bitartrate). Other dyes that accelerate fibre degradation include *suo*, *akane* with all mordants, and finally *beni* associated with alum.
The consistency between the results obtained with the two techniques (ATR-FTIR and TGA) clearly indicates that there is a strong correlation between the use of certain dye/mordant combinations and fibre degradation. In particular, some combinations have the ability to slow down degradation, while others accelerate it.

It is observed that dyes play a more crucial role in promoting degradation than the mordants they are bound to, as for some specific dyes degradation occurs regardless of the specific mordant used. The role of the only mordant with respect to unmordanted silk is not clear, as higher values of oxidation are observed, but lower shift ratio values. The data obtained from TGA are not definitive as they can be biased by the fire-retardant properties of some mordants. It is likely that mordanting with $FeSO_4$ turns into a higher degradation extent for the samples, characterized by particularly high levels of oxidation. The finding is in accordance with the results of other authors [8,9]. As for the other mordants, it seems that their presence has a protective role against the degradation of the fibre, as only mordanted silk generally shows lower degradation indicators with respect to white silk. Many of the treatments provided significant protection against phototendering, but the mechanisms behind this protection appear to vary. In cases where initial photostrengthening of silk occurred, it is likely due to intermolecular protein crosslinking triggered by light-induced free radical generation. Metal ions seem to promote the formation of these free radicals, which then undergo coupling to

create protein crosslinks. This process occurs in preference to free radicals that result from the cleavage of peptide chains, helping to maintain the structural integrity of silk [10].

While certain mordants may appear more frequently in heavily degraded samples, the extent of degradation in mordanted silk is far less pronounced compared to dyed samples. This suggests that the dye itself has a more significant impact on silk degradation than the mordant.

A list of the dyes considered in this study, divided according to their supposed protective or sensitizer properties, are listed below (Table 12).

UV-protective	Colouring molecule	Photosensitizers	Colouring molecule
Beni	Carthamin (benzoquinone)	*Yamahaji*	Fustin, ellagic acid, gallic acid (hydrolysable tannin)
Enju	Rutin (condensed tannin)	*Ukon*	Curcumin (carotenoid)
Shikon	Shikonin (anthraquinone)	*Suo*	Brasilin, Brasilein, hematoxylin (homoisoflavonoid)
Ai	Indigo (indigoid)	*Akane*	Alizarine, purpurine (anthraquinone)
Kihada	Berberine (alcaloid)		

Table 12. List of the dyes considered in this study, divided according to their supposed protective or sensitizer properties

A hypothesis regarding the photoprotective mechanism suggests that if dye decomposition occurs before fibre degradation, the loss in physical properties can be delayed, as the fibre is protected while the dye fades [8]. Yet, the evidence that *shikon* suffers from a dramatic fading yet offering protection from degradation suggests that the mechanism for photo-protection and for photo-tendering may involve various ways. For example, a possible photochemistry reaction is reported by Feng [11], where *shikonin* undergoes a photochemical reaction but it can return to the initial state thanks to a fluorescence mechanism involving the cleavage of H-O. Therefore, it can be proposed that the cleavage of hydrogen bonds in the molecules of some natural dyes contributes to their capacity to absorb UV light in a catalytic cycle (Figure 84). Again, an additional stabilising effect is for some anthraquinones can be given by the ability of the dye to dissipate absorbed energy through the rotation of bulky groups, such as benzene rings, (phenyl groups). This leads us to another structural factor influencing the stability of some anthraquinone dyes [12].

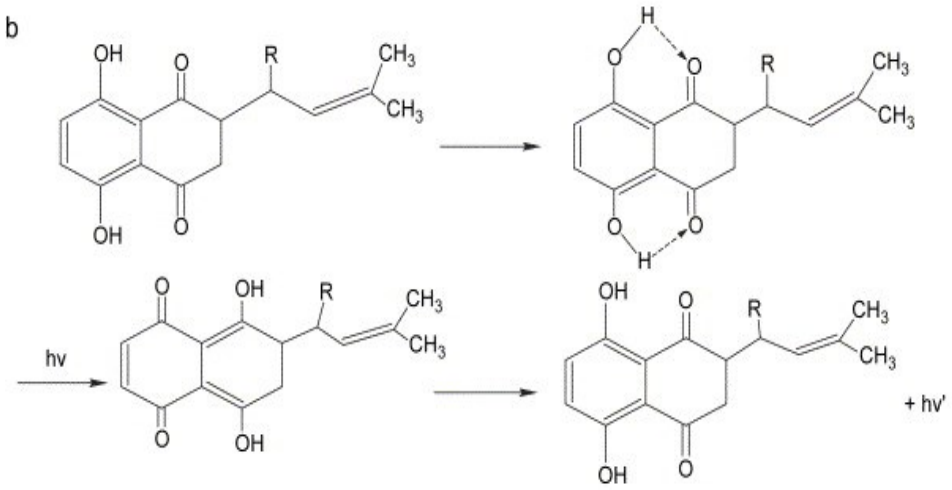

Figure 84. Depiction of UV-absorptive scheme for the natural dye shikon (Reproduced by [11])

Another case highlights the complexity of the interactions between dyes and their effects on textiles. Polyphenols, known for their ability to scavenge reactive oxygen species (ROS) and act as antioxidants [13], demonstrate varying effects when used as dyes, as seen with *enju* and *yamahaji*. Metal ion-mordanted polyphenolic dyes are not merely passive UV-screening agents. Instead, they engage actively in UV and visible light-induced reactions with silk, leading to changes in its mechanical properties. These photoreactions generate free radicals, which can either result in chain scission or crosslinking within protein matrix. The outcome depends largely on the mordant [9].

In the case of *enju*, a photoprotective effect is observed, suggesting that its antioxidant properties help shield the fibres. Conversely, *yamahaji* shows the opposite effect, leading to fibre deterioration. This difference could be attributed to the presence of other compounds in *yamahaji*, such as ellagic acid and gallic acid, or to the formation of photoproducts like 4-hydroxybenzoic acid during exposure to light [14]. These additional components may interfere with the dye's protective function, leading to increased fiber degradation.

The investigation of these degradation mechanisms goes beyond the scope of this current study and should be explored in future research. Specifically, a deeper analysis of the degradation products formed on the silk surface during accelerated ageing tests would provide valuable insights. This could include identifying the chemical byproducts and understanding their contribution to the overall degradation process, which may help elucidate the precise interactions between dyes, mordants, and fibre substrates under UV exposure.

3.7.5 Conclusion

Influence of mordants

When the effects of visible light and UV light ageing are compared, it appears that undyed silk exposure to visible light cannot produce measurable damage within 30 days of ageing.

The treatment of silk with a mordant induces a deep colour change in tannin and iron mordanted silk. It also induces significant increase of oxidative damage, which is further increased by UV ageing, with iron mordanted silk appearing as the most deeply affected. The other indicators of ageing show trends which are similar to those of white silk. Visible light exposure does not cause significant changes.

Influence of dyes

In examining the effects of visible and UV light on silk samples dyed with various mordants, distinct patterns of degradation emerge. When exposed to visible light, the samples show noticeable discoloration, but there is little evidence of fibre degradation or changes in their secondary structure. This suggests that visible light primarily affects the dye rather than the silk itself. Fibre oxidation increases for dyed samples respect to white silk, likely due to the dyeing conditions and the nature of the dye, as oxidation extent is different for each dye. Visible light ageing slightly increases oxidation values.

Conversely, UV light exposure causes more intense degradation to silk. UV ageing in air induces breakdown of the polymer and reduction of the amino acids in the amorphous region, which are converted into oxidation products. The samples exhibit significant discoloration, and the thermal analysis indicates clear changes compared to a reference sample of white silk. The ATR-FTIR analysis highlights some shifts in the Amide I region, pointing to conformational changes in the silk which are comparable to changes taking place in white silk. The most evident indicator of increased damage is oxidation, showing a marked increase for all the samples. The extent of degradation varied depending on the dye and mordant combination used, with tannin and iron mordanted samples generally showing the highest extent of oxidation.

A closer look at the data revealed a strong correlation between specific dye/mordant combinations and the level of fibre degradation. The most degraded samples can be identified both by ATR-FTIR and thermal analyses, whose results basically overlap. Certain dyes were found to play a critical role in degradation, regardless of the mordants. Conversely, some dyes protect the fibre, even when treated with mordants which promotes oxidative damage when considered alone. It emerges that dye plays a bigger role than mordant. For instance, dyes like *beni*, *enju*, *shikon*, and *ai* appeared to offer protective effects against degradation, while others such as *yamahaji*, *ukon*, *suo*, and *akane* seemed to promote it.

Impact on conservation

Specific mordants and dyes promote oxidative damage of silk. This information provides valuable insights for conservators responsible for the care and preservation of natural-dyed fabrics. Even fabrics that have not undergone extreme "weighting" processes, which are

common in some Western textiles, can still face substantial risk of physical damage due to light exposure. For instance, if a fabric is mordanted with iron or dyed with madder, a significant loss in physical properties can occur when subjected to light. Thus, faded objects are particularly vulnerable to further degradation if exposed to additional light, keeping in mind that exposures are cumulative when considering treatment, storage, or exhibition protocols. Understanding the presence of phototendering dyes is crucial for assessing the risk of degradation when exposed to light. This information can be gathered easily and non-invasively using techniques such as Fiber Optic Reflectance Spectroscopy (FORS) or Surface-Enhanced Raman Spectroscopy (SERS). For more detailed analysis, High-Performance Liquid Chromatography (HPLC) can be employed, though it is micro-destructive. By identifying these dyes, conservators can better gauge the potential vulnerability of the historical fabrics to light exposure and make informed decisions regarding their preservation and care.

An important aspect of this research involves the identification of early warning markers that allow for an objective assessment of silk fibre degradation at the molecular level long before visible signs of fibre breakdown occur. These markers have been validated using a dataset of undyed and dyed silk test fabrics, both before and after accelerated ageing. A strong correlation has been found between these markers and the chemical breakdown of fibroin. This understanding of degradation is particularly significant, especially for textiles that still bear considerable weight, such as garments and tapestries. The early warning system developed for monitoring oxidative deterioration in silk fibers serves as a micro-invasive yet highly effective tool, providing vital, objective insights into the chemical deterioration of textile fibers at an early stage. Such information is crucial for conservators and restorers, empowering them to take proactive measures during conservation and restoration efforts, thus protecting these delicate textiles from further damage.

3.7.6 References

[1] M.A. Koperska, D. Pawcenis, J. Bagniuk, M.M. Zaitz, M. Missori, T. Łojewski, J. Łojewska, Degradation markers of fibroin in silk through infrared spectroscopy, Polym Degrad Stab 105 (2014) 185–196. https://doi.org/10.1016/j.polymdegradstab.2014.04.008.

[2] S. Baltova, V. Vassileva, Photochemical behaviour of natural silk-II. Mechanism of fibroin photodestruction, 1998.

[3] G.D. Kang, K.H. Lee, Crosslinking reaction of Phenolic Side Chains in silk fibroin by Tyrosinase, Fibers and Polymers 5 (2004) 234–238.

[4] R. Dang, Y. Kang, H. Tan, Y. Yang, Color Damage of Visible Light on Plain-Woven Silk in Different Conservation States of Paintings and Calligraphy in Collections, Fibers and Polymers 25 (2024) 235–242. https://doi.org/10.1007/s12221-023-00414-2.

[5] S. Lee, S.H. Kim, Y.Y. Jo, W.T. Ju, H.B. Kim, H. Kweon, Effects of ultraviolet light irradiation on silk fibroin films prepared under different conditions, Biomolecules 11 (2021) 1–11. https://doi.org/10.3390/biom11010070.

[6] D.S. Bakirtzis, V.C. Tsapara, K.G. Kolovos, S.E. Liodakis, Assessment of the impact of fire retardants on the combustion of natural polymers employing DTG and LOI, Fire Mater 39 (2015) 109–118. https://doi.org/10.1002/fam.2232.

[7] M. Strlic, J. Kolar, Ageing and Stabilization of Paper, National and University Library, Ljubljana, Slovenia, 2005.

[8] M. Yatagai, Y. Magoshi, M.A. Becker, C. Sano, H. Ikuno, N. Kohara, M. Saito, Degradation and color fading of silk fabrics dyed with natural dyes and mordants, ACS Symposium Series 779 (2001) 86–97. https://doi.org/10.1021/bk-2001-0779.ch007.

[9] G.J. Smith, I.J. Miller, V. Daniels, Phototendering of wool sensitized by naturally occurring polyphenolic dyes, J Photochem Photobiol A Chem 169 (2005) 147–152. https://doi.org/10.1016/j.jphotochem.2004.06.014.

[10] I.J. Miller, G.J. Smith, Protection against phototendering of wool by metal salts and mordanted dyes, Journal of the Society of Dyers and Colourists 111 (1995) 103–106.

[11] X.X. Feng, L.L. Zhang, J.Y. Chen, J.C. Zhang, New insights into solar UV-protective properties of natural dye, J Clean Prod 15 (2007) 366–372. https://doi.org/10.1016/j.jclepro.2005.11.003.

[12] N.S. Allen, Photofading and light stability of dyed and pigmented polymers, Polym Degrad Stab 44 (1994) 357–374.

[13] P.G. Pietta, Flavonoids as antioxidants, J Nat Prod 63 (2000) 1035–1042. https://doi.org/10.1021/np9904509.

[14] M.P. Colombini, A. Andreotti, C. Baraldi, I. Degano, J.J. Łucejko, Colour fading in textiles: A model study on the decomposition of natural dyes, Microchemical Journal 85 (2007) 174–182. https://doi.org/10.1016/j.microc.2006.04.002.

4. Appendix: list of publications